Istituto Nazionale di Fisica Nucleare
LABORATORI NAZIONALI DI FRASCATI
SIS – Pubblicazioni

LNF–08/ 13 (P)
8 May, 2008

Papers presented at PAC 2007

Accelerator Division

Presented at the
2007 Particle Accelerator Conference (PAC 2007)
Albuquerque, New Mexico, USA, June 25-29, 2007

CONTENTS

NEW DEVELOPMENTS IN SUPER B-FACTORIES

P. Raimondi, INFN, Laboratori Nazionali di Frascati, Italy

Abstract

A Super Flavor Factory, an asymmetric energy e^+e^- collider with a luminosity of order 10^{36} cm^{-2}s^{-1}, can provide a sensitive probe of new physics in the flavor sector of the Standard Model. The success of the PEP-II and KEKB asymmetric colliders [1,2] in producing luminosity above 10^{34} cm^{-2}s^{-1} has taught us about the accelerator physics of asymmetric e^+e^- colliders in a new parameter regime. Furthermore, the success of the SLAC Linear Collider and FFTB [3], and the subsequent work on the ILC [4] allow a new Super-Flavor collider to also incorporate linear collider techniques. This paper describes the parameters of an asymmetric Flavor-Factory collider at a luminosity of order 10^{36} cm^{-2}s^{-1}at the Y(4S) resonance and 10^{35} cm^{-2}s^{-1} at the τ production threshold. Such a collider would produce an integrated luminosity of about 14,000 fb^{-1} (14 ab^{-1}) in a running year (10^7 sec) at the Y(4S) resonance. In the following only the parameters relative to the Y(4S) resonance will be shown, the ones relative to the lower energy operations are still under study.

INTRODUCTION

The construction and operation of multi-bunch e^+e^- colliders have brought about many advances in accelerator physics in the area of high currents, complex interaction regions, high beam-beam tune shifts, high power RF systems, controlled beam instabilities, rapid injection rates, and reliable uptimes (~95%).

The present B-Factories have proven that their design concepts are valid:

1) Colliders with asymmetric energies work well
2) BeamBeam energy transparency conditions are weak
3) Interaction regions with two energies can work
4) IR backgrounds can be handled successfully
5) High current RF systems can be operated (3x1.8 A)
6) Beam-beam parameters reach 0.06 up to 0.09
7) Continuous injection is done in production
8) The electron cloud effect (ECI) can be managed
9) Bunch-by-bunch feedbacks at the 4nsec spacing work well.

Lessons learned from SLC and subsequent linear collider studies (for ILC) and experiments (FFTB, ATF, ATF2) have also shown new successful concepts:

1) Small horizontal and vertical emittances can be produced in a damping ring with a short damping time
2) Very small beam spot sizes and beta functions can be achieved at the interaction region

All of the above techniques can be incorporated in the design of a future Super-Flavor Factory (SuperB) collider.

THE CRAB WAIST COLLISION SCHEME

The design is based on a new collision scheme, that we call a “crab waist”. This new scheme will allow SuperB to reach a luminosity of the order of 10^{36} cm^{-2}s^{-1} by overcoming some of the issues that have plagued earlier super e+e. collider designs, such as very high beam currents and very short bunches. In this section we will review the crab waist concept and address key issues related to high luminosity colliders, such as luminosity with a crossing angle, beam lifetime and injection, backgrounds, beam emittances and stability, polarization, power and costs.

In high luminosity colliders, one of the key requirements is very short bunches, since this allows a decreased β_y at the IP, thereby increasing the luminosity. However, β_y cannot be made much smaller than the bunch length without incurring an “hourglass” effect. Moreover, high luminosity requires small vertical emittance, together with large horizontal beam size and horizontal emittance, to minimize the beam-beam effect. It is, unfortunately, very difficult to shorten the bunch length σ_z in a ring.

This problem can be overcome with the recently proposed crab waist scheme [5] for beam-beam collisions, which can substantially increase luminosity without having to decrease the bunch length, since it combines several potentially advantageous ideas.

The first idea is the use of a large Piwinski angle: for collisions at a crossing angle θ, the luminosity L, the horizontal ξ_x and the vertical ξ_y tune shifts scale according to [6]:

$$\mathcal{L} = \frac{\gamma^+ \xi_y N^+ f_c}{2 r_e \beta_y}\left(1+\frac{\sigma_y}{\sigma_x}\right) \propto \frac{N^+ \xi_y}{\beta_y}$$

$$\xi_y = \frac{r_e N^-}{2\pi\gamma^+}\frac{\beta_y}{\sigma_y\left(\sigma_x\sqrt{1+\varphi^2}+\sigma_y\right)} \propto \frac{N^-\sqrt{\beta_y}}{\sigma_y\sigma_z\theta}$$

$$\xi_x = \frac{r_e N^-}{2\pi\gamma^+}\frac{\beta_x}{\sigma_x^2\left[(1+\varphi^2)+\frac{\sigma_y}{\sigma_x}\sqrt{1+\varphi^2}\right]} \propto \frac{N^-\beta_x}{(\sigma_z\theta)^2}$$

The idea of colliding with a large Piwinski angle is not new (see for example [7]). It has been also proposed for the LHC upgrade [8], to increase the bunch length and the crossing angle. In such a case, if it were possible to increase N in proportion to $\sigma_x\theta$, the vertical tune shift ξ_y would indeed remain constant, while the luminosity would grow proportional to $\sigma_z\theta$. Moreover, the horizontal tune shift ξ_x drops like $1/(\sigma_z\theta)^2$ so that for very large Piwinsky angle the beam-beam interaction can be considered, in some sense, one-dimensional, since the horizontal footprint in the tune plane shrinks. However, as distinct from [8], in the crab waist scheme described here, the Piwinski angle is increased by decreasing the horizontal beam size and increasing the crossing angle. In this way, the luminosity is increased, and the horizontal tune shift due to the crossing angle decreases. The most important effect is that the overlap area of colliding bunches is reduced, as it is proportional to σ_x/θ. Thus, if the vertical β-function β_y can be made comparable to the overlap area size:

$$\beta_y \sim \sigma_x, \quad \theta \ll \sigma_z,$$

Several advantages are gained:

- small spot size at the IP, i.e., higher luminosity
- reduction of the vertical tune shift
- suppression of vertical synchrobetatron resonances [9]

There are additional advantages in such a collision scheme: there is no need to decrease the bunch length to increase the luminosity, as proposed in standard upgrade plans for B and Φ-Factories [10–12]. This will certainly ease the problems of HOM heating, coherent synchrotron radiation of short bunches, excessive power consumption, etc... Moreover the problem of parasitic collisions (PC) is automatically solved by the higher crossing angle and smaller horizontal beam size, which makes the beam separation at the PC large in terms of σ_x.

However, a large Piwinski angle itself introduces new beam-beam resonances and may strongly limit the maximum achievable tune shifts (see for example [13]). This is where the crab waist innovation is required. The crab waist transformation boosts the luminosity, mainly by suppression of betatron (and synchro-betatron) resonances that usually arise (in collisions without the crab waist) through vertical motion modulation by horizontal beam oscillations [14]. A sketch of the crab waist scheme is shown in Fig.1.

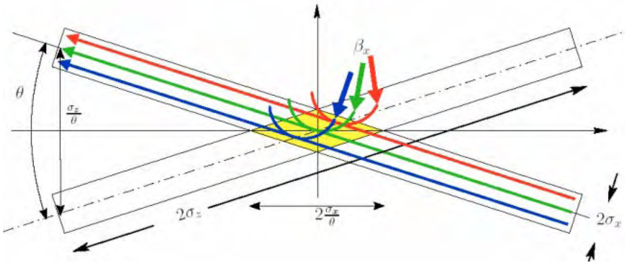

Figure 1 Large Piwinsky angle and crab waist scheme. The collision area is shown in yellow

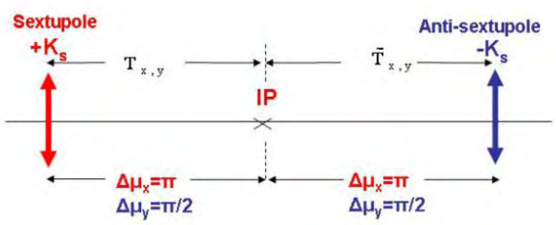

Figure 2 Crab waist correction by sextupole lenses

The crab waist correction scheme can easily be realized in practice with two sextupoles magnets in phase with the IP in the x plane and at $\pi/2$ in the y plane, on both sides of the IP, as shown in Fig. 2.

LUMINOSITY

For very flat beams, luminosity can be written as:

$$L = \frac{\gamma}{2er_e}\,\frac{I\,\xi_y}{\beta_y}$$

where I is the beam current, γ is the Lorentz factor, ξ_y the vertical tune shift, β_y is the vertical beta at the Interaction Point.

2. Synchrotron radiation power: Power dissipation is related to the beam current I and to the energy loss per turn U_o via:

$$P = I\,U_o.$$

All colliders aim to maximize L while keeping P as small as possible. The SuperB design is based on a “large Piwinski angle” and crab waist scheme as described above. This allows us to lower β_y to 0.2mm and increase ξ_y to 0.2. These values should be compared with the present KEKB parameters of β_y = 6 mm and ξ_y = 0.06. The SuperB parameters result in a luminosity about two orders of magnitude larger than that achieved at KEKB, with beam currents and power consumption essentially unchanged.

3. Detector backgrounds: Maintaining beam power as low as possible is important to minimize backgrounds, which scale with the beam currents. The interaction region (IR) design also plays a fundamental role. The combination of large crossing angle and small beam sizes, emittances and beam angular divergences at the IP in the SuperB design is very effective in further decreasing the absolute background levels with respect to the current B Factories. These same factors also relax design requirements for the IR. Luminosity-related backgrounds must, of course, be taken into account, and can impose serious shielding requirements.

4. Beam lifetime: In the current e^+e^- factories, beam lifetime is determined mainly by ring characteristics such as vacuum quality, dynamic aperture, etc. In SuperB, beam lifetime is instead almost entirely dominated by the luminosity itself: radiative Bhabhas limit the lifetime to a few minutes for both rings. All other contributions are much smaller, except for the Touschek lifetime of the low energy beam, which causes a worsening by about a factor 1.3. Given the short beam lifetime, the injection system must be able to provide particles at a rate about 10 times larger than those for the present factories.

5. Beam emittance: The horizontal emittance ε_x is determined mainly by the ring lattice optics; the vertical emittance ε_y is dominated by ring imperfections, which must be tightly controlled to reach the design value. The current factories, and most of the other e^+e^- colliders, have achieved vertical/horizontal emittance ratios similar to the SuperB design. However, the absolute values for SuperB are much smaller; they are similar to those at the test damping ring for the ILC project, the ATF [15]. Thus, tolerances, stability levels and tuning constraints are also

tighter than those for the current factories. Instead, they are very similar to those for the ATF and the design values for the ILC Damping Rings, which will produce beams very similar to those of SuperB.

6. Polarization: SuperB can provide collisions with longitudinally polarized electrons by using a polarized electron gun and spin rotators in the ring. Polarized positrons could be provided as well, but further study is required to evaluate whether the additional physics benefit outweighs the added complexity.

A vigorous R&D program is being pursued by the ILC community to provide a polarized positron source. Production rates required by SuperB are 100 times less demanding than those for the ILC, so such a source could be feasible by the time SuperB is funded.

7. Cost: In the conventional Super B Factory designs, the cost is dominated by the requirements for dealing with higher currents and shorter bunches: for example, substantial additions to the RF system, engineering design for larger HOM power due to shorter bunches, and the cooling and vacuum challenges posed by larger synchrotron radiation power. Most of these problems do not exist in the SuperB design; the absolute cost of SuperB is therefore very similar to the present machines. In addition, the SuperB design allows the reuse of a great deal of PEP-II hardware, resulting in substantial savings for the project, even at a new site.

SUPERB PARAMETERS

The IP and ring parameters have been optimized based on several constraints. The most significant are:

- maintaining wall plug power, beam currents, bunch lengths, and RF requirements comparable to present B-Factories;

- planning for the reuse as much as possible of the PEP-II hardware;

- requiring ring parameters as close as possible to those already achieved in the B-Factories, or under study for the ILC Damping Ring or achieved at the ATF ILC-DR test facility [15];

- simplifying the IR design as much as possible. In particular, reduce the synchrotron radiation in the IR, reduce the HOM power and increase the beam stay-clear. In addition, eliminate the effects of the parasitic beam crossings;

- relaxing as much as possible the requirements on the beam demagnification at the IP;

- designing the Final Focus system to follow as closely as possible already tested systems, and integrating the system as much as possible into the ring design.

Columns 1,2 of Table 1 show a parameter set that closely matches these criteria.

Many of the nominal SuperB design parameters could, in principle, be pushed further to increase performance. This provides an excellent upgrade path after experience is gained with the nominal design. The upgrade parameters are based on the following assumptions:

- beam currents could be raised to the levels that PEP-II should deliver in 2008;

- vertical emittance at high current could be reduced to the ATF values;

- the lattice supports a further reduction in β_x and β_y;

- beam-beam effects are still far from saturating the luminosity.

In principle, the design supports these improvements, so a luminosity higher than nominal may well be feasible. In addition, it should be pointed out that, since the nominal design parameters are not pushed to maximum values, there is flexibility in obtaining the design luminosity by relaxing certain parameters, if they prove more difficult to achieve, and pushing others. Columns 3,4 and 5,6 of Table 1 show two potential upgrade paths.

Table 1. SuperB Parameters list

PARAMETER	LER	HER	LER	HER	LER	HER
Particle type	e+	e-	e+	e-	e+	e-
Energy (GeV)	4	7	4	7	4	7
Luminosity x 10^{36}	1,0		2,4		3,4	
Circumference (m)	2250	2250	2250	2250	2250	2250
Revolution frequency (MHz)	0,13	0,13	0,13	0,13	0,13	0,13
Eff. long. polarization (%)	0	80	0	80	0	80
RF frequency (MHz)	476	476	476	476	476	476
Harmonic number	3570	3570	3570	3570	3570	3570
Momentum spread	8,4E-04	9,0E-04	1,0E-03	1,0E-03	1,0E-03	1,0E-03
Momentum compaction	1,8E-04	3,0E-04	1,8E-04	3,0E-04	1,8E-04	3,0E-04
Rf Voltage (MV)	6	18	6	18	7,5	18
Energy loss/turn (MeV)	1,9	3,3	2,3	4,1	2,3	4,1
Number of bunches	1733	1733	3466	3466	3466	3466
Particles per bunch x10^{10}	6,16	3,52	5,34	2,94	6,16	3,52
Beam current (A)	2,28	1,30	3,95	2,17	4,55	2,60
Beta y* (mm)	0,30	0,30	0,20	0,20	0,20	0,20
Beta x* (mm)	20	20	20	20	20	20
Emit y (pmr)	4	4	2	2	2	2
Emit x (nmr)	1,6	1,6	0,8	0,8	0,8	0,8
Sigma y* (microns)	0,035	0,035	0,020	0,020	0,020	0,020
Sigma x* (microns)	5,657	5,657	4,000	4,000	4,000	4,000
Bunch length (mm)	6	6	6	6	6	6
Full Crossing angle (mrad)	34	34	34	34	34	34
Wigglers (#)	4	2	4	4	4	4
Damping time trans/long(ms	32/16	32/16	25/12.5	25/12.5	25/12.5	25/12.5
Luminosity lifetime (min)	10,4	5,9	7,4	4,1	6,1	3,5
Touschek lifetime (min)	5,5	38	2,9	19	2,3	15
Effective beam lifetime (min)	3,6	5,1	2,1	3,4	1,7	2,8
Injection rate pps (100%)	4,9E+11	2,0E+11	1,5E+12	5,0E+11	2,1E+12	7,2E+11
Tune shift y (from formula)	.17	.17	0.16	0.16	0.02	0.02
Tune shift x (from formula)	0.004	0.004	0.007	0.007	0.009	0.009
RF Power (MW)	17		35		44	

RING AND INTERACTION REGION LATTICE

A detailed description of the lattice is presented in [16].

The Main ring lattice is composed by 6 arcs and two insertions, one for the Final Focus, and one for the Injection and tunes trombone etc. The straight sections in between the arcs are also suitable for installing 10m long wigglers. The basic arc cell, with a phase advance μ_x=0.5, μ_y=0.2, provides a much smaller emittance with respect to the TME cell adopted for the ILC damping ring, allowing a very compact ring, despite the need of very small emittances. The ring optical functions are shown in Figure 3.

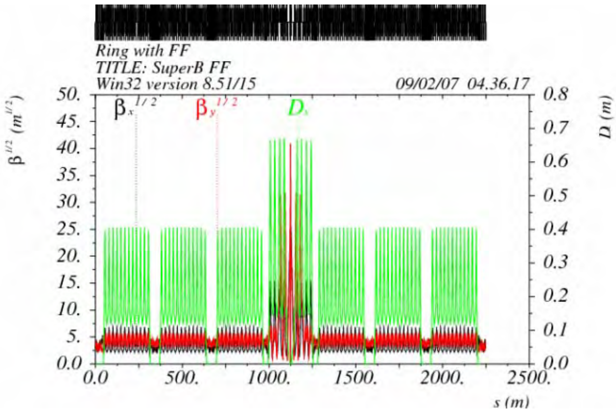

Figure 3 SuperB Optical Functions

The Interaction Region is being designed to leave about the same longitudinal free space as that presently used by *BABAR* but with superconducting quadrupole doublets as close to the IR as possible [17].

Recent work at Brookhaven National Laboratory on precision conductor placement of superconductors in large-bore low-field magnets has led to quadrupoles in successful use in the interaction regions for the HERA collider in Germany [18]. A minor redesign of these magnets will work well for the SuperB.

A design of the Final Focus, similar to the NLC/ILC ones, has been performed for the IP parameters in Table 1. The total FF length is about 2*150 m and the final doublet is at 0.3 m from the IP. The Final Focus is inserted in one of the straight sections of the ring. It also has to be noted that the Final Focus produce a net bend angle of about 43 degrees, roughly 2/3 of the one produced by one of the 6 ring arcs. The optical functions in the incoming half of the FF region are shown in Fig. 4.

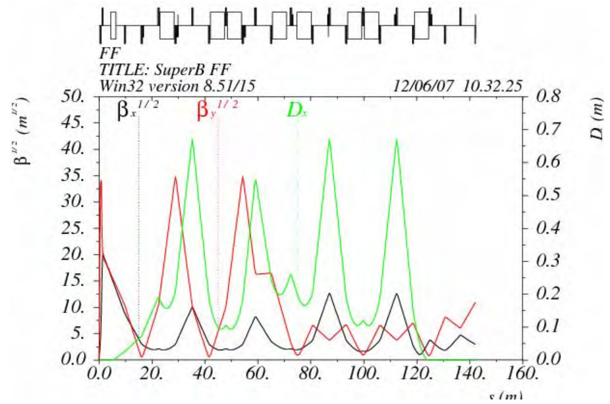

Figure 4 Optical functions in half Final Focus region.

The need for a finite crossing angle at the IP greatly simplifies the IR design, since the two beams are now naturally separated at the parasitic collisions. An expanded view of a preliminary IR layout is shown in Fig. 5. The LER radiative Bhabhas trajectories for several energies are also shown.

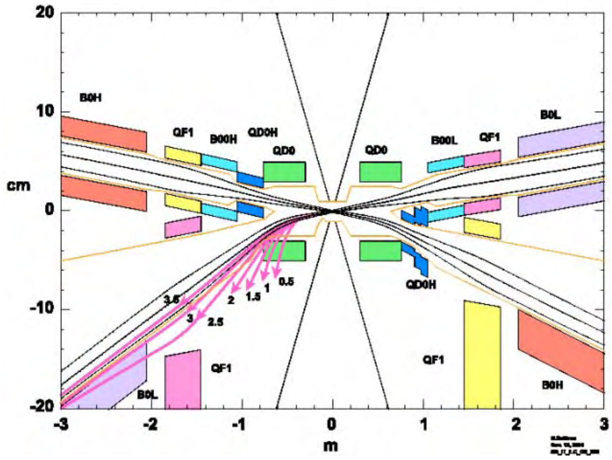

Figure 5 Plan view of a possible IR layout.

INJECTOR CONCEPT AND PARAMETERS

The injector for the Super Flavor Collider will make up for lost particles with the finite beam lifetime in the damping rings and the losses from collisions. The injector will be similar to the SLAC injector delivering about 10^{10} electrons or positrons per pulse at about 50 Hz each. The present scheme requires a 7GeV Linac to accelerate the electrons up to the nominal HER energy. A positron converter will be installed in the Linac at about 3GeV. The remaining 4GeV Linac will accelerate the positron up to the nominal LER energy. If the positron emittance results too large to allow an efficient continuous injection, a 1GeV damping ring will be necessary as well.

POWER REQUIREMENTS

The power required by a collider is the sum of a site base and the accelerator operation. The damping ring power (about 12 to 30 MW) to replace the synchrotron radiation loss will be the dominant factor in this Super-F Factory. About 6MW are needed to power up the rings magnets and 5MW for the injection system. Overall power consumption will range between 25MW up to 50MW for the ultimate parameters. Better estimates and optimizations are under study.

SYNERGY WITH ILC

There are significant similarities between the SuperB storage rings and the ILC damping rings [19]. Beam energies and beam sizes are similar. The ILC damping rings have a circumference three times larger than the SuperB rings (because of the need to store a long train of bunches with bunch spacing sufficiently large to allow injection and extraction of individual bunches); the nominal bunch charge is smaller in the ILC damping rings than in the SuperB storage rings, leading to a lower average current. Nevertheless, one may expect the overall beam dynamics in the two facilities to be in comparable regimes. A similar lattice design is used in both cases, the main difference being a reduction in circumference and the insertion of an interaction region in the case of SuperB.

The ILC damping rings and the SuperB storage rings will face similar demands on beam quality and stability: the SuperB rings for direct production of luminosity, and the ILC damping rings for reliable tuning and operation of the downstream systems, to ensure efficient luminosity production from the extracted beams.

The interaction regions have very similar characteristics with flat beams and overall geometries. The ratio of IP beta functions are similar (10-30 mm horizontally and 0.1-0.5 mm vertically). The collimation schemes are comparable. The chromatic correction of the final doublets using sextupoles is very similar and almost identical to the one tested in the FFTB experiment.

Other significant issues common to both the SuperB rings and the ILC damping rings include:

- alignment of the magnets, including orbit and coupling corrections, with the precision needed to produce vertical emittances of a few pm on a routine basis;
- reduction of magnet vibration to a minimum, to ensure beam orbit stability at the level of a few microns;
- optimization of lattice design and tuning to ensure sufficient dynamic aperture for good injection efficiency (for both SuperB and the ILC damping rings) and lifetime (particularly for the SuperB LER);
- bunch-by-bunch feedbacks to keep the beam instabilities and beam-beam collisions under control;
- control of beam instabilities, including electron cloud and ion effects.

These are all active areas of research and development for the ILC damping rings. In general, the similarity of the proposed operating regimes for the ILC damping rings and the SuperB storage rings presents an opportunity for a well-coordinated program of activities that could yield much greater benefits than would be achieved by separate, independent research and development programs.

DESIGN PROGRESS

The parameter optimization is continuously going on and we hope to further reduce the criticality of several machine constraints. In addition more careful studies are needed to make sure that the current constraints are valid.

The present scheme seems very promising but, given the rapid evolution of the concepts, it might still have some weak points that can jeopardize it. In addition new ideas and breakthroughs could also further change and improve the design.

It has also to be pointed out that with the present scheme the SuperB luminosity performance is a weak function with respect to the total length of the ring. The present length (about 2.2 Km) provides the best performances so far, but if there are strong constrains in terms of space and costs, it could be reduced together with a re-optimization of the other parameters.

ACKNOWLEDGMENTS

This document has come out of several SuperB workshops, with the most recent one being in Paris (France) on May 9-11, 2007. We appreciate very much the useful discussions with the participants in these workshops. We also appreciate the discussions of the parameters with members of the ILC collaboration.

REFERENCES

[1] KEKB Status report PAC 2005 Knoxville, TN.
[2] PEP-II Status report PAC2005 Knoxville, TN.
[3] The SLC Design Handbook, SLAC November 1984.
[4] ILC Technical Review Committee, Second Report 2003, ICFA SLAC-R-606.
[5] P. Raimondi, 2nd LNF Workshop on SuperB, Frascati, 16-18 March 2006, http://www.lnf.infn.it/conference/superbf06/
[6] P. Raimondi, M. Zobov, DAΦNE Tech.Note G-58, April 2003; D. Shatilov, M. Zobov, ICFA Beam Dynamic Newsletter 37, 99 (2005).
[7] K. Hirata, Phys. Rev. Lett. 74, 2228 (1995).
[8] F. Ruggiero, F. Zimmermann, Phys. Rev. ST Accel. Beams 5, 061001 (2002).
[9] D.V.Pestrikov, Nucl. Instr. Methods Phys. Res., Sect. A 336, 427 (1993).
[10] J. Seeman et al., Proc. of PAC05, 2333 (2005).
[11] H. Koiso, Proc. of PAC05, 64 (2005).
[12] "DANAE Letter of Intent," http://www.lnf.infn.it/lnfadmin/direzione/roadmap/DANAE LOI.pdf.
[13] K. Ohmi et al., Phys. Rev. ST Accel. Beams 7, 104401 (2004).
[14] P. Raimondi, D. Shatilov, M Zobov, LNF-07/003 (IR), Jan.2007.
[15] Y. Honda et al, Phys. Rev. Lett. 92, 054802 (2004).
[16] Y.Ohnishi et al, TUPAN049, This Conference.
[17] M. Sullivan, TUPAS066, This Conference.
[18] B. Parker et al., PAC 1999, New York, p. 308.
[19] "ILC Baseline Configuration Document": http://www.linearcollider.org/wiki/doku.php?id=bcd:bcd home.

EXPERIMENTAL RESULTS WITH THE SPARC EMITTANCE-METER*

D. Alesini, M. Bellaveglia, S. Bertolucci, R. Boni, M. Boscolo, M. Castellano, E. Chiadroni, A. Clozza, L. Cultrera, G. Di Pirro, A. Drago, A. Esposito, M. Ferrario, D. Filippetto, V. Fusco, A. Gallo, G. Gatti, A. Ghigo, M. Incurvati, C. Ligi, M. Migliorati, A. Mostacci, E. Pace, L. Palumbo, L. Pellegrino, R. Ricci, C. Sanelli, M. Serio, F. Sgamma, B. Spataro, F. Tazzioli, S. Tomassini, C. Vaccarezza, M. Vescovi, C. Vicario, INFN-LNF, Frascati, RM, Italy.
L. Giannessi, M. Quattromini, C. Ronsivalle, ENEA C.R. Frascati, RM, Italy.
L. Catani, A. Cianchi, INFN-Roma II, RM, Italy.
M. Petrarca, INFN-Roma I, Roma, Italy.
A. Bacci, S. Cialdi, A.R. Rossi, L. Serafini, INFN-Mi, Milano, Italy.
A. Cook, M. Dunning, P. Frigola, P. Musumeci, J. Rosenzweig, UCLA, Los Angeles, CA, USA.

Abstract

The SPARC project foresees the realization of a high brightness photo-injector to produce a 150-200 MeV electron beam to drive a SASE-FEL in the visible light. As a first stage of the commissioning a complete characterization of the photoinjector has been accomplished with a detailed study of the emittance compensation process downstream the gun-solenoid system with a novel beam diagnostic device, called emittance meter. In this paper we report the results obtained so far including the first experimental observation of the double emittance minimum effect on which is based the optimised matching with the SPARC linac.

INTRODUCTION

The SPARC project comprises an R&D photo-injector facility devoted to the production of high brightness electron beams to drive a SASE-FEL experiment in the visible light. The high beam quality produced by SPARC will also allow investigations into the physics of ultra-short beams, plasma wave-based acceleration, and production of X-ray Compton back-scattering. Moreover SPARC is the injector prototype of the recently approved SPARX project, that foresees the construction in the Frascati area of a new high brightness electron linac for producing SASE-FEL radiation in the range of 10-1 nm wavelength. The first phase of the SPARC project, that is now concluded, consists in characterizing the electron beam out of the photoinjector, a 1.6 cell S-band RF gun, at low energy (5.6 MeV with 120 MV/m peak field on the cathode), before the installation of the 3 S-band accelerating sections, which will boost the beam energy up to 150-200 MeV. In order to study the first few meters of beam propagation where space charge effects and plasma oscillations dominate the electron dynamics, a new sophisticated diagnostic tool has been installed and commissioned: the movable emittance-meter [1]. This device has allowed measuring the evolution of beam sizes, energy spread, rms transverse emittances and transverse phase space at different locations along the beamline. The experimental layout of the first phase of the project is shown in Fig. 1.

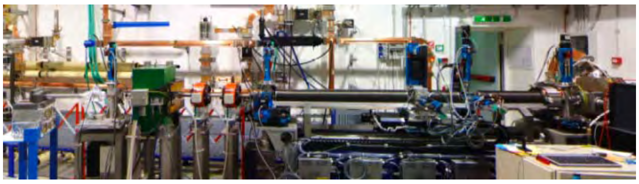

Figure 1: Picture of the SPARC photoinjector showing the RF gun with its solenoid (right end) the emittance meter (centre), the energy spectrometer and the beam dump (left end).

THE LASER SYSTEM

The SPARC laser is a 10 Hz TW system produced by Coherent [2]. It is composed by a Ti:Sa oscillator generating 100 fs pulses with a repetition rate of 79.3 MHz and an energy of 10 nJ. An acousto-optic programmable dispersive filter called “DAZZLER” used to modify the spectral amplitude and phase function, is placed between the oscillator and the amplifier to obtain the target temporal profile. After the amplification process the system delivers pulses at λ=800 nm with energy of about 50 mJ and a repetition rate of 10 Hz. At the output of the amplifier the IR pulses go to a third harmonic generator, where UV pulses with an energy of up to 4 mJ are produced. At the end of the laser chain there is a grating stretcher based on a pair of 4350 groove/mm UV reflecting gratings that is used to stretch the pulses temporally up to 8–12 ps and to reduce the pulse rise time. The optical transfer line to the cathode has been designed to increase the pointing stability, easily change the spot dimension and provide a normal incidence on the cathode surface. In combination with a quite high Quantum Efficiency (QE) up to 10^{-4} of the copper photocathode, obtained after a dedicated laser cleaning, the nominal electron beam parameters have been obtained with 50 μJ laser pulse energy at 120 MV/m peak field on the cathode.

* This work has been partially supported by the EU Commission in the sixth framework program, Contract No. 011935 EUROFEL and by Italian Minister of Research MIUR

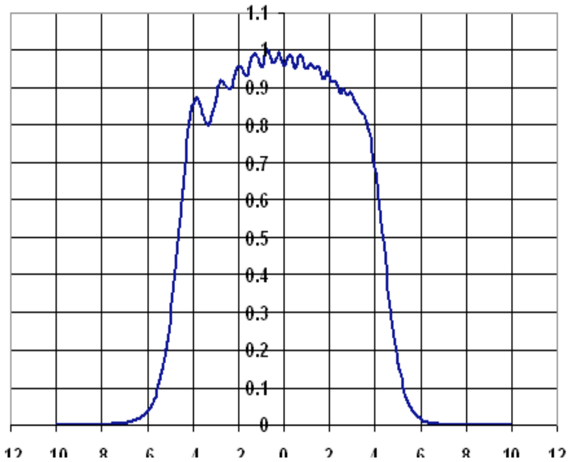

Figure 2: “Flat top” temporal laser pulse shape with 8.9 ps FWHM and 2.6 ps rise time.

A flat top laser pulse, retrieved from the spectral measurement, is shown in Fig. 2 and in Fig. 3 the corresponding emittance measurements. Additional work is under way to make this result more stable and improve also the uniformity of the transverse distribution.

THE EMITTANCE METER

In order to perform beam quality measurements at different locations along the beam line, a dedicated movable emittance measurement device, the emittance-meter, has been developed, see Fig. 1. This device allowed measurements of beam parameters in the range 1000 mm to 2100 mm from the cathode location, the so called Z-scan. The technique of measuring beam emittance and phase space distributions in the horizontal and vertical planes, makes use of a double system of horizontal and vertical slit masks. Each mask consists of a slit array (7 slits, 50 μm width spaced of 500 μm, 2 mm thick) and two single slits, 50 and 100 μm width). The beamlets emerging from the slit-mask are measured by means of a downstream Ce:YAG radiator. Images are acquired using digital CCD cameras (Basler 311f) equipped with simple 105 mm "macro" type objectives from SIGMA. The magnification used of about 0.66 gives a calibration near to 15 μm per pixel and a field of view of the screen around 9.6 x 7.2 mm. The resolution in the beam divergency is 100 μrad. Using a large number of samples (13 moving the single slit over the beam) it's possible to reconstruct the beam transverse phase space and follow its evolution along the beam line.

EXPERIMENTAL RESULTS

Measurements of emittance evolution along the photoinjector were the main goal of the first SPARC commissioning phase. Several runs were dedicated to compare of the dynamics of the beam under different conditions: moving the injection phase, changing the solenoid strength, and varying the longitudinal profile of the laser. The design goal in terms of peak current (92 A with 0.8 nC) and emittance (1.6 μm), corresponding to a peak brightness of 7 x10^{13} A/m^2, has been successfully achieved with a UV “flat top” laser pulse illuminating the cathode, see Fig. 2 and Fig. 3.

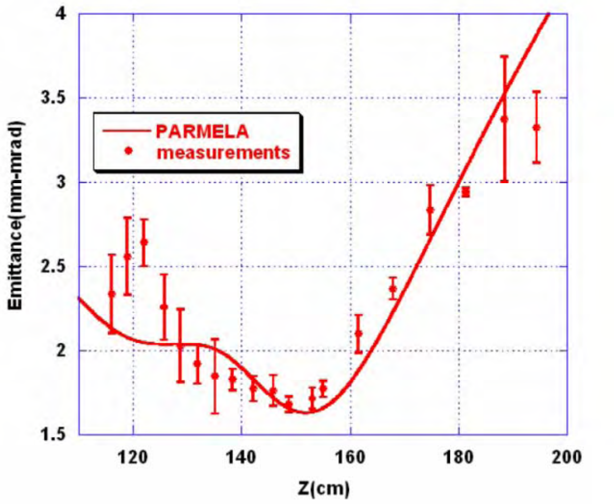

Figure 3: Emittance evolution, “flat top” case, measurements and PARMELA simulations

Of particular interest we found the comparison between a “flat top” longitudinal pulse with 85 A current 8.5 ps long, 2.5 ps rise time, and a Gaussian beam with the same FWHM length and current, as shown in Fig. 4. Superimposed in the figure are the results of PARMELA simulations using actual beam parameters, such as laser pulse length, beam size, launch phase, [3]. The results obtained confirm [4] the improved performances of the “flat top” charge distribution versus the Gaussian profile. Another important result is the first experimental observation of the double emittance minimum in the drift downstream the RF gun, in agreement to what expected from our theoretical model and numerical simulations.

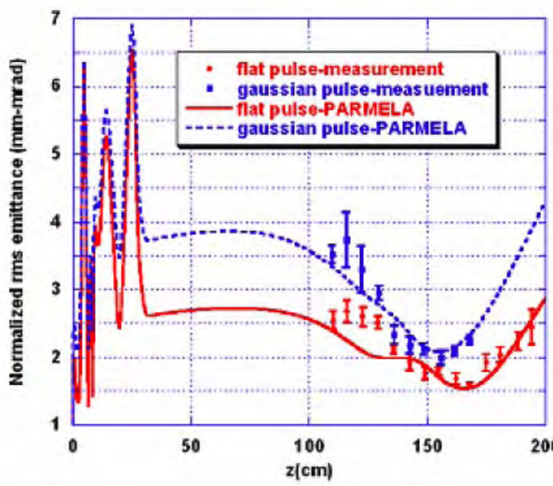

Figure 4 : Emittance evoution of Gaussian and “flat top” beams. Measurements and PARMELA simulations.

The optimized matching with the SPARC linac, will be based on this peculiar space charge regime acting in the flat top pulse mode [5] which foresees a matching to the invariant envelope in the Linac sections assuring the minimum emittance at the Linac exit [6]. Emittance oscillations of this kind have been explained as produced by a beating between head and tail plasma frequencies caused by correlated chromatic effects in the solenoid [7, 8]. We have obtained a direct evidence of this type of oscillation working with short laser rise time (1.5 ps) and moving the injection phase behind the maximum energy gain phase, thus inducing a higher energy spread in the beam, even if the minimum achievable emittance is larger in this case.

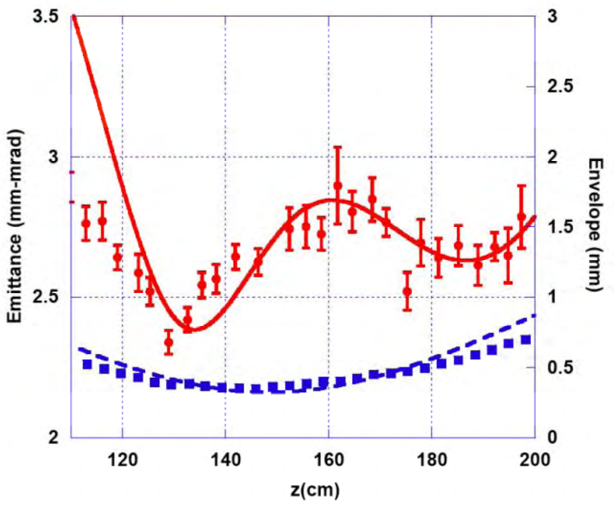

Figure 5: Envelope and Emittance downstream the RF gun of a “flat top” bunch.

The typical cross shape, shown by simulations in the transverse phase space of a flat top distribution at its relative emittance maximum, is also visible when reconstructed from beam measurements as reported in Fig. 6. In this case the head and tail of the bunch experience a different focal length when passing through the solenoid, caused by the space charge correlated energy spread that is strongly enhanced at the bunch ends.

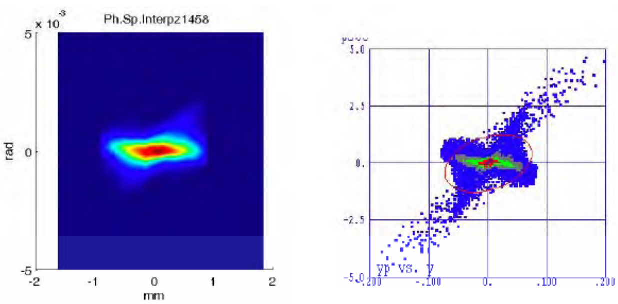

Figure 6: Transverse phase space at z=150 cm. Same beam of fig. 5

Under laminar conditions, i.e. when the solenoid field is not too high to cause cross-over, the space charge dominated waist is reached at different positions by the head and the tail slices of the bunch, so that when the bunch tail is already diverging the bunch head is still converging. In the Gaussian pulse case this cross shape in phase space is weaker since the slice current at the bunch “ends” is smaller. In particular, the bunch tails actually go through a cross-over, which prevents them from correctly undergoing the emittance correction process: this bifurcation is irreversible, leaving a part of the beam propagating as a split beam.

In Fig. 7 are shown the results of emittance versus solenoid magnetic field measurements at a fixed position (z=150 cm) for the same beam. The agreement with simulation is satisfactory when charge fluctuations of 6 % are taken in to account, a reasonable assumption in such a time consuming measurement. Notice that the emittance oscillation is visible also in this case. By increasing the solenoid field in fact the emittance oscillation tends to occur closer to the cathode. Thus, exploring the emittance at a fixed location by varying the B field, is equivalent to a continuous shift from different Z-scan curves.

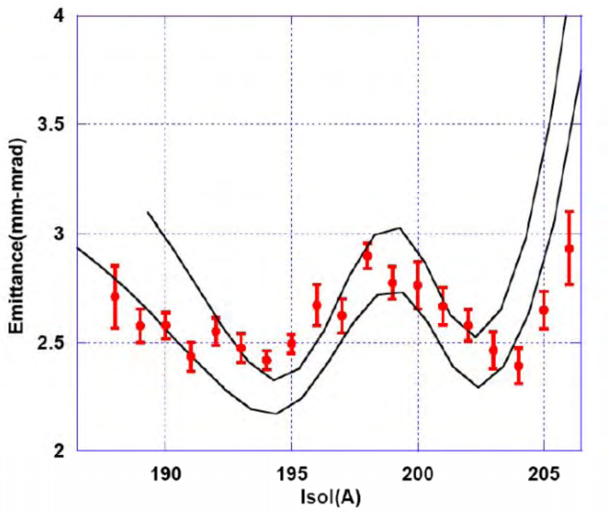

Figure 7: Emittance versus solenoid magnetic field at a fixed position (z=150 cm). Same beam of fig. 5. Simulations with charge fluctuations of 6 % are shown.

REFERENCES

[1] A. Cianchi et al., “Advanced Measurements at the SPARC Photoinjector” Proceedings of DIPAC (Venezia), 2007

[2] C. Vicario et al., “Drive Laser System for SPARC Photoinjector”, these Proceedings

[3] C. Ronsivalle et al., “Comparison Between SPARC E-Meter Measurements and Simulations” these Proceedings

[4] J. Yang et al., Journal of Applied Physics, V. 92, n, 3, (2002).

[5] M. Ferrario et al., “HOMDYN study for the LCLS RF photoinjector”, SLAC-PUB-8400, (2000).

[6] L. Serafini, J. B. Rosenzweig, Phys. Rev. E **55** (1997) 7565.

[7] M. Ferrario et al., “Recent Advances and Novel Ideas for High Brightness Electron Beam Production Based on Photo-Injectors”, SPARC-BD-03/003

[8] C. Wang et al., “Criteria for Emittance Compensation in High-brightness Photoinjectors”, these Proceedings.

DAΦNE Φ-FACTORY UPGRADE FOR SIDDHARTA RUN

M. E. Biagini, D. Alesini, D. Babusci, S. Bettoni, R. Boni, M. Boscolo, F. Bossi, B. Buonomo, A. Clozza, G. Delle Monache, T. Demma, G. Di Pirro, A. Drago, A. Gallo, S. Guiducci, C. Ligi, F. Marcellini, G. Mazzitelli, C. Milardi, F. Murtas, L. Pellegrino, M. Preger, L. Quintieri, P. Raimondi, R. Ricci, U. Rotundo, C. Sanelli, G. Sensolini, M. Serio, F. Sgamma, B. Spataro, A. Stecchi, A. Stella, S. Tomassini, C. Vaccarezza, M. Zobov, INFN Laboratori Nazionali Frascati, Frascati, Italy
K. Ohmi, KEK, Ibaraki, Japan
I. Koop, E. Levichev, P. Piminov, D. Shatilov, V. Smaluk, BINP, Novosibirsk, Russia

Abstract

An upgrade of the DAΦNE Φ-Factory [1] at LNF is planned in view of the installation of the Siddharta detector [2] in fall 2007. A new Interaction Region suitable to test the large Piwinski angle and *crab waist* (CW) collision schemes will be installed. Other machine improvements, such as new injection kickers, bellows and beam pipe layouts will be realized, with the goal of reaching luminosity of the order of 10^{33}/cm^2/s. The principle of operation of the new scheme, together with hardware designs and simulation studies, are presented.

DAΦNE PERFORMANCES

DAΦNE is an electron-positron collider working at the c.m. energy of the Φ resonance (1.02 GeV) to produce a high rate of K mesons. The collider complex consists of two independent rings having two common Interaction Regions (IR) and an injection system composed of a full energy linear accelerator, a damping/accumulator ring and transfer lines. Since 2000 DAΦNE has been delivering luminosity to three experiments, KLOE [3], FINUDA [4] and DEAR [5] steadily improving performances in terms of luminosity, lifetime and backgrounds. The DEAR experiment was performed in less than 5 months in 2002-2003, collecting about 100 pb^{-1}, with a peak luminosity of 0.7x10^{32} cm^{-2}s^{-1}. The KLOE experimental program has been completed in year 2006, acquiring more than 2 fb^{-1} on the peak of the Φ resonance, more than 0.25 fb^{-1} off-resonance and performing a high statistics resonance scan. The best peak luminosity obtained during this run was 1.5x10^{32} cm^{-2}s^{-1}, with a maximum daily integrated luminosity of about 10 pb^{-1}. In April 2006 started the second run of FINUDA [6], which collected 0.96 fb^{-1}. During this run a peak luminosity of 1.6x10^{32} cm^{-2}s^{-1} has been achieved, while a maximum daily integrated luminosity similar to that in the KLOE run has been obtained with lower beam currents, lower number of bunches and higher beta functions at the collision point. Fig.1 shows the daily peak luminosity for KLOE, DEAR and FINUDA runs. In fall 2007 a new setup will be installed for the Siddharta experiment, and a test of the new CW collision scheme will be performed. Beam-beam, backgrounds and dynamic aperture studies have been performed, showing the possibility of very good luminosity performances.

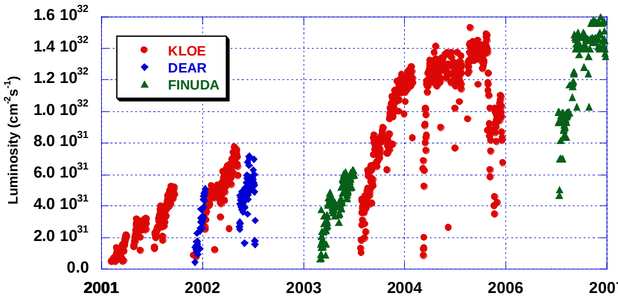

Figure 1: DAΦNE peak luminosity for KLOE (red), DEAR (blue) and FINUDA (green).

A NEW COLLISION REGIME

One of the key requirements in high luminosity colliders is a very small β_y^* at the IP. However, β_y^* cannot be much smaller than the bunch length without incurring in a “hourglass" effect, and this sets a stringent requirement on the bunch length σ_z. Indeed it is very difficult to shorten σ_z in a high current ring, as proposed in standard upgrade plans for Factories, without the problems of HOM heating, coherent synchrotron radiation, excessive power consumption and instabilities. The recently proposed CW scheme for collisions holds the promise of increasing the luminosity of storage-ring colliders by more than two orders of magnitude beyond the current state-of-the-art, without any significant increase in beam current and without reducing the bunch length. Moreover parasitic collisions (PC) become negligible because of the higher crossing angle and smaller horizontal beam size, which makes the beam separation at the PC large in terms of σ_x.

The main features of the CW scheme can be summarized as:

1. use of a large Piwinski angle, to decrease the length of the overlap area;
2. smaller β_y^* (of the same order of the length of the overlap area): this is the main source of the luminosity increase;
3. CW sextupoles to suppress the synchro-betatron resonances arising from the large crossing angle, which allow for significant ξ_y and luminosity increase, and avoiding vertical beam-beam blow-up.

A more detailed description of the principle can be found in [7, 8] this Conference.

The DAΦNE upgrade beam parameters are listed in Table 1: those corresponding to the KLOE run in 2006 are shown in parenthesis. With this new scheme it will be possible to reach a luminosity of the order of 10^{33} cm^{-2} s^{-1}, with very little modifications of the machine and beam currents similar to the already operational ones.

Table 1: DAΦNE Upgrade Beam Parameters

β_x^*(m)	0.2 (1.7)	**β_y^* (cm)**	0.65 (1.7)
σ_x (mm)	0.2 (0.7)	**σ_y (μm)**	2.6 (7)
ε_x (mm.mrad)	0.2 (0.3)	**Coupling**	0.5%
σ_z (mm)	20 (25)	**θ_{cross} (mrad)**	50 (25)
I_{bunch} (mA)	13 (13)	**$N_{bunches}$**	110 (110)
L x10^{32} (cm^{-2} s^{-1})	10 (1.5)	**N_{part}/bunch**	2.65x10^{10}

BEAM-BEAM STUDIES

Beam-beam studies have verified the validity of the CW idea [1, 8]. The effect of the betatron resonances suppression by the CW becomes obvious when looking at the luminosity scan versus betatron tunes. Fig. 2 shows a luminosity scan in the tunes plane performed for DAΦNE in the Siddharta configuration [1]. The scan on the left is with the CW sextupoles, the right one without. The red color corresponds to the maximum luminosity, the blue one to the minimum. With the CW many X-Y betatron resonances disappear or become much weaker, so the good working area is significantly enlarged, and the maximum luminosity is increased: a peak of 2.97x10^{33} cm^{-2} s^{-1} compares with L_{max} = 1.74x10^{33} cm^{-2} s^{-1} without CW.

Moreover in the CW collision a high luminosity can be obtained at the working points presently used at DAΦNE, like (0.09, 0.16). It should be noted that the worst luminosity value obtained in the CW collisions, 2.52x10^{32} cm^{-2} s^{-1}, is still higher than the present best luminosity obtained at DAΦNE.

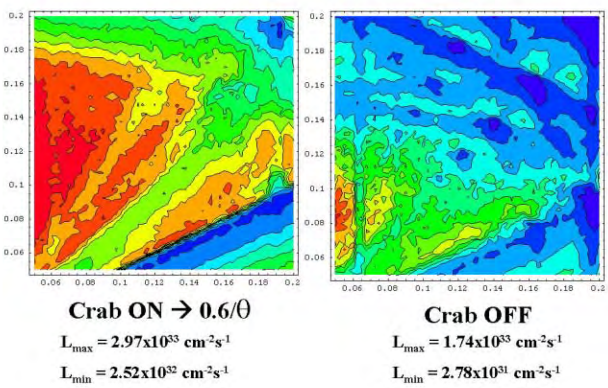

Figure 2: Luminosity vs tunes scan. CW ON, 0.6/θ (left). CW OFF (right).

An important limitation arising from the beam-beam interaction is the lifetime reduction. The beam-beam collisions create non-Gaussian tails in the transverse beam charge distributions. If the tails reach the physical or dynamic aperture the particles get lost, leading to lifetime degradation. In order to simulate the beam-beam induced tails the numerical code LIFETRAC [9] has been used. The CW sextupoles have been inserted in an implicit way, as lattice elements satisfying the CW conditions, i.e. having the required strength and betatron phase advances. Fig. 3 shows the beam distribution contour plots in the space of the normalized transverse amplitudes A_x/σ_x and A_y/σ_y. For all the plots the maximum horizontal amplitude A_x is 12σ_x and the vertical one 160σ_y. The successive contour levels are at a constant ratio of $e^{1/2}$ between each other. Each column contains plots for different strengths of the crabbing sextupoles K: K = 1 means the exact crabbed waist condition, for K = 0 the crabbing sextupoles are off.

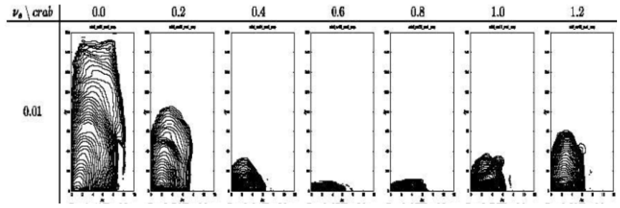

Figure 3: Distribution tails vs crabbing sextupole intensity.

A peak luminosity of about 3x10^{33} cm^{-2} s^{-1} is achieved. The maximum luminosity is obtained for slightly lower sextupole strengths (K=0.6÷0.8) than required for the "exact" CW condition (K=1). The luminosity optimum corresponds also to the shortest distribution tails. With stronger or weaker sextupoles the tails start growing indicating possible lifetime problems. It is worth remarking that even without crabbing sextupoles (see the plots with K=0), a peak luminosity higher than 1.0x10^{33} cm^{-2} s^{-1} can be achieved. Clearly the tails are much longer in this case. However, the lifetime can be improved with dynamic aperture optimization or by using slightly lower bunch currents.

BACKGROUND STUDIES

Machine backgrounds and lifetime will be dominated by the single Touschek scattering, as it is for the DAΦNE present configuration. Simulations of the Touschek effect with the CW scheme have been performed [10]. Particle losses due to Touschek effect are expected to be quite high with the Siddharta optics, mainly due to the smaller emittance. However, the longitudinal position of collimators has been optimized for the new optics and they are expected to be very efficient, even if a good compromise between losses and lifetime has necessarily to be found experimentally. In addition, careful design of the detector shielding is underway.

DYNAMIC APERTURE STUDIES

Dynamic aperture studies have been performed with the Acceleraticum code developed at BINP [11], where a numerical algorithm is used to choose "the best" pairs of sextupole magnets in order to optimize the chromaticity correction. Moreover a tune working point was chosen which satisfies the requirements of high luminosity and large dynamic aperture. The “best pair” optimization method provides a dynamic aperture ≥20 σ_x off-coupling and >250 σ_y full coupling, with an energy acceptance of ~1%. These values seem quite satisfactory to provide high luminosity and a successful experimental run. It is worth noting that one of the promising tune points {5.105, 5.16} practically coincides with the present operational values. Fig. 4 shows the optimized DA for three different working points, corresponding to good areas in the luminosity versus tunes plot.

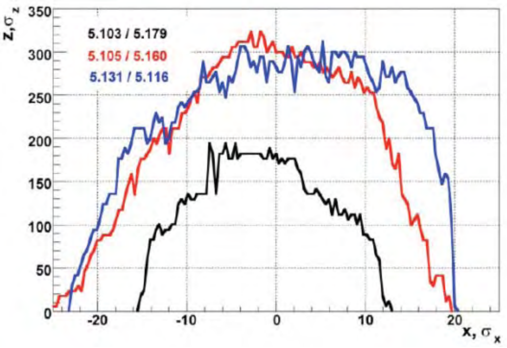

Figure 4 - Optimized DA for different working points.

HARDWARE MODIFICATIONS

A layout of the upgraded DAΦNE is shown in Fig. 5, and the main hardware changes are briefly illustrated in the following. Details are available in the papers presented at this Conference [12,14].

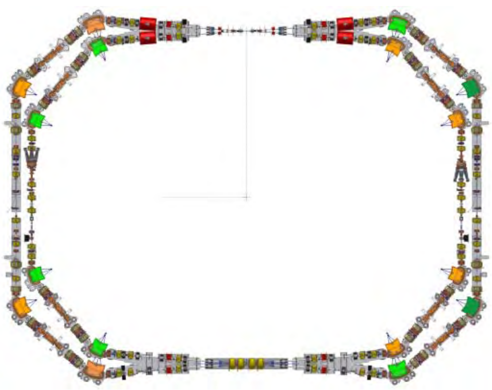

Figure 5: Upgraded DAΦNE layout.

Interaction Regions layout

IR1 has been modified [12] for the installation of the Siddharta experiment, and equipped with new quadrupoles to be able to lower β^* at the IP. The total crossing angle has been increased from 30 mrad to 50 mrad. Existing sextupoles will be used as CW sextupoles. New beam pipes have been designed for this scheme. In IR2 the beams will travel through vertically separated vacuum chambers without low-β focusing.

IR1 quadrupoles

Two new permanent magnet quadrupole doublets are needed in order to focus the beams to the smaller β^* at the IP. The first quadrupole of the doublet is horizontally defocusing, common to both beams in the same vacuum chamber: it provides a strong separation of the beams. The following QFs are particularly small, in order to fit separated beam pipes for the two beams.

Fast Injection kickers

New, fast kickers have been designed and built [13], based on a tapered strip with rectangular vacuum chamber cross section. The deflection is given by both the magnetic and the electric fields of a TEM wave traveling in the structure. Compared to the present DAΦNE injection kickers the new ones have a much shorter pulse (~12 ns instead of ~150 ns), better uniformity of the deflecting field, lower impedance and the possibility of higher injection rate (max 50 Hz).

New bellows

Four new bellows [14] are placed in each sector, connecting pipes with circular cross section (D = 88 mm). A RF shield is necessary to hide the chamber discontinuity to the beam. The coupling impedance of the structure has been evaluated in a frequency range from DC to 5 GHz and comes out to be very low.

CONCLUSIONS

Past approaches of collider optimization, followed over several decades, have now run into a dead end. The novel collision scheme with large crossing angle and CW uses hitherto frozen variables in parameter space to ascend to a new luminosity scale, by effectively exchanging the roles of the longitudinal and transverse dimensions. A new IR layout for the Siddharta run, compatible with the new scheme, has been designed and built. Operation will start in fall 2007. The predicted luminosity boost is based both on geometric and beam dynamics considerations, fully supported by extensive beam-beam simulations. With the test of the new idea at DAΦNE top-of-the-line accelerator physics should be at reach.

REFERENCES

[1] D. Alesini et al, LNF-06/033 (IR), 2006.
[2] Siddharta Coll., EPJ A31 (2007), 537-539.
[3] KLOE Coll., Nucl. Inst. Meth. A 482, 363-385 (2002).
[4] FINUDA Coll., Proc. HYP2000 (Torino, 2000).
[5] DEAR Coll., Physics Letters **B**, Vol. 535 (2002) 52.
[6] C. Milardi et al, TUPAN033, This Conference.
[7] P. Raimondi, MOZAKI02, This Conference.
[8] M. Zobov et al, TUPAN037, This Conference.
[9] D. Shatilov, Particle accelerators 52, 65 (1996).
[10] M. Boscolo et al, TUPAN031, This Conference.
[11] E. Levichev et al, DAΦNE Tech. Note G-59, 2006.
[12] S. Tomassini et al, TUPAN036, This Conference.
[13] D. Alesini et al, DAΦNE Tech. Note I-17, 2006.
[14] F. Marcellini, FRPMN028, This Conference.

ABSOLUTE BUNCH LENGTH MEASUREMENTS AT THE ALS BY INCOHERENT SYNCHROTRON RADIATION FLUCTUATION ANALYSIS*

F. Sannibale, M. S. Zolotorev, LBNL, Berkeley, CA 94720, U.S.A.
D. Filippetto INFN-LNF, Frascati, Rome, Italy.
G. V. Stupakov, SLAC, Stanford, CA 94309, U.S.A.

Abstract

By analysing the pulse to pulse intensity fluctuations of the radiation emitted by a charge particle in the incoherent part of the spectrum, it is possible to extract information about the spatial distribution of the beam. At the Advanced Light Source (ALS) of the Lawrence Berkeley National Laboratory, we have developed and tested a simple scheme based on this principle that allows for the absolute measurement of the bunch length. A description of the method and the experimental results are presented.

INTRODUCTION

Several different processes allow for the emission of photons from moving charged particles: synchrotron radiation, Cerenkov radiation, transition radiation, etc. In all these processes the presence of incoherent radiation is due to the fact that particles are randomly distributed along the beam. For example, in the case of an ideal coasting beam composed by a large number of particles equally separated by a longitudinal distance *d* and moving along a circular trajectory, there is no synchrotron radiation emission up to those frequencies whith wavelength < *d*. In fact below those frequencies, the interference between the radiation emitted by the evenly distributed electrons will produce a vanishing net electric field. In a more realistic coasting beam, the same particles are now randomly distributed along the orbit causing a small modulation of the beam current. The effect of such a random modulation is that the interference is not fully destructive anymore and a net nonzero electric field shows up. If the turn by turn position of the particles along the beam changes (due for instance, to longitudinal dispersion or to path length dependence on transverse position), then the modulation changes and the energy radiated in a single pass fluctuates turn by turn. By measuring the radiation intensity over multiple passages, we find that for a sufficiently large sample, the measured spectrum converges to the characteristic incoherent spectrum of the radiation process under observation (synchrotron radiation in our example). The passage from the coasting to the bunched beam case introduces a strong coherent emission at those wavelengths comparable or longer than the bunch length, but does not modify the higher frequency part of the spectrum.

It has been shown for the case of a bunched beam [1], that by measuring the pulse to pulse intensity fluctuation of the radiation within a bandwidth $\Delta\omega$ in a region of the spectrum where no coherent emission is present, it is possible to perform absolute measurements of the bunch length. A frequency domain version of such a technique has been already proved experimentally by using a configuration that requires a photon spectrometer [2-4].

In this paper, we describe a significantly simplified scheme that does not require complex and expensive intrumentation and that allows for accurate absolute measurements of the bunch length. We tested the technique at the ALS and the results were compared with the ones from streak camera measurements.

METHOD DESCRIPTION

In this scheme, the energy radiated by the bunch in a single pass is measured. The photons are collected within a narrow band around a frequency where no coherent emisssion is present. Values of radiated energy per passage *W* are measured and recorded for many passages of the beam. *W* fluctuates passage to passage and its relative rms variation of δ, is given by [1]:

$$\delta^2 = \frac{\sigma_W^2}{\langle W \rangle^2} = \int_{-\infty}^{\infty}\int_{-\infty}^{\infty} dt dt' \frac{\left|K(t-t')\right|^2}{\left|K(0)\right|^2} I(t) I(t') \qquad (1)$$

whith *I* the normalized longitudinal bunch distribution and *K* the time domain response of the system to a delta function excitation (if a bandpass filter is used, *K* is the inverse Fourier transform of the filter transmission curve).

For the case of a gaussian beam with rms length in time units σ_τ and of a gaussian filter with rms bandwidth σ_ω, Eqn. (1) can be readily integrated:

$$\delta^2 = 1\Big/\sqrt{1+4\sigma_\tau^2\sigma_\omega^2} \qquad (2)$$

This last expression shows that if σ_ω is known, then by measuring δ one can derive the absolute value of the rms bunch length. Expression (2) has been obtained for gaussian beams, but numerical integration of (1) for nongaussian distributions showed that the accuracy of (2) is good at the few percent level for most of the distributions, as long as they are represented by their rms length and do not include microstructures with characterisitc length much smaller than the bunch length.

For $\sigma_\tau >> 1/(2\sigma_\omega)$, we have $\delta^2 \sim 1/(2\sigma_\tau \sigma_\omega)$, and using the fact that the longitudinal coherence length for an

* Work supported by the Director, Office of Science, of the U.S. Department of Energy under Contract DE-AC02-05CH11231.

electromagnetic mode with frequency content σ_ω is $\sigma_{tc} = 1/(2\sigma_\omega)$** we can write:

$$\delta^2 = \sigma_{tc}/\sigma_\tau = 1/M \quad (3)$$

where M is the number of modes contained in the bunch. Equation (3) leads to the nice physical interpretation that the intensity fluctuation is due to M independent modes radiating randomly within the bunch.

The results presented so far assumed a bunch with no transverse size. By including the effect of the finite transverse size for the example case of gaussian transverse distributions we obtain:

$$\delta^2 = \left(1+\sigma_\tau^2/\sigma_{tc}^2\right)^{-\frac{1}{2}}\left(1+\sigma_x^2/\sigma_{xc}^2\right)^{-\frac{1}{2}}\left(1+\sigma_y^2/\sigma_{yc}^2\right)^{-\frac{1}{2}} \quad (4)$$

with σ_x and σ_y the rms horizontal and vertical beam sizes respectively and σ_{xc} and σ_{yc} the coherence sizes of the related transverse electromagnetic modes at the wavelength of operation. Such quantities are defined by the properties of the radiation process and must include diffraction effects due to limiting apertures.

It can be shown that the statistical error on δ^2 when N_s samples are collected is given by:

$$\sigma_{\delta^2}/\delta^2 = \sqrt{2/N_s} \quad (5)$$

EXPERIMENTAL SETUP

Figure 1, shows the experimental setup for the measurements performed at the beamline BL7.2 of the Advanced Light Source (ALS) in Berkeley. Such a beamline collects the synchrotron radiation from a dipole magnet and has a total angular acceptance of 5.5 mrad and 2.8 mrad for the horizontal and vertical plane respectively (represented by the limiting aperture in Fig. 1). BL7.2 spectrum ranges from the far-infrared up to the top part of the visible portion.

In our application we used visible light, which is in the incoherent part of the spectrum and allows using the large variety and relatively inexpensive optical components and detectors readily available for such a frequency range. A 1 m focal length lens was used to focus, through a flat mirror, the beam on the photocathode plane of a streak camera (Hamamatsu C5680). The mirror could be retracted in order to allow for the light to go into another branch for the fluctuation measurement. An interferometric filter (Melles Griot) with gaussian transmission curve centered at 632.8 nm and with peak transmission of 55% selected the photons within a bandwidth of 1 nm FWHM. The first lens focal length was chosen for keeping the angle between the incoming photon trajectories and the normal to the filter plane small enough to avoid broadening of the filter bandwidth. Downstream the filter the transmitted photons were finally focused by a microscope objective (Edmund DIN 10, F 0.25) on the 0.2 mm^2 sensitive area of an avalanche photodiode (Perkin Elmer C30902S, gain 250, ~600 MHz bandwidth, ~ 60% quantum efficiency at 632.8 nm). The signal from the photodiode was amplified (Hamamatsu C5594, 50k-1.5G Hz bandwidth, 36 dB gain) and sent to a digital oscilloscope (LeCroy Wavepro 7300 A, 3 GHz bandwidth and 20 Gsamples/sec) for data recording and analysis. The oscilloscope was triggered with the ~ 1.5 MHz revolution clock of the ALS.

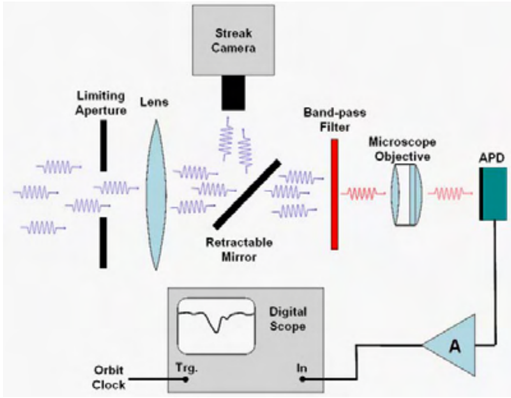

Figure 1: Schematic diagram of the experimental set-up used for the measurement at BL 7.2.

Figure 2, shows the typical signal visible at the scope when measuring the light from a single passage of a single ALS bunch. The typical rms length of the electron beam is ~ 25 ps so that the shape of the pulse in Fig.2 was totally defined by the response of the measurement system. The oscilloscope was set in order to measure the areas S_{AB} of the signal between points A and B, and S_{CD} between points C and D in Fig. 2. S_{AB} is proportional to the number of photons impinging on the detector plus the contribution due to the noise in the signal, while S_{CD} is a measure of this noise contribution. The lengths of the segments AB and CD were set to be the same.

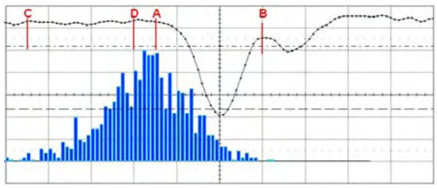

Figure 2: Oscilloscope window showing the track of a typical signal from the photodetector and the histogram of the measured values of the signal area between points A and B. The horizontal scale is 500 ps/div while the vertical is 50 mV/div.

The scope was also set to calculate the average values for such areas and their standard deviations over 5000 samples per each bunch length measurement (~ 1 min per measurement) in order to keep according to (5), the statistical error at ~ 2%. In this configuration, <W> the average energy radiated per passage by the electron beam is proportional to <S_{AB}> – <S_{CD}>, while its variance σ_W^2 is proportional to σ_{SAB}^2 - σ_{SCD}^2. By comparing different amplitude signals, we also verified that the shape of the signal itself did not depend on the amplitude.

** For a gaussian pulse the uncertainty principle requires $\sigma_\tau\sigma_\omega = 1/2$.

EXPERIMENTAL RESULTS

Simulations and analytical calculations showed that in our configuration, the diffraction due to the finite beamline acceptance fully defines the shape for both the transverse modes, which can be well described by the $[\sin(\xi)/\xi]^2$ function typical of a plane wave diffracting through a finite aperture. Nevertheless, numerical calculations also showed that it is still possible to use the gaussian formula (4) if one fits the central peak of the $[\sin(\xi)/\xi]^2$ function with a gaussian, and uses for the coherence length the rms width of the fit divided by $\sqrt{2}$. For $\lambda = 632.8$ nm and for the acceptances of BL7.2 we obtained $\sigma_{xc} = 29.8$ µm and $\sigma_{yc} = 59.5$ µm. The ALS measurements were performed at the two beam energies of 1.2 and 1.9 GeV. The rms beam sizes at BL7.2 source point were $\sigma_x = 64.8$ µm and $\sigma_y = 6.3$ µm at 1.2 GeV and $\sigma_x = 103.0$ µm and $\sigma_y = 10.0$ µm at 1.9 GeV.

Equation (4) was derived according to classical field theory, the proper quantum treatment requires the addition of the shot noise term $1/N$, with N the number of photons impinging on the detector. Additionally, photodiodes, avalanche photodiodes and photomultipliers all exploit stochastic phenomena for the photon-electron conversion and amplification. This must be accounted by using a modified shot noise term $\kappa^2 = \zeta/(\eta N)$, where ζ is the excess noise factor, a constant ≥ 1 related to the avalanche process and η is the detector quantum efficiency. Putting all the contributions together and indicating with $\delta_M^{\ 2}$ the measured fluctuation variance one finally obtains for the rms length of the bunch:

$$\sigma_\tau^2 = \frac{1}{4\sigma_\omega^2}\left[\left(\delta_M^2-\kappa^2\right)^{-2}\left(1+\frac{\sigma_x^2}{\sigma_{xc}^2}\right)^{-1}\left(1+\frac{\sigma_y^2}{\sigma_{yc}^2}\right)^{-1}-1\right] \quad (6)$$

The κ^2 term can be measured by performing 2 or more measurements of $\delta_M^{\ 2}$ for the same bunch length for different number of photons impinging on the detector (using neutral density filters for instance). All the terms on both sides of (6) remain the same with the exception of the shot noise one. From that, and considering that $< N > \propto (< S_{AB} > - < S_{CD} >)$, κ^2 can be evaluated.

Figure 3 shows 2 examples of measurements performed for different beam conditions. The agreement with streak-camera data acquired right after each fluctuation measurament is remarkably good especially considering that no parameter has been adjusted to match the data.

The typical rms difference between the streak camera and the fluctuation data was ~ 4 %. This is larger than the 2% contribution due to (5). The extra error is probably associated with the shot noise term that in our measurements was comparable to δ^2.

POSSIBLE UPGRADES & CONCLUSIONS

By splitting the light from the source in two paths and using for each of them a bandpass filter with different central wavelength but same bandwidth, it is possible to discriminate between the transverse and longitudinal components in Eq. (4) by exploiting the fact that the longitudinal term depends only on the bandwidth while the transverse ones depend only on the central wavelength. Such a capability allows removing the dependence on the transverse plane and can be useful when the transverse beam size changes during operation.

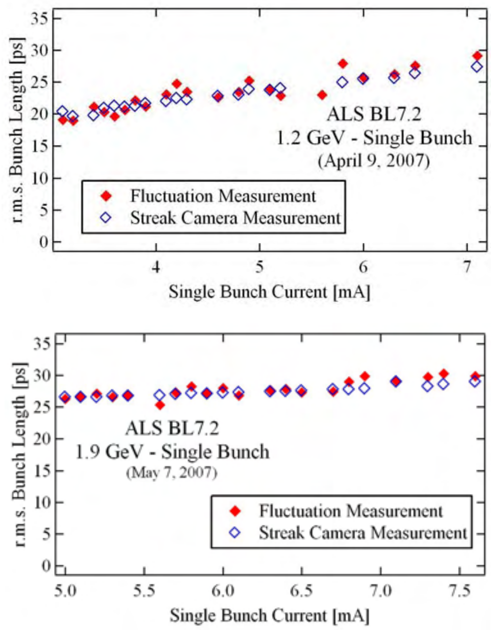

Figure 3: Examples of fluctuation and streak-camera bunch length measurements at the ALS for different beam parameters.

We want also test the system by coupling the light from the source into an optical fiber. This will allow having the measurement setup separated from the source area for an easy accessibility and tuning of the system.

In summary, we have demonstrated an absolute bunch length measurement technique based on the analysis of the fluctuations in the incoherent part of the radiation emitted by a particle beam. The scheme is non-destructive, shows a remarkable simplicity and can be applied in both circular and linear accelerators including cases where the very short length of the bunches makes difficult the use of other techniques.

ACKNOWLEDGEMENTS

The authors want to thank John Byrd, Stefano De Santis and Josef Frisch for their contributions.

REFERENCES

[1] M. Zolotorev, G. Stupakov, SLAC PUB 7132 (1996).

[2] P. Catravas et al., Phys. Rev. Letters 82, 5261, (1999).

[3] V. Sajaev, "Determination of Longitudinal Bunch Profile using Spectral Fluctuations of Incoherent Radiation," Proceedings of EPAC 2000, Vienna.

[4] M. Yabashi et al., Phys. Rev. Letters 97, 084802 (2006).

CONTROL AND MEASUREMENTS OF LONGITUDINAL COUPLED-BUNCH INSTABILITIES IN THE ATF DAMPING RING*

D. Teytelman†, J. Fox, SLAC, Menlo Park, CA 94025, USA
W. Cheng, J. Flanagan, T. Naito, M. Tobiyama, KEK, Tsukuba, Japan
A. Drago, LNF-INFN, Frascati, Italy

Abstract

Damping ring at the Accelerator Test Facility (ATF) is a storage ring with 714 MHz RF frequency and harmonic number of 330. The ring is used in both single and multi-bunch regimes. In both cases, significant longitudinal dipole motion has been observed in the ring. A prototype longitudinal feedback channel using a Gproto baseband processing channel and a set of horizontal striplines has been constructed for the machine. The prototype allowed both suppression of the longitudinal motion and studies of the motion sources. In this paper, we present the results of these studies including measurements of steady-state oscillation amplitudes, eigenmodal patterns, and growth and damping rates. Using measured growth rates we estimate the driving impedances. We also present the effect of the longitudinal stabilization on the energy spread of the extracted beam as documented by a screen monitor.

INTRODUCTION

Longitudinal instabilities have been historically observed in the ATF damping ring [1]. A series of feedback experiments described here has been performed with two goals: to characterize the instabilities and to demonstrate longitudinal stabilization.

EXPERIMENTAL SETUP

Feedback system configuration used for this experiment is shown in Figure 1. Beam signal from a single beam position monitor (BPM) was passed through a 4-cycle comb generator at 2856 MHz, amplified, and mixed against a carrier signal, phase locked to the master oscillator. After low-pass filtering, the phase detector output was sampled by the Gproto bunch-by-bunch feedback system. Since in the ATF damping ring every other RF bucket can be populated, beam signal was sampled at RF/2 (357 MHz). Feedback output signal drove in-phase a set of horizontal striplines, which served as a low shunt impedance longitudinal kicker. Triggered diagnostic features of the Gproto were extensively used to tune the feedback loop and to study system performance. Since the ATF damping ring is a pulsed machine all data acquisition was triggered by the injection signal. Using a delay generator, the data recording snapshot

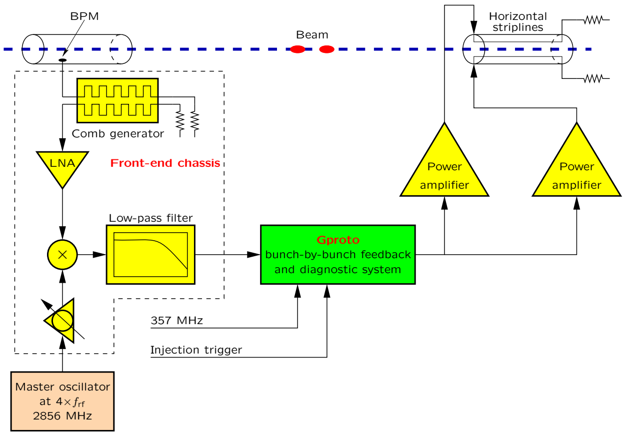

Figure 1: Block diagram of the experimental setup.

window was positioned at different points during the storage cycle to study injection transients and steady-state performance.

Feedback processing algorithm used a 16-tap finite impulse response (FIR) filter with a downsampling factor of 16. That is, the correction kick for a given bunch on turn N used bunch position information sampled on turns $[N, N-16, N-32, \ldots]$. On turn $N+1$ the kick signal was computed from turns $[N+1, N-15, N-31, \ldots]$. In this approach the feedback correction signal uses information from 256 revolutions - 120 μs, comparable to the synchrotron period of 90 μs. This method of downsampling can be compared to the traditional approach, where the kick for a given bunch is computed and then repeated for $N_{\rm ds}$ turns. The new approach provides lower feedback channel group delay: $T_{\rm rev}/2$ versus $T_{\rm rev}N_{\rm ds}/2$. Technically, the processing was configured for a ”virtual” ring with harmonic number $N_{\rm ds}$ times the actual ring size, that is $16 \times 165 = 2640$.

SINGLE-BUNCH MEASUREMENTS

Initial feedback studies focused on quantifying and suppressing single-bunch motion in the ring. In Fig. 2(a) single-bunch motion after injection without feedback is shown. Beam is longitudinally stable in this case and the motion decays exponentially with 19.6 $\rm ms^{-1}$ damping rate. This rate is very close to nominal 19.5 $\rm ms^{-1}$ longitudinal radiation damping rate. Once the feedback loop is closed, as shown in Figure 2(b), the injection transient damps much faster with the damping rate of 1.5 $\rm ms^{-1}$. Initial damping

* Work supported by U.S. Department of Energy contract DE-AC02-76SF00515 and by the US-Japan collaboration in High Energy Physics
† dim@slac.stanford.edu

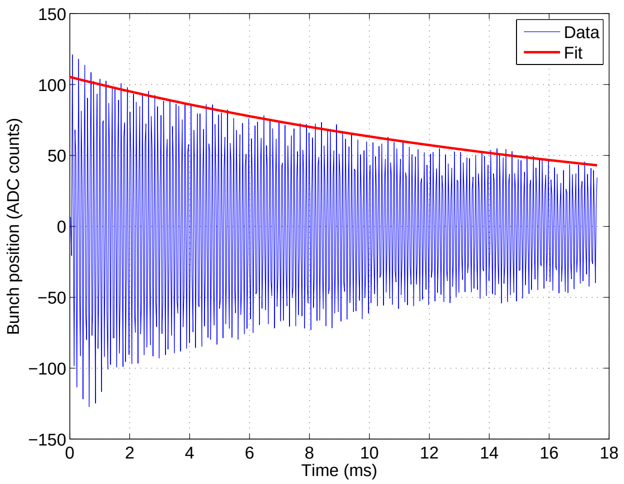

(a) Open-loop

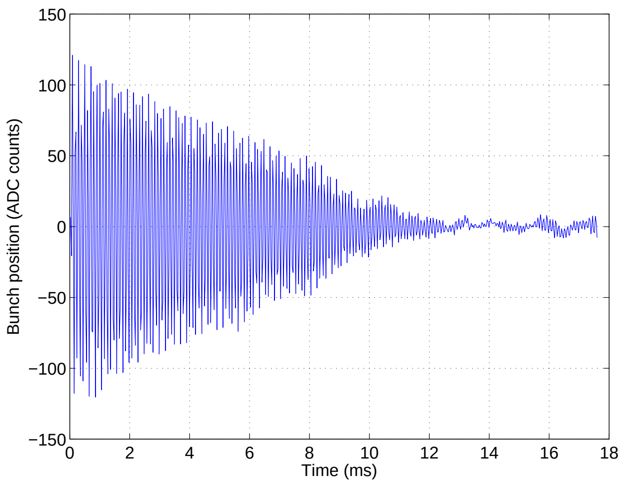

(b) Closed-loop

Figure 2: Single-bunch longitudinal motion immediately after injection

from 0 to 8 ms is linear due to feedback saturation.

Measurements with longer trigger delay showed that after injection transient damping there is significant residual motion, most likely driven by the RF system. The residual motion is strongly suppressed when the feedback loop is closed.

MULTI-BUNCH MEASUREMENTS

After optimizing the feedback setup in the single-bunch regime we continued the studies with multiple bunches in a 45 bunch fill pattern. In the multi-bunch regime, we observed the traditional coupled-bunch instability with a band of even-fill eigenmodes (EFEMs) excited. The excited band is centered around mode 120 and is likely an artifact of the uneven filling pattern. In Fig. 3 a grow/damp measurement at 20 mA is illustrated. Note the bursting excitation of low-frequency modes driven by the RF system. Fitting complex exponentials to the growing and damp-

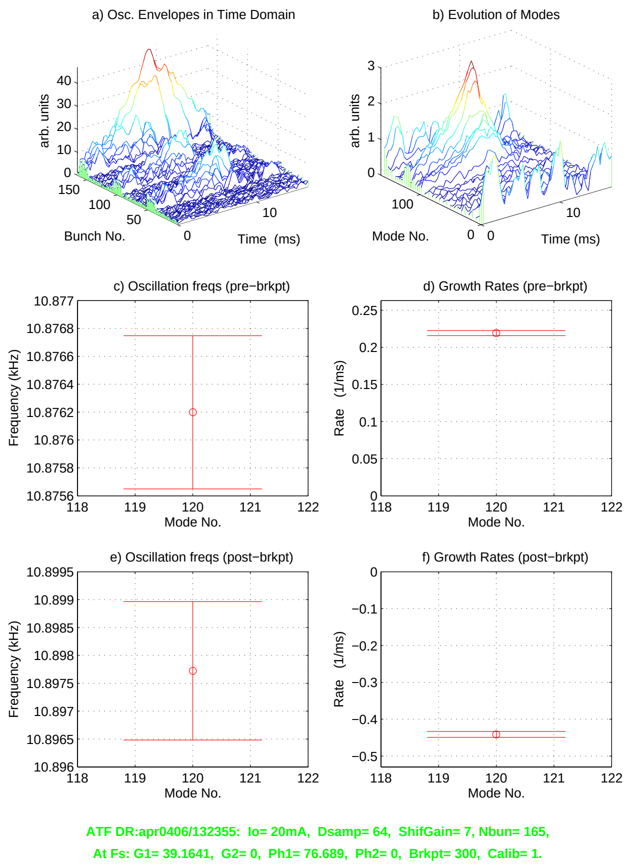

Figure 3: Grow/damp experiment: 45 bunches, 20 mA.

ing parts of the transient for EFEM 120 we extract the growth rate of $0.219 \pm 0.003\ \mathrm{ms}^{-1}$ and the damping rate of $0.441 \pm 0.008\ \mathrm{ms}^{-1}$.

Due to aliasing of the HOM impedances by the beam, identifying the unstable mode restricts possible HOM frequencies to $259 + n \cdot 357$ MHz. A known cavity HOM around 2.36 GHz [2] is the likely source of the instability. By performing growth rate measurements at 20 mA and 40 mA and assuming the driving impedance at 2.4 GHz we can estimate the effective longitudinal impedance of the HOM as 33 kΩ.

ENERGY SPREAD IN THE EXTRACTION LINE

As an independent measurement of feedback performance, we observed the transverse beam profile in a dispersive region of the extraction line using a screen monitor. In this case, the horizontal profile of the beam is a superposition of the following contributions:

- Horizontal beam size;
- Intra-bunch energy spread;
- Inter-bunch energy spread (multi-bunch case).

Collecting screen images for both single-bunch and multi-bunch fill patterns allows us to separate the contributions from the intra and inter-bunch energy spreads. Figures 4(a)

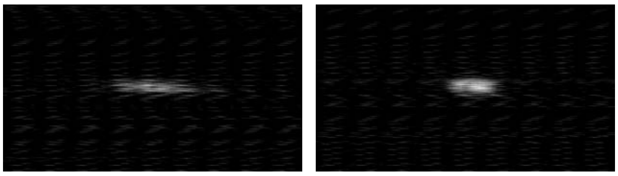

(a) Open-loop (b) Closed-loop

Figure 4: Screen monitor images in the multi-bunch regime

and 4(b) show the screen monitor snapshot for the open and closed-loop conditions respectively. There is a visible reduction in the horizontal spot size. To quantify the effect, we performed Gaussian fits to horizontal projections of the

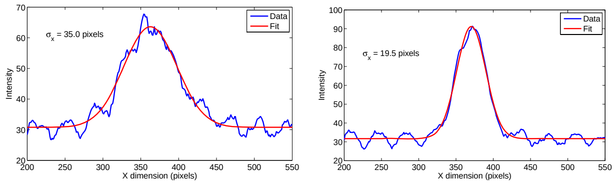

(a) Open-loop (b) Closed-loop

Figure 5: Gaussian fits to the horizontal projections of the screen monitor images

snapshots as illustrated in Fig. 5. The spot size RMS is reduced from 35 to 19.5 pixels in this case. Results of the fits to 28 images collected in different ring conditions is summarized in Fig. 6.

When the longitudinal feedback is operational, the horizontal spot size is held constant in both single and multi-bunch modes. Turning off the feedback produces a significant spot size increase in the multi-bunch case. This increase is mostly driven by the large bunch-to-bunch energy spread. With unstable beam there is a large variation of the spot size shot-to-shot due to the variability of the saturation mechanisms and the modal beating patterns. An interesting feature of this measurement is a consistent single-bunch energy spread increase without feedback. Since the data is from a single-shot single-bunch image, it suggests a mechanism of the intra-bunch energy spread increase due to RF-driven centroid oscillation.

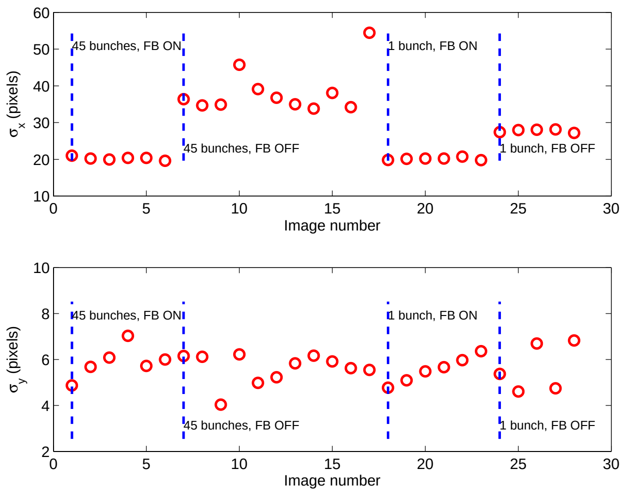

Figure 6: Horizontal and vertical spot sizes for multiple screen monitor images.

Horizontal spot size measurements presented in Fig. 6 are summarized in Table 1. Additional studies are needed

Table 1: Extraction line measurement summary

Fill	Parameter	FB OFF	FB ON
Single	σ_x, pixels	28.02 ± 0.25	20.26 ± 0.13
bunch	σ_x, μm	925 ± 8	668 ± 4
Multi	σ_x, pixels	38.8 ± 1.8	20.26 ± 0.18
bunch	σ_x, μm	1281 ± 59	669 ± 6

for more precise quantification of the extracted beam energy spread and of the observed single-bunch energy spread change with feedback.

SUMMARY

We have demonstrated control of longitudinal coupled-bunch instabilities in the ATF damping ring. Unstable beam motion has been analyzed to extract instability growth rates and the feedback damping rates. Observed spectral information has been used to link the unstable modes to known RF cavity HOMs. These measurements can be used to determine the necessary kicker voltage, if a permanent feedback system is desired. Observations of the beam spot size in the dispersive region of the extraction line show significant reduction in the extracted beam energy spread.

REFERENCES

[1] M. Ross and R. Meller, "Detection and feedback of synchrotron oscillations in the ATF damping ring," Tech. Rep. ATF-04-06, ATF, Tsukuba, Japan, 2005.

[2] S. Sakanaka *et al.*, "Low power measurement on a HOM damped cavity for the ATF damping ring," Tech. Rep. KEK-PREPRINT-94-79, KEK, Tsukuba, Japan, 1994.

STATUS OF Nb-Pb SUPERCONDUCTING RF-GUN CAVITIES

J. Sekutowicz, J. Iversen, D. Klinke, D. Kostin, W. Möller, A. Muhs, DESY, Hamburg, Germany
P. Kneisel, TJNAF, Newport News, USA
J. Smedley, T. Rao, BNL, Upton, USA
P. Strzyżewski, A. Soltan INS, Swierk/Otwock, Poland
Z. Li, K. Ko, L. Xiao, SLAC, Menlo Park, USA
R. Lefferts, A. Lipski, SUNY, Stony Brook, USA
M. Ferrario, INFN, Frascati, Italy

Abstract

We report on the progress and status of an electron RF-gun* made of two superconductors: niobium and lead [1]. The presented design combines the advantages of the RF performance of bulk niobium superconducting cavities and the reasonably high quantum efficiency of lead. The design of RF-gun and performance of 3 test cavities without and with the emitting lead spot are reported in this contribution. Measured quantum efficiency for lead at 2K is presented briefly. More details are reported in [9].

INTRODUCTION

Motivation

Improvement in RF performance of superconducting (sc) cavities over the past decade has made feasible continuous wave (cw) and near-cw operations of superconducting electron linacs at high accelerating gradients. Both operation modes require injectors operating at cw or near-cw, providing low emittance electron beams. An example of such an injector (so called split injector) is discussed in [2]. The most demanding component of a cw injector is the RF-gun, operating in a cw mode and delivering highly populated (~1 nC) low emittance bunches. When generating highly populated low emittance bunches, both room temperature and superconducting RF-guns have to be operated at high accelerating gradients to suppress space charge effects that dilute the emittance. Normal conducting RF-guns face difficulties in meeting this requirement in the cw or near-cw mode. Their copper walls dissipate many kilowatts of power in fulfilling high gradient conditions even when they operate at low pulse repetition rate. Superconducting RF-guns (SRF-guns) dissipate orders of magnitude less power than the normal conducting devices. They can be operated at high duty factor. The challenge here is integration of a non superconducting photo-cathode into a sc cavity [3] in a way that preserves its original high intrinsic quality factor Q_o (small cryogenic losses). One possible solution to this problem, based on a choke filter design, is investigated at Forschungszentrum Rossendorf [4, 5]. Another approach, very attractive and technically feasible for miliampere-class SRF-guns, is to use a superconducting material as the photo-cathode. In this case, difficulties arise from the moderate quantum efficiency (*QE*) of the superconducting materials, which must be compensated with shorter wave-length and higher pulse energy of the illuminating laser. The niobium cathode proposed and tested at BNL [6] demonstrates rather poor *QE*. A complementary approach with lead [7] is discussed in the following section.

LEAD *QE* AND RF-DESIGN

QE of Lead

Lead has superior *QE* to niobium. Test results of lead *QE* at room temperature were reported by us in [8]. Fig. 1 shows the summary of the tests at 300 K vs. photon energy E_p for niobium, bulk lead and lead samples deposited with various techniques. The highest *QE* of 0.55% has been measured for the arc-deposited sample illuminated with 6.5 eV photons. For 5.8 eV photons (5th harmonics of 1064 nm infrared laser) the *QE* of that sample was still 0.25%. *QE* of the electroplated and magnetron deposited samples at this photon energy is ~0.17%. Generation of 1 nC bunch with this *QE* will require 3.4 μJ energy per pulse on the cathode. The cold *QE* test was done very recently and is reported elsewhere in these proceedings [9].

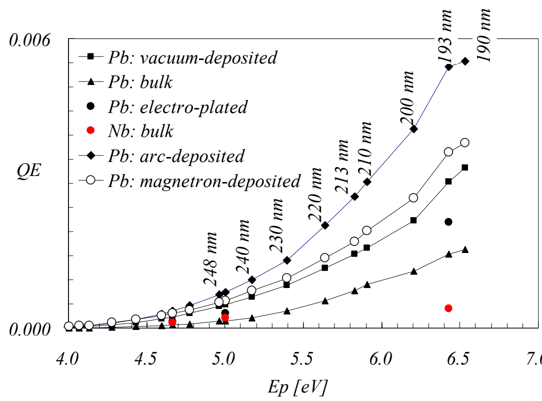

Figure 1: Measured QE of lead deposited with various coating methods. Bulk Pb and Nb data are displayed for comparison.

RF-Design

In the hybrid Pb-Nb gun, a small emitting spot of lead (Ø<3 mm) will be located in the center of the back wall of

* This work has been partially supported by the EU Commission, contract no. 011935 EUROFEL-DS5 and US DOE under contract number DE-AC02-98CH10886.

the 0.6-cell of a 1.6-cell[†] cavity (Fig. 2), which will be made of high purity niobium. The cavity, equipped with two HOM couplers, input coupler and pickup probe will be assembled for operation in a dedicated cryostat. The gun is designed to be implemented in the split injector. A solenoid, installed directly after the cavity, will be used for emittance growth compensation. Tables 1 and 2 and Figure 3 show RF-parameters and the Higher Order Mode (HOM) suppression (Q_{ext}) for the present design. The damping of HOMs in a SRF-gun is crucial for the beam quality, which can be diluted by the interaction between non-relativistic electrons (in the first 0.6-cell) with deflecting dipole modes. The operating electric field on the lead cathode E_{peak} will not exceed 60 MV/m. At this field, the emitting spot will be exposed to B = 4 mT, which is much smaller than the lead critical magnetic flux B_c = 70 mT.

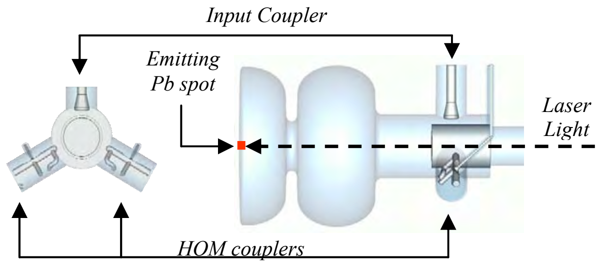

Figure 2: 1.6-cell SRF-gun cavity with 2 HOM couplers and the input coupler.

Table 1: RF-parameters of the 1.6-cell SRF gun

Parameter	Unit	Value
π-mode frequency	[MHz]	1300
0-mode frequency	[MHz]	1286.5
Cell-to-cell coupling	-	0.015
Active length 1.6·λ/2	[m]	0.185
Nominal E_{cath} at cathode	[MV/m]	60
Energy stored at nominal E_{cath}	[J]	20
Nominal beam energy	[MeV]	6

Table 2: HOMs of 1.6-cells

Mode	f [MHz]	(R/Q)
Dipole: TE111-1a	1641.8	1.85 [Ω/cm^2]
Dipole: TE111-1b	1644.9	1.30 [Ω/cm^2]
Dipole: TM110-1a	1883.5	10.1 [Ω/cm^2]
Dipole: TM110-1b	1884.0	9.99 [Ω/cm^2]
Dipole: TM110-2a	1957.0	3.90 [Ω/cm^2]
Dipole: TM110-2b	1957.1	3.85 [Ω/cm^2]
Monopole: TM011	2176.5	43.2 [Ω]

Two types of half-cell resonators have been built to measure the QE of lead at 2 K and to test the RF performance of Nb-Pb cavities. Both types are shown in Fig. 4. The left one was built at TJNAF. It has an opening in the center of the back wall, which is vacuum sealed with a niobium plug and an indium gasket. The advantage of this cavity type is that plugs can be easily coated with emitting materials to test various deposition methods and various superconductors for photoemission.

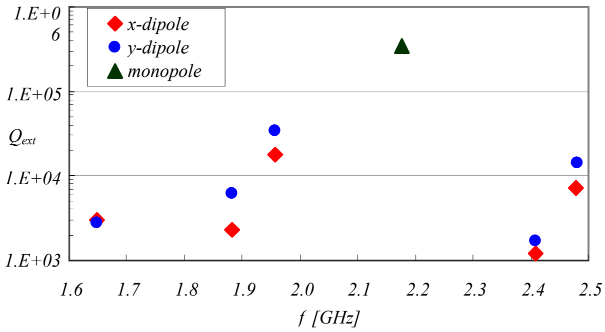

Figure 3: 3D modelling of the HOM suppression for the 1.6-cell SRF-gun.

It can be an alternative solution to the second cavity type, built at DESY (Fig. 4, right), in which, the technically difficult coating is done directly on the back wall. An additional difficulty in this version is that the emitting spot must withstand cleaning procedures applied to the cavity. Two of the cleaning steps could degrade QE: chemical treatment and high pressure water rinsing. Both procedures are essential for good performance of sc cavities. On the other hand, two features make this version very attractive: the smooth back wall does not enhance locally the electric field near the cathode and there is no RF electric contact needed in the high field region, which may reduce the intrinsic Q_o of the cavity. The plug cavity and the first DESY cavity were tested several times without and with lead coating. The baseline test without the coating, of the second DESY cavity fabricated in 2006, was recently carried out at TJNAF.

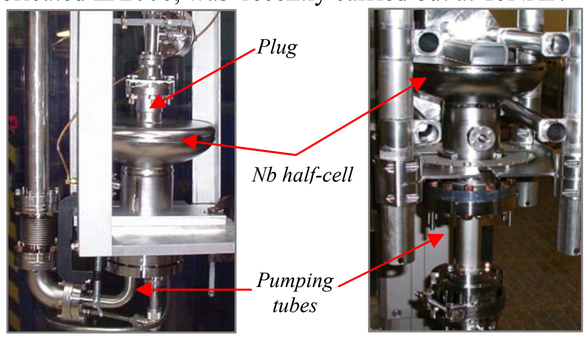

Figure 4: Test half-cell cavities built at TJNAF (left) and at DESY (right) assembled on inserts for the RF-cold test.

RF-PERFORMANCE TEST

Cold Test without Coating

Figure 5 displays the best results for the half-cell cavities without lead coating on the back wall and on the plug. The tests showed that chemical treatment and high pressure water rinsing are challenging for the half-cells and need to be improved in the future. We observed,

[†] The first cell is 0.6· λ/2 long. This length provides the lowest emittance growth.

testing DESY type cavities, few multipacting levels between 30 and 40 MV/m, which could be processed for cavities without lead. It took some time to overcome these levels by RF-processing. In the plug cavity, we observed heating of the first plug version, which was due to insufficient cooling by LHe. The cooling was improved for the tests shown.

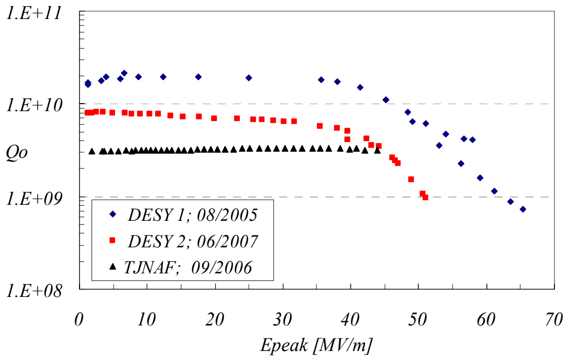

Figure 5: Cold (2K) RF-test results without lead coating.

Cold Test with Lead Coating

The emitting 4 mm diameter lead spot at the center of the back wall of the DESY cavity was deposited by the arc-discharge method at A. Soltan INS. The 7 mm diameter plug of the TJNAF cavity was electroplated with lead at Stony Brook University. As mentioned before, the final cleaning of the cavities is challenging, especially for the DESY type when coated. That cavity reached 40 MV/m peak field (Fig. 6), but a lot of processing events and heavy radiation was observed during the cold test. The second DESY cavity will be coated and tested soon. The TJNAF cavity is somewhat easier to clean because of the absence of the coated plug during surface treatment. It demonstrated almost the same performance as without lead, which confirms our expectation that the emitting spot located on axis should not limit the performance.

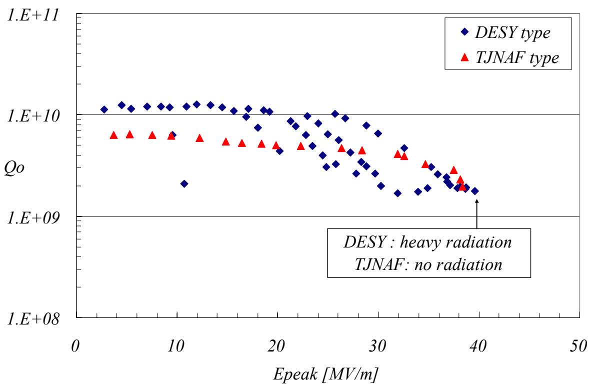

Figure 6: Cold (2K) RF-test results with lead coating.

Irradiation with Laser

One of our concerns from the very beginning of this project was the recombination time of broken Cooper pairs in the emitting spot by the irradiating laser. The theoretical investigation presented in [1] led to the conclusion that the recombination time strongly depends on temperature. Fortunately, the time is shorter for higher temperature. The 248 nm excimer laser used for the cold tests generated 5.3 ns long pulses (FWHM) at up to 250 Hz repetition frequency. The maximum energy per pulse was 5.5 mJ. Half of it could be transferred to the cavity for the *QE* and relaxation time experiments. The maximum available peak power of 0.518 MW at the cathode was two times higher than the power needed for the nominal operation of the gun, when 1 nC bunches are generated within 20 ps. The preliminary relaxation time experiment was performed with the TJNAF cavity, operating at 1.42 GHz. For that experiment the cavity had to be attached to a straight vacuum tube oriented vertically upward, to enable direct irradiation with the laser light via the sapphire window installed at the top-plate of the vertical cryostat. The 3 m long vacuum tube contaminated the cavity with particulates and degraded its performance. At 3 MV/m Q_o was only $2.25{\cdot}10^9$, almost 3 times lower than Q_o measured at this gradient in the RF-performance test. When the Nb wall was irradiated with the maximum available laser power, Q_o dropped to ~$1.6{\cdot}10^9$, but the cavity did not quench and behaved still very stable. The additional dissipation, due to the locally broken Cooper pairs in the irradiated area, was 5.2 mW. The surface resistance, r_s , of the irradiated area increased during the laser pulse by a factor of 630. The ratio of r_s after and before the irradiation indicates that the concentration of quasi-particles rose to their equilibrium concentration at 8 K. According to the theoretical model, their relaxation time is shorter than 100 ps at this temperature.

ACKNOWLEDGMENT

We would like to express our gratitude to colleagues at DESY, BNL, INS and TJNAF from whom we received technical support.

REFERENCES

[1] J. Sekutowicz et al., “Nb-Pb Superconducting RF-gun”, TESLA-FEL Report 2005-09, DESY, 2005.
[2] M. Ferrario, NIM A 472, (2001), 303-308.
[3] J. Sekutowicz, Proceed. ICFA Workshop on The Physics and Applications of High Brightness Electron Beams, Erice, Italy, 9-14 October, 2005; http://www.physics.ucla.edu/PAHBEB2005/talks/10_oct_2005/index.htm
[4] A. Michalke et al., Proc. EPAC92, Berlin, Germany, 1992, p. 1014, http://www.jacow.org.
[5] D. Janssen et al., Proc. PAC97, Vancouver, Canada, 1997, p. 28238, http://www.jacow.org.
[6] T. Srinivasan-Rao et al., Proc. PAC03, Portland, Oregon, p. 92, http://www.jacow.org..
[7] J. Sekutowicz et al., “Nb-Pb Superconducting RF-Gun”, TESLA-FEL Rep.-2005-09, DESY, 2005.
[8] J. Smedley et al., Proc. EPAC2004, Lucerne, Switzerland, p. 1126, http://www.jacow.org.
[9] J. Smedley et al., “Photoemission Tests of a Pb/Nb Superconducting Photoinjector”, these Proceedings.

COMPARISON BETWEEN SPARC E-METER MEASUREMENTS AND SIMULATIONS*

C. Ronsivalle, L. Giannessi, M. Quattromini, ENEA C.R. Frascati, Frascati(Roma), Italy
A. Bacci, A.R. Rossi,L. Serafini, INFN-Milano, Milano, Italy
M. Boscolo, E. Chiadroni, M. Ferrario, D. Filippetto, V. Fusco, G. Gatti, M. Migliorati, A. Mostacci, C. Vaccarezza, C. Vicario, INFN/LNF, Frascati(Roma), Italy
A. Cianchi, INFN-Roma II, Roma, Italy
M. Petrarca, Università di Roma I La Sapienza, Roma, Italy

Abstract

For the SPARC photoinjector commissioning the emittance compensation process has been studied experimentally under different beam conditions (variation of charge, spot size, beam shape….) by a novel device called "emittance-meter", consisting in a movable emittance measurement system based on the 1D pepper pot method scanning a region 1.2 m long downstream the RF-gun. The results of a detailed comparison between the measurements and beam dynamics simulations performed by the codes (PARMELA,HOMDYN,TREDI) employed for SPARC design are presented and discussed here.

STRATEGY FOR COMPARISON

During the first stage of the SPARC photoinjector commissioning aimed to characterize the beam at the exit of the RF gun, the beam size, the emittance and the energy-spread at different z positions from the cathode have been measured by using the so-called movable emittance-meter [1]. This novel device allowed to perform very detailed tests of beam dynamics numerical codes.

All the simulations have been performed by PARMELA [2], which has been extensively used in the SPARC design. Crosschecks with other codes also employed for SPARC beam dynamics studies, TREDI [3] and HOMDYN [4], have been done as well.

Fitting Procedure

The aim of the measurements-simulation comparison was to verify the consistency of the experimental data with a numerical model describing a beam equivalent to the real one in conditions near to the machine operation.

The emittance is a function of the different parameters listed in table 1 with their uncertainties. These uncertainties represent the variation range of the parameters used in the numerical model to fit the emittance measurements.

The first step of the fitting procedure has been the matching of the measured envelope by adjusting the two parameters that mainly affect it, i.e. the initial spot size and the magnetic field strength, and keeping the other parameters fixed to their nominal value. Afterwards a fine adjustment has been done by tuning the other parameters.

*Work supported by the EU Commission in the sixth framework program, Contract No. 011935 EUROFEL.

Table 1: Variation Range Of Parameters

Parameter	**Variation range**
Energy	Measured ±5%
Charge	Measured ±10%
Spot size	Retrieved from the virtual cathode image ±10%
Solenoid current	Measured ±0.5%
Rf phase	Measured ±2°

Beam Model

In PARMELA simulations the input beam longitudinal distribution has been directly retrieved by the measured temporal distribution. The two different techniques used to reconstruct the time profile based respectively on a cross-correlator and a spectrometer give a resolution of 0.5 psec. This value has been assumed as to the precision of the pulse length determination. The input transverse distribution has been retrieved from the so-called "virtual cathode" image obtained splitting the laser beam before it enters the vacuum system. It is generated cutting the edges of a transverse Gaussian profile in order to obtain an almost round and homogeneous intensity distribution and can be approximated by two types of 2D models: a truncated gaussian or a stack of uniform disks. The use of these 2D models in PARMELA (Nr=number of radial meshes= 20, Nz=number of longitudinal meshes=200, a radial mesh size automatically adjusted by the code, a variable longitudinal mesh size between 1 and 0.5 cm, Np=number of particles=20K) gives the possibility to get a fast tuning of fitting parameters. Checks by more time consuming 3D computations (Np=100K) showed that the above approximations are very satisfying in most of the cases. The same approach has been adopted also in TREDI simulations.

Experimental Data Representation

A code dedicated to the data analysis reconstructs in a very accurate way the emittance from acquired pepper-pot images and estimates the relative uncertainty as the experimental standard deviation of the mean [5]. This uncertainty multiplied by a factor corresponding to a gaussian confidence interval of 95% determines the error bars associated to the experimental data and shown in the plots.

COMPARISON RESULTS

Measured Emittance for Different Pulse Shapes

The dynamic behaviour induced by different pulse shapes during the emittance compensation process was extensively investigated. The emittance-envelope plot of fig. 1 shows an optimum agreement between measurements and PARMELA simulations for a gaussian pulse with a FWHM of 10 psec and the parameters reported in the second column of table 2.

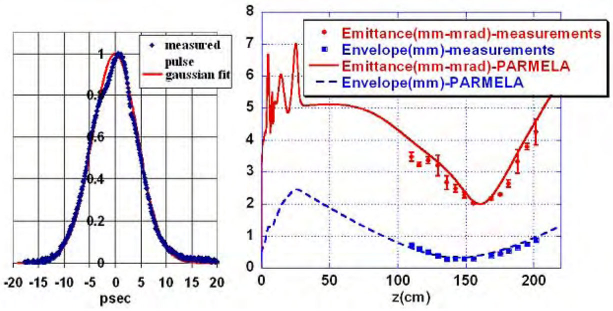

Figure 1: Measured pulse and corresponding envelope-emittance plot: measurements and PARMELA results.

A direct comparison of different pulse shapes is shown in fig. 2: both pulses have a FWHM of 8.7 psec (the other parameters are in the third column of table 2) and the comparison puts in evidence that the minimum emittance value is reduced from 2 to 1.5 mm-mrad by using a flat-top shape instead of a gaussian pulse, accordingly with PARMELA simulations.

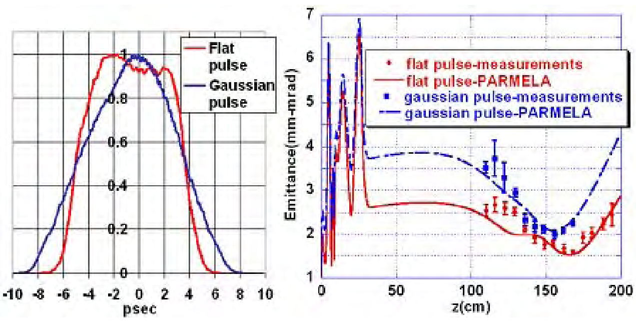

Figure 2: Measured pulses and corresponding emittance plots with measurements and PARMELA results.

The best brightness was achieved by the flat-top pulse (FWHM=8.9 psec) shown in fig.3 together with the PARMELA simulation based on the parameters of the fourth column of table 2.

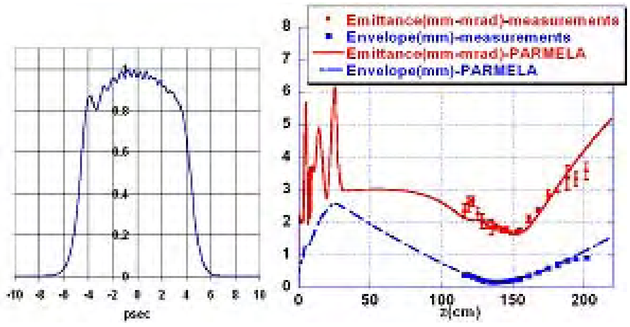

Figure 3: Measured pulse and corresponding emittance – envelope plot with measurements and PARMELA results.

A crosscheck of PARMELA fit with TREDI code was done in this case (fig. 4) showing a satisfying agreement between measurements and numerical predictions within the measures uncertainties and the intrinsic differences between the two codes.

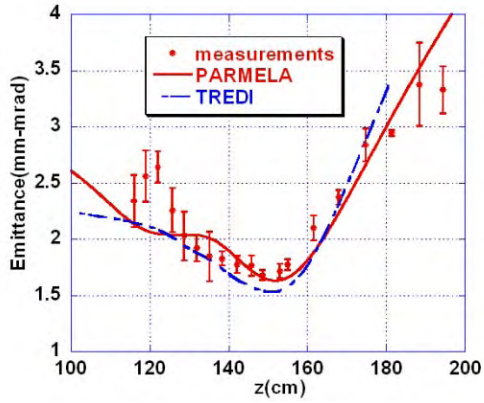

Figure 4: Emittance plot with PARMELA-TREDI vs measurements for the case of fig.4.

Table 2: Measured Parameters

Parameter	**Case of fig.1**	**Case of fig.2**	**Case of fig.3**
Energy	5.65 MeV	5.4 MeV	5.65 MeV
Charge	1 nC	0.74 nC	0.825 nC
Spot size, <σ>	450 μm	310 μm	360 μm
Rf phase, φ-φ_{max}*	-5°	-8°	-8°
Solenoid current	209 A	199 A	209 A

*(φmax=phase corresponding to the maximum energy gain)

All the above flat-top pulses have a rise/fall time around 2.6 psec. A reduction of the rise time to ~1.5 psec was obtained by shorting the pulse length to ~ 5 psec.

As it is shown in figure 5 such short rise time pulse allowed to measure for the first time the so-called “double emittance minimum” observed up to now only in numerical simulations. The oscillation was put in evidence by moving the phase of 12 degrees behind the phase of maximum energy gain (see table 3) in order to increase the beam energy spread accordingly with the chromatic nature of the effect [6].

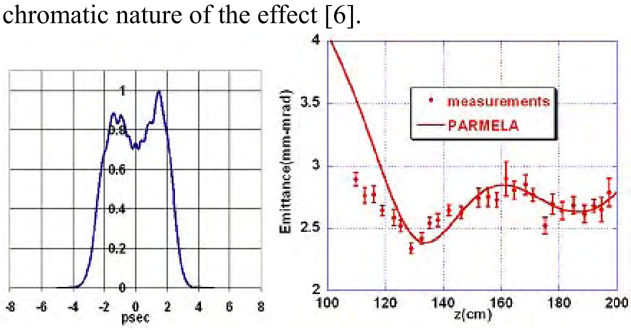

Figure 5: Measured pulse and corresponding emittance – plot with measurements and PARMELA results.

Table 3: Measured Parameters

Parameter	Value
Energy	5.5 MeV
Charge	0.5 nC
Spot size, <σ>	450 μm
Rf phase, φ-φ_{max}	+12°
Solenoid current	198 A

Energy Spread Vs Z Measurements

Figure 6 shows the evolution of the energy spread measured by cutting the beam by one slit at different z positions for two different values of beam charge.

The results have been compared with PARMELA simulations based on the measured parameters of table 4.

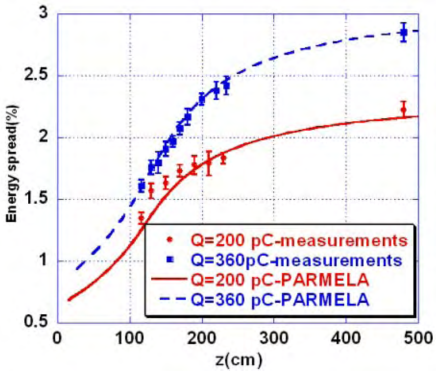

Figure 6: Energy spread vs z evolution.

Table 4: Measured Parameters

Parameter	Value
Energy	5.5 MeV
Spot size, <σ>	450 μm
Rf phase, φ-φ_{max}	+12°
Pulse shape	Flat top, FWHM=5 psec
Solenoid current	195 A

The excellent agreement between the measurements and the PARMELA model, that does not take into account the wake-fields effect, confirms that the effect of the long emittance-meter bellows is negligible.

HOMDYN Simulation

In fig.7 we show a comparison between the HOMDYN code and a one day measure at SPARC (measured parameters in table 5). The agreement is quite satisfying if we consider the intrinsic limit of the code. HOMDYN, is indeed a very fast semi-analytical code whose main approximation lies on the assumption that the bunch is a uniformly charged cylinder divided into slices [5].

The difference between the code and the measure is mainly due to the pulse rise/fall time, to the non perfect uniformity of the charge distribution and to the non linearity in the associated electromagnetic fields neglected by the code. It is interesting to compare the HOMDYN result with the PARMELA fit of the same case as it is shown in fig. 8: the main effect is the disappearance both in the measurements and in PARMELA of the first emittance minimum in the emittance oscillation shown by HOMDYN.

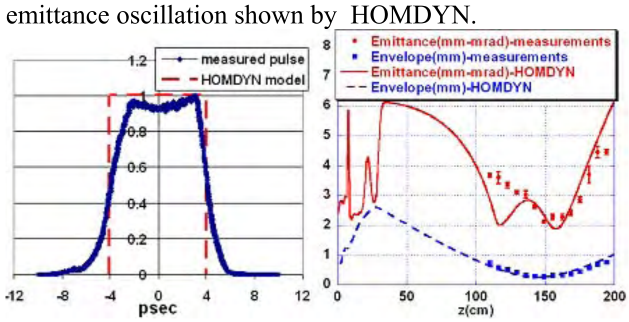

Figure 7: Measured pulse shape compared with the HOMDYN model and corresponding emittance-envelope plot with measurements and HOMDYN results.

Table 5: Measured Parameters

Parameter	Value
Energy	5.65 MeV
Charge	1 nC
Spot size, <σ>	390 μm
Solenoid current	209 A
Rf phase, φ-φ_{max}	0°

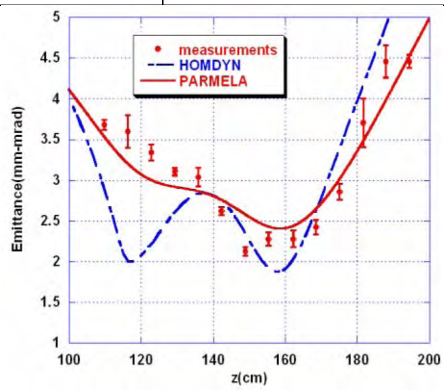

Figure 8: Emittance plot with HOMDYN-PARMELA vs measurements for the case of fig.7.

REFERENCES

[1] A. Cianchi et al., "Advanced Measurements at the SPARC Photoinjector", Proceedings of DIPAC07

[2] L. M. Young, PARMELA, Los Alamos National Laboratory report LA-UR-96-1835

[3] L. Giannessi, M. Quattromini, PRST-AB 6 120101 (2003), Web site : http://www.tredi.enea.it

[4] M. Ferrario et al., "HOMDYN study for the LCLS RF photoinjector", SLAC-PUB-8400, (2000).

[5] D. Filippetto, "A robust algorithm for beam emittance and trace space evolution reconstruction", SPARC/EBD-07/002, June 2007

[6] M. Ferrario et al., "Experimental results with the SPARC Emittance-meter", these Proceedings

GENERATION OF A MULTIPULSE COMB BEAM AND A RELATIVE TWIN PULSE FEL

M. Boscolo[a,*], I. Boscolo[b], F. Castelli[b], S. Cialdi[b], M. Ferrario[a], V. Petrillo[b], C. Vaccarezza[a]
[a] INFN/LNF, Via Enrico Fermi 40, 00044 Frascati (Roma), Italy
[b] University and INFN/MI, Via Celoria 16, 20133 Milano, Italy

Abstract
A radiofrequency electron gun driven by a train of laser pulses joined to a compressor generates trains of THz-subpicosecond e- pulses. Assuming a prompt electron emission, the laser train generates a train of electron disks at the cathode, then the disk train evolves towards a slug with a slight density modulation but also with a peculiar sawtooth energy modulation. This kind of energy modulation is transformed into a density modulation by a buncher recovering at a good extent the initial intensity beam profile. The THz electron beam formation and the FEL interaction are studied, from start-to-end, by simulations for the SPARC machine, with two electron pulses generated through that mechanism.

INTRODUCTION

Electron pulse trains of some hundreds pC charge, sub-picosecond length and repetition frequency of some THz can be useful to drive FEL experiments, plasma accelerators and efficient generation of THz radiation [1]. A radio-frequency (rf) electron gun whose photocathode is illuminated by a comb-like laser pulse generates at the cathode subpicosecond high charge disk trains.

It is well known in fact that a disk-like bunch, i.e. a bunch with longitudinal dimension γL (in the bunch moving frame) shorter than its transverse dimension R, corresponding to an aspect ratio: $A=(R/\gamma L)>>1$ has a longitudinal space charge field component linear along the bunch [2,3,4]. The normalized longitudinal space charge field as a function of the aspect ratio A for a uniform charge distribution of length L is given by [5]:

$$E_Z = \sqrt{A^2 + \left(1-\frac{z}{L}\right)^2} - \sqrt{A^2 + \left(\frac{z}{L}\right)^2} \; .$$

During acceleration the bunch aspect ratio scales like $1/\gamma$ while the longitudinal space charge force decreases like $1/\gamma^2$. It results that at the exit of the gun cavity the work done by the longitudinal space charge force along the bunch produces a linear correlation in the longitudinal phase space, if acceleration takes place fast enough to prevent transition at low energy from disk like bunch (A>1) to cigar like bunch (A<1). This is a very attractive feature for a subsequent bunch compression, since the final bunch length after any compressor device is limited by the longitudinal emittance resulting from non-linearities in the accelerating and longitudinal phase space fields. The work done by the space charge force produces an energy modulated electron beam, of about $\Delta E\sim 0.4$ MeV, with a sawtooth profile. Such an energy distribution can be exploited to restore the initial density profile either by means of an rf accelerating structure operating in the velocity bunching mode [6] or by a magnetic compressor [7,8,9] with negative R_{56}.

The amplitude of the energy modulation depends on the number and initial thickness of the electron micro-bunches. Given the charge per macrobunch, the thinner the microbunches the higher the resulting energy spread at the end of the rf-gun and, in turn, the tighter turns the current modulation after a compression. The beam dynamics inside the rf-gun and downstream inside a velocity-buncher is studied by simulations with the PARMELA [10] code and here we present the results relative to six and two microbunches train generation. In the latter case, the twin micropulses electron beam exiting the beamline is then transported and focused into the undulator for the FEL simulation with the GENESIS [11] code. These studies are carried out on the LNF-SPARC machine; the parameter set for the case under discussion is reported in Table 1.

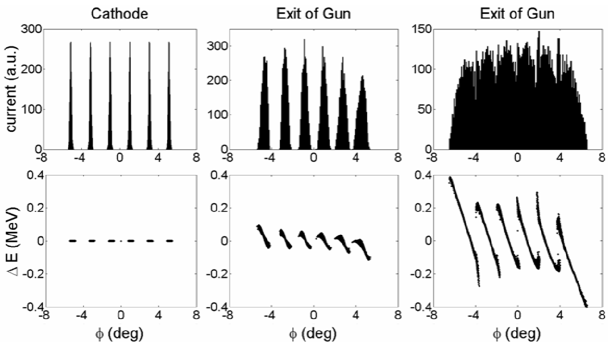

Fig. 1: Evolution of a six bunches train: at cathode, at exit of gun (left and middle plots) and at the entrance of the first linac section at z=1.5 m (right plots). Upper row: longitudinal profile, lower row: ΔE(MeV) versus length .

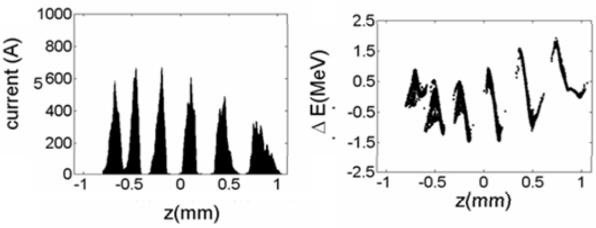

Fig. 2: Beam current and ΔE(MeV) at the end of three TW structures, that is at 12 m far from cathode, as a function of longitudinal coordinate z(mm), left and right plot respectively.

Table 1. Parameters for the rf-gun (first column), velocity bunching cavity (second column) and two accelerating cavities (third and fourth column) used for the compressed twin pulse simulation in the SPARC accelerator.

	Rf-gun	I TW section	II TW section	III TW section
Gradient [MV/m[	120	25	25	21.3
Energy [MeV]	5.6	16.5	91.2	155.5
Phase ϕ [deg]	32	-93	0 (on crest)	0 (on crest)
Solenoid field [Gauss]	2730	1100	1100	0
length [cm]	15	300	300	300

BEAM SIMULATION RESULTS

We present the dynamics of a possible comb beam generation experiment at the SPARC photoinjector [12], under commissioning at the INFN national laboratories in Frascati. The SPARC photoinjector consists in a 1.6 cell rf gun operated at S-band with a peak field on the cathode of 120 MV/m followed by an emittance compensating solenoid and three accelerating cavities 3 m long of the SLAC type, the first two embedded in a solenoid field as foreseen for the velocity bunching experiments. The photocathode in the rf electron gun is illuminated by a Ti:Sa laser providing, in the standard operation, 10 ps long rectangular (1 ps rise time) light pulses at 266 nm (third harmonic) and delivering about 500 µJ energy per pulse. Electrons emitted by the cathode are accelerated in the gun up to 5.6 MeV. Then, they drift for about 1.5 m and afterwards they enter the three accelerating sections to reach the final energy of 150 MeV.

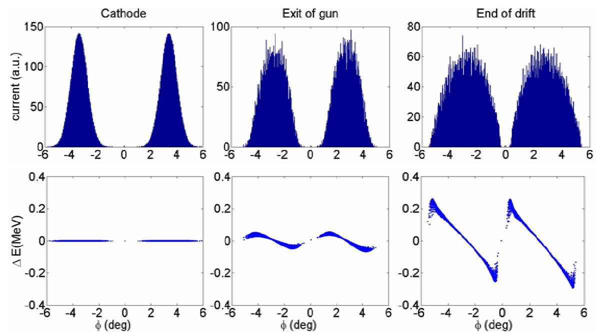

Fig. 3: Evolution of a 10 ps comb beam at cathode, at exit of gun (left and middle plots) and at the entrance of the first linac section at z=1.5 m (right plots). Upper row: longitudinal profile, lower row: ΔE [MeV] versus length.

An example of the results of PARMELA simulations is shown in Fig. 1: the features of initial density washing out and the sawtooth shape of the energy modulation are evident. Fig. 2 shows the restored density beam modulation after passing through a velocity buncher. The beam enters the first TW section at -101° off crest and beam energy at the end of beamline is about 90 MeV; the total charge of the six bunches train is the nominal SPARC bunch charge Q_{tot}= 1.1 nC.

An analogous study for a twin pulse generated at the cathode is shown in Fig. 3; each one of the two Gaussians has a longitudinal sigma of σ_t=0.6 ps and they are far from each other ~2 mm. The radial spot has been decreased accordingly to the charge reduction. In fact, emittance has been optimized at expenses of the two microbunches charge, being the total charge halved with respect to nominal value. Nevertheless, two peaks with current of the order of I_{peak}~400 A are obtained at the end of the three accelerating cavities (as shown in the upper left plot of Fig. 4). The corresponding beam emittance and envelope evolution along the beamline are shown in Fig. 5, in red and blue are shown the rf compressed and uncompressed cases, respectively. The projected rms emittance results $\varepsilon_{x,rms}$=1.4 µm and rms energy spread $(\Delta E/E)_{rms}$=0.14 % without rf compression at 12 m, while $\varepsilon_{x,rms}$=3.3 µm and $(\Delta E/E)_{rms}$=0.3 % with rf compression (with the parameter set reported in table 1).

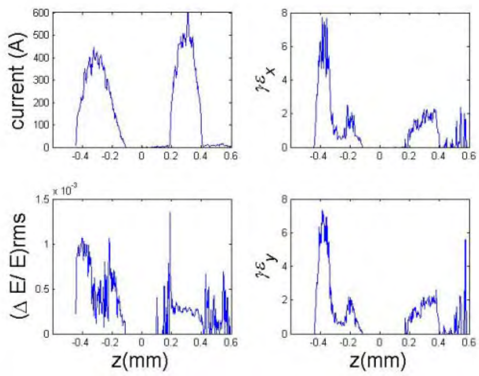

Fig. 4: Beam current (upper left) of a twin compressed pulse beam at the end of three TW structures, rms radial and vertical projected emittance (upper and lower right, respectively) and rms energy spread (lower left).

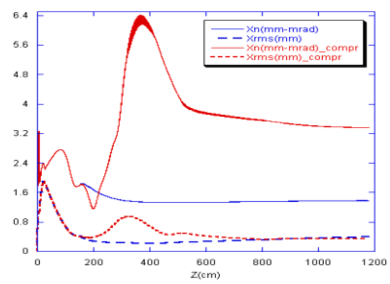

Fig. 5: Evolution of beam emittance (full line) and envelope (dotted line) with rf compression (red) and uncompressed case (blue) for the twin pulse beam case.

This twin pulse beam, exiting the three accelerating cavities with a slice emittance of about $\varepsilon_{slice}\leq 2$ µm and energy spread $(\Delta E/E)_{slice}\leq 0.1\%$ (see Fig. 4), is then focussed and sent though the undulator with the goal of producing two separated but close radiation spikes, useful for pulse-probe experiment.

FEL SIMULATIONS

The FEL radiation emitted by the twin pulse comb beam has been computed by means of the code GENESIS. The undulator parameters assumed in the simulations are the wiggler period λ_w=2.8 cm and the wiggler parameter A_w=1.47, according to the nominal values of the SPARC project.

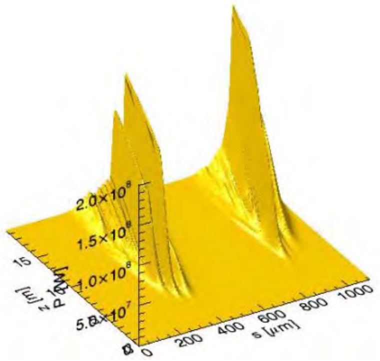

Fig. 6: Radiation power along the undulator (z) and along the bunch (s).

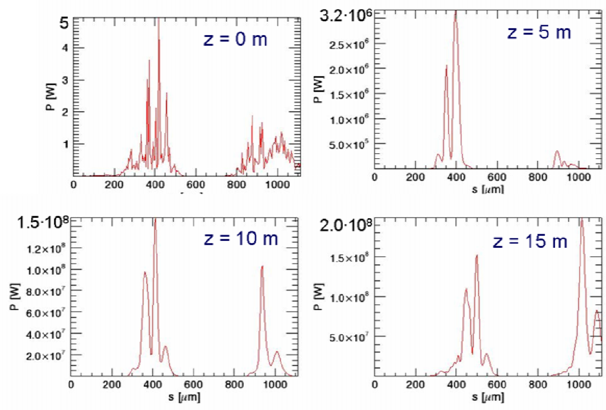

Fig. 7: Radiation power P in Watts versus the coordinate s along the bunch in μm at z=0, 5, 10 and 15 m.

The beam given by PARMELA has been focussed and matched to the undulator, the r.m.s. value of x at the entrance of the undulator being 87 μm. The simulation has been followed up to saturation (wiggler length L_w= 19 m) in the undulator. Fig. 6 shows a plot of the radiation power versus both the coordinate z along the undulator and the coordinate s on the bunch. In Fig. 7 four snapshots of the radiation pulses at z=0, z=5 m, z=10 m and z=15 m are presented. As appears from Fig. 7 the radiation produced by the trailing bunch (the structure on the right of the figures) saturates before 10 m, reaching a power peak value of P_{peak}=1.5 10^8 W, while the leading bunch produces P_{peak}=2 10^8 W in about 14 m.

The radiation wavelength is around 0.48 μm, and the parameter ρ calculated for each single bunch is of the order of $\rho \approx 10^{-2}$. The three dimensional gain length L_g is about 0.35 m. The slippage length is of the order of 100 μm, resulting smaller than the distance between the two peaks of the radiation; hence the two pulses do not overlap. We notice that the two radiation bunches have different values of $<\gamma>$, in fact for the leading bunch it is $<\gamma>$=305.74 while the trailing bunch $<\gamma>$=304.96, so they have two slightly different values of the radiation wavelengths.

CONCLUSIONS

Simulations show that an rf-gun driven by a laser subpicosecond pulse train in connection with a buncher can transform that laser pulse train into a subpicosecond electron beam pulse train. The beam features in terms of peak current, energy spread and emittance are very sensitive to the injection phase into the rf-cavity, to the charge of the macro-pulse and to the compensating solenoidal fields. The injection phase into the velocity buncher cavity has to be around -100° because a phase space rotation of 270° is required in order to obtain the whole compression.

The exploitation of the presented technique for the generation of two high current peaks in SPARC machine has shown that the energy spread and emittance of the two 0.6 ps long electron pulses are good enough for the FEL interaction in the SPARC undulator. The FEL simulation of the twin peaks shows that they do not interfere, thus leading to two neatly separated powerful radiation pulses useful for pump-probe experiments.

ACKNOWLEDGEMENTS

This work has been partially supported by the EU Commission in the sixth framework program, contract n. 011935 EUROFEL and n. RII3-CT-PHI506395CARE.

REFERENCES

[1] P.O.Shea et al., in: Proc. of 2001 Part. Acc. Conf., Chicago, IEEE, NJ, p.704 (2001).
[2] L. Serafini, AIP Conf. Proc. **413**, p.321 (1997).
[3] O.J.Luiten et al., Phys. Rev. Lett., **93,** p.094802 (2004).
[4] J.B. Rosenzweig et al., Nucl. Instr. and Meth. A **557** p.87 (2006).
[5] M. Ferrario et al., SLAC-PUB-8400 (2000).
[6] L. Serafini, M. Ferrario, AIP Conf. Proc. **581,** p.87 (2001).
[7] M.Boscolo et al. in: Proc. of EPAC06, p. 98 (2006).
[8] M. Boscolo, M. Ferrario, C. Vaccarezza, I. Boscolo, S. Cialdi, F. Castelli, , Int. J. Mod. Phys. B 21, p.415 (2007).
[9] M. Boscolo, M. Ferrario, I. Boscolo, F. Castelli and S. Cialdi, Nucl. Instr. and Meth. A, (2007) http://dx.doi.org/10.1016/j.nima.2007.04.129
[10] J.Billen, PARMELA, LA-UR-96-1835 (1996).
[11] S. Reiche: Genesis 1.3.
[12] M.Ferrario et al., this Conf.

LASER AND RF SYNCHRONIZATION MEASUREMENTS AT SPARC

Alessandro Gallo, Marco Bellaveglia, Giancarlo Gatti, Carlo Vicario, INFN/LNF, Frascati (Roma)

Abstract

The SPARC* project consists in a 150 MeV S-band, high-brilliance linac followed by 6 undulators for FEL radiation production at 530 nm. The linac assembly has been recently completed. During year 2006 a first experimental phase aimed at characterizing the beam emittance in the first 2m drift downstream the RF gun has been carried out. The low level RF control electronics to monitor and synchronize the RF phase in the gun and the laser shot on the photocathode has been commissioned and extensively tested during the emittance measurement campaign. The laser synchronization has been monitored by measuring the phase of the free oscillation of an RF cavity impulsively excited by the signal of a fast photodiode illuminated by the laser shot. Phase stability measurements are reported, both with and without feed-back correction of the slow drifts. A fast intra-pulse phase feedback system to reduce the phase noise produced by the RF power station has been also positively tested.

INTRODUCTION

The SPARC project presently under commissioning at the Frascati Labs of INFN is a compact test facility aimed to generate FEL radiation in the visible spectrum (530 nm). The required nominal beam energy (150 MeV) is obtained from an S-band linac consisting in an RF gun followed by 3 TW accelerating sections (SLAC type), while an RF deflector dedicated to bunch longitudinal phase space diagnostics is placed at the linac end. As shown in Fig. 1, the linac total length is ≈ 15 m, while the whole machine is accommodated in a 36 m long experimental hall.

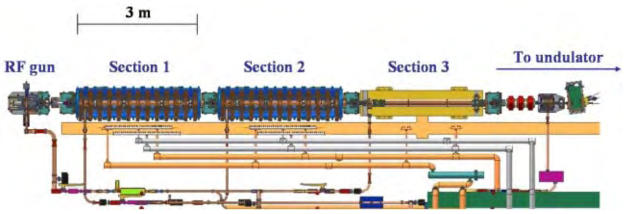

Figure 1: SPARC hall CAD top view.

The problem of keeping laser systems, RF systems and accelerator diagnostics extremely well synchronized is a crucial issue for the successful operation of the various FEL radiation sources presently in the construction or design phase [1]. For some projects the synchronization specifications are so tight that technological developments beyond the state-of-the-art are required to cope with them.

The general plant of synchronization systems consists in a distribution network to provide optical or electrical reference signals to the devices (lasers, RF stations, streak cameras, ...), and in a variety of equipments to measure and lock the device phase to the local reference.

Details on the architecture of the SPARC synchronization system and on the hardware used for this task have been already published [2].

The CW reference signal is generated by a commercial μ-wave frequency synthesizer (Rohde-Schwarz SMT) at the linac frequency (the SLAC standard 2856 MHz), then it is amplified by a solid state RF amplifier before being passively split in a number of reference signals distributed all over the machine.

Due to the limited linear dimensions of the machine, the commercial, coaxial, thermally compensated cable Andrew FSJ4-50B has been used for the reference distribution and RF signal transport to the central demodulation board. According to the producer specifications, the cable phase stability is better than 20fs/m/°C and the attenuation is ≈0.25dB/m @ 2856MHz. The SPARC hall is thermally stabilized within ±2°C.

The RF signal monitoring is performed by custom I&Q mixers followed by sampling boards of different types (ADLINK 9812 12-bit, 4-channels, 20 Ms/s; NI PXI 5105 12-bit, 8-channels, 60 Ms/s). A demodulation channel phase resolution of ≈ 10 fs for 4 μs flat RF pulses has been measured on the bench.

Pulse-to-pulse phase variations can be monitored and corrected by slow feedback systems. Being 10 Hz the linac rep. rate, from Nyquist theorem follows that only phase noise in a band up to 5 Hz can be correct. We conventionally call "drift" the noise inside and "jitter" the noise outside this bandwidth. Pulse-to-pulse feedback systems can only correct the phase drift, which however includes all the thermal effects. The main synchronization goals for the various operational phases of the SPARC project are summarized in Table 1. The phase I goal is to drive the FEL process to saturation and an rms phase stability $\sigma_t < 1500$ fs is required, mainly between the UV laser shot and the accelerating field in the RF Gun.

The synchronization specifications will be tighter for phase II, where bunch RF compression will be tested, and for the SPARC next generation experiments, and will involve a larger number of the machine sub-systems.

Table 1: SPARC synchronization goals

	Goal	Critical sub-systems	RMS time jitter [fs]
SPARC Phase I	FEL radiation @ 530 nm	Laser, RF Gun	1500
SPARC Phase II	RF bunch compression	Laser, RF Gun, 1st TW section	500
SPARC next generation experiments	FEL seeding, Plasma accel. ...	Photocathode laser, seeding laser, RF power stations, ...	100 ÷ 300

* This work has been partially supported by the EU Commission in the sixth framework programme, contract no. 011935 - EUROFEL-DS3

PHOTOCATHODE LASER SYNCHRONIZATION MEASUREMENTS

The SPARC photocathode laser system has been purchased by Coherent Inc. It consists in CW passive mode-locked IR oscillator (the MIRA 900 S) with 79.33 MHz pulse rep. rate, followed by a regenerative and 2 multi-pass amplifiers, UV conversion on a non-linear crystal, pulse stretcher and a transfer line to the photocathode. The final 10 ps flat-top pulse has a rep. rate of 10 Hz, with an energy per pulse of ≈ 100 μJ [3].

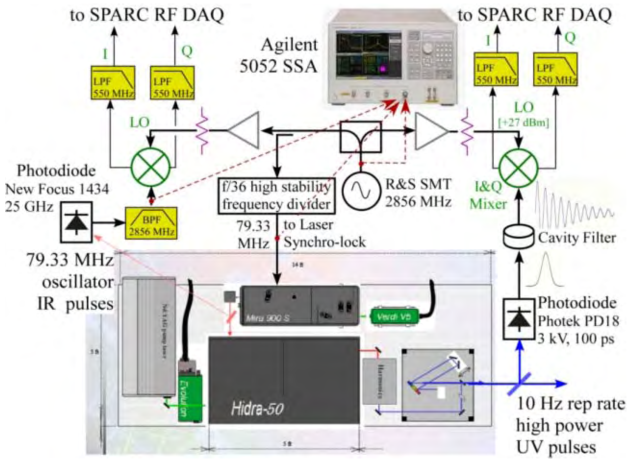

Figure 2: laser synchronization measurements.

The synchronization with the RF reference is obtained at the laser oscillator level. The frequency of the reference signal is reduced to RF/36 by means of a custom prescaler board based on fast and precise ECL technology [4]. The laser oscillator pulse repetition is locked to the RF/36 signal thanks to the Synchrolock system, which is a special PLL acting on the laser cavity mirrors through fast piezo-controllers. The fast mechanical control of the laser cavity length allows the Synchrolock bandwidth to extend typically up to ≈ 2 kHz.

Different kind of measurements on the laser-to-reference phase stability have been performed during the 2006 runs dedicated to the emittance experimental characterization in the 2 m drift downstream the RF gun. The complete schematic layout to measure the laser system phase stability is shown in Fig. 2.

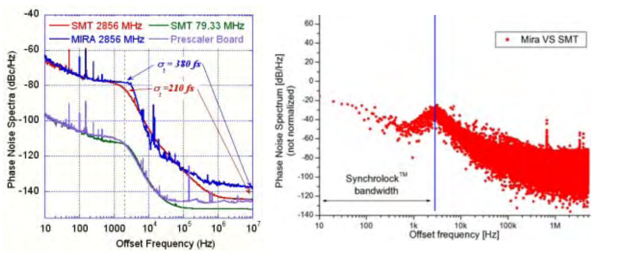

Figure 3: reference source and laser oscillator phase noise.

Laser Oscillator Phase Noise Measurements

The phase noise spectra of the reference source and of the synchro-locked laser oscillator converted with a fast photodiode have been measured. The measurement has been made with the Source Signal Analyzer Agilent 5052A SSA, which is a standard instrument for characterize source phase noise. Measurement results are summarized in the Fig. 3 left plots, showing that laser oscillator and reference are well locked in a frequency range up to 1 kHz. The residual integrated phase noise outside the Synchrolock bandwidth is ≈ 210 fs for the source and ≈ 380 fs for the laser oscillator.

The residual phase jitter outside the Synchrolock bandwidth results in a relative jitter between the two sources. A time-domain sample of relative jitter has been measured with the standard mixing technique and acquired, and then converted in frequency-domain by applying FFT. The result, reported in the right plot of Fig. 3, is a noise spectrum peaking at ≈ 3 kHz, showing that the Synchrolock loop gain is properly set close to the limit. The standard deviation of the data sample is ≈ 350 fs, in good agreement with SSA measurements.

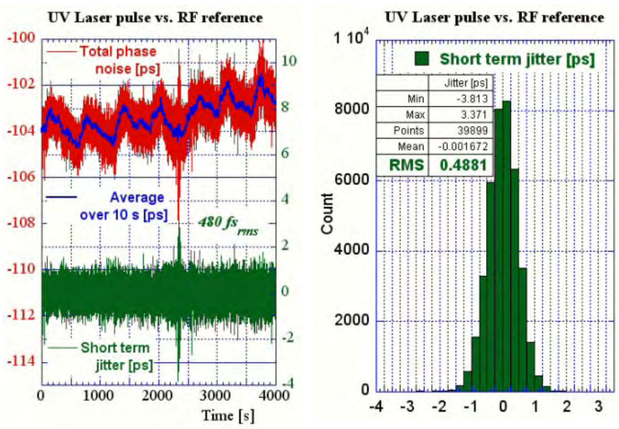

Figure 4: Phase jitter of the UV laser pulses.

UV Laser Pulse Phase Jitter Measured at 10 Hz

The laser rep. rate is reduced first to 1 kHz and finally to 10 Hz along the amplification chain. In order to measure the phase stability of the laser output pulses, we make use of a high-voltage photodiode and of a dedicated RF cavity filter to convert the laser pulse in a long-lasting, decaying sine-wave voltage. The cavity free oscillations are "triggered" by the laser pulse arrival, so that the information on the pulse synchronism is encoded in the RF phase of the cavity oscillations which is measurable with the standard mixing technique. The demodulated amplitude and phase of the cavity free oscillations have respectively exponential and linear profiles. The laser shot arrival phase is given by the intercept of the linear fit on the RF phase data, while the slope of the fit is a measure of the detune of the cavity with respect to the frequency of the reference source. This allows tuning the cavity by means of a remotely controlled mechanical plunger in order to maintain its natural frequency as close as possible to the reference frequency.

Measurement results are reported in Fig. 4. The phase of the UV laser shots has been acquired at 10 Hz for about 4000 s. Data vs. time are plot in the left, showing a slow time-varying structure (in blue). The short-term jitter, i.e. the difference between the phase data and the low frequency structure is plot in green. The measured standard deviation on this data sample is $\sigma_t \approx 490$ fs. The lowest time jitter measured on the SPARC laser UV beam is $\sigma_t \approx 400$ fs, obtained on a data record of ≈ 120 s. Being this figure very similar to the relative phase noise measured on the laser oscillator, we may conclude that the laser amplification chain contributes very little to the total jitter of the laser beam

Recently, the cavity filter has been rebuilt to resonate at 3/4 RF = 2142 MHz to reject the large environmental noise at 2856 MHz that affects the measurement when the RF power stations are working. The new cavity has been designed to work on the TE011 solenoidal mode, which provides a large Q-value improving the quality of the phase linear fit. The upgraded measurement set-up has shown excellent performances.

RF STATION PHASE NOISE CURES

The RF power stations introduce a non-negligible amount of phase noise that has to be limited or cured to improve the machine global synchronization. The RF phase of each station can be measured pulse-by-pulse, and corrected by a slow feedback loop in a band extending up to 5 Hz. To correct also the high-frequency jitter introduced by the station (mainly due to its high-voltage supply) we have designed and built a fast, intra-pulse feedback loop capable of correcting the station phase deviation within the 4.5 µs time duration of the RF pulse.

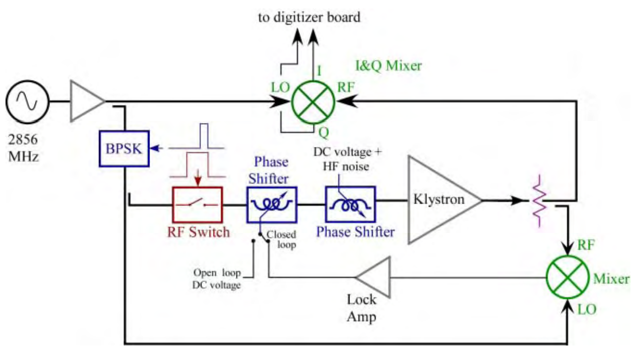

Figure 5: Intra-pulse phase lock schematics.

The schematics of the intra-pulse phase lock feedback loop is shown in Fig. 5. This kind of feedback loop requires a fast, analog controlled phase shifter and a broadband lock amplifier, together with short connections to limit the total open loop group delay. The lock amp is a real integrator circuit based on broadband current-feedback operational amplifiers.

The RF station phase noise has been measured in open and closed loop condition, and results are reported in Fig. 6. Again the phase noise jitter appears to be superimposed to a slow, low frequency structure that can be corrected by pulse-to-pulse feedback loop. The phase jitter is noticeably reduced by one order of magnitude from ≈ 230 fs to ≈ 23 fs. Also the low-frequency structure of the global phase noise sample is strongly reduced by the intra-pulse feedback loop, being mainly generated by temperature drift of the klystron cooling water.

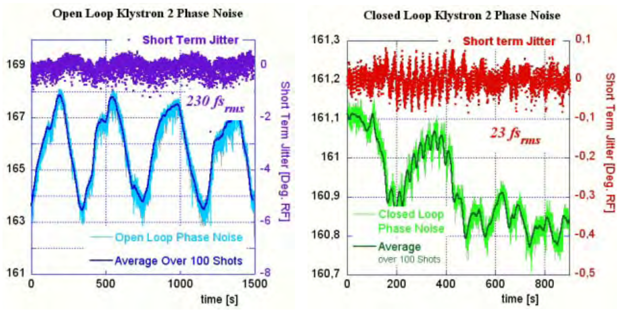

Figure 6: Open and closed loop RF station phase noise.

CONCLUSIONS

The SPARC synchronization and low-level RF system has been extensively tested during the 2006 run dedicated to the emittance characterization downstream the RF gun.

Results show that the 10 Hz UV laser pulses sent to the photocathode are synchronized to the RF reference within ≈ 400 fs rms, and that this jitter mainly comes from the synchronization of the laser oscillator to the reference accomplished by the Synchrolock servo-loop.

The inherent phase jitter of the RF station output is ≈ 230 fs rms and it is reduced to ≈ 23 fs rms by using a dedicated intra-pulse phase lock feedback loop. Therefore the contribution of the RF stations to total synchronization noise of the machine can be made negligible.

The reported results already comply with the specifications for the SPARC experimental phases I and II. SPARC next generation experiments may require improvements of the phase noise quality of the laser and µ-wave sources, and/or modification of the system architecture to reach global synchronization in the scale of ≈ 100 fs rms.

ACKNOWLEDGMENTS

The authors wish to thank D. Alesini, R. Boni, A. Drago, G. Di Pirro, A. Ghigo, P. Musumeci, M. Petrarca and F. Tazzioli for helpful discussions and experimental support. All the used hardware has been assembled and put in operation by L. Cacciotti, while A. Sprecacenere has cabled the whole system.

REFERENCES

[1] J. Kim et al., “Femtosecond synchronization and stabilization tecniques”, Proc. FEL06, Berlin

[2] A. Gallo, et al., “The SPARC RF synchronization system”, Proc. of PAC05, Knoxville

[3] C. Vicario et al., “Commissioning of the laser system for SPARC photoinjector”, Proc. of EPAC06, Edinburgh

[4] A. Drago, “The SPARC timing system”, INFN/LNF Tech. Note, in publication, www.lnf.infn.it

POWER TESTS OF A PLD FILM MG PHOTOCATHODE IN A RF GUN

G. Gatti, L. Cultrera, F. Tazzioli, INFN/LNF, Frascati, Roma, A. Perrone INFN-Lecce (Lecce University), P. Musumeci, J. Moody, UCLA, Los Angeles, CA

Abstract

Metallic film photo-cathodes are rugged, have a fast response and good emission uniformity. Mg has also a relevant Quantum Efficiency (QE) in the near UV. A cathode suitable for a 1.5 cells S-band RF gun has been produced by depositing an Mg film on Cu by Pulsed Laser Deposition (PLD) technique. After different optimizations, stable good results have been reached in the low field measurement scenario. A sample was deposited on a gun flange and tested in the 1.6 cell injector at UCLA Pegasus facility to prove cathode resistance in a high field environment. The results are described.

INTRODUCTION

Mg films deposited by PLD have shown a long term stability performance in the framework of low field testing [1]. Advantages are good uniformity of emission through the surface (better than 20%) and a QE response in the near UV one order of magnitude higher than conventional copper cathodes. Performances in high field environment have still to be proved. Troubles could be given by poor adhesion of the film to the substrate, both during normal operating conditions and especially during the gun conditioning process. In fact, the frequent strong arch events could remove completely the coating from the substrate. That is why the power test represents the key step for proving the convenience in the use of this deposition technique for realization of cathodes suitable for rf photo-injectors.

CATHODE PREPARATION

Deposition is achieved in UHV chanber using the UCLA/BNL type 1.6 cell gun back flange as a substrate ablating a Mg rotating target surface by mean of a XeCl excimer laser. The ejected material impinges on the substrate, located in front of the target itself at 5.5 cm distance. Laser wavelenght is 308 nm and pulse lenght is 30 ns. Deposition took place in vacuum environment whose pressure was 5E-8 mbar. 5000 laser shots were delivered in order to remove the polluted layers of the target; during this time, the substrate was shielded to avoid contaminants. Afterwards, the deposition took place using a mask for delimiting the area to be covered. The sample taken in consideration here under test has been deposited through 30000 shots with a fluence of 10 J/cm^2, for a final thickness of about 0.5 μm.

INSTALLATION AND CONDITIONING

After deposition, the cathode has been shipped for being installed inside Pegasus photo-injector at UCLA. Since no closed gas environment has been used for transportation, the sample is expected to be polluted. In fact the formation of the oxide layer over Mg, when exposed to air is very fast, as proven for the samples tested in low field environment [2]. As widely known, it is necessary, after exposure to air, to operate a surface activation (e.g. laser cleaning) in order to recover the high Mg QE. During the installation of the cathode, the gun was easily tuned through the standard capacitive back flange deformation. After a visual inspection, and standing to the good vacuum conditions (pressure better than 1E-8 mbar) it can be stated that mechanical stress in the cathode addressed by the tuning process didn't affect the Mg film in a negative way. Afterwards, no difference was noted in the conditioning process respect to the copper case, while scratches on the cathode surface [3] would have generated strong archs, making conditioning very slow, and probably impossible to get to high fields. After conditioning process, the RF gun was able to operate routinely at 100 MV/m peak field for some months, and the Mg cathode is still installed in order to test its long term resistance.

DARK CURRENT MEASUREMENT

The experimental apparatus, showed in Fig.1 is composed by the gun, focusing solenoid and Faraday cup (FC), plus the signal acquisition section.

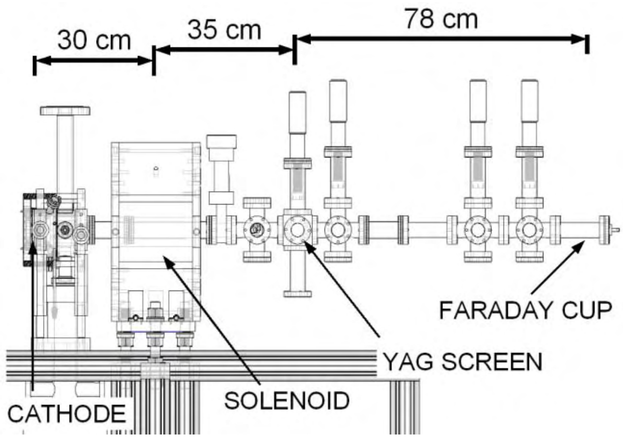

Figure 1: Measurement setup layout.

The current coming out of the FC was read by mean of a noise filter and an oscilloscope. Obviously, the current pulse was occuring during the RF pulse duration, 1.5 μs long in this case. Moreover, inside this time slot, the dark current structure is given by a train of pulses centered on the RF peak field [4]. Inside this framework the dark current was measured integrating all the peak contributions over the RF pulse duration giving average current values on the order of some μA (charge of some pC). This situation can be modelled modifying conventional Fowler-Nordheim formula for a sine wave variable field case[3]

$$\bar{I}_F = \frac{5.7 X A_e (\beta E_0)^{2.5}}{\phi^{1.75}} \exp\left(\frac{-6.53 X 10^9 X \phi^{1.5}}{\beta E_0}\right)$$

It was not necessary to change the focusing strenght of the solenoid, in order to collect all the charge in the FC for different field values. I.e. the solenoid field was hence fixed at 1300 kG where the charge was maximum.

In Fig.2 it is shown the value of the collected current vs. the applied peak field.

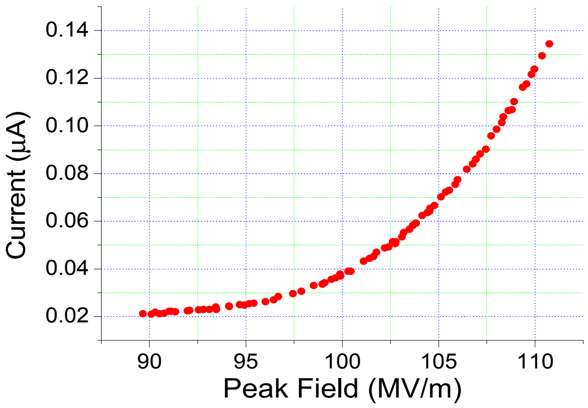

Figure 2: Darck current vs. accelerating RF field.

In order to extract information from this measurement, some assumptions have to be done. First of all it is assumed that the main contribution for the current comes from the cathode area, and the other zones emitted electrons are not delivered by the system to the FC [4]. Afterwards, some assumptions on the cathode work function φ can be done to get an estimate of the cathode field enhancement factor β and emission effective area A_e. Putting the previous data in the form of a Fowler plot, Fig.3 is obtained.

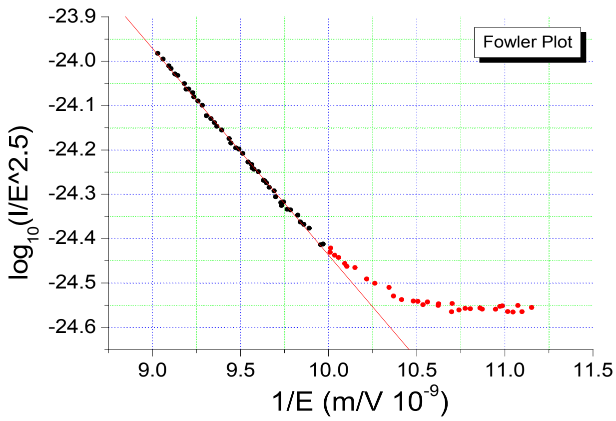

Figure 3: Fowler plot of the cathode dark current.

What theory states is a linear behaviour for the Fowler-Nordheim plot. Moreover it can be seen that for large field values, the curve becomes linear as expected. It could be assumed that the "shoulder" of the plot is given from an intermediate level in which different areas start to emit at a different field level, according to their local geometric enhancement factor. Above this treshold, the total emission area stays the same, and the cathode emission finally obeys Fowler-Nordheim theory. Here it will be considered just the part of the curve above the treshold. A linear fit of such a plot gives the values for the field enhancement factor and the emission area. Just an assumption on the working function of the cathode is necessary. Taking in account that for clean Mg the working function is 3.6 eV [2], what can be expected is a higher value generated by the oxide layer. Moreover, past quantum yield measurements on oxided samples conducted with 4.66 eV photons [5] (266 nm wavelenght) showed that in this case the work function is above the photon energy, with a two-photon emission response (4.66 eV <φ< 9.32 eV).

Plotting the enhancement factor versus the workfunction, the situation is the one depicted in Fig. 4.

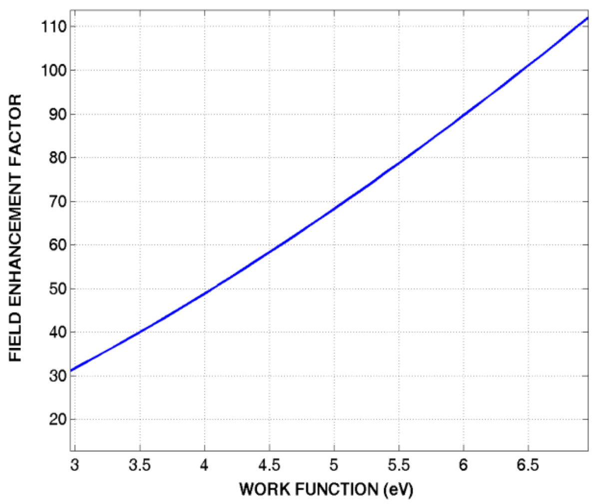

Figure 4: Field local enhancement factor vs. work function.

It is known from literature [3], that acceptable values for the enhancement factor are within the interval 40-100, for normal surface roughnesses. This would bring a workfunction greater than 3 eV, as already stated.

QE MEASUREMENT

Dark current measurement was followed by the quantum efficiency evaluation. The cathode was illuminated by a Ti:Sa laser (Pegasus photo-injector driver), able to deliver up to 10 μJ on its third harmonic (266 nm) on a time duration of 30 fs FWHM. The spot size on the cathode was set at 0.7 mm radius. Recalling generalized Fowler-Dubridge theory on multi-photon emission [7] it is possible to write the expression for the cathode current as a superposition of different contributions:

$$J(r,t)=\sum_{-\infty}^{+\infty} J_n(r,t)$$

where

$$J_n(r,t)=a_n\left(\frac{e}{h\nu}\right)^n A(1-R)^n I(r,t)F\left(\frac{nh\nu-\phi}{kT(r,t)}\right)$$

Here A is the Richardson coefficient, e the electron charge, $(1\text{-}R)^n$ the nonlinear bulk absorption coefficient, T is the sample temperature, I the laser intensity, and F is Fowler function a_n is an empyrical parameter linked to the probability for the n-photon emission. Dropping out the zero order one (i.e. thermoionic emission) the dominant contributions are the n-th where nhυ>φ. For low enough intensity, the dominant term is given by the lower order multi-photon emission above the treshold (work function). This information can be very useful in order to give an estimate of the cathode working function. In fact, looking at the emitted charge versus incident laser energy (Fig. 5).

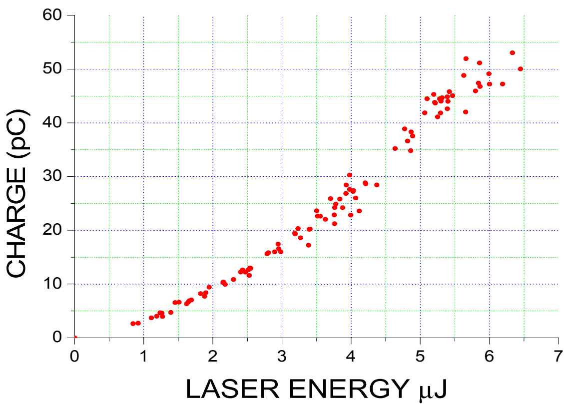

Figure 5: Cathode Quantum yield at 266 nm.

It is straightforward to notice that the emission plot has a nonlinear behaviour, most likely quadratic. This is a proof that the sample got oxided, increasing its work function to a value higher than the single photon energy and lower than two-photon energy at 266 nm (at 90 MV/m). This measurement proves the need for a future surface activation process. The peak QE in this case is 3E-5; anyway the quantum yield here expressed is not laser intensity indipendent as for the linear photo-emission [7] , so it is a parameter to be specified together with the working intensity level.

In the near future it will be operated a surface activation by mean of laser irradiation. During this operation, the laser fluence will be set slightly above the surface ablation treshold in order to remove only the oxide layer and not to damage the actual cathode. Special care will be addressed in setting up such a procedure, because the Mg cleaning treshold was retrieved in the low field testing (Pth≈0.1 GW/cm^2), operating with ps laser pulses. Several studies [8] reveal different phenomenas occuring when a metal surface is irradiated in the picosecond rather than the femtosecond regime. That is why classical empyrical scaling laws, such as

$$P_{Th} \propto \sqrt{\tau_{PULSE}}$$

would give a rough approximation of the right power to be delivered on the sample.

CONCLUSIONS

PLD Mg cathode has shown to be resistant in the RF gun environment, withstanding the conditioning process. As expected, dark current and quantum efficiency show that the cathode work function rose for effect of the oxide layer generated by air exposure. A surface activation through laser irradiation will be made soon in order to restore clean Mg QE. Special care must be addressed in this task, using femtosecond laser pulses, since conventional scaling laws cannot be applied. Further tests on this sample are foreseen.

REFERENCES

[1] L. Cultrera et al., Appl. Surf. Sci. 2007.
[2] H. Sommer, “Photoemissive Materials”, New York, Wiley 1968.
[3] J. W. Wang and G. A. Loew, “Field emission and rf breakdown in high gradient room-temperature linac structures”, SLAC-PUB-7684, 1997.
[4] I. Bohnet et al., “Dark current measurement at the PITZ rf gun” , Proc. of DIPAC 2003.
[5] G. Gatti et al., proc. of PAC 2005, 1350.
[6] L. Cultrera et al., Proc. of Linac 2006, 356.
[7] Bechtel et al., Opt. Commun. 13, 56 (1975).
[8] A. Semerok et al., Appl Surf. Sci. 138-139 (1999) 311-314.

COHERENT CHERENKOV RADIATION AS A TEMPORAL DIAGNOSTIC FOR MICROBUNCHED BEAMS

Giancarlo Gatti, INFN/LNF, Frascati (Roma)
Alan Cook, James Rosenzweig, Rodion Tikhoplav, UCLA, Los Angeles, California

Abstract

Cherenkov radiation of a relativistic e-beam traversing a thin section of aerogel is analized, putting the stress on the coherent contribution due to the intra-beam, transverse and longitudinal structure. The use of this tool as a temporal diagnostic for micro-bunched beams makes possible to improve the amount of collected power at the microbunching frequency several orders of magnitude more respect to the uncoherent Cherenkov contribution. The non-idealities of a real beam are taken in account, and some techniques aimed on enhancing the coherent part of radiation are proposed and analized analitically.

COHERENT LONGITUDINAL DIAGNOSTIC

The use of e-beam emitted radiation (e.g. SR, TR, CR) as a tool for complete reconstruction of the bunch structure, must take in consideration the coherent contribution of such a radiation, no matter which is the physical source generating the phenomenon. More in detail, assuming a process in which every particle of the beam radiates in the same way [1], just an intra-beam particle displacement (i.e. delay) will affect the total coherent contribution.

In such a way it is possible to write a general form of such a radiation, indipendently of the specific physical process that generates it. Let's assume a single particle angular spectrum $S(\boldsymbol{k})$, where $|\boldsymbol{k}|$ is the vacuum wave vector, then the whole bunch far field spectral response [Desy] will be:

$$T(\boldsymbol{k}) = S(\boldsymbol{k})(N + N(N-1)F(\boldsymbol{k}))$$

with N is the number of particles in the bunch, and $F(\boldsymbol{k})$ the so-called form factor , i.e. 3-D Fourier transform of the bunch particle distribution f. The second term in the spectrum expression, the one to deal with, is the radiation coherent contribution with its characteristic N^2 scaling.

The coherent contribution has extensively been used for longitudinal diagnostic (i.e. bunch lenght measurement), and, in some case, for the whole beam reconstruction purpose, for example employing transition radiation [2][3]. Hence, the total beam spectral response will experience both the contribution of the single particle emission and the collective bunch effect.

Cherenkov Radiation Coherent Diagnostic

The advantage in the use of Cherenkov radiation would be given by the wide and flat spectral response (cut-off wavelenghts on the order of the electron classical radius)

$$\frac{\partial N_{ph}}{\partial k \partial \vartheta} = L_d \alpha (1 - \frac{1}{\beta^2 n^2}) \delta(\vartheta - \vartheta_c)$$

in terms of number of photons per unit frequency, where α is the fine structure constant, n the medium index of refraction, β the particle velocity in speed of light units θ_c the Cherenkov angle, and L_d the lenght of the radiator. Defining the refracting index of the Cherenkov radiator as n=1+Δ, where delta ranges inside the interval 0.006-1.13 [4] the Cherenkov angle can be easily expressed as

$$\vartheta_c = \sqrt{2\Delta}$$

Hence it is natural to use this property to explore high frequency components (very fine bunch details), such as the microbunching deriving from the FEL and IFEL processes (Fig. 1).

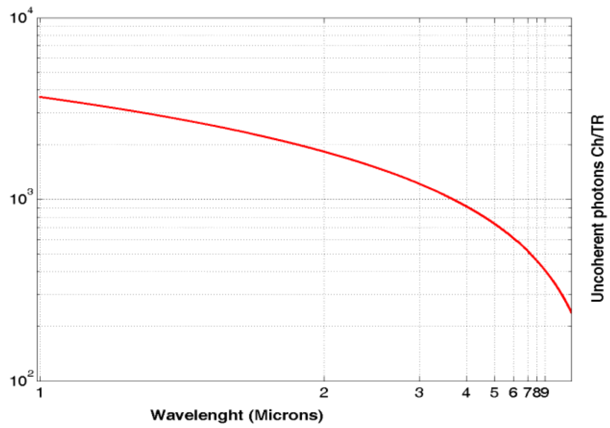

Figure 1: Uncoherent Cherenkov over uncoherent transition radiation photons vs. wavelenght

Form Factor Influence

Restricting the present framework to the case of a microbunched beam at the fundamental wavelenght λ_r, and assuming that the electrons distribution can be splitted in the product of longitudinal and transverse part, the complete form factor expression can be written as: $F(k)=F_t(k_t)F_l(k_l)$, with k_t, k_l respectively $k\sin\theta$ $k\cos\theta$. As a first example, assuming both a gaussian radial (transverse) and longitudinal distribution (whose standard deviation are, respectively σ_x=σ_y=σ_t and σ_l), the form factors become:

$$F_t(k_t) = \exp[-(\sigma_t k_t)^2] \,,$$

$$F_t(k_l) \approx \sum_{-\infty}^{+\infty} |A_n|^2 \exp[-\sigma_l^2 (k_l - n_h k_r)]^2$$

Here, the longitudinal part is expressed as a superposition of the different microbunching harmonics with weight A_n on the n-th component. The trivial integration over emission angles gives for the coherent contribution:

$$\frac{\partial N_{ph}}{\partial k} \approx L_d N_b^2 \alpha (1-\frac{1}{\beta^2 n^2}) \exp[-(\sigma_t k \sin \vartheta_c)^2]$$

$$\sum_{-\infty}^{+\infty} |A_n|^2 \exp[-\sigma_l^2 (k \cos \vartheta_c - n_h k_r)^2]$$

It is worth noting that the main limitation in generating high microbunching frequencies is given by the transverse term strong suppression. Moreover, it can be defined a "coherence angle": for a given wavelength this is the emission angle in which the transverse part "cuts" half of the photons emitted. Beyond this limit there's very strong suppression of coherence. Looking at the limitation for the longitudinal (microbunching) wavelenght, in the gaussian case above discussed, it is, for small values of the Cherenkov angle

$$\tan(\vartheta_{cohr}) \approx \vartheta_{cohr} \leq \frac{\sqrt{2}}{\sigma_t k_r}$$

This result shows how the transverse part influence grows for bigger angles. On the other side, when the emission is strongly peaked on a small angle, the transverse particles don't influence each other. One way to "restore" coherence at a given wavelenght and a given Cherenkov angle is to transversely squeeze the beam, and make it small, compared to such a wavelenght so that the transverse particle displacementes contributions can add inside a coherent lenght.

PRACTICAL APPLICATIONS

It can be useful to compare the difference in the employment of TR and CR for some experimental situations.

Considering a typical setting for the UCLA Neptune accelerator: γ=28, N_b=6E9 (i.e. Q=1nC), **Δ**=*0.008*, L_d=2.5 mm, σ_t=50 μm (that is a well focused beam), σ_l=500 μm and looking at the contribution of the single n-th microbunching harmonic, Cherenkov coherent photons are

$$N_{ph}^{CH} \approx \sqrt{\pi} L_d N_b^2 \frac{\alpha}{\sigma_l} |A_n|^2 (1-\frac{1}{\beta^2 n^2}) \exp[-(n_h k_r \sigma_t \vartheta_c)^2]$$

transition radiation ones, in the same case are:

$$N_{ph}^{TR} \approx \frac{\alpha}{2\sigma_l \sqrt{\pi} n_h k_r} N_b^2 |A_n|^2 [\frac{\gamma}{n_h k_r \sigma_t}]^4$$

It must be noted, anyway, that for such a situation, θ_c=7.2 deg, while the peak of TR is for θ_{TR} =2.04 deg, that explains a stronger suppression. In Fig. 2 the two curves are represented in a wavelenght range of 0-16 μm for a microbunching factor $|A_n|^2$ =1. It can be seen that TR dominates for the wavelenght range (0.1-15 μm), even though the decay of the Cherenkov due to the transverse exponential factor is quite abrupt. This suggests that the employment of different transverse shapes could overcome this drawback, extending the cut-off frequency.

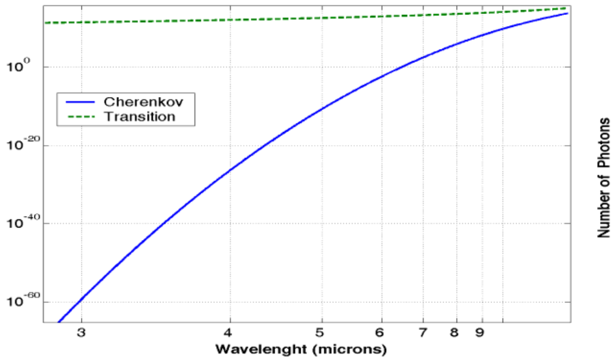

Figure 2: Gaussian beam coherent Cherenkov and TR contribution

Looking at a hard edge uniform distribution beam on the transverse dimension, with the same gaussian distribution on the longitudinal one from the previous example, the form factor changes. Being the electron radial distribution

$$f(\rho) = \frac{1}{\pi \sigma_t^2} rect_{\sigma_t}(\rho)$$

the form factor becomes

$$F(\boldsymbol{k}) = 4N_b^2 [\frac{J_1(\sigma_t k_t)}{\sigma_t k_t}]^2 \sum_{-\infty}^{+\infty} |A_n|^2 \exp[-\sigma_l^2 (k_l - nk_r)^2]$$

with J_1 first order, first type Bessel function.

Once again, taking in consideration the number of photons inside a (narrow) longitudinal microbunching peak:

$$N_{ph} \approx 4\sqrt{\pi} L_d N_b^2 \frac{\alpha}{\sigma_l} |A_n|^2 (1-\frac{1}{\beta^2 n^2}) [\frac{J_1(\sigma_t n_h k_r \vartheta_c)}{\sigma_t n_h k_r \vartheta_c}]^2$$

The improvement given by the form factor is showed in Fig. 3, where the two distributions are compared.

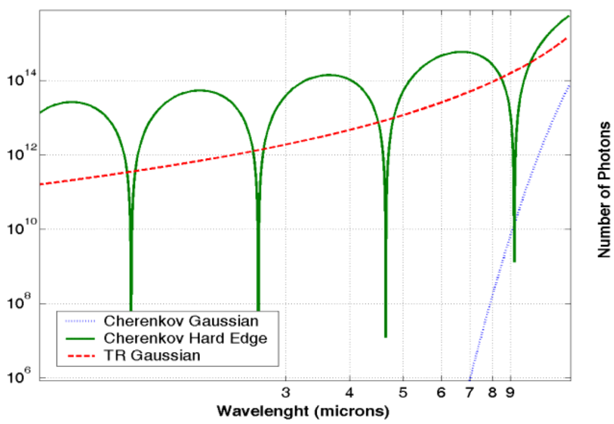

Figure 3: Hard edge/Gaussian beam Cherenkov coherent contributions. Gaussian TR is also showed

BEAM CUT EFFECT

Improvement of the bunch response at short wavelenghts could be achieved through transverse cutting of the beam. Modelling the trasverse cut with a delta functions comb gives an idea of the spectral response extension given by acting a cut. Anyway, since the delta cut is not realistic, the spectral extension would be infinite, that is obviously a not physical result. Let's assume a periodic trasverse modulation of the beam (e.g. Grid of wires). The only assumption is for the cutting period (λ_0, λ_1) to be shorter than the beam dimension. In such a way the distribution along the cartesian coordinates will be

$$f_t(x) = f(x)\sum_{-\infty}^{+\infty} A_L \exp(jLk_0 x)$$

$$g_t(y) = g(y)\sum_{-\infty}^{+\infty} C_M \exp(jMk_1 y)$$

using the Fourier expansion for the periodic modulation. Still the longitudinal contribution will have the same form *h(z)* very similar to the transverse one, but given by the microbunching components. Taking in consideration the gaussian case (but it would be valid anyway) and using the previous assumption on the cut period:

$$\lambda_0 \le 2\sigma_x$$

it leads to

$$k_0 = \frac{2\pi}{\lambda_0} \ge \frac{\pi}{\sigma_x} \ge \frac{2}{\sigma_x}$$

This gives the possibility to write the expressions of the trasverse spatial spectrum dropping out the cross product terms:

$$\left|F(k_x)\right|^2 = \left|\sum_{-\infty}^{+\infty} A_L \tilde{f}(k_x - Lk_0)\right|^2 = \sum_{L=-\infty}^{+\infty} \left|A_L\right|^2 \left|\tilde{f}(k_x - Lk_0)\right|^2$$

Assuming once again a full 3D gaussian distribution, as beam dimensions will be larger, in order to allow a physical easy way to cut. It will be σ_x, σ_y = 250μm for a squared train of cut of period λ_0, λ_1 equal to 500μm period and cut width Δ equal to 50μm so to get

$$A_L = \frac{\Delta}{\lambda_0} \sin c(\frac{\Delta}{\lambda_0} L)$$

with longitudinal dimension of the beam still 500μm. Assuming the microbunching spectral line very sharp respect to trasverse spectral distribution variation, the number of photons over this line is

$$\frac{\partial N_{ph}}{\partial \phi} = \frac{\sqrt{\pi}}{2\pi\sigma_l} L_d N_b{}^2 \alpha \left[1 - \frac{1}{\beta^2 n^2}\right] \exp[-(k \sin \vartheta_c \sin \phi \sigma^y)^2]$$
$$\sum_{-\infty}^{+\infty} \left|A_L\right|^2 \exp[-(k_r \sin \vartheta_c \cos \phi - Lk_0)^2 \sigma_x^2]$$
$$\sum_{-\infty}^{+\infty} \left|B_M\right|^2 \exp[-(k_r \sin \vartheta_c \sin \phi - Lk_1)^2 \sigma_y^2]$$

The cut of the beam results in a big improvement respect to the plain gaussian contribution; moreover it must be noted that, for modelling a realistic cut, the beam size has been assumed one order of magnitude bigger than the plain gaussian case. Even though, the spectral response of the cut beam is extended beyond the one of the tight focused beam.

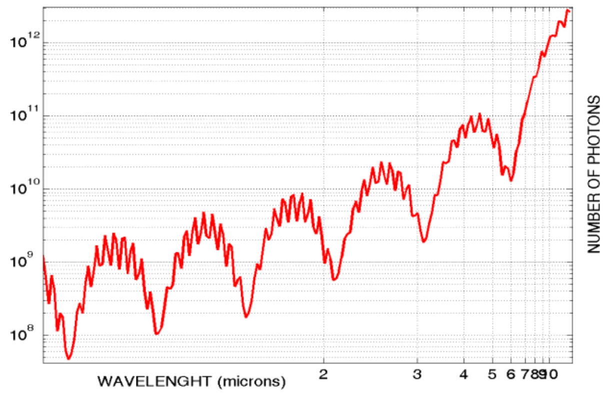

Figure 4: Coherent Cherenkov photons on a Periodic cut gaussian beam

CONCLUSIONS

The use of coherent Cherenkov radiation could be extremely useful as a longitudinal diagnostic tool, expecially moving to short wavelenghts thanks to the Cherenkov flat spectral response. Moreover, the limiting factor is given by the trasverse form factor of the beam. Different beam shapes cases have been taken in consideration, showing the possibility of drastic improvements, for example acting a transverse cut on the beam. Moreover still some effect such as divergence of the beam, radiator dispersion, electrons and light scattering inside radiator will be taken in consideration, since they are likely to make the form factor suppression less steep.

REFERENCES

[1] O. Grimm et al., DESY, April 24, 2006, internal report
[2] Y. Shibata et al., Phys. Rev. E 50, 1479-1484, 1994
[3] M. Castellano et al., Phys. Rev. E 63, 056501, 2001
[4] J. Bar et al., Nucl Inst. And Meth. A, 538 (1), p.597-607, Feb 2005

STATUS OF THE SPARC-X PROJECT*

C. Vaccarezza, D. Alesini, M. Bellaveglia, S. Bertolucci, R. Boni, M. Boscolo, M. Castellano, A. Clozza, L. Cultrera, G. Di Pirro, A. Drago, A. Esposito, M. Ferrario, L. Ficcadenti, D. Filippetto, V. Fusco, A. Gallo, G. Gatti, A. Ghigo, C. Ligi, A. Marinelli, M. Migliorati, A. Mostacci, E. Pace, L. Palumbo, L. Pellegrino, M. Preger, R. Ricci, C. Sanelli, M. Serio, F. Sgamma, B. Spataro, A. Stella, F. Tazzioli, M. Vescovi, C. Vicario, INFN-LNF, Frascati, RM, Italy
F. Ciocci, G. Dattoli, A. Dipace, A. Doria, F. Flora, G.P. Gallerano, L. Giannessi, E. Giovenale, G. Messina, P.L. Ottaviani, S. Pagnutti, G. Parisi, L. Picardi, M. Quattromini, A. Renieri, G. Ronci, C. Ronsivalle, M. Rosetti, E. Sabia, M. Sassi, A. Torre, A. Zucchini, ENEA C.R. Frascati, RM, Italy
M. Mattioli, D. Pelliccia, Università di Roma I La Sapienza, Roma, Italy
L. Catani, E. Chiadroni, A. Cianchi, E. Gabrielli, C. Schaerf , INFN-Roma II, RM, Italy
P. Musumeci, M. Petrarca, INFN-Roma, Roma, Italy
F. Alessandria, A. Bacci, R. Bonifacio, I. Boscolo, F. Broggi, C. De Martinis, F. Castelli, S. Cialdi, D. Giove, A. Flacco, C. Maroli, V. Petrillo, A.R. Rossi, L. Serafini, INFN-Milano, Milano, Italy
A. Perrone, INFN-Lecce, Lecce, Italy
M. Labat, O. Tcherbakoff, G. Lambert, D. Garzella, M. Bougeard, P. Breger, P. Monchicourt, H. Merdji, P. Salières, B. Carré, Service des Photons Atomes et Molécules, CEA Saclay, DSM/DRECAM, France
M. E. Couprie, SOLEIL, Sant-Aubin, Gif-sur-Yvette CEDEX, France
P. Emma, SLAC, Menlo Park, CA, USA
C. Pellegrini, S. Reiche, J. Rosenzweig, UCLA, Los Angeles, CA, USA

Abstract

SPARC-X is a two branch project consisting in the SPARC test facility dedicated to the development and test of critical subsystems such as high brightness photoinjector and a modular expandable undulator for SASE-FEL experiments at 500 nm with seeding, and the *SPARX* facility aiming at generation of high brilliance coherent radiation in the 1.5-13 nm range, based on the achieved expertise. The projects are supported by MIUR (Research Department of Italian Government) and Regione Lazio. SPARC has completed the commissioning phase of the photoinjector in November 2006. The achieved experimental results are here summarized together with the status of the second phase commissioning plans. The *SPARX* project is based on the generation of ultra high peak brightness electron beams at the energy of 1 and 2 GeV generating radiation in the 1.5-13 nm range. The construction is at the moment planned in two steps starting with a 1 GeV Linac. The project layout including both RF-compression and magnetic chicane techniques has been studied.

SPARC 1^ST PHASE COMMISSIONING RESULTS

The goal of the SPARC-X project is the realization of a X-ray coherent radiation source of high brilliance and tunable to the needs of the users community scientific case [1]. SPARC is meant to be a test facility for the high brightness photoinjector prototype of the SPARX project producing a 150-200 MeV electron beam to drive a SASE-FEL in the visible light and exploring all the most critical issues of the future X-Ray source subsystems. The relevance of the first phase commissioning results lies in the detailed study of the emittance compensation process of the gun-solenoid system and in the novelty of the employed diagnostic devices, so called emittance meter [2], that allowed the measurement of the electron beam features downstream the gun and the first experimental observation of the double emittance minimum effect as predicted by the theory [3]. The results relied on extensive manipulation of both transverse and longitudinal laser pulse profile [4], and were confirmed by a careful benchmarking of the numerical codes employed for tracking so far [5]. In Fig. 1 the emittance meter device is shown with a picture superposition of an example of transverse phase space reconstruction along

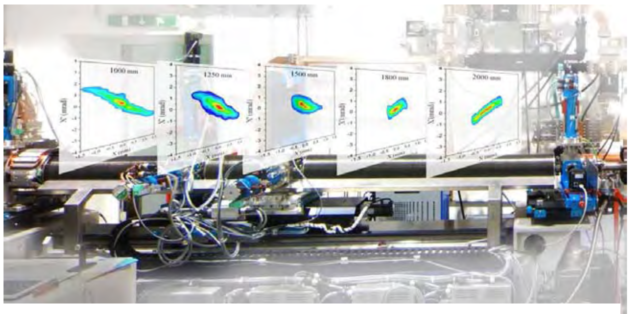

Figure 1: The SPARC emittance-meter: a movable slits plus screen system that allows the beam transverse phase space characterization along its propagation.

*Work partially supported by the EU Commission in the sixth framework program. Contract No. 011935 EUROFEL and MIUR (Research Department of Italian Government.

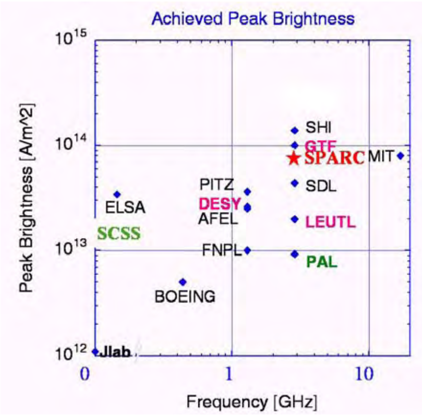

Figure 2: Achieved beam brightness.

the beam propagation. The best achieved beam brightness is about 7×10^{13} A/m^2 , with a peak current of 92 A, 0.8 nC charge, 8.9 ps FWHM (rise time < 2.6ps), and emittance 1.6 µm as it was the SPARC project design goal [4]. In Fig. 2 the SPARC result is reported together with others worldwide.

SPARC 2ND PHASE COMMISSIONING PLANS

The relevance of the obtained results during the SPARC commissioning first phase lies in the gained expertise on tuning the gun-solenoid-laser system in order to produce a beam with the high brightness design value, but mainly on the agreement between the experimental results and the beam emittance longitudinal evolution as predicted by the theory [6]. The reason is that the optimized photoinjector working point performance is based on the proper matching between the SPARC linac and the beam emittance oscillation downstream the gun.

The Linac

According to the above mentioned scheme three s-band accelerating sections have been installed, after the emittance meter removal, at the exit of the gun as shown in Fig. 3, to rise the beam energy up to 150÷200 MeV., with an accelerating gradient of 25 MV/m. To compensate the longitudinal phase space curvature a bi periodic X-band cavity working on $\pi/2$ mode has been studied and realized at LNF [7]. The 17 cell cavity length is 9 cm and it will be placed right at the exit of the RF gun. A high energy diagnostic set up is provided in the transfer line from the linac to the undulator, equipped with a 26 cm long RF-SW deflector cavity developed at LNF, to measure the bunch length with a precision of about 40 µm [8]. Downstream the RF deflector a 15 degrees by-pass beamline is provided as a spectrometer section. The coupled system RF-deflector plus dispersive element allows the 6-D reconstruction of the beam phase space and the slice emittance measurements in both horizontal and vertical plane. The by-pass will host also a magnetic chicane for bunch compression tests. These will also be performed with the alternative velocity bunching scheme.

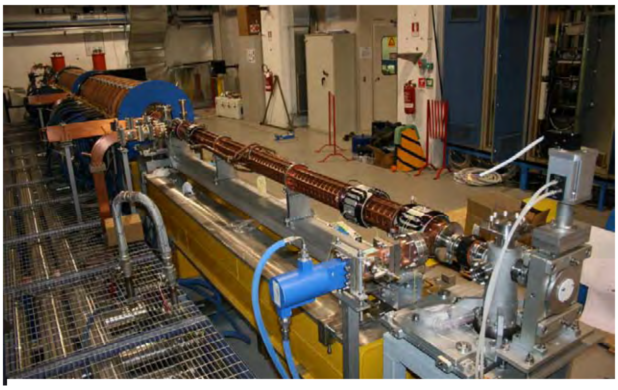

Figure 3: The SPARC linac with the s-band accelerating sections installed.

The Undulator

The installation of the six 2m long undulator sections will be completed by the end of 2007. Besides the SASE radiation scheme a seeding experiment is foreseen at the SPARC facility [9]; the seed source will be obtained with higher order harmonics of a Ti:Sa laser generated in crystals and in gas. In the latter case the seed is generated in the chambers shown in Fig. 4, which has been developed and tested at CEA-Saclay within the EUROFEL programme.

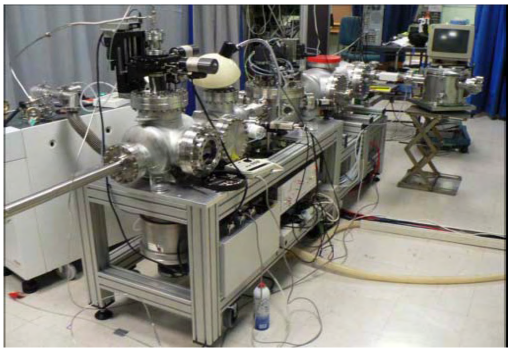

Figure 4: Harmonic Gas generation chamber

THE SPARX PROJECT LAYOUT

The first phase of the *SPARX* facility has been recently approved and funded. The project is based on the generation of ultra high peak brightness electron beams at the energy of 1 and 2 GeV generating FEL radiation in the 1.5-13 nm range. The machine design is intended to be modular and planned in two steps at 1 and 2 GeV respectively. The project layout includes both RF-compression and magnetic chicane techniques.

The Linac

The basic *SPARX* linac layout is based on s-band RF-TW accelerating sections, with an accelerating gradient around 25 MV/m. Downstream the SPARC-like photoinjector a first linac section rises the beam energy up to ≈ 300 MeV before the first magnetic chicane BC1, that brings the beam peak current from 100 A (SPARC design value) up to 300 A, followed by a second accelerating

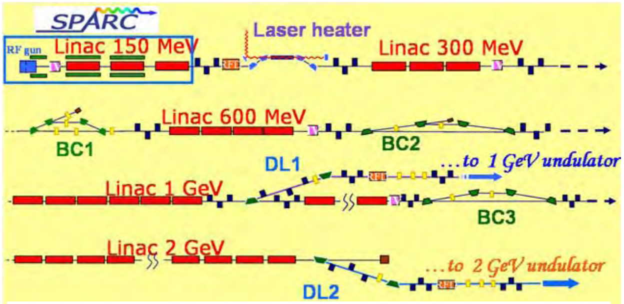

Figure 5: SPARX project schematic layout

section up to 600 MeV and the magnetic compressor BC2 to obtain a peak current $I_{pk} \approx 1$ kA. A hybrid compression scheme with velocity bunching and BC2 only is nevertheless foreseen and RF compression tests will be performed at the SPARC facility in the second half of 2007. After the BC2 compressor the energy of the beam is raised up to 1 GeV and the first dogleg DL1 delivers the beam to the 1 GeV undulator system, where both SASE

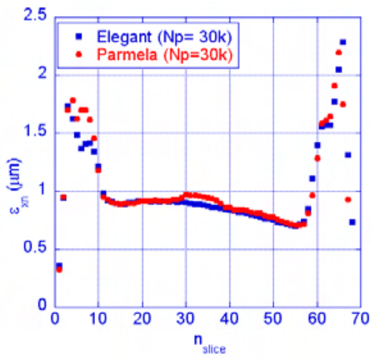

Figure 6: Slice analysis of the horizontal beam emittance after BC2 compressor as obtained with Elegant and Parmela code simulation.

and seeded radiation schemes are foreseen for a radiation length in the range of $\lambda_r \approx 13 \div 5$ nm. After the 1 GeV DL1 dogleg insertion another linac section brings the beam energy up to 1.5 GeV where the third magnetic compressor BC3 is located, in order to reach a peak current of the order of $I_{pk} \approx 2.5$ kA. After the last linac, at around 2 GeV, a second dogleg DL2 brings the beam to the second undulator system for radiation length in the range of $\lambda_r \approx 1.5 \div 5$ nm. A special attention is devoted to the space charge effect relevance in both the BC2 and BC3 compressors: in Fig. 6 the simulation results for the transverse beam emittance are reported as obtained with the Elegant and Parmela codes. A projected emittance dilution of the 30% is obtained so far; the compressor optimization is still in progress in order to further reduce the transverse dilution due to the space charge effect.

The Undulator and FEL

Both SASE and seeded radiation modes are foreseen at each of the two energy steps of the SPARX channel. As an example in Table 1 the very preliminary parameter list is reported for the two undulators of a possible seeding experiment at 2.3 GeV.

Table 1: Preliminary Parameter list of Seeding Experiment example at 2.3 GeV. (Fig. 7)

	Undulator 1	Undulator 2
Periods	21	42
Sections	9	10
Period (cm)	5.4	2.7
K	4.299	2.51

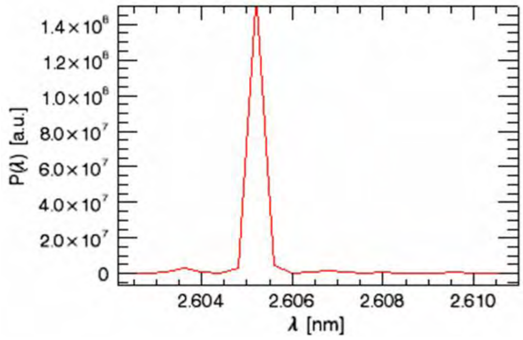

Figure 7: Radiation Spectrum of the fifth harmonic for a possible seeded scheme at 2.3 GeV.

In Fig. 7 the radiation spectrum is shown for the fifth harmonic of the λ=13 nm seed. An intensive study is ongoing to explore the most suitable configurations according to the user community needs.

PROJECT SCHEDULE

The first phase of SPARC commissioning successfully ended by Dec. 2006, the second part is meant to be completed by the end of 2007 with the SASE experiment at 530 nm, and SASE& seeding HHG test at 260-160-114 nm. For the *SPARX* source the project schedule foresees the facility TDR and the Building Project completed by the end of 2007, while the tunnel and building construction by the end of 2008. The installation is foreseen to be completed by the end of 2010, then after one year of Sub-system tests, the Commissioning of the machine will start in 2012.

REFERENCES

[1] http://www.lnf.infn.it/conference/sparx05/Giornate di Studio SPARX e Applicazioni
[2] A. Cianchi, *et al.*, Proc. of DIPAC07, Venice, Italy
[3] M. Ferrario, *et al.*, “Experimental results with the SPARC emittance-meter”, these Proceedings
[4] C.Vicario, *et al.*, “Laser and RF Synchronization Measurements at SPARC”, these Proceedings
[5] C. Ronsivalle *et al.* "Comparison Between SPARC E-Meter Meas. and Simulations", these Proceedings
[6] http://www.lnf.infn.it/acceleratori/sparc/SPARC Technical Design Report
[7] B. Spataro, *et al*, “A Bi-periodic X-band RF cavity for SPARC”, Proc. of EPAC06, Edinburgh, Scotland
[8] L. Ficcadenti, *et al*, “RF measurements results of the final brazed SPARC RF deflector”, these Proceedings
[9] L. Giannessi, *et al*, “Future Seeding Experiment at SPARC”, Proc. of FEL 2006, Berlin, Germany.

DRIVE LASER SYSTEM FOR SPARC PHOTOINJECTOR*

C. Vicario, D. Filippetto, G. Gatti, A. Ghigo, M. Bellaveglia, A. Gallo, INFN-LNF, Frascati, Italy
P. Musumeci, M. Petrarca, INFN-Roma1, Roma, Italy
S. Cialdi, INFN-Milano, Milano, Italy

Abstract

In this paper we report the progress of the SPARC photoinjector laser system. In the high brightness photoinjector the quality of the electron beam is directly related to the photocathode drive laser. In fact the 3D distribution of the electron beam is determined by the incoming laser pulse. The SPARC laser is a 10 Hz frequency-tripled TW-class Ti:Sa commercial system. To achieve the required flat top temporal shape we perform a manipulation of the laser spectrum in the fundamental wavelength and in the third harmonic. The optical transfer-line has been implemented to limit the pointing instabilities and to preserve to the cathode the temporal and spatial features of the laser pulse. We present the recorded performances in terms of time pulse shape and rf-to-laser synchronization.

INTRODUCTION

The SPARC project is an R&D photo-injector facility at LNF-INFN, devoted to the production of high brightness electron beam at 150 MeV for a SASE-FEL experiment at 500 nm [1]. SPARC will allow also investigations into the physics of ultra-short beams, plasma wave acceleration, and X-ray Compton back-scattering.

Specs on SPARC laser system were fixed within the phase of the machine design. The goal is to provide photo-injector (RF-gun) with a proper laser pulse between 5 and 12 ps, able to generate an electron beam with a normalized transverse emittance less than 2 mm-mrad and a current of 100 A. We currently use a Cu cathode with a quantum efficiency of $2\cdot10^{-4}$ at 120 MV/m [2] therefore it is required about 50 μJ at 266 nm to extract 1 nC.

Challenging requests are made on laser temporal pulse profile (flat top pulse with 1 ps rise time and ripples limited to 30%) to minimize the e-beam emittance; a pulse shaping activity is in progress and some results have been presented [3, 4]. In the following we first describe the laser system and then we report the measured performances in term of temporal pulse shape and laser to radio frequency (RF) time jitter.

LASER SYSTEM

The SPARC laser is a TW-class Ti:Sapphire system produced by Coherent. The laser consists of a Ti:Sa oscillator that generates 100 fs, 12 nm pulses. The oscillator operates at a repetition rate of 79+1/3 MHz corresponding to the 36th of the RF frequency. An acousto-optic programmable filter called “DAZZLER,” [3] upstream the amplifier, is used to modify the laser spectrum in order to obtain the target temporal profile[5].

The laser amplification process is carried out by one regenerative pre-amplifier pumped by 10 W Nd:YLF laser and a two double passes stages which are excited by the second harmonic of a Nd:YAG with an energy of 0.5 J per pulse. The system delivers pulses at λ=800 nm with energy of about 50 mJ and a repetition rate of 10 Hz.

At the output of the amplifier the IR pulses is sent to a third harmonic generator, where UV pulses hundreds fs long with an energy of up to 3 mJ are produced. The up-conversion is required to generate photon with energy larger than the work function of the photocathode. The third harmonic generator consists of two type I beta barium borate (BBO) crystals of 0.5 and 0.3 mm: the harmonic generator produces first the second harmonic signal and then the third harmonic signal, at λ=266 nm, by frequency sum.

The harmonic generation is followed by an UV stretcher to lengthen the pulse up to 15 ps. An optical transfer line is used to image the beam onto the cathode.

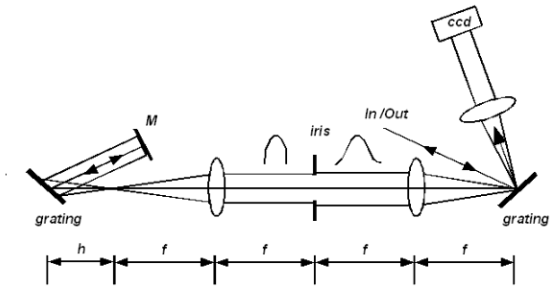

Figure 1: Layout of the UV stretcher.

TWO STAGES PULSE SHAPING

Previous measurements showed that the achievable rise time in the UV using the DAZZLER is too long: about 3 ps [3]. In fact, due to the finite bandwidth of the non-linear crystals, the steepness of the rise and fall time of the resulting flat-top pulses can not be fully controlled by the DAZZLER. A second result we found is that, after the UV stretcher, due to the applied large chirp, there is a full correspondence between spectral and temporal pulse profiles. This observation suggests that to improve the rise time the spectral tail has to be sharply clipped. To perform this manipulation we modified the UV stretcher to have a spatial dispersion of the wavelengths.

*Work partially supported by the EU Commission in the 6th FP, Contract No. 011935 EUROFEL, contract No. RII3-CT-2003-506395 CARE and by Italian Minister of Research MIUR
#carlo.vicario@lnf.infn.it

The modified stretcher is a particular version of the 4f optical scheme with two gratings and two lenses as shown in Fig. 1 [4]. A collimated beam is sent onto a diffraction grating having 4350 lines/mm at an incidence angle of 43°. The dispersed wavelengths are then focused using f=500mm lens located at a distance f from the grating.

On the lens focal plane each spectral component will reach a focus in a different spot. In other words on this plane (henceforth named Fourier plane) there is full correlation between wavelength and transverse position. This allows any desired, high-resolution, amplitude modulation on the spectrum simply placing a filter or mask at this plane. The beam is then re-collimated by a second lens and sent to another grating which compared to a classical 4f system is shifted from the symmetry position by a distance h. The spectral components are then retro-reflected by the mirror M and retrace back their path through the system. The shift of the second grating produces an outgoing pulse length proportional to h.

In our UV pulse shaping after the second pass the fraction of the beam reflected by the grating is focalized by a 30 cm lens onto the plane of a CCD camera. In this way a high-resolution (≈ 0.005 nm) spectrometer is integrated in the shaping system.

Summarizing, the functions of the described optical system are: i) the change of the pulse length; ii) the spectral amplitude modulation; iii) the single shot measurement of the spectrum of the output pulse.

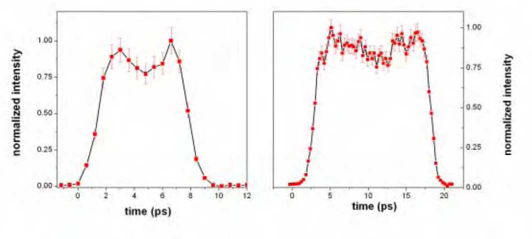

Figure 2: Cross-correlation measurement for a 6 ps and 15 ps UV pulse duration.

Cutting the spectral tails we observed a net reduction on the rise time. The temporal profile has been traced by a UV-IR cross-correlator [10]. In this device the UV pulse is gated by the amplified IR pulse. By changing the delay of the IR pulse it is possible to reconstruct the time intensity of the UV beam with a resolution depending on the duration of the gate pulse.

In the Fig. 2 we report two cross-correlation traces with the error bars, obtained for two distances h in the stretcher, in order to obtain the output pulse length of 6 ps and 15 ps FWHM. The rise time, in both cases, are about 1.8 ps slightly longer than the calculated value. In fact the cross-correlation has been measured using a relatively long IR gate pulse >1 ps. The long gate pulse induces an overestimation on the rise time. Including this effect the actual rise time is 1.4 ps. The described pulse shaping technique has been used to generate high brilliance e-beam, for more details [1].

The obtained rise time cannot be improved by increasing the steepness of the spectral cut. In fact, below 1.4 ps rise time, sharper cut causes overshoots in the time profile, without benefits in terms of rise time.

The overall efficiency of the shaper is limited to 20% due to the high diffraction losses of UV gratings the losses introduced by the filter. In our measure a pulse with energy of about 2 mJ is sent to the shaping system and the resulting output rectangular pulse has energy greater than 350 µJ.

It is important to stress the fact that the quality of the beam transverse profile is not affected by the cut of the spectral tails.

UV PULSE SHAPING

We show here that a Gaussian spectrum like the one naturally produced by the laser system is actually ideal if one aims at a flat-top longitudinal profile, thus removing the need of expensive and complex shaper systems in the IR. The simple idea at the basis of the described shaper is to eliminate the spectral tails of a natural spectrum of the lasers, by using an iris on the Fourier plane. Simulations show that a sharp cut of the spectrum induces overshoots in the temporal profile of the pulse, which could be used to balance the curvature of the Gaussian spectrum. In this simple way it would be possible to obtain a flat top laser pulse starting from a Gaussian-like spectrum.

Moving away from the Fourier plane the iris, one can also change the sharpness of the applied cut to adjust for the required curvature compensation. An optimal cut resolution is 0.05 nm that can be achieved by placing the iris 1 cm from the Fourier plane.

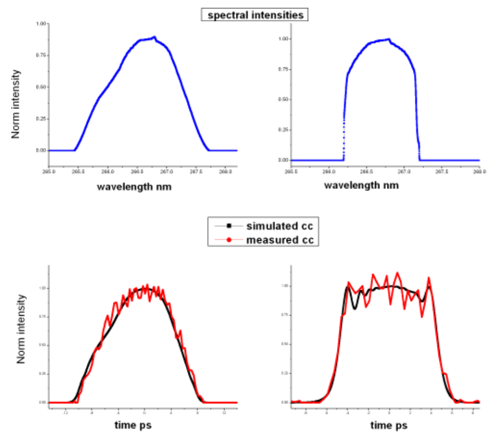

Figure 3: On the top Gaussian and cut spectra, and above the corresponding time intensity distributions measured (red) and calculated (black)

In Fig. 3, we report the experimental results obtained with this pulse shaper. On the left side we show the initial bell-shaped spectrum (blue curve) and the corresponding temporal profile measured with a cross-correlation (red curve). The black line represents the simulated cross-correlation obtained from the measured spectrum taking into account the chirp introduced by the stretcher and the finite length of the probe pulse. In the top-right corner we show the spectrum after the tails have been removed. Below we display the corresponding measured cross-correlation and the calculated one. The experimental cross-correlation presents ripples due to the pulse-to-pulse laser fluctuations. From these measurements we deduce two main results: 1) cutting the spectrum tails with the iris we measured a rise time of 1.55 ps. Since the cross-correlation has been obtained with a 750 fs long IR gate the real rise time is 1.4 ps comparable with the two stages pulse shaping 2) if the applied chirp is known, with a single shot measurement of the spectrum one can calculate with a good approximation the final temporal profile. Due to the wavelength filtering, the losses are 20 % larger respect to the two stages pulse shaping. This make the two stages pulse shaper more convenient.

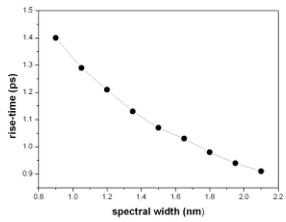

Figure 4: Rise time vs UV bandwidth.

In Fig. 4 we show the simulated rise time as function of the bandwidth of the spectrum. This simulation assumes that the chirp introduced by the stretcher has to be adjusted to maintain the same final pulse length (10 ps). For spectral bandwidth > 1.7 nm it is possible to obtain rise times < 1 ps. Further studies are going on to get this bandwidth by changing the harmonic crystals.

LASER TO RF SYNCHRONIZATION

A precise synchronization between the photocathode drive laser and the accelerating wave is necessary to have a fixed and stable time-of-arrival of the photons on the cathode with respect of the phase of the 2856 MHz RF field. This condition is very important to guarantee the stability and the shot-to-shot reproducibility of crucial beam parameters such as the beam charge, energy, emittance and energy spread. Beam dynamics simulations indicate a time jitter within ± 1 ps around the optimal phase is acceptable for the SPARC phase-1 experiment in order to limit the emittance growth to less than 10%.

To synchronize the laser respect to the RF clock the laser oscillator length is kept constant by an active feedback loop. This assures a stable repetition rate at 79+1/3 MHz which is the 36th sub-harmonic of the RF frequency. We measured at oscillator level, a time jitter characterized by a standard deviation of 350 fs [5].

To have information on the phase noise of the single laser UV pulse, we mix the signal comes from a RF cavity tuned at ¾ RF with the corresponding sub-harmonic of the RF master clock. The cavity was fed by a fast photodiode illuminated by the optical pulse. The photodetector is a bi-planar vacuum photodiode with of 100 ps a rise time operating at 2.5 kV bias voltage. The cavity grants an exponential decaying pseudo-sinusoidal signal with duration of about 1.5μs and allows a consistent relative phase measurement.

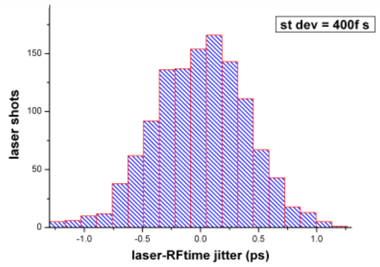

Figure 5: Relative phase between the UV pulse and the RF clock recorded over 2 minutes.

As reported in Fig 2 the time jitter standard deviation, recorded over few minutes, is about 400 fs [5]. This result is comparable to the jitter measured at the oscillator and indicates the amplifier contributes very little to the final phase noise. The good level of synchronization is confirmed by the stability of the e-beam parameters.

CONCLUSIONS

This paper reports the performances of the SPARC laser system. The activities and the major results on the time pulse shaping program have been presented. Two schemes have been applied at the production of the flat top target pulse. The results indicate, for both schemes, that rise time of 1.4 ps can be achieved. Sharper edges require larger bandwidth and it the topic of future investigations. Measurement of the phase noise indicates standard deviation less than 0.5 ps of the UV pulse respect to the RF system.

REFERENCES

[1] M. Ferrario et al., “Experimental results with the SPARC emittance meter”, these Proceedings.

[2] C. Vicario et al, “Commissioning of the Laser System for SPARC Photoinjector”, Proceeding EPAC, p. 3146, Edinburgh, Scotland, 2006.

[3] S. Cialdi, M. Petrarca and C. Vicario, “High power third harmonicflat pulse laser generation” Opt. Lett. 31, (2006), 2885.

[4] S. Cialdi, C. Vicario, M. Petrarca and P. Musumeci, Appl. Opt., Doc. ID 82759, (Posted 05/15/2007, in press).

[5] A. Gallo, M. Bellaveglia, G. Gatti, C. Vicario “Laser and RF Synchronization Measurements at SPARC” these Proceedings.

SIMULATION OF AN IRIS-GUIDED INVERSE FREE-ELECTRON LASER MICRO-BUNCHING EXPERIMENT

J. Frederico, G. Gatti, S. Reiche, J. Rosenzweig, R. Tikhoplav
UCLA, Los Angeles, CA 90095, USA

Abstract

This paper presents a detailed computational examination of various physical effects that enter into an innovative approach to inverse free-electron laser (IFEL) acceleration and microbunching experiments, involving use of irises to guide the high power laser beam.

In IFELs, there is a great advantage to using long wavelength, and thus diffractive lasers, which are also quite high power. As this scenario presents challenges to the final focusing optics, one must consider guiding, which for present schemes is either too lossy (in metallic guides), or incapable of supporting high fields (as in dielectric guides). Hence we are driven to examine an alternative scheme, that of using the effects of diffraction off of periodically placed metallic irises which have an inner diameter in a relatively low field region. We present below a computational analysis of the wave dynamics associated with the laser beam in this scheme. We then proceed to integrate this type of circularly polarized electromagnetic radiation field into a self-consistent simulation of beam dynamics inside of a helical undulator under construction at the UCLA Neptune Laboratory inverse free-electron laser. With this integrated tool, we then study the degree of microbunching bunching at the laser optical wavelength induced in a relativistic electron beam. Finally, we study the propagation of the beam after the IFEL interaction, including beam self-force (single component plasma) effects, to predict the level of microbunching at the fundamental (laser) frequency and its harmonics that are observed at a detector using coherent transition radiation.

INTRODUCTION

There are broad applications of a tunable coherent radiation source, ranging from medical uses to materials research and more. Current laser technology is not always completely tunable in terms of wavelength and generally has limits on achievable power. The free-electron laser (FEL) presents a solution in the form of a laser that can be tuned from centimeter wavelengths to the UV range [1]. The FEL also shows promise in the hard x-ray range compared to other approaches [2]. A bunched electron beam is a by-product of the FEL process, but can also be formed by a partial application of the process which is known as the inverse free-electron laser (IFEL).

For a FEL/IFEL application to be practical, it must be efficient. At longer wavelengths, diffraction causes a reduction in intensity at the electron beam, which must be addressed. In particular, the longer the FEL is, the more the diffractive effects accumulate. A guide is an inviting solution; however, typical waveguides such as dielectric or metallic guides have inherent limitations concerning high-power radiation. In particular, dielectrics suffer material breakdown due to high fields especially near the center of the radiation field. Metallic guides rely on conductive boundary conditions to guide radiation, so at high power the walls are a source of strong resistive losses.

An iris-loaded guide, however, introduces physical structures in relatively low field regions [3]. The objective is to greatly reduce diffractive losses by sacrificing smaller power losses. However, physical trial and error to determine optimal operating parameters is impractical due to factors such as construction and installation. Computer simulation of the FEL process can provide insights into operating conditions under different scenarios.

EXPERIMENT

Experimental Set-up

The experiment simulated focuses on an IFEL application. The scheme to achieve bunching is a 10-cm IFEL section with included waveguide followed by a 30-cm drift section. The IFEL introduces electron beam energy modulation without significantly affecting bunching. The drift section converts energy modulation to bunching. The bunch period length is given by $2\pi/(k+k_U) = 10.5923\,\mu$m.

Standard IFEL. The IFEL section is a typical helical undulator configuration with the iris-loaded waveguide. The undulator satisfies the resonant condition in order to couple the electron beam to the radiation field [1]. The following equations [1] can be integrated to show energy and position modulation:

$$z = c\beta_0 t + z_0 \quad (1)$$
$$\dot{\gamma} = \frac{eE_0K}{mc\gamma}\sin\left[(k+k_u)\,z - \omega t\right] \quad (2)$$

where $\beta_0 = \left[1-\left(1+K^2/2\right)/\gamma^2\right]^{1/2}$. The result is a sinusoidal energy modulation with no change in longitudinal particle position.

Iris-loaded Waveguide. The iris-loaded waveguide is within the undulator. In this region, the IFEL is designed to have an input radiation field that is orders of magnitude greater than the spontaneous radiation of the electrons; electron radiation is then overwhelmed by the input radiation. Since a Gaussian radiation field is fed into the iris waveguide and matched into its fundamental mode, a good approximation is that of the power contributing entirely to the fundamental mode. The power of the fundamental mode is then given by the power transmission of a Gaussian beam through the radius a of the iris apertures.

For a Gaussian beam, which would be the diffraction situation present in a standard IFEL, power transmission through a circular area of radius r is [4]:

$$T_{gauss}(r, z) \quad = \quad 1 - e^{-2r^2/w(z)^2} \tag{3}$$

where $\omega(z) = w_0\sqrt{1 + (z/z_R)^2}$ and $z_R \equiv (\pi w^2)/\lambda$. Power transmission of free-space must be compared to that of an iris-loaded waveguide. A simple approximation is to consider only the power transmission in free space through the space defined by the geometry of the waveguide. As the radius of the waveguide is a, this power transmission is given by $T_{gauss}(a, z)$.

An iris-loaded waveguide is a regularly-spaced series of irises. Xie studied the second mode for Gaussian radiation [3]. This application is of the fundamental mode, and so the Bessel function of interest is J_0, and its zeroes, ν_{0n}. This change does not affect the theory, and can be applied to our configuration. Power flow through these series of apertures is

$$T_{iris}(z) \quad = \quad e^{-2\alpha_r z} \tag{4}$$

where $\alpha_r \equiv \left[4\nu_{0n}^2\eta\,(M+\eta)\right]/L\left[(M+\eta)^2+\eta\right]^2$, ν_{0n} is the nth zero of the Bessel function J_0, or $J_0(\nu_{0n}) = 0$; $M = \sqrt{8\pi N}$; $N = a^2/\lambda L$; $\eta = -\xi(1/2)/\sqrt{\pi} \approx 0.824$, $\xi(z)$ is Riemann's Zeta function; and a is the aperture radius, L is the distance between apertures, and λ is the radiation wavelength. (Note that $\alpha_r(a, L, \lambda)$, and that a valid approximation for the scenario is only considering the dominant mode $n = 1$ for small diffraction loss $N \ll 1$.) [3] The waist of the radiation is matched to the iris aperture radius, such that $a \approx 3.23w/2$, so $T_{iris}(0) = T_{gauss}(\pi w_0/2, 0) = 1 - e^{-\pi^2/2} \approx 0.9928$. It is then possible to calculate the power transmission for a given distance z, $T_{iris}(z) = 0.9928e^{-2\alpha_r z}$.

Comparing the two power transmissions $T_{gauss}(\pi\omega_0/2, z)$ and $T_{iris}(z)$ using experimental parameters (see Table 1) yields Fig. 1. This view of transmission is, of course, incomplete. Especially in the beginning, the Gaussian wave cannot be perfectly matched into the main mode of the iris waveguide. A close examination would show that the dashed iris transmission is not continuous, as power is trimmed at irises and not continuously. However, as transmission differences increase, these details become negligible. It

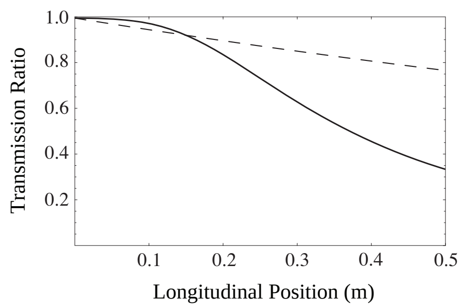

Figure 1: Transmission of power in free-space (solid) and iris waveguide (dashed)

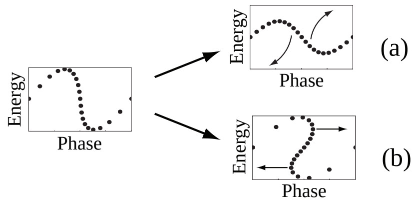

Figure 2: (a) Space charge effects dominate. (b) Space charge effects negligible

is expected, for our undulator that is only 0.1 m, that an iris IFEL should be nearly the same as a standard IFEL. It should also be noted that for a longer undulator, power transmission is significantly greater with an iris waveguide when compared to free-space propagation.

Drift Section. The dynamics in the drift section are influenced by space charge and can be described as a plasma oscillation of the electron beam.

For relatively low power, in the region where space charge is a significant factor, particles in phase space will be unable to fold over or over-compress. Electrons at the back of the bunch will lose energy as they are repulsed by electrons ahead of them, and similarly electrons at the front will gain energy as they are repulsed by those behind them. After reaching a maximum compression, bunches will spread out again. (See Fig. 2a.)

For negligible space charge, electrons will not interact with each other. The phase space will fold over (over-compress) and after maximum bunching, will spread out. (See Fig. 2b.) Maximum bunching would then be expected at the boundary between over-compression and under-compression.

In either scenario, modeled as a plasma, the distance $\lambda_p/2 = \pi/k_p$ to reach maximum bunching can be determined and is $k_p = \sqrt{4\pi r_e n_e/\beta^2\gamma^3}$ where $r_e = 2.8 \times 10^{-15}$ m, $n_e = I/(ec2\pi\sigma_x\sigma_y)$, σ_x and σ_y are the rms sizes of the electron beam, β is the beam velocity which can be solved from γ, and of course γ is given [5]. After manipulation, $\lambda_p/2 = 1.22$ m for given conditions and a current of 45 amps. It is worthwhile to note that $\lambda_p \propto I^{-1/2}$.

Genesis 1.3 was used to simulate the experiment [6]. The

Table 1: Experiment Parameters.

Radiation	
Wavelength (λ_r)	10.6×10^{-6} m
Intensity (I)	6×10^{11} W/cm^2
Peak E-field (E_0)	1.94×10^9 N/C
Waist (w_0)	0.7 mm
Electron Beam	
Energy (γ_0)	26.3
Current	45-1005 amps
Space Charge	First-order
Undulator	
Constant (K_u)	0.0940
Period (λ_u)	14.6 mm
Length	10 cm
Iris Guide	
Aperture Radius	1.13×10^{-3} m
Period	3 mm
Drift Section	
Length	30 cm

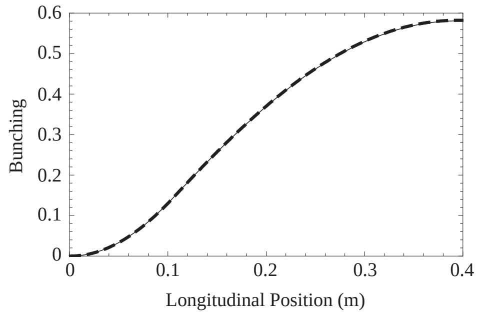

Figure 3: Simulated bunching as a function of position. 45 amps, 1.670304×10^8 watts. Dashed line indicates iris-loaded guide, thin line is standard.

code was modified to periodically remove radiation beyond the iris radius in order to model the iris-loaded waveguide.

RESULTS & DISCUSSION

Bunching Comparison. Bunching for a reasonable current of 45 amps with and without an iris waveguide gives nearly identical results as expected (Fig. 3). The bunching maximum for both is near the predicted value given by the plasma approximation.

Achievable Bunching. Both types of space charge effects can be seen in the IFEL interactions. However, the importance is not in the type of compression and decompression that occurs, but the distance at which maximum compression occurs. Note that the maximum bunching is at about 0.4 m which is on the order of the theoretical 1.22 m calculated earlier. (See Fig. 3.) As current increases over the range from 45-1005 amps, the agreement between the

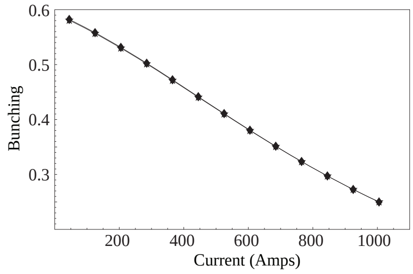

Figure 4: Simulated bunching, maximized at 0.4 m, as a function of current. Diamond indicates standard IFEL, star indicates iris IFEL.

bunching peak and the plasma length becomes much better. By 1005 amps, the theoretical plasma length is 0.259 m and maximum bunching occurs at approximately 0.243 m.

Of practical interest is the maximum bunching achievable at a measurable point in the experiment, which is in this case at 0.4 m. Bunching was maximized at this distance by adjusting power, for given currents. Again, both iris and standard IFEL profiles are nearly identical. (See Fig. 4.) For higher currents, the plasma oscillation dominates. A bunching maximum occurs earlier and at 0.4 m the bunching is decreased as it follows the plasma oscillation.

CONCLUSION

The data verifies the validity of an iris simulation using this method, as results closely match a non-iris situation, as expected. The simulation is then an early proof-of-concept for including an iris-loaded guide in an IFEL experiment. Iris-loaded guide scenarios must be tested more extensively in hopes of improving efficiency more dramatically. Longer IFEL/FEL experiments can be tested confidently using this approach. If efficiency is significantly improved in simulation, comparable real-world experiments can be performed as a final proof-of-concept. Increased efficiency in a proof-of-concept experiment would allow for application in generic IFEL/FEL processes and may prove to be a step toward practical applications of the technology.

REFERENCES

[1] J. Murphy, C. Pellegrini, Introduction to the Physics of the Free Electron Laser. Upton, NY. p. 163-216.

[2] S. Leone, Report of the Basic Energy Advisory Committee Panel on Novel Coherent Light Sources. 1999, University of Colorado.

[3] M. Xie, Laser Acceleration in Vacuum with an Open Iris-Loaded Waveguide. 1997, Lawrence Berkeley National Laboratory: Berkeley, CA.

[4] A. Siegman, *Lasers.* 1986, Sausalito, California: University Science Books.

[5] J. Rosenzweig, P. Musumeci, Phys. Rev., 1998. 58(3): p. R2738-R2740.

[6] S. Reiche, Nucl. Instr. & Meth. A429 (1999) 243

TOUSCHEK BACKGROUND AND BEAM LIFETIME STUDIES FOR THE DAFNE UPGRADE

M. Boscolo, M. Biagini, S. Guiducci, P. Raimondi, INFN-LNF, Frascati, Italy

Abstract

For the low energy collider DAΦNE the machine induced backgrounds into the experiments as well as the beam lifetime are dominated by the Touschek effect. Many efforts have been put in its reduction: by adjusting optical parameters, by inserting additional collimators, as well as by simulating and tracking scattered particles in order to find the proper actions that allow reducing particle losses especially at the interaction region.

Studies on the distribution and trajectories of the Touschek particles along the ring are discussed here for the Siddharta run configuration with the crabbed waist scheme, together with an evaluation of the corresponding beam lifetime. Efficiency of the collimators has been investigated with the new machine configuration and new optimized positions along the ring have been found.

INTRODUCTION

An upgrade of DAΦNE exploiting the crabbed waist idea will shortly be tested [1,2]. A luminosity increase up to values of the order of 10^{33} cm^{-2} s^{-1} is expected to be given by a combination of large crossing angle, very small transverse beam sizes at the interaction point (IP) and the 'crabbed vertical waist'. Relatively small modifications of the machine are required for this scheme, to be realized between summer and fall 2007. Machine backgrounds and lifetime will be dominated by the single Touschek scattering [3], as it is for the DAΦNE present configuration. Simulations of the Touschek effect with the crabbed waist optics have been performed using an upgraded version of the simulation code used for the lattice of the KLOE [4,5] runs.

TOUSCHEK EFFECT AT DAϕNE

Touschek effect is a source of background due to the off-energy particles arising from the elastic scattering of particles within a bunch. Touschek scattered particles have a betatron oscillation given by

$$x = \frac{\Delta p}{p}\left(|D| + \sqrt{H\beta}\right),$$

proportional to the dispersion D, to the momentum spread $\Delta p/p$ and to the invariant H defined by [6]: $H = \gamma_x D_x^2 + 2\alpha_x D_x D_x' + \beta_x D_x'^2$ (upper plot of Fig. 1). Essentially all losses arise from the Touschek scattered particles in dispersive regions (see Fig.1). The generation of the scattering events in the simulation code is done continuously all over the ring, averaging the Touschek probability density function on every three machine elements. The lower plot in Fig. 1 shows how total particle losses (white histogram) come from the highly dispersive regions; the indicated rates are expressed in KHz and they are referred to a 13 mA bunch. Losses only at the interaction region (IR) are reported in the superimposed yellow histogram; the comparison indicates that most of the particles are lost at the IR.

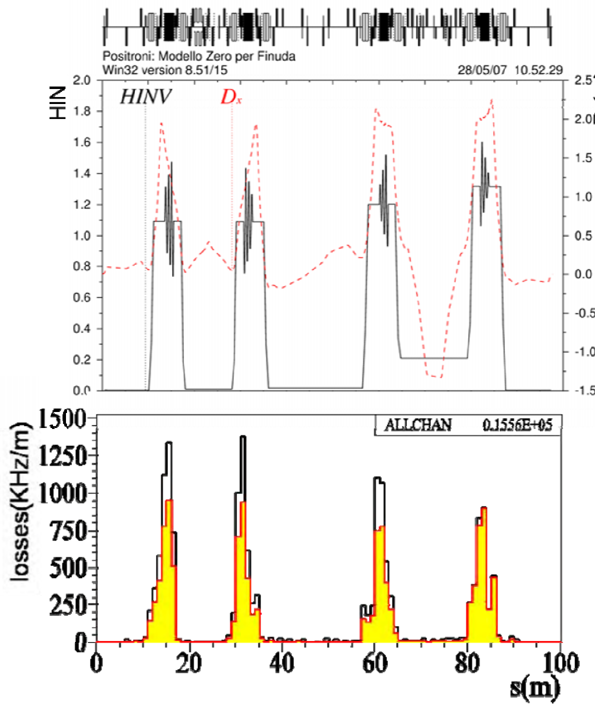

Fig. 1: Upper plot: H and dispersion functions for the DAΦNE upgrade optics. Lower plot: Distribution of Touschek scattering position for losses all over the ring or only at the IR, white and yellow histogram, respectively. The IP is at s=0.

In the simulation Touschek particles are taken within one transversely Gaussian bunch with the proper energy spectra. Particles are tracked over many turns or until they are lost. In this way an estimate of the Touschek losses along the whole ring and at the IR is performed.

Table 1: Relevant beam parameters used for Touschek background simulations.

N_{part}/bunch	$2.6\cdot10^{10}$
I_{bunch} (mA)	13
ε_x (μm)	0.2
Coupling (%)	0. 5
σ_z (mm)	20

Sextupoles are included in the tracking. Recently, the simulation code has been upgraded in order to estimate also the Touschek lifetime τ_{TOU}. This estimate is obtained from the the relation $\tau_{TOU} \cong N/\dot{N}$, where the total

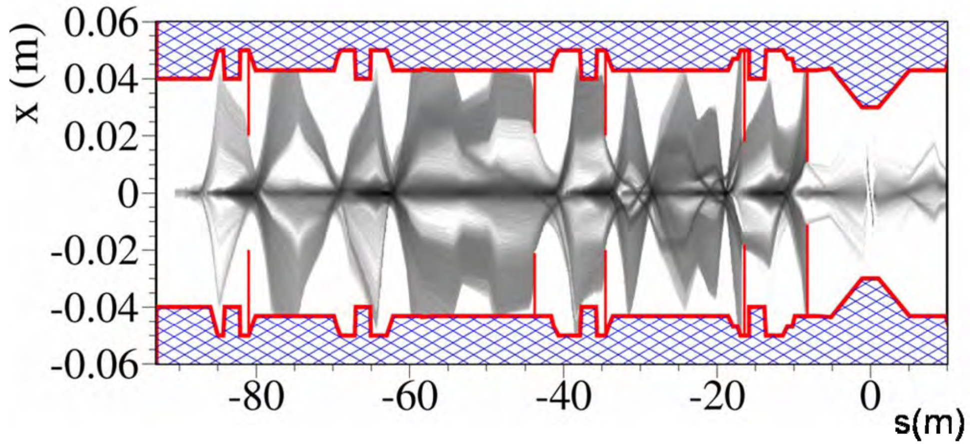

Fig. 2: Touschek particles trajectories plotted with all machine collimators inserted. The IP is at s=0.

particle losses along the ring $\dot{N}$ is given by the tracking simulation and N is the number of particles per bunch (see table 1). Particles within an energy deviation of 0.1% and 4% are tracked for a sufficient number of machine turns, checking at every turn whether they exceed rf or physical acceptance. Results are in agreement with the simulation code used up to now for DAΦNE [7] within ~15%.

SIMULATIONS

Touschek background with this new machine lattice is expected to be high with respect to the rates we have had with the old one. In fact, the strong IR quadrupole doublet requires a small physical aperture. So, the squeezing the beam at the IP that enhances luminosity induces also many particle losses at the focusing low-β quadrupole. For this reason a masking system between the pipe and the low-β quadrupoles will be incorporated to shield the detector from beam-generated background.

The beam parameters used for these simulations are reported in Table 1. Full tracking has been performed for one machine turn, and only particles with a relative energy deviation between 0.003 and 0.02 have been simulated, as particles with higher energy deviations get lost locally and do not contribute to backgrounds in the experiment, and particles with relative energy deviation <0.003 are practically always kept inside the beam pipe.

Table 2: Lost particles per bunch per beam with a beam current of 13mA.

Total losses without collimators (KHz)	$15.5\cdot 10^3$
IR losses without collimators (KHz)	$11.3\cdot 10^3$
IR losses with collimators (KHz)	94.2

Careful studies have been performed to estimate efficiency of the five available horizontal collimators. Each one has an external and an internal jaw that can be separately inserted in the vacuum pipe. Tracking studies have indicated for the new optics a better longitudinal position for three of them, and they will be moved accordingly. Fig. 2 shows the trajectories of Touschek particles lost along the ring with the optimized opening of the jaws. It appears that three of them are very efficient; they are, starting from the IP: at s = -8.2 m (SCHPL101), at -16.7 m (SCHPL110) and at -43.7 m (SCHPS201). We remark that these are just the three collimators which have been moved to improve their efficiency for the new optics. Fig. 3 shows the losses over the ring, after the insertion of collimators, indicating also their efficiency in stopping particles. Table 2 reports the calculated rates, from which not only the great efficiency of collimators can be noticed, but also that most of the particle losses are concentrated at the IR.

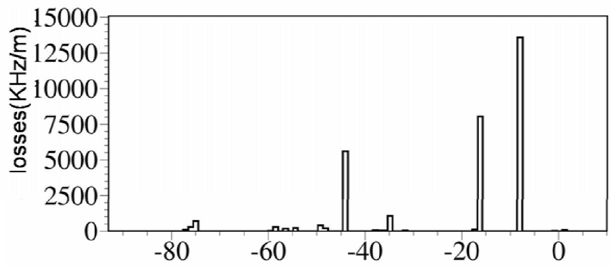

Fig. 3: Distribution of total losses plotted with all machine collimators inserted. The IP is at s=0.

The calculated opening of the IR collimator jaws (SCHPL101) is up to 11 mm from the center of the beam pipe, corresponding to 8.5 σ_x, while for SCHPL110 it is at 18 σ_x and for SCHPS201 at 21 σ_x. Similarly to the KLOE and FINUDA runs, the largest reduction of IR losses associated with Touschek scattering is achieved by the collimator closest to the IR: its optimized longitudinal position is found to be just after a horizontally focusing quadrupole, corresponding to a maximum of β_x.

A scan of the IR losses versus openings of the IR collimator is reported in Fig. 4 (upper plot) together with the corresponding lifetime (lower plot). The collimator openings are measured from the center of the beam axis and expressed in number of σ_x. Black markers are for the particles lost upstream the IP, red dots for the downstream ones. In this simulation all other collimators are inserted.

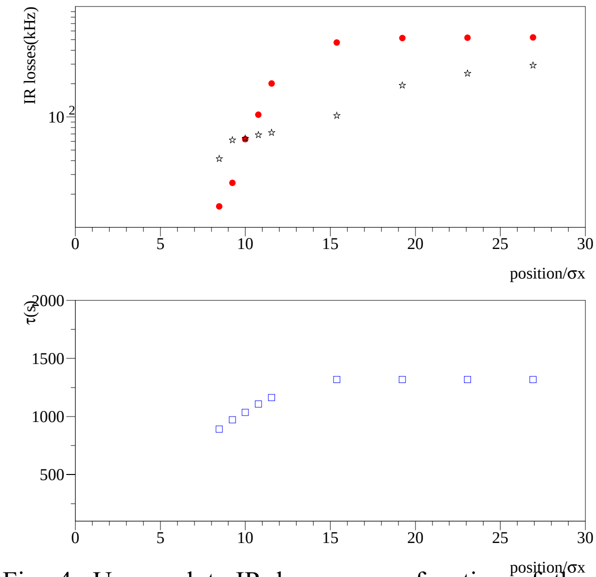

Fig. 4: Upper plot: IR losses as a function of the IR collimators openings measured in number of σ_x from the center of the beam axis. Black dots are losses downstream the IP, red dots are the upstream ones. Lower plot: corresponding Touschek lifetime.

Beam lifetime without collimators is estimated to be about 35 minutes; when all but IR collimators are inserted it drops to 28 minutes. When also IR collimator is at its optimized position, the lifetime is further reduced by about a factor 1/3, down to 19 minutes. So, as expected, studies have shown that there is a trade off between beam lifetime and minimization of background by the collimators and this is true in particular with the insertion of the IR one.

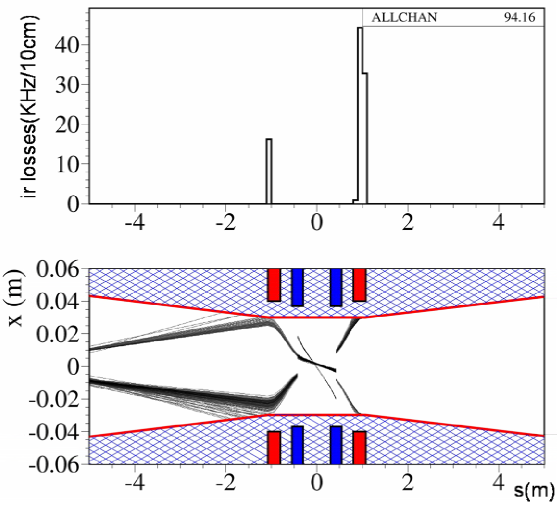

Fig. 5: Distribution (upper) and trajectories (lower) of particle losses at the IR with all machine collimators inserted. Rates are given for a 13mA bunch. The IP is at s=0.

Fig. 5 shows the calculated distribution and trajectories of IR losses with collimators inserted. Most of Touschek particles are lost at the focusing quadrupole of the IR doublet, as expected. Luckily, most of the particles are lost downstream the IP. When collimators are inserted the particle losses at the IR come from the closest arc to the IR, as shown in Fig. 6. These Touschek particles can only be stopped by the IR collimator, thus resulting the most dangerous source of background for the experiments. This background will be reduced with a proper shielding of the detector, as it has been done fruitfully for KLOE and DEAR.

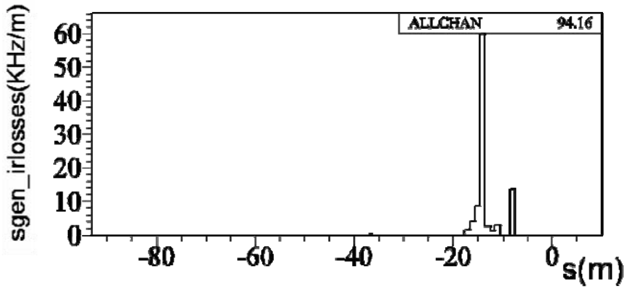

Fig. 6. Location source of Touschek particles getting lost at the IR, with insertion of collimators. Only particles generated in the last arc before the IR are still dangerous for the detector.

CONCLUSIONS

The simulation code for tracking of Touschek particles is now more accurate, as it calculates particle losses all over the ring together with Touschek lifetime. Particle losses due to Touschek effect are expected to be quite high with the Siddharta optics. However, the longitudinal position of collimators has been optimized for the new optics and they are expected to be very efficient, even if a good compromise between losses and lifetime has necessarily to be found experimentally. In addition, careful shielding of the detector is underway.

REFERENCES

[1] P. Raimondi, "Status of SuperB Effort", 2nd SuperB Workshop, LNF, Frascati, March 2006, http://www.lnf.infn.it/conference/superb06/talks/raimondi1.ppt

[2] M. Biagini et al, 'DAFNE upgrade for Siddharta run', these Proc.

[3] C. Bernardini, et al., Phys. Rev. Lett., vol. 10, 1963, p. 407.

[4] M. Boscolo, M. Antonelli and S. Guiducci, proc. of EPAC02, Paris, France, 2002.

[5] M. Boscolo, S. Guiducci, DAΦNE Techn. Note IR-10, 2001.

[6] R.H. Helm, M.J. Lee, P. L. Morton and M. Sands, IEEE Trans. Nucl. Sci Ns-20 (1973).

[7] S.Guiducci, proc. of EPAC02, Paris, France, 2002.

DAΦNE SETUP AND PERFORMANCES DURING THE SECOND FINUDA RUN

C. Milardi, D. Alesini, S. Bettoni, M.E. Biagini, C. Biscari, R. Boni, M. Boscolo, B. Buonomo, A. Clozza, G. Delle Monache, T. Demma, E. Di Pasquale, G. Di Pirro, A. Drago, A. Gallo, A. Ghigo, S. Guiducci, P. Iorio, C. Ligi, F. Marcellini, C. Marchetti, G. Mazzitelli, L. Pellegrino, M. Preger, L. Quintieri, P. Raimondi, R. Ricci, U. Rotundo, C. Sanelli, M. Serio, F. Sgamma, B. Spataro, A. Stecchi, A. Stella, S. Tomassini, C. Vaccarezza, M. Zobov INFN/LNF, Frascati (Roma); E. Levichev, S. Nikitin, P. Piminov, D. Shatilov BINP SB RAS, Novosibirsk; J. Fox, D. Teytelman SLAC, Menlo Park, California

Abstract

Beam operations at DAΦNE restarted in October 2006 after a four months shut-down to remove the KLOE experimental detector and to install the FINUDA one. This period has been also used for maintenance and implementation of several upgrades.

Already in the first two months of operation the peak and integrated luminosity exceeded the values obtained during the first FINUDA run by 20%, and have been steadily improving toward the end of the operation. By June 2007 ~ 1 fb^{-1} integrated luminosity has been logged by the experiment.

The collider performances during the run are presented together with the improvements obtained in terms of beam dynamics and beam-beam behaviour coming from several collider modifications.

INTRODUCTION

DAΦNE [1], the Frascati lepton collider, is now in its sixth year of operation. Since 2001 it has been delivering luminosity, at the energy of the Φ resonance (1.02 GeV c.m.), to three different experiments: KLOE, DEAR and FINUDA, one at a time.

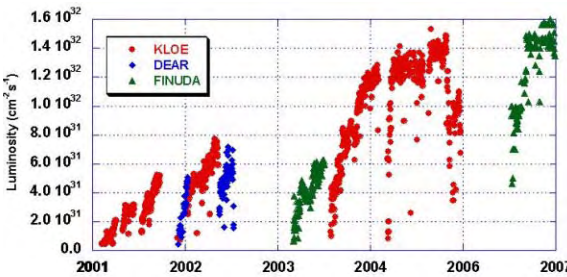

Figure 1: DAΦNE peak luminosity trend.

DAΦNE consists of two independent rings, each ~ 97m long, sharing two interaction regions IR1 and IR2 where the KLOE and DEAR or FINUDA detectors are respectively installed. An injection system, including a S-band linac, 180m long transfer lines and an accumulator/damping ring, provides the e^+ and e^- beams, with the required emittance and energy.

The DAΦNE complex runs also a beam test facility, providing e^-/ e^+ beams from the linac in the energy range 25÷725 MeV with tunable intensity from 10^{10} to a single particle per pulse.

Three independent beam lines, collecting the radiation emitted in one wiggler and one bending magnet of the e^- ring, provide a synchrotron radiation facility.

In these years DAΦNE has undergone several progressive upgrades [2], aimed at improving the collider performances (see Fig.1) which have been implemented exploiting the shut-downs required for detectors changeover.

DAΦNE SHUTDOWN ACTIVITIES

During the last shut-down, March 2006 ÷ July 2006, a maintenance program has been undertaken involving all the DAΦNE plants: electric, cooling and cryogenic, and all machine subsystems: linac, control system, magnet power supplies, RF system, vacuum system and wigglers. At the same time the FINUDA detector has been installed on IR2 while the KLOE one has been removed from IR1.

As usual several upgrades have been implemented relying on the experience gained during the last KLOE run [3].

The interaction region IR1 has been substituted with a straight section equipped with four electromagnetic quadrupoles, a much more flexible configuration to detune the optical functions in the unused IP, which does not contribute to betatron coupling.

Several broken Ion Clearing Electrods (ICE) and all those installed in the e^- ring wigglers have been removed, since theoretical studies [4] indicated the ICEs in the wigglers as the main source of the larger coupling impedance measured in the e^- ring with respect to the e^+ one.

Wires for beam-beam long range compensation (BBLR) [5] have been installed in IR2 following the successful tests done during the KLOE data taking.

New Beam Position Monitors (BPMs) [6], with turn by turn measurement capabilities, have been installed in the DAΦNE main rings in order to have fast and accurate linear and non linear beam optics measurements as well as to estimate driving terms impact on the main rings beam dynamics.

A new commercial processor (Pentium/Linux) has been implemented in the control system; this will progressively replace the original home designed front-end processors.

Third generation bunch by bunch feedbacks [7], based on field programmable gate array and developed for the Super B-factory in the framework of the SLAC-KEK-LNF collaboration, have been tested and implemented to stabilize the four transverse motions.

FINUDA RUN

Commissioning & Main Ring Optics

DAΦNE operation for FINUDA [8] restarted in October 2006 with the goal to deliver 1 fb^{-1} integrated luminosity by mid June 2007.

The optimum vacuum conditions have been recovered in few weeks while commissioning the collider and in November the first luminosity has been delivered.

Commissioning included, as usual, ring optics tuning, closed orbit optimization, linear betatron coupling correction and feedback systems setup.

The bare beam orbit in both ring has been drastically reduced by beam based alignment involving the FINUDA detector solenoid.

The ring optics for the collision at FINUDA has been designed in order to have a beam emittance $\varepsilon_x = 0.34\ \mu$ and low beta parameters at the main IP2 $\beta_x^* = 2$ m and $\beta_y^* = 0.019$ m. The vertical betatron function at IP1 has been tuned in order to trade off between an efficient beam-beam separation and the need to keep under control the blow-up due to beam-beam long range interaction; for this reason the β_y^{IP1} value after two months of operation has been halved and set to $\beta_y^{IP1} = 11$ m. Beam-beam simulations, showing the beam-beam blow-up dependence on parasitic crossings, for a given beam-beam separation, have been useful in this optimization process.

Betatron coupling compensation has been achieved by rotating the permanent quadrupoles inside the FINUDA solenoid, reaching an optimal value of ~0.3%

The magnetic field of the four wigglers installed in each DAΦNE ring to increase radiation damping has been reduced by 5% (1.68 T) with respect to the last KLOE run resulting in a ~1.5 MW total wall-plug power reduction since they were operated in the field saturation region. The new wiggler field setup produces a negligible effect on the damping times, improves the ring energy acceptance, reduces the non linear terms contribution in the tune shift on energy dependence and is compatible with the operation of the x-ray beam line being the critical energy, and consequently the photon flux, reduced by 10% only.

During the luminosity adiabatic tuning the main ring working points (asymmetric at DAΦNE) have been progressively moved toward the integer

$\nu^-_{x,y} = 5.086\ ,\ 4.156\ \text{->}\ 5.076\ ,\ 4.140$

$\nu^+_{x,y} = 5.109\ ,\ 4.192\ \text{->}\ 5.096\ ,\ 4.168$

to reduce the beam transverse dimension growth driven by the beam-beam interaction at high current, confirmed by experimental evidence and theoretical simulation.

Beam Dynamics

The ICE in the e^- ring wigglers have been removed since they were responsible for the factor 2 higher coupling impedance measured in the DAΦNE e^- ring with respect to the e^+ one (Z/n = 1.1 Ω and Z/n= .54 Ω respectively). This difference produced several observed detrimental effects on the e^- ring beam dynamics and collider luminosity as well.

The e^- bunch length was 30% longer than the e^+ one causing a geometric luminosity reduction due to the hour glass effect. For such a longer bunch synchro-betatron beam-beam resonances, due to the collision scheme based on crossing angle, were more harmful. Single bunch instabilities, mainly longitudinal quadrupole oscillations [9], depending inversely on the coupling impedance, appeared at lower bunch current in the e^- ring. Transverse beam size blow-up, mainly in the vertical plane, has been observed beyond the microwave instability threshold.

Beam measurements taken during commissioning confirmed that the e^- beam dynamics, after ICEs removal, is almost comparable to that of the e^+ beam [10]. The e^- bunch length is 25÷30 % shorter (see Fig.2) and there is no evidence of quadrupole instability threshold neither vertical beam blow-up at the operating bunch current (~ 15 mA).

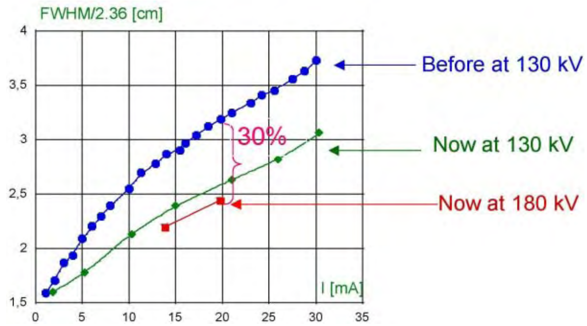

Figure 2: Bunch lengthening before (blue) and after (green) ICE removal.

Since the first phase of commissioning the e^+ beam showed a threshold in the maximum storable current due to a fast horizontal instability depending on the current and on the beam fill pattern, compatible with an e-cloud driven instability. The phenomenon had been observed even during the KLOE data-taking with 1.4 A current threshold in collision. During the FINUDA operation the threshold seemed to be much more harmful, in fact in November only 0.4 A e^+ current was storable in collision. This limit progressively increased by improving the injection process and the feedback systems.

The injection optimization was aimed at reducing the oscillation amplitude of the stored beam by moving the e^+ stored beam orbit closer to the injection septum, reducing strength and pulse length (150 ns to 90 ns) of the injection kickers, and tuning the phase advance between the injection kickers, by means of the newly installed BPMs with turn by turn orbit measurement capability.

The new feedback systems are based on a digital signal processing relying on a programmable gate array. It has enhanced diagnostics and remotization capabilities, can deal with any betatron and synchrotron tune, does not require fixed phase advance between pick-up and kicker and is much less sensitive to the injection oscillation amplitude transient. The new hardware has been implemented progressively for the two rings transverse feedbacks, giving a relevant contribution to the transverse beam dynamics control and to the enhancement of the e^+ maximum storable current.

Luminosity

Since the first two months of operation the luminosity has been significantly higher than during the previous 2003÷2004 FINUDA run, as shown in Table 1. The peak luminosity measured by the FINUDA detector has been almost doubled; correspondingly the maximum monthly integrated luminosity has been increased by a factor ~3.

This large gain is a direct consequence of the several implemented upgrades.

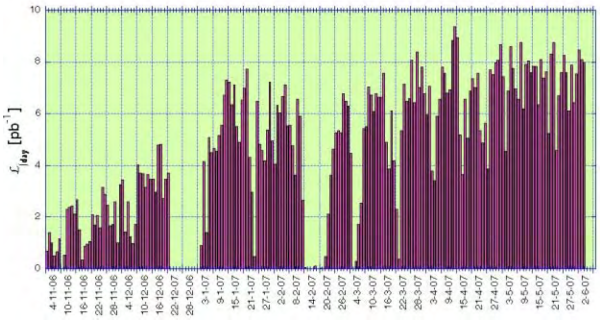

Figure 3: Daily integrated luminosity measured by FINUDA.

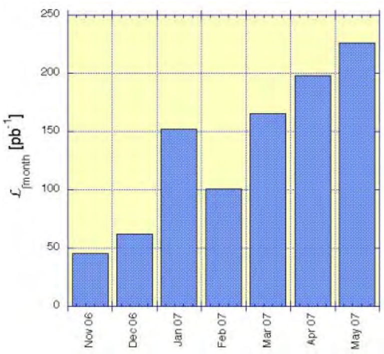

Figure 4: Monthly integrated luminosity.

An improvement can be noticed even with respect to the last KLOE run, with a peak luminosity increased by few percent, althogh the low beta parameters have not been pushed to the lowest possible values, due to the short time available for machine studies and tuning and putting in collision smaller currents and less bunches. This gain can be ascribed to the higher geometric luminosity due to the ICEs removal. Correspondingly 8% gain in terms of maximum monthly integrated luminosity (see Fig.4) has been obtained due to the higher collider uptime (> 80%), to the careful subsystems maintenance and upgrade and to the longer beam lifetimes obtained from the wires for BBLR compensation installed in both interaction regions.

The background rate seen by the FINUDA detector has been progressively reduced, by tuning the collider optics and adjusting the collimators, and made lower than during the 2003-2004 FINUDA run. Due to the higher luminosity and uptime and to the lower background the delivered luminosity and the statistical sample acquired by FINUDA have been 5 and 7 times larger with respect to the previous run in approximately the same data-taking time. Moreover these results have been obtained with ~30% reduction in the wall-plug power.

FUTURE PLANS

In the next months the FINUDA detector will be removed and the DAΦNE interaction regions will be replaced [11] in order to implement the 'crab waist' collision scheme [12], aiming at a luminosity of the order of 10^{33}cm^{-2}s^{-1} with beam currents similar to the present ones.

The operation restart is scheduled for the end of 2007 with the Siddharta experiment installed on IP1. The SIDDHARTA detector [13] is a compact table-top device without solenoidal field providing a suitable configuration to test the effectiveness of the 'crab waist' concept.

Table 1: DAΦNE luminosity performances and low-beta parameters at IP2 during the last runs.

	FINUDA Oct 03 Mar 04	**KLOE** May 04 Nov 05	**FINUDA** Nov 06 Jun 07
L_{peak} [cm^{-2}s^{-1}]	0.85	1.53	1.6
$L^{MAX}_{\int day}$ [pb^{-1}]	3.9	9.8	9.4
$L^{MAX}_{\int month}$ [pb^{-1}]	65	209	226
I^{-MAX}_{coll} [A]	1.1	1.4	1.5
I^{+MAX}_{coll} [A]	1.0	1.2	1.1
$n_{bunches}$	100	111	106
$L_{\int logged}$ [fb^{-1}]	0.192	2	0.966
β_x^* [m]	2.33	1.5	2.0
β_y^* [m]	0.024	0.018	0.019
ε_x [10^{-6} m rad]	0.34	0.34	0.34
κ (%)	0.3	0.3	0.3

CONCLUSIONS

DAΦNE has completed the run for the FINUDA experiment delivering ~ 1fb^{-1} in six months of operation. All the upgrades have been effective in optimizing machine operation and uptime, as well as in providing efficient and accurate diagnostic tools. The e^- ring coupling impedance has been made comparable with the e^+ one resulting in improved e^- beam dynamics and geometric luminosity. The peak and integrated luminosity have reached the highest value ever obtained during the whole DAΦNE operation.

The run efficiency and the high quality of delivered data is raising the experiment groups interest for future physics enterprises at DAΦNE.

REFERENCES

[1] G. Vignola et al., PAC93, p. 1993
[2] C. Milardi et al., e-Print: physics/0408073.
[3] A. Gallo et al., Edimburgh 2006, EPAC p. 604-606.
[4] B. Spataro et al., DAΦNE Tech. Note G-64, 2005.
[5] C. Milardi et al., e-Print: physics/0607129.
[6] A. Stella et al., EPAC 2006, p. 1124.
[7] A. Drago, private communication, Apr 2007.
[8] FINUDA Coll., Phys. Rev. Lett. 94:212303, 2005.
[9] A. Drago et al., PRSTAB.6:052801, 2003.
[10] M. Zobov et al., e-Print: arXiv:0705.1223.
[11] M. E. Biagini et al., this conference, MOOBKI02.
[12] P. Raimondi et al., this conference, TUPAN037.
[13] SIDDHARTA Coll., EPJ A31 (2007) 537-539.

SUPER-B FACTORY USING LOW EMITTANCE STORAGE RINGS AND LARGE CROSSING ANGLE*

Y. Cai, S. Ecklund, A. Fisher, S. Heifets, A. Novokhatski, M. Pivi,
J. Seeman[+], A. Seryi, M. Sullivan, U. Wienands,
SLAC, 2575 Sand Hill Road, Menlo Park, CA 94025, USA
M. Biagini, S. Guiducci, P. Raimondi, INFN-LNF, Frascati, Italy
I. Koop, D. Shatilov, M. Zobov, Budker Institute, Novosibirsk, Russia.

Abstract

Parameters are being studied for a high luminosity e+e- collider operating at the Upsilon 4S that would deliver a luminosity of over $10^{36}/\text{cm}^2/\text{s}$. This collider, called a Super-B Factory, would use a novel combination of linear collider and storage ring techniques. In this scheme an electron beam and a positron beam are stored in low-emittance damping rings similar to those designed for a Linear Collider (LC). A LC style interaction region is included in the ring to produce sub-millimeter vertical beta functions at the collision point. A large crossing angle (+/- 17 mrad) is used at the collision point to allow beam separation and reduce the hourglass effects. Beam currents of about 2.3 A x 1.3 A at 4 x 7 GeV in 1733 bunches can produce a luminosity of $10^{36}/\text{cm}^2/\text{s}$. Such a collider would produce an integrated luminosity of about 10,000 fb^{-1} (10 ab^{-1}) in a running year (10^7 sec) at the Y(4S) resonance.

DESIGN FROM PAST SUCCESSES

The construction and operation of modern multi-bunch e^+e^- colliders [1,2] have brought about many advances in accelerator physics in the area of high currents, complex interaction regions, high beam-beam tune shifts, high power RF systems, controlled beam instabilities, rapid injection rates, and reliable uptimes (~90%):

1) Colliders with asymmetric energies can work.
2) Beam-beam energy transparency conditions are weak.
3) Interaction regions with two energies can work.
4) IR backgrounds can be handled successfully.
5) High current RF systems can be operated (3 A x 1.9 A).
6) Beam-beam vertical parameters can reach 0.06 to 0.09.
7) Continuous injection is done during data production.
8) The electron cloud effect (ECI) can be managed.
9) Bunch-by-bunch feedbacks at 4 nsec spacing work.

Lessons learned from the SLC and subsequent linear collider studies and experiments (FFTB, ATF) [3,4] are:

A) Small horizontal and vertical emittances can be produced in a damping ring with a short damping time.
B) Very small beam spot sizes and beta functions can be achieved at the interaction region.
C) Interaction regions can have very small vertical betas.

*Supported by US DOE contract DE-AC02-76SF00515.
†seeman@slac.stanford.edu

LUMINOSITY AND CROSSING ANGLE

The design of a 10^{36} $\text{cm}^{-2}\text{s}^{-1}$ e^+e^- collider combines extensions of the design of the present *B* Factories and linear collider concepts to allow improved beam parameters to be achieved. The luminosity L and beam-beam parameters, ξ_y, ξ_x, in an e^+e^- collider are given by the expressions:

$$\mathcal{L} = \frac{\gamma^+ \xi_y N^+ f_c}{2\, r_e\, \beta_y}\left(1 + \frac{\sigma_y}{\sigma_x}\right) \propto \frac{N^+ \xi_y}{\beta_y}$$

$$\xi_y = \frac{r_e N^-}{2\pi\gamma^+}\frac{\beta_y}{\sigma_y\left(\sigma_x\sqrt{1+\varphi^2}+\sigma_y\right)} \propto \frac{N^-\sqrt{\beta_y}}{\sigma_y\sigma_z\theta}$$

$$\xi_x = \frac{r_e N^-}{2\pi\gamma^+}\frac{\beta_x}{\sigma_x^2\left[(1+\varphi^2)+\frac{\sigma_y}{\sigma_x}\sqrt{1+\varphi^2}\right]} \propto \frac{N^-\beta_x}{(\sigma_z\theta)^2}$$

where f_c is the frequency of collision of each bunch, N is the number of particles in the positron (+) and electron (-) bunches, σ is the beam size in the horizontal (x) and vertical (y) directions, γ is the normalized beam energy, ε is the beam emittance, β is the beta function (cm) at the collision point for each plane and θ is the crossing angle. The Piwinski angle is ϕ.

SUPER-B FACTORY PARAMETERS

A schematic drawing of the Super-B Factory is shown in Figure 1. There are two rings each with six arcs and six small straight sections. Two of the straights are for injection, two for possible interaction regions and two for damping wigglers. There are RF stations in three straights per ring. The crossing angle at the interaction point is shown in Figure 2 where the long-thin-flat bunches are made to collide. Sextupoles near the interaction region in a dispersive section are used to create a longitudinal waist shift over the width of the beam to correct the beam-beam hour-glass effects, dubbed crab waist correction [5-9]. An arc lattice cell is shown in Figure 4 to produce low emittances.

The parameters of the Super-B Factory are listed in Table 1. Note the beam currents are lower than present B-Factories at 2.3 A x 1.3 A for e- and e+ at 4 x 7 GeV.

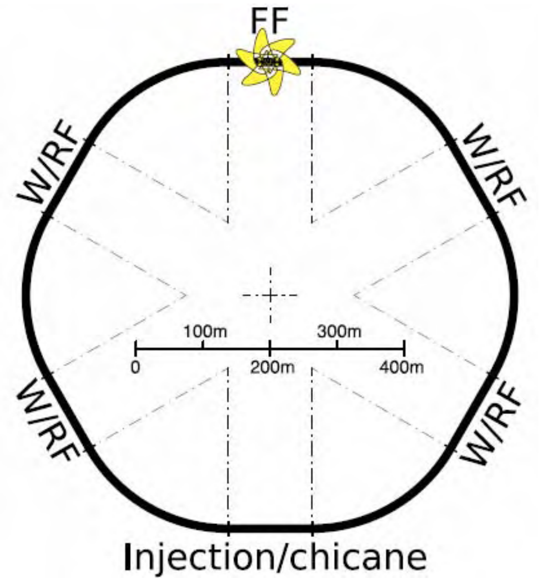

Figure 1: Super-B Factory with circumference = 2250 m.

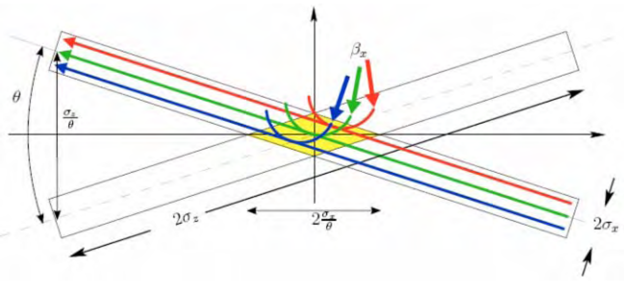

Figure 2: Interaction region showing two thin beams crossing at a large angle with crab waist to improve the beam-beam interaction.

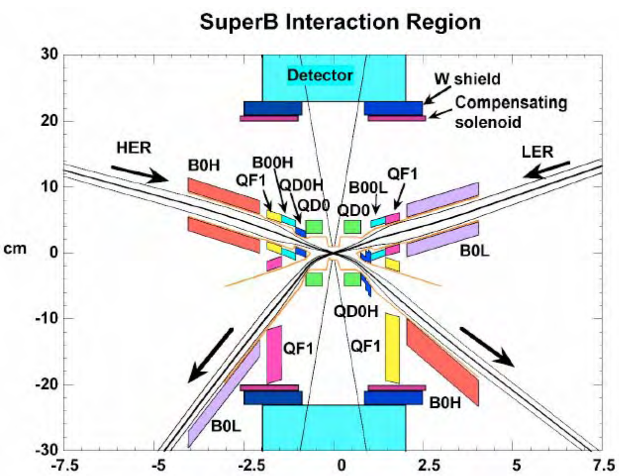

Figure 3: Interaction region for two asymmetric beams.

Table 1: Super-B Factory accelerator/collision parameters

	Low Energy Ring	High Energy Ring
σ_x* (μm)	5.7	5.7
η_x (mm)	0.0	0.0
σ_y* (nm)	35	35
β_x* (mm)	20	20
β_y* (mm)	0.3	0.3
σ_z* (mm)	6.0	6.0
σ_E*/E	0.84x10^{-3}	0.9x10^{-3}
RF voltage	6	18
ε_x (nm)	1.6	1.6
ε_y (nm)	0.004	0.004
RF freq	476	476
θ_x (mrad)	2x17	2*17
Num wigglers	4	2
Lifetime (min)	3.6	5.1
N_{part} (10^{10})	6.2	3.5
$N_{bunches}$	1733	1733
I (A)	2.28	1.30
Circ (m)	2250	2250
$\tau_{x,y}$ (ms)	32	32
τ_z (ms)	16	16
f_{coll} (MHz)	238	238
y/x Tune Shift	0.17/0.004	0.17/0.004
L_{umi} (10^{36})	1.0	1.0

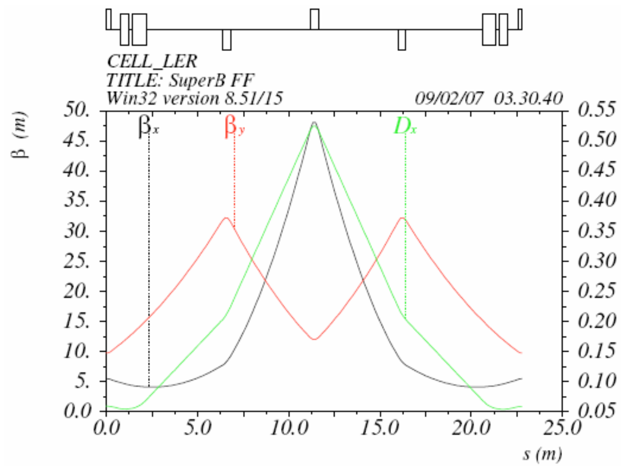

Figure 4: LER arc lattice cell.

INTERACTION REGION PARAMETERS

The interaction region (Figure 3) is being designed to leave about the same longitudinal free space for the detector as that presently used by *BABAR* or *BELLE* but with superconducting quadrupole doublets QD0/QF1 as close to the interaction region as possible [10].

A preliminary design of the Final Focus, similar to those of the NLC/ILC, has been performed for the IP parameters in Table 1. The total FF length is about 160 m and the final doublet is at 0.5m from the IP. A plot of the optical functions in the incoming half of the FF region is presented in Figure 5. The choice for a finite crossing angle at the IP greatly simplifies the IR design (Figure 3), since the two beams are now naturally separated at the parasitic collisions. The resulting vertical beta is 0.3 mm and the horizontal 20 mm. These beta values are much closer to a linear collider design than a traditional circular collider. The beams enter the interaction point nearly straight to minimize synchrotron radiation and lost particle backgrounds. The beams are bent more while exiting the IR to avoid parasitic collisions and the resulting beam-beam effects.

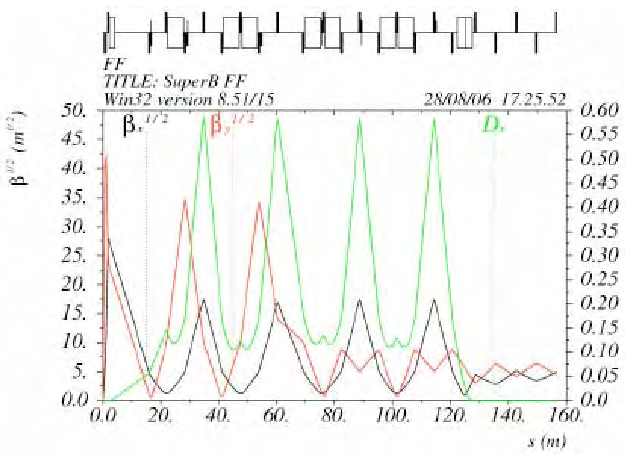

Figure 5: IR optical parameters for a Super-B-Factory.

Table 2: Super-B factory AC power requirements

Parameter	Units	Value
Beam energy (HER/LER)	GeV	7.0/4.0
Beam current (HER/LER)	Amp	1.3/2.3
HER RF power	MW	8.6
LER RF power	MW	8.6
HER magnet power	MW	4.0
LER magnet power	MW	3.0
Cooling system power	MW	2.4
Control power	MW	0.5
Injection system power	MW	4.0
Lights and HVAC	MW	3.0
Total site power for accelerator	MW	34.1

POWER REQUIREMENTS

The power required for this collider is the sum of power for the magnets, RF system, cooling water, controls, and the accelerator operation. The present estimates indicate about 34 MW total as shown in Table 2. These values do not include the campus power requirements or that of the particle physics detector. There are upgrade possibilities for this collider to 2 to 3 times the design luminosity that will require more power [8]. Due to the advantages of the very low emittances and the crab waist with this design, the power requirements here are lower than at present B-Factory colliders.

INJECTION REQUIREMENTS

The injection system needed for the Super-B is similar to that for PEP-II or a scaled-up version of the DAPHNE injector. Table 3 shows the basis injector parameters. Since the beam lifetimes are below 10 minutes, continuous injection is needed. The injector will operate at about 100 Hz and inject about 2 bunches per pulse. The numbers shown here are for the upgraded collider to a higher luminosity. The injector could be shared with other projects as needed.

Table 3: Super-B Injection Parameters

Parameter	Unit	e+	e-
Linac energy	GeV	4	7
Damping ring energy	GeV	1	1
Linac frequency	MHz	2856	2856
Bunches per pulse		2	2
Injection efficiency	%	67	85
Pulse rate per beam	Hz	75	25
Injected particles/pulse	10^{10}	4	5.1
Injection rate total	10^{12}/sec	2.0	2.6

REFERENCES

[1] PEP-II Status Report PAC 2007 Albuquerque, NM.
[2] KEKB Status Report PAC 2007 Albuquerque, NM.
[3] The SLC Design Handbook, SLAC November 1984.
[4] International Linear Collider Technical Review Committee, Second Report 2003, ICFA SLAC-R-606.
[5] P. Raimondi, “Super-B Design Directions,” PAC 2007 Albuquerque, NM.
[6] M. Biagini *et al.*, “Beam-Beam Simulations for a Single Pass Super-B Factory,” EPAC 2006 proceedings, June 2006.
[7] D. Shatilov, M. Zobov, “Tune shift in Beam.Beam collisions with an arbitrary crossing angle”, DAΦNE Tech. Note G-59, May 1003.
[8] Super-B Factory CDR, March 2007 SLAC-R-856.
[9] Y. Cai, A. Chao, S. Tzenov, “Simulation of the beam-beam effects in e^+e^- storage ring with a method of reduced region of mesh”, PRST, AB, Vol.4, 2001.
[10] M. Sullivan, “Super B Interaction Region, PAC 2007.

REDUCTION OF NON-LINEARITIES IN THE DAΦNE MAIN RINGS WIGGLERS*

S. Bettoni, S. Guiducci, M. Preger, P. Raimondi, C. Sanelli, LNF-INFN, Frascati, Italy

Abstract

The wigglers of the DAΦNE main rings have been the main source of non-linearities for the beam dynamics in the collider. This paper describes a method to reduce the integrated odd multipoles (the even ones tend to vanish for the periodicity of the magnet) by alternatively displacing the magnetic axis of the poles to compensate the integrated odd multipoles in each half-period of the wiggler. In order to check the effectiveness of this approach, tracking studies have been performed. Tracking results have been used to tune the MAD model of the wiggler.

INTRODUCTION

Since the beginning of DAΦNE operation the eight normal conducting wigglers, used to reduce the damping time of the rings, have been an important source of non linearity for the lattice of the collider, because of the field roll-off combined with the large excursion of the beam trajectory from the axis (about 1.3 cm). This was experimentally demonstrated in fall 2000, when tune shift measurements, performed by creating closed orbit bumps, evidenced a large integrated octupole in these magnets [1].

This non-linearity has been reduced by a factor 2.5 by improving the transverse field uniformity by means of pole shims. To further reduce the non-linearities another more drastic approach has been studied [2].

After briefly recalling the method, a more convenient optimization, which is easier to be implemented and allows to produce higher fields, is presented.

METHOD

Let $\overline{z}$ be a position along the longitudinal axis of the magnet, y the vertical, x and $\tilde{x}$ the horizontal transverse coordinates with respect to $\overline{z}$ and to the beam trajectory respectively. The magnetic field seen by a particle passing in the magnet can be expanded around the beam trajectory $(x_{TR}, 0, \overline{z})$ in the mid-plane as:

$$B_y(\tilde{x}, \overline{z}) \equiv \sum_{n=0}^{\infty} {b_n}^T \tilde{x}^n \tag{1}$$

where the coefficients ${b_n}^T$, defined as:

$$ {b_n}^T \equiv \frac{1}{n!} \left. \frac{\partial^n B_y(\tilde{x}, \overline{z})}{\partial \tilde{x}^n} \right|_{\tilde{x}=0} \tag{2}$$

correspond to the multipoles with respect to the beam trajectory (${b_0}^T$ to the dipole, ${b_1}^T$ to the quadrupole, $\cdots$).

It can be shown that each multipole with respect to the beam trajectory can be written as a function of those calculated with respect to the axis of the wiggler, ${b_k}^A$, as:

$$ {b_n}^T = \sum_{k=n}^{\infty} \frac{k!}{n!(k-n)!} \, {b_k}^A \, {x_{TR}}^{k-n} \tag{3}$$

The effects of the non-linearities on the beam dynamics depend on the integral of these coefficients, I_n, defined as:

$$I_n \equiv \int_{Magnet} {b_n}^T \, ds \quad n = 2, 3, \ldots \tag{4}$$

where s is the coordinate along the reference trajectory.

Because of the alternating sign of the current from a pole to the next one and the left-right symmetry of the magnet, the integral of the even terms ${b_{2j}}^T$ tends to cancel in each period. On the contrary the integral of the odd terms ${b_{2j+1}}^T$ does not, because in Eq. (3) both the even terms with respect to the axis and the powers of x_{TR} change sign from a pole to the next one, so that their contributions add along the magnet.

In particular from these considerations and substituting Eq. (3) in Eq. (4) the only integrals to be reduced have the form:

$$\begin{aligned} I_{2j+1} = \int & (c_{2j+2} \, {b_{2j+2}}^A \, x_{TR} + \\ & + c_{2j+4} \, {b_{2j+4}}^A \, x_{TR}^3 + \cdots) \, ds \end{aligned} \tag{5}$$

The method consists in alternatively displacing the magnetic axis of each pole so that the odd powers of x_{TR} change sign inside each half-period of the magnet. In this way the contributions to I_{2j+1} from the regions inside the poles tend to be compensated by those coming from the regions between the poles.

OPTIMIZATION

Several methods to displace the magnetic axis of the poles can be envisaged:

- Apply pole shims;
- Cut the poles;
- Shift the poles.

The first option has been rejected because the solution would strongly depend on the current and on the specific properties of the iron used in the simulation. The second possibility has been already explored and described in detail in [2]. In this case the pole width is reduced, so that pole

* Work supported by the Commission of the European Communities under the 6th Framework Programme "Structuring the European Research Area", contract number RIDS-011899.

shims need to be added to reduce the strong dependence of the integrated multipoles with respect to the beam-wiggler misalignment. The new proposal of shifting the poles consists instead in displacing the axis of each pole without reducing their width, so that the shims are no longer necessary and, as a consequence, the wiggler gap can be smaller.

Until 2006 the wigglers have been powered at 693 A, and a full map at this current has been measured. Recently the wigglers work at 550 A, and the corresponding map is not yet available. The field maps of both the shifted and unshifted poles configurations have been simulated to compare the results of the optimization.

The shifted poles configuration

The main operational parameters of the wigglers are shown in table 1.

Table 1: Main wigglers parameters.

	Full pole	**Half pole**
Number of poles	5	2
Nominal current (A)	550	390
Peak field (T)	1.70	1.43
Gap (cm)	3.7	
Pole width (cm)	14	
Beams particles	electrons and positrons	
Beam energy (MeV)	510	

To move the magnetic axis each pole has to be horizontally shifted, as shown in Fig. 1 in the x-y plane and in Fig. 2 in the z-x one.

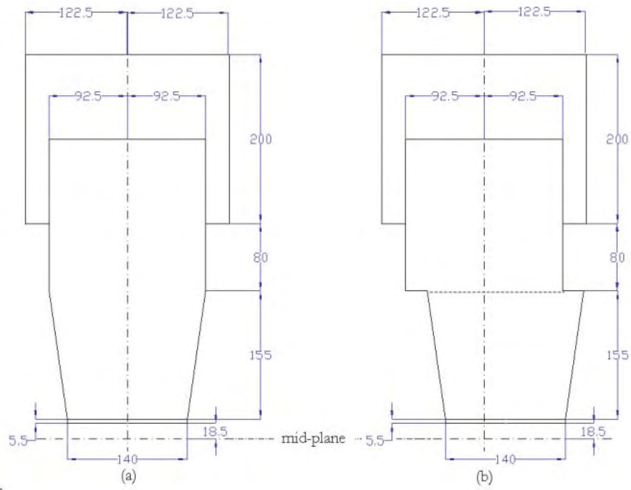

Figure 1: Drawing of a pole in the x-y plane (a) before and (b) after the modification. The case refers to a pole where the particle is on the right of the vertical symmetry axis (geometric axis). Dimensions are in mm.

To find the displacement of the magnetic axis which makes the integrated octupole vanish, several configurations of the wiggler [3] with different displacements have been simulated to determine I_3 as a function of the x-shift, as shown in Fig. 3.

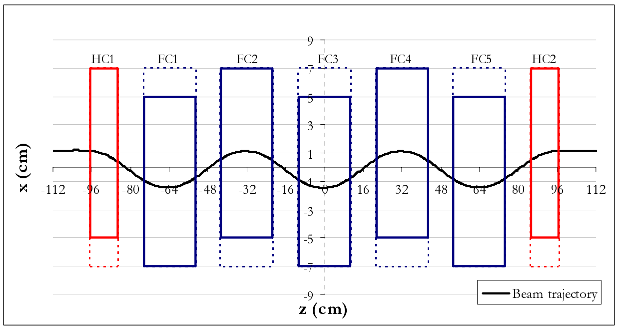

Figure 2: Section of the modified wiggler in the z-x plane (solid lines). The configuration of the poles before the modification is also shown (dashed lines).

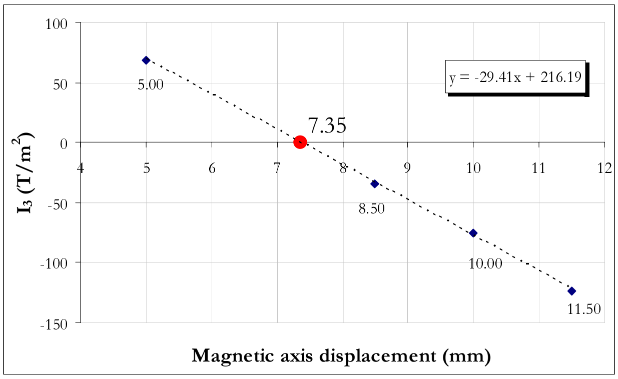

Figure 3: Integrated octupole as a function of the magnetic axis displacement. The straight line which fits the points and the value corresponding to the optimal position of the magnetic axis are also indicated.

The values of the multipoles integrated over the entire wiggler after the ± 7.3 mm shift (shifted poles) compared to those of the starting configuration (aligned poles) are reported in table 2.

Table 2: Integrated multipoles in the aligned poles and in the shifted poles configuration. The units of I_j are Tm^{1-j}.

	I_0	I_1	I_2	I_3	I_4
Aligned poles	0.00	2.58	-1.10	279.61	314.4
Shifted poles	0.00	2.10	-1.38	0.07	-62.9

The behavior of ${b_3}^T$ as a function of z in the whole wiggler is shown in Fig. 4.

To verify the impact of the modification on the beam trajectory inside the wiggler, test particles with different initial conditions have been tracked through the simulated field maps. The position and the angle at the end of the wiggler are shown in Fig. 5 and in Fig. 6 as a function of the initial position for both the original and the modified configurations.

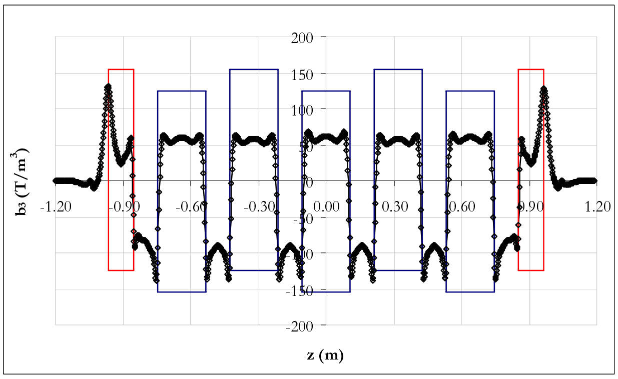

Figure 4: ${b_3}^T$ as a function of z in the configuration of poles shifted by $\pm$ 7.3 mm.

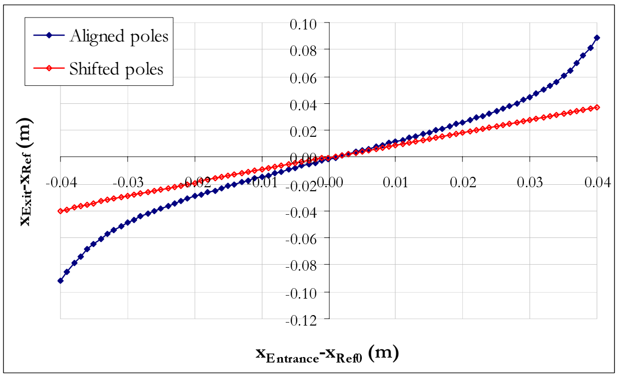

Figure 5: x exit as a function of the entrance x with respect to the reference trajectory.

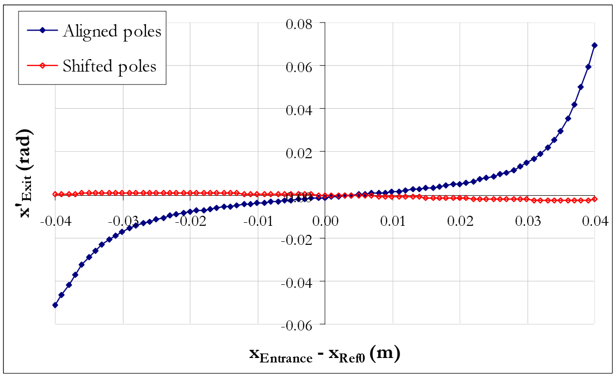

Figure 6: Exit angle as a function of the entrance x with respect to the reference trajectory.

The MAD model

A MAD model of the magnet has been written to be inserted in the model of the whole ring for beam dynamics calculations.

Each half-period of the wiggler has been split in bending magnets (one for the terminal poles and two for the full poles), whose bending angle and length have been determined to reproduce the reference trajectory determined by Tosca, thin lenses (two for the terminal poles and three for the full poles), to take in account quadrupole and higher order terms of the field expansion, and drift spaces.

The tracking curves obtained from the MAD model have been compared to those obtained by tracking with Tosca. The results are shown in Fig. 7 and Fig. 8 respectively.

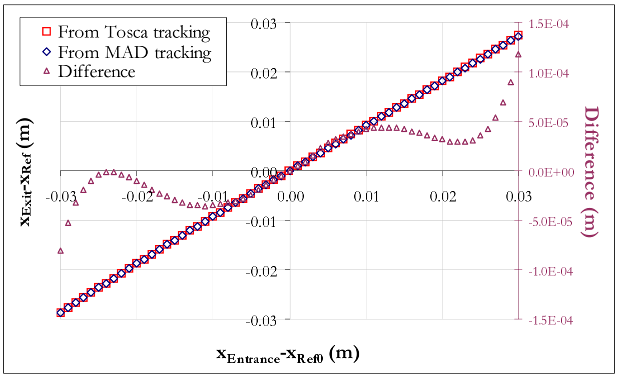

Figure 7: x exit as a function of the x entrance with respect to the reference trajectory. The difference is also shown.

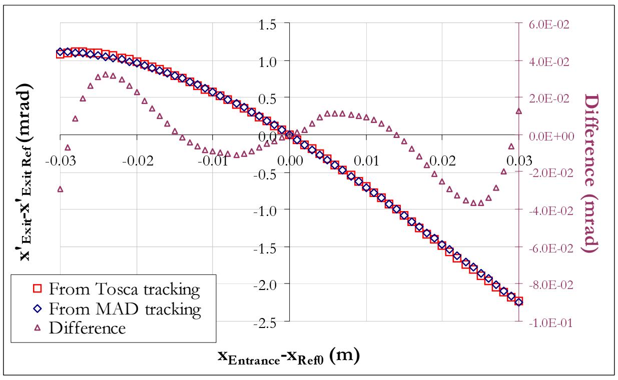

Figure 8: Exit angle as a function of the x entrance with respect to the reference trajectory. The difference is also shown.

The agreement of these curves to those obtained from the Tosca tracking using the coefficients from the expansion of the fit is satisfactory.

CONCLUSIONS

A method to reduce the non-linearities in the wigglers of DAΦNE has been presented. The simulation indicates that the shifted poles method could strongly reduce the non-linearities in these wigglers. The modification should be implemented in DAΦNE to confirm the results of the simulations, and, if successful, the same method could be used in future design of more ideal wigglers.

REFERENCES

[1] A. Battisti et al., *The modified wiggler of the DAΦNE main rings*, DAΦNE Technical Note MM-34 (2004).

[2] S. Bettoni, *Reduction of integrated odd multipoles in periodic magnets*, Phys. Rev. ST-AB, **10**, 42401 (2007).

[3] The models have been implemented in Opera 3D, Vector Fields Analysis, version 11.009.

DAΦNE UPGRADE: A NEW MAGNETIC AND MECHANICAL LAYOUT

S. Tomassini[#], D. Alesini, A. Beatrici, A. Clozza, E. Di Pasquale, M. Esposito, G. Fontana, F. Marcellini, G. Mazzitelli, M. Paris, P. Raimondi, G. Sensolini, C. Sanelli, F. Sgamma, M. Troiani, M. Zobov, A. Zolla, Frascati National Laboratory, Frascati, Italy

Abstract

The DAΦNE Φ-Factory upgrade, foreseen for the SIDDHARTA detector run in 2007, requires a new magnetic and mechanical layout to exploit the "large Piwinski angle" and "crab waist" concepts [1]. New permanent quadrupole magnets and aluminium vacuum chamber with thin window have been designed for the new interaction region, with the aim to reuse as far as possible the present magnetic and vacuum chamber components. A vacuum chamber of novel design will allow separating the beams at the second interaction region. The new layout together the new hardware components are presented.

INTRODUCTION

The SIDDHARTA experiment will be ready to be installed in DAΦNE by fall 2007. A new Interaction Region (IR) suitable to exploit the "large crossing angle" and "crab waist" concepts has been designed and is under construction. This new scheme for luminosity increase in e^+e^- colliders, first presented at the 2nd Frascati Workshop on SuperB-Factory, March 2006 [2], is compatible with the SIDDHARTA setup. A combination of large crossing angle, together with very small beam sizes at the IP, and the "crab vertical waist", is expected to give the possibility of reaching a luminosity of the order of 10^{33} cm^{-2} s^{-1}, with small modifications to the machine and beam currents similar to those reached during the KLOE run.

DAΦNE UPGRADE GENERAL LAYOUT

The need to have a very small β_y and a large crossing angle requires two new IR geometries. Defocusing and focusing (QD, QF) quadrupoles on both sides of the interaction point (IP) will provide the necessary beam focusing and beam separation. Further trajectory separation will be provided by two small dipole correctors upstream and downstream the quadrupole doublets. Other three quadrupoles will be used to match the betatron functions in the arcs. In this scheme there will be no need for the presently used splitter dipoles. The general layout of DAΦNE upgrade is shown in figure 1.

IR1 Magnetic and mechanical layout

The total crossing angle at the IP1 will be 50 mrad (25 mrad per beam). The low-β section quadrupoles near the IP are of permanent magnet (PM) type.

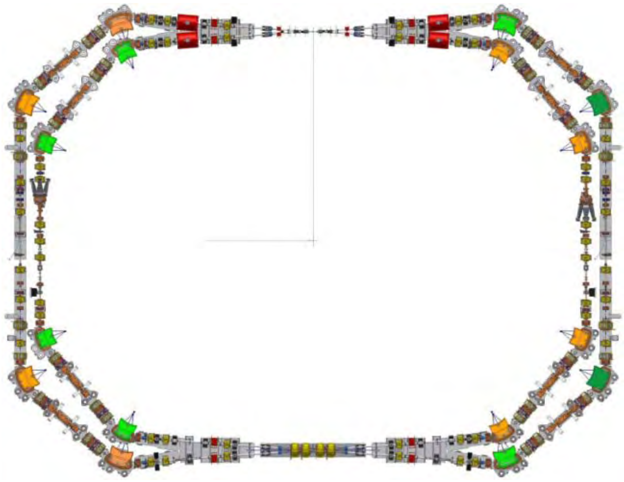

Figure 1: DAΦNE upgrade general layout.

A set of two QD and four QF is required. Their characteristics have been studied and a summary of them is given in table 2. A close-up of the near IP1 region is shown in figure 2.

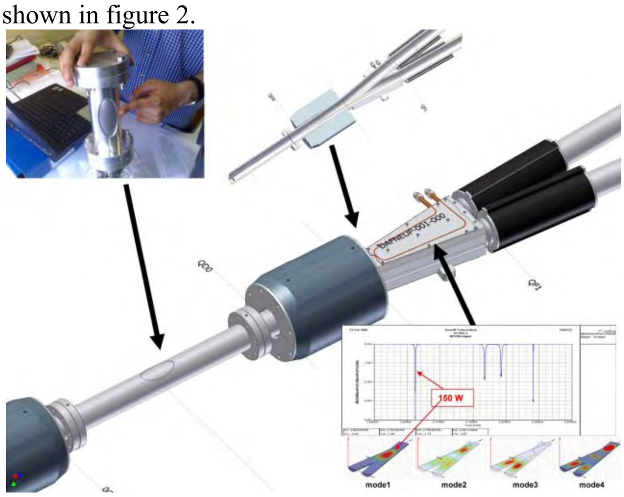

Figure 2: IP1 low-β permanent magnet and thin chamber.

Four corrector dipoles will be used with deflection of 9.5 mrad to match the inlet and outlet arc chamber flanges. Sextupoles for the crab waist are placed at 9.3 m from the IP1. Bending dipoles facing the IRs will be rotated and the field adjusted according to table 1.

Table 1: Bending Dipoles Adjustment

Dipole name	Rotation angle (deg)	Bending radius(mm)
Sector Long	+2.19	1528.11
Sector Short	-2.19	1269.76

#sandro.tomassini@lnf.infn.it

Other elements just after the doublets (quadrupoles, sextupoles and correctors) are those already in place; only their positions have to be rearranged. Figure 3 shows a drawing of half the modified (top) and old (bottom) IR1.

Table 2: low-β PM quadrupoles specifications

Designation	**QD**	**QF**
Quantity	2	4
Minimum clear inner radius (mm)	33	30
PM inner radius (mm)	34	30.5
Maximum outer radius (mm)	100	45
Magnetic length (mm)	230	240
REM physical length (mm)	230	240
Maximum mechanical length (mm)	240	250
Nominal gradient (T/m)	29.2	12.6
Integrated gradient (T)	6.7	3.0
Good field region radius (mm)	20	20
Integrated field quality |dB/B|	5.00E-04	5.00E-04
REM stabilization temperature (°C)	150	150
Magnet material type	SmCo2:17	SmCo2:17
Magnet construction	2 halves	2 halves

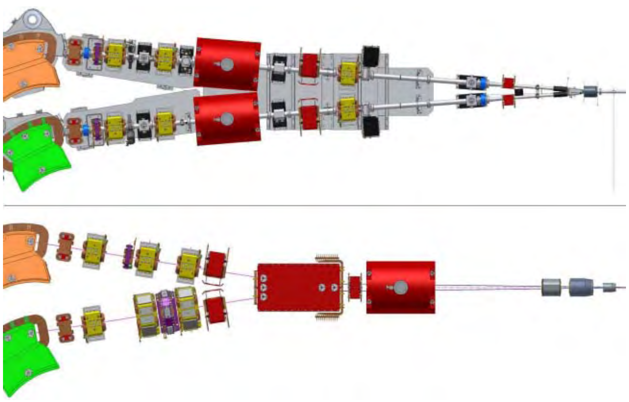

Figure 3: View of the new (top) and old (bottom) IR1 region (half).

Solenoid compensator magnets (the red cylinders in figure 3) will not be installed for the SIDDHARTA experiment because there is no detector solenoid at the IP but the new layout already foresees the possibility to reinstall KLOE or FINUDA in the future. Most vacuum chambers and pumps will be reused. The beam pipe around IP1 and in the two QDs will be common to the two beams and will start to bifurcate just before the QFs. For the SIDDHARTA experiment, which will be installed on the IP1, a new aluminium alloy (AL6082T6) chamber has been designed with two thin windows (0.3mm ±0.02 thickness) in the top and bottom sides (see figure 2). A prototype has been built and a mechanical and vacuum test performed. In the Y-chamber junction, in the worst possible scenario, when one of the powerful beam spectrum lines (at RF frequency harmonics) is in full coupling with this mode, the power loss will not exceed 200 W. Despite such a power seems to be manageable, we still decided to cool the chamber as shown in figure 2. This additional cooling will play a double role: to eliminate heating due to the high order modes (HOM), if necessary, and to shift the mode frequency with respect to the dangerous power spectrum lines, thus reducing the heating itself. Horizontal collimators are placed at 8 m from the IP.

IR2 Magnetic and Mechanical Layout

Similar modifications were made in the second interaction region, where the beams will not experience a low-beta insertion and will be vertically separated in order to avoid collisions. A layout of half IR2 is presented in figure 4, the original layout was very similar to the old IR1 section shown in figure 3. The magnet layout is almost the same as IR1 with the exception of sextupoles for crab waist, not present here and four large aperture quadrupoles in IP2. A new design of the central IR2 beam pipe, where the two beams are vertically separated, is shown in figure 5. The two vacuum chambers are completely separated and the cross section is "half moon" like.

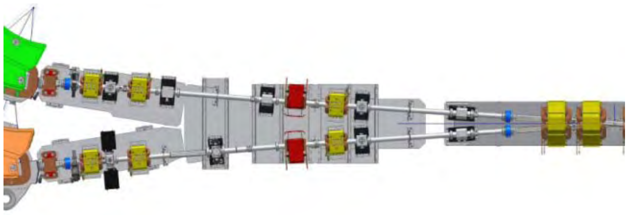

Figure 4: View of the modified IR2 region (half).

Figure 5: View of the IP2 beam pipe.

NEW Shielded Bellows

In order to keep the beam coupling impedance low, attention has been paid in designing the Y-shaped vacuum chamber as above described, but also the number of bellows has been reduced to the minimum necessary to compensate the thermal strain and mechanical misalignment. In each crossing region only 4 bellows per beam have been used [3]. The technology of copper-beryllium strips has been adopted minimizing the cost and maximizing the shielding performance. The working axial stroke is ±7 mm and the radial offset ±3 mm. See figure 6 where a section view of the bellows is shown.

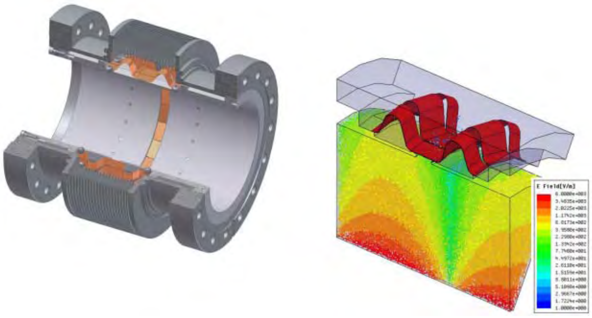

Figure 6: Copper-Beryllium Strip Shielded Bellows.

NEW Fast Injection Kickers

The design of the new kickers [4] is based on a tapered strip with rectangular vacuum chamber cross section, see figure 7, in order to simultaneously:

- improve the deflecting field quality obtaining a uniform horizontal deflection as a function of the transverse coordinate
- reduce the beam coupling impedance by means of the tapered transition between the beam pipe and the kicker structure
- have a uniform beam pipe cross section between the dipole region and the kickers region. This also reduces the total beam coupling impedance of the machine
- obtain a better matching between the generator and the kicker structure at high frequency. This can avoid multiple reflections of the deflecting pulse in the kicker structure that can perturb the stored bunches. Moreover it can allow extracting all the power released to the HOM of the structure by the beam

The 50kV feed-through has been tested successfully and the delivery of the first one is expected by the end of June.

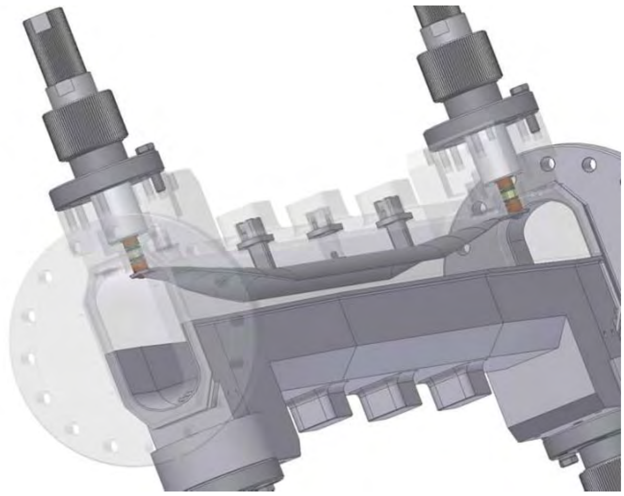

Figure 7: Mechanical drawing of the new fast kicker.

SIDDHARTA SETUP

The new IP1 for the SIDDHARTA experiment, compatible with the large crossing angle and crab waist option [5], is represented in figure 8. The experimental detector is visible in the top side and the two calorimeters to measure the machine luminosity from Bhabha events. The machine luminosity monitor is actually composed by three different devices: small angle Bhabha tile calorimeter composed by 20 sectors (30 degrees each) made of alternating lead and scintillating tiles, covering a vertical acceptance between 17.5 and 27 degrees; a GEM tracker placed in front of the tile calorimeters allowing a redundant measurements of Bhabha events to prevent background; a single bremsstrahlung gamma detector [6].

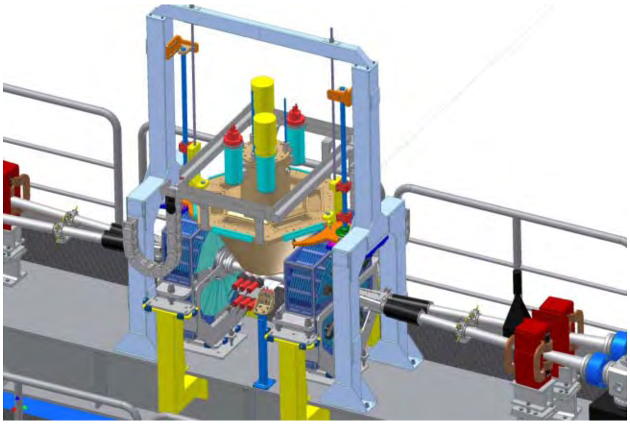

Figure 8: IP1 with SIDDHARTA installed.

CONCLUSIONS

The DAΦNE upgrade design compatible with the large crossing angle and crab waist option has been completed. All new components are under construction and the decommissioning of the old DAΦNE IRs started on mid June. New IRs components installation will start in few weeks. We expect to commission the machine by the end of October and give data to the SIDDHARTA experiment by the end of 2007. The compatibility of the DAΦNE upgrade with the KLOE and FINUDA detectors has also been foreseen.

REFERENCES

[1] M. Biagini et al., “DAΦNE Phi-Factory Upgrade for Siddharta Run”, this conference, MOOBKI02

[2] P. Raimondi, “Status of SuperB effort”, 2^{nd} SuperB workshop, LNF, Frascati, March 2006.

[3] F. Marcellini, “Design and Electromagnetic analysis of the new DAΦNE interaction region”, this conference, FRPMN028.

[4] D. Alesini et al, “DAΦNE tec. Note, G-59, 2006.

[5] SIDDHARTA call, EPJ A31, (2007) 537-539.

[6] G. Mazzitelli, et al., Nucl. Instr. and Meth. A 486 (2002) 568.

BEAM-BEAM SIMULATIONS FOR PARTICLE FACTORIES WITH CRABBED WAIST

P. Raimondi, M. Zobov, LNF-INFN, Frascati, Italy
D. Shatilov, BINP, Novosibirsk, Russia

Abstract

The recently proposed “crabbed waist” scheme for beam-beam collisions can substantially increase luminosity since it combines several potentially advantageous ideas. Large crossing angle together with small horizontal beam size allow having very small beta-functions at the interaction point (IP) and ordinary bunch length without incurring in the "hourglass" effect. The other main feature of such a collision scheme is the "crabbed waist" transformation, which is realized by two sextupoles placed in proper betatron phases around the IP. Such a transformation can strongly suppress the beam-beam betatron resonances induced in collisions with large Piwinski angle, thus providing significant luminosity increase and opening much more room for choices of the working point. In this paper we present the results of beam-beam simulations performed in order to optimize the parameters of two currently proposed projects with the crabbed waist: the DAΦNE upgrade and the Super B-factory project.

INTRODUCTION

In high luminosity colliders with standard collision schemes the key requirements to increase the luminosity are: the very small vertical beta function β_y at the interaction point (IP); the high beam intensity I; the small vertical emittance ε_y and large horizontal beam size σ_x and horizontal emittance ε_x required to minimize beam-beam effects. However, β_y can not be much smaller than the bunch length σ_z without incurring in the “hour-glass” effect. It is, unfortunately, very difficult to shorten the bunch in a high current ring without exciting instabilities. In turn, the beam current increase may result in high beam power losses, beam instabilities and a remarkable enhancement of the wall-plug power. These problems can be overcome with the recently proposed Crabbed Waist (CW) scheme of beam-beam collisions [1] where a substantial luminosity increase can be achieved without bunch length reduction and with moderate beam currents.

These advantages have triggered several collider projects exploiting the CW collision potential. In particular, the upgrade of the Φ-factory DAΦNE is aimed at increasing the collider luminosity up to 10^{33} cm^{-2}s^{-1} [2] to be compared with $1.6\text{x}10^{32}$ cm^{-2}s^{-1} obtained during the last DAΦNE run for the FINUDA experiment [3]. The first crabbed waist collisions are expected already by winter 2007/2008 [4], when the collider will run for the SIDDHARTA experiment. Besides, the physics and the accelerator communities are discussing a new project of a Super B-factory with luminosity as high as 10^{36} cm^{-2}s^{-1} [5], i.e. by about two orders of magnitude higher with respect to that achieved at the existing B-factories at SLAC [6] and KEK [7]. The decision on the Super B-factory construction will depend much on the results of the CW collision tests at DAΦNE.

In the following we briefly discuss the Crabbed Waist collision concept and present results of beam-beam simulations for the DAΦNE upgrade and for the Super B-factory project.

CRABBED WAIST CONCEPT

The Crabbed Waist scheme of beam-beam collisions can substantially increase collider luminosity since it combines several potentially advantageous ideas.

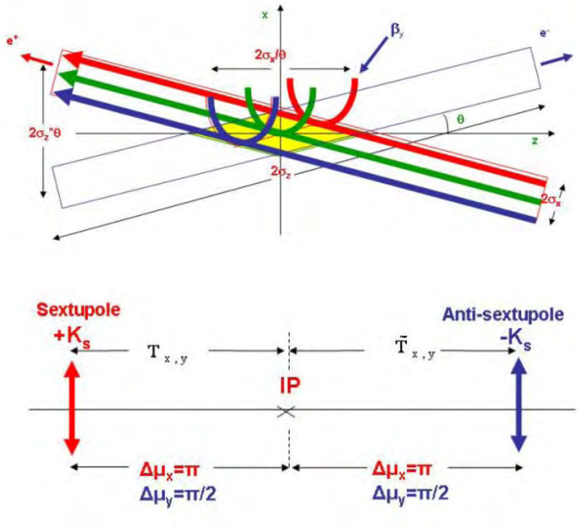

Figure 1: Collision scheme with large Piwinski angle and crabbing sextupoles.

The first one is large Piwinski angle. For collisions under a crossing angle θ the luminosity L and the horizontal ξ_x and vertical ξ_y tune shifts scale as (see, for example, [8]):

$$L \propto \frac{N\xi_y}{\beta_y} \propto \frac{1}{\sqrt{\beta_y}}; \quad \xi_y \propto \frac{N\sqrt{\beta_y}}{\sigma_z\theta}; \quad \xi_x \propto \frac{N}{(\sigma_z\theta)^2}$$

Here the Piwinski angle is defined as:

$$\phi = \frac{\sigma_z}{\sigma_x} tg\left(\frac{\theta}{2}\right) \approx \frac{\sigma_z}{\sigma_x}\frac{\theta}{2}$$

with N being the number of particles per bunch. Here we consider the case of flat beams, small horizontal crossing angle $\theta << 1$ and large Piwinski angle $\phi >> 1$.

In the CW scheme described here, the Piwinski angle is increased by decreasing the horizontal beam size and increasing the crossing angle. In such a case, if it were possible to increase N proportionally to $\sigma_z\theta$, the vertical tune shift ξ_y would remain constant, while the luminosity would grow proportionally to $\sigma_z\theta$.. Moreover, the horizontal tune shift ξ_x drops like $1/\sigma_z\theta$.. However, the most important effect is that the overlap area of the colliding bunches is reduced, as it is proportional to σ_x/θ (see Fig. 1). Then, the vertical beta function β_y can be made comparable to the overlap area size (i.e. much smaller than the bunch length):

$$\beta_y \approx \frac{\sigma_x}{\theta} << \sigma_z$$

We get several advantages in this case:

- Small spot size at the IP, i.e. higher luminosity L.
- Reduction of the vertical tune shift ξ_y.
- Suppression of synchrobetatron resonances [9].

Besides, there are additional advantages in such a collision scheme: there is no need to decrease the bunch length to increase the luminosity as proposed in standard upgrade plans for B- and Φ-factories [10, 11, and 12]. This will certainly helps solving the problems of HOM heating, coherent synchrotron radiation of short bunches, excessive power consumption etc. Moreover, parasitic collisions (PC) become negligible since with higher crossing angle and smaller horizontal beam size the beam separation at the PC is large in terms of σ_x.

However, large Piwinski angle itself introduces new beam-beam resonances which may strongly limit the maximum achievable tune shifts (see [13], for example). At this point the crabbed waist transformation enters the game boosting the luminosity. This takes place mainly due to suppression of betatron (and synchrobetatron) resonances arising (in collisions without CW) through the vertical motion modulation by the horizontal oscillations [14]. The CW vertical beta function rotation is provided by sextupole magnets placed on both sides of the IP in phase with the IP in the horizontal plane and at $\pi/2$ in the vertical one (see Fig. 1). A numerical example of the resonance suppression is shown in Fig. 2.

DAΦNE UPGRADE SIMULATIONS

In order to estimate the achievable luminosity in DAΦNE with the crabbed waist scheme and to investigate distribution tails arising from beam-beam collisions, which may affect the beam lifetime, simulations with the code LIFETRAC [15] have been performed. The beam parameters used for the simulations are summarized in Table 1. For comparison, the parameters used during the last DAΦNE run with the KLOE detector (2005-2006) are also shown.

As discussed above, in order to realize the crabbed waist scheme in DAΦNE, the Piwinski angle $\phi=\theta\sigma_x/\sigma_z$ should be increased and the beam collision area reduced: this will be achieved by increasing the crossing angle θ by a factor 1.5 and reducing the horizontal beam size σ_x. In this scheme the horizontal emittance ε_x will be reduced by a factor 1.5, and the horizontal beta function β_x lowered from 1.5 to 0.2 m. Since the beam collision length decreases proportionally to σ_x/θ, the vertical beta function β_y can be also reduced by a factor 3, from 1.8 cm to 0.6 cm. All other parameters will be similar to those already achieved at DAΦNE.

Table 1: Comparison of beam parameters for KLOE run (2006) and for DAΦNE upgrade for SIDDHARTA run

Parameters	KLOE Run	Siddharta Run
L (cm^{-2} s^{-1})	$1.5x10^{32}$	$>10^{33}$
N_{bunch}	110	110
N_{part}/bunch	$2.65*10^{10}$	$2.65*10^{10}$
I_{bunch} (mA)	13.	13.
ε_x (nm)	300.	200.
ε_y (nm)	1.5	1.
Coupling (%)	0.5	0.5
σ_x (μm)	700.	200.
σ_y (μm)	15 (blow up)	2.4
σ_z (mm)	25.	20
β_x (m)	1.5	0.2
β_y (mm)	18.	6.
θ (mrad)	2x16	2x25

Using the parameters of Table 1 and taking into account the finite crossing angle and the hourglass effect luminosity in excess of $1.0x10^{33}$ $cm^{-2}s^{-1}$ is predicted with the achieved beam currents during the KLOE run, about 6 times higher than the one obtained until now. The only parameter that seems to be critical for a low energy machine is the high vertical tune shift: ξ_y = 0.08, to be compared with the value of 0.03 so far obtained at DAΦNE. In order to check whether these tune shifts (and the luminosity) are achievable we have performed the luminosity tune scans. Figure 2 shows 2D luminosity contour plots in the tune plane for the crabbed waist collisions with the crabbing sextupoles on (left) and off (right), for comparison.

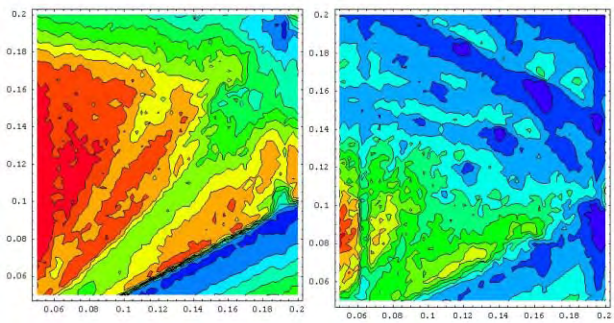

Figure 2: Luminosity tune scan (ν_x and ν_y from 0.05 to 0.20). W sextupoles on (left), CW sextupoles off (right).

"Geographic map" colors are used to produce the plots: the brighter red colors correspond to higher luminosities (mountains), while the blue colors are used for the lowest ones (rivers and oceans). For each plot 10 contour lines between the maximum and minimum luminosities are drawn. Comparing the two plots in Fig. 2 one can see that the good luminosity region with crabbing sextupoles on is much wider than with sextupoles off since many more betatron resonances arise without CW. The absolute luminosity values are higher in the crabbed waist collisions: a peak luminosity of 2.97×10^{33} cm^{-2} s^{-1} is foreseen against $L_{max} = 1.74 \times 10^{33}$ cm^{-2}s^{-1} in the case without CW. It should be noted that the worst luminosity value obtained with CW (2.5×10^{32} cm^{-2}s^{-1}) is still higher than the present luminosity record at DAΦNE. Without CW the lowest luminosity value drops by an order of magnitude, down to $L_{min} = 2.78 \times 10^{31}$ cm^{-2}s^{-1}.

SUPERB BEAM-BEAM SIMULATIONS

Beam-beam studies for SuperB started with a beam parameters set similar to that of the ILC damping ring (Table 2). Numerical simulations with LIFETRAC have shown that the design luminosity of 10^{36} cm^{-2}s^{-1} is achieved already with $2\text{-}2.5 \times 10^{10}$ particles per bunch. According to the simulations, for this bunch population the beam-beam tune shift is well below the maximum achievable value. Indeed, as one can see in Fig.3, the luminosity grows quadratically with the bunch intensity till about 7.5×10^{10} particles per bunch. We have used this safety margin to significantly relax and optimize many critical parameters, including damping time, crossing angle, number of bunches, bunch length, bunch currents, emittances, beta functions and coupling, while maintaining the design luminosity of 10^{36} cm^{-2}s^{-1}. The optimized set of beam parameters is shown in the second column of Table 2.

Table 2: Parameters for early ILC-like design and current SuperB design. For the SuperB, the first entry is for LER and the bracketed numbers are for HER

Parameters	ILC-like	SuperB
ε_x (nm-rad)	0.8	1.6
ε_y (pm-rad)	2	4
β_x (mm)	9	20
β_y (mm)	0.08	0.30
σ_x (μm)	2.67	5.66
σ_y (nm)	12.6	35
σ_z (mm)	6	6
σ_e ($\times 10^{-4}$)	10	8.4 (9.0)
θ (mrad)	2x25	2x17
N_{part}/bunch ($\times 10^{10}$)	2.5	6.2 (3.5)
N_{bunch}	6000	1733
Circumference (m)	3000	2250
Damping time τ_s (ms)	10	16
RF frequency (MHz)	600	476

In order to define how large is the “safe” area with the design luminosity, a luminosity tune scan has been performed for tunes above the half integers, which is typical for the operating B-factories. The resulting 2D contour plot is shown in Fig.4. Individual contours differ by 10% in luminosity. The maximum luminosity found inside the scanned area is 1.21×10^{36} cm^{-2}s^{-1}, while the minimum one is as low as 2.25×10^{34} cm^{-2}s^{-1}. We can conclude that the design luminosity can be obtained over a wide tune area. It has also been found numerically that for the best working points the distribution tails growth is negligible.

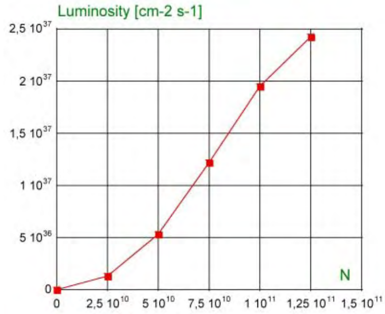

Figure 3: SuperB luminosity versus bunch intensity.

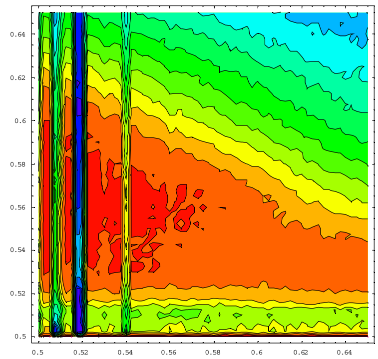

Figure 4: SuperB luminosity tune scan (horizontal axis - ν_x from 0.5 to 0.65; vertical axis – ν_y from 0.5 to 0.65).

CONCLUSIONS

The numerical simulations indicate that by exploiting the crabbed waist scheme of beam-beam collisions the luminosity of the Φ-factory DAΦNE can be pushed beyond 10^{33} cm^{-2}s^{-1} level, while the luminosity of the low emittance Super B-factory can be as high as 10^{36} cm^{-2}s^{-1}.

REFERENCES

[1] P. Raimondi, 2nd SuperB Workshop, Frascati, 2006.
[2] D. Alesini et al., LNF-06/33 (IR), 2006.
[3] C. Milardi et al., TUPAN033, this conference.
[4] M. Biagini et al., MOOBKI02, this conference.
[5] SuperB CDR, INFN/AE-07/2, SLAC-R-856, 2007.
[6] J. Seeman et al., EPAC06, p. 643.
[7] Y. Funakoshi et al., PAC05, p. 1045.
[8] D. Shatilov and M. Zobov, ICFA BDN 37, 99 (2005).
[9] D. Pestrikov, Nucl. Instrum. Meth. A336, 427 (1993).
[10] J. Seeman, PAC05, p. 2333.
[11] H. Koiso, PAC05, p. 64.
[12] DANAE Letter of Intent, see http://www.lnf.infn.it.
[13] K. Ohmi et al., PRSTAB 7, 104401 (2004).
[14] P. Raimondi et al., e-Print:physics/0702033, 2007.
[15] D. Shatilov, Particle Accelerators 52, 65 (1996).

BEAM-BEAM EFFECTS IN CRAB CROSSING AND CRAB WAIST SCHEMES

K. Ohmi[1], M. Biagini[2], Y. Funakoshi[1], P. Raimondi[2] and M. Zobov[2] *
[1]KEK, Tsukuba, Japan
[2]INFN, Frascati, Italy

Abstract

To boost up the luminosity performance in B factories, crab crossing and crab waist schemes are proposed. The crab crossing scheme compensates crossing angle, while the crab waist scheme compensates nonlinear tems induced by crossing angle with sextupole magnets. We discuss which nonlinear terms in the beam-beam map are enhanced by the crossing angle and which terms are compensated by the crab waist sextupole.

INTRODUCTION

We discuss the transfer map of the beam-beam interaction with or without crossing angle. Crab crossing and crab waist schemes have been proposed to improve the beam-beam performance for a finite crossing angle. The crab cavity realizes the collision without crossing angle effectively [1], while the crab waist scheme controls the vertical waist position along x so as to match the longitudinal axis of colliding beam [2]. The crab cavity or sextupole magnets are used for the crab crossing or the crab waist scheme, respectively. The transfer map represented by the Taylar expansion is obtained for the collision with or without crossing angle in this paper. The transfer map with applying the crab waist sextpoles is also obtained. We study which nonlinear terms are varied for the crossing angle, and how the nonlinear terms behave for the crab waist sextpole.

TREATMENT OF THE BEAM-BEAM INTERACTION

The Beam-beam interaction is expressed by a transfer map at the collision point as follows,

$$\boldsymbol{x}(+0) = S\exp\left[-:\int_{-\Delta}^{\Delta} V_0^{-1}(s) H_{bb} V_0(s) ds: \right] \boldsymbol{x}(-0), \tag{1}$$

where S means s ordered product and $\pm\Delta$ is the interaction region of the two beams. [1] V_0 is the transfer map in the drift space,

$$\begin{aligned} V_0(s) &\equiv V_0(s,0) = S\exp\left[-:\int_0^s H_0 ds:\right] \\ &= \exp\left[-:\frac{p_x^2+p_y^2}{2}s:\right], \end{aligned} \tag{2}$$

where $p_{x(y),\pm}$ is the momentum of positrons/electrons. Note that $:p_x:x = [p_x, x] = -1$ and $:p_x:x = 0$, where [ ] is the Poisson bracket. The drift map V_0 can be replaced by the map in the solenoid magnet as the need arises. H_{bb} is a term which represents the beam-beam interaction. The relativistic beam induces an electro-magnetic field in the transverse plane. The field can be expressed by a two-dimensional static potential. The other beam experiences the electro-magnetic field. We use the weak-strong model for the beam-beam interaction: i.e., the Hamiltonian H_{bb} is expressed by a static potential as $H_{bb} = \phi(\boldsymbol{x})$.

For a Gaussian beam, the transfer map for ϕ as a function of s [3],

$$\begin{aligned} &exp(-:\phi_\pm(x,y,z;s):)(p_y+ip_x) \\ &= \frac{N_\pm r_e}{\gamma}\sqrt{\frac{2\pi}{\sigma_x^2-\sigma_y^2}}\left[w\left(\frac{x+iy}{\sqrt{2(\sigma_x^2-\sigma_y^2)}}\right)\right. \\ &\left. -\exp\left(-\frac{x^2}{2\sigma_x^2}-\frac{y^2}{2\sigma_y^2}\right) w\left(\frac{\frac{\sigma_y}{\sigma_x}x+\frac{\sigma_x}{\sigma_y}y}{\sqrt{2(\sigma_x^2-\sigma_y^2)}}\right)\right] \end{aligned} \tag{3}$$

Since ϕ is also a function of z, a kick for p_z [4] arises. The beam envelope matrix is deformed due to the beam-beam interaction at each integration step. For an arbitrary s in an integration step, the rms beam sizes or more generally beam envelope matrix is transferred by

$$\langle \boldsymbol{x}(s')\boldsymbol{x}^t(s')\rangle = V_0(s',s)\langle \boldsymbol{x}(s)\boldsymbol{x}^t(s)\rangle V_0^t(s',s), \tag{4}$$

where $V_0(s',s)$ is the transfer matrix for s to s'.

The complex error function is expanded by Tayler polynomial as

$$w(z;\sigma_x,\sigma_y) = e^{-z^2}(1-erf(-iz)) \tag{5}$$

$$erf(z+z_0) = erf(z_0) + \frac{2}{\sqrt{\pi}n!}\sum_{n=1}(-1)^{n-1}H_{n-1}e^{-z_0^2}z^n \tag{6}$$

where $H_n(z)$ is the Hermite polynomial, and $z = x+iy$.

The coefficient of the polynomial during the whole interaction 1 is integrated along z, with the result that Taylar expansion of the beam-beam map is obtained.

The crossing angle is approximately represented by a transformation before and after the beam-beam interaction,

$$exp(\mp:\theta p_x z:)(x,p_z) = (x+\pm\theta z, p_z \mp \theta x). \tag{7}$$

[1] S ordered product is the same concept as T ordered product popularly used.

The crab cavity gives the same transformation as Eq.(7). The transformations of Eq.(7) and crab cavity can be an approximately identical transformation by choosing the voltage as

$$V = \frac{cE\tan\theta}{\omega_{RF}\sqrt{\beta_{x,crab}\beta_x^*}}. \tag{8}$$

where ω_{RF} is frequency of the crab cavity.

The map is factorized as [5]

$$\exp(-:F_2:)\exp(-:F_{\leq 3}:), \tag{9}$$

where $\exp(-:F_2:)$ and $\exp(-:F_{\geq 3}:)$ are the linear and nonlinear maps, respectively. The linear map, which is represented by a matrix transformation, includes the tune shift of the beam-beam interaction. The nonlinear map $F_{\geq 3}$ is a polynominal higher than 3-rd order for dynamical vaiables. The terms contributes resonance, for example $x^n y^m z^k$ term $n\nu_x + m\nu_y + k\nu_s$ =integer.

TRANSFER MAP FOR CROSSING ANGLE AND CRAB WAIST

Low beta option for KEKB is evaluated. The parameters are the energy $E = 3.5$ GeV, the beta functions at collision point $\beta_{x/y/z} = 0.2/0.003/5.7$ m, and the emittances $\varepsilon_{x/y/z} = 1.8 \times 10^{-8} / 1.8 \times 10^{-10} / 2.8 \times 10^{-6}$. The bunch poplation of the interacting beam and the half crossing angle are varied $N = 1 - 10 \times 10^{10}$ and $\theta = 0 - 22$ mrad, respectively. Piwinsky angle, the ratio of the crossing angle and beam aspect ratio in $x - z$ plane, $\theta\sigma_z/\sigma_x = 0 - 1.5$.

Figure 1 shows the coefficients of nonlinear terms of $F_{\geq 3}$. The number with 6 digit "abcdef" is that of $X^a P_X^b Y^c P_Y^d Z^e P_Z^f$, where the varables are normalized by β function: i.e., $X = x/\sqrt{\beta_x}$ and so on. The five lines correspond to the different bunch poplation for the interacting beam, $N_b = 1, 2, 3, 4$, and 5.5×10^{10}. The nominal beam-beam parameter is $\xi = 0.1 N_b/10^{10}$. Plots (a) depict the coefficient of X^4 term, which is one of the dominant term for the head-on collision. The coefficient decreases as increasing the crossing angle. The terms for $X^2 P_X^2$ and P_X^4 is neglisible small compare than the x^4 term, because the beam-beam force is a function of X, but is not that of P_X. These terms give perturbation

$$F_{400} = \frac{a_{400000}}{8} J_x^2 (3 + 4\cos 2\phi_x + \cos 4\phi_x) \tag{10}$$

The three terms of F_{400} give an amplitude dependent tune shift, and contribute 2-nd and 4-th order resonances, respectively. For the present, if we use the tune shift, the resonance width, which characterize its strength Other nonlinear terms give tune shift. In the head-on collision, only symmetric terms, which are even order for x and y, appear in the transfer map. Only a_{400000} in x^4 terms is significant, while all terms a_{004000}, a_{002200} and a_{000400} in y^4 are significant. It is due to that the betatron phase variation is meaningful for the vertical motion ($\beta_y \approx \sigma_z$).

For increasing the crossing angle, asymmetric terms, which are odd order, appear and increase. To compare the values of each coefficient, they have to be normalized by the emittances: i.e., $a_{abcdef}\varepsilon_x^{-(a+b)/2}\varepsilon_y^{-(c+d)/2}\varepsilon_z^{-(e+f)/2}$.

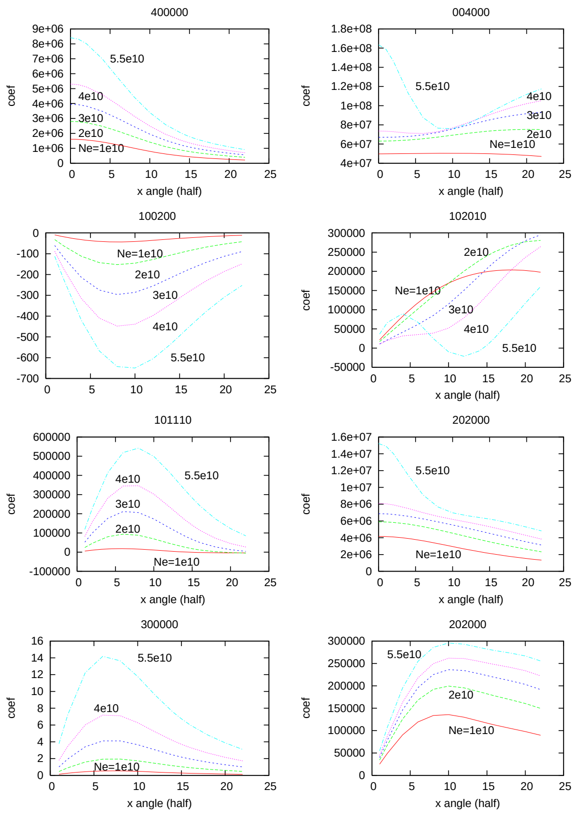

Figure 1: Coefficients of nonlinear terms as functions of the crossing angle. The nonlinear term is printed in each plot.

The crab waist scheme is

$$exp(\mp : \frac{K_w}{2} x p_y^2 :)(p_x, y) = (p_x \pm \frac{K_w}{2} p_y^2, y \mp K_w x p_y) \tag{11}$$

The transformation is realized by putting sextupole magnets an integer or a half integer betatron phase difference in horizontal, and a qurter integer (1/4 or 3/4) in vertical. This transformation shifts the waist position of the vertical beta function as $K_w x$. The essentials of the crab waist scheme is to choose $K_w \approx 1/2\theta$.

Figure 2 shows the coefficients as functions of the strength of the crab waist sextupole magnets. The terms of X^4, X^3 and $X^3 Z$ are not affected by the crab waist sextupole, while the coupling terms XY^2 and $XY^2 Z$ clearly depend on the sextupole strength.

CONCLUSION

Coefficient of the nonlinear map for the beam-beam ineteraction was obtained with or without crossing angle.

Odd order terms for x and y are appear and enhanced by the crossing angle. These terms seem to degrade the lumi-

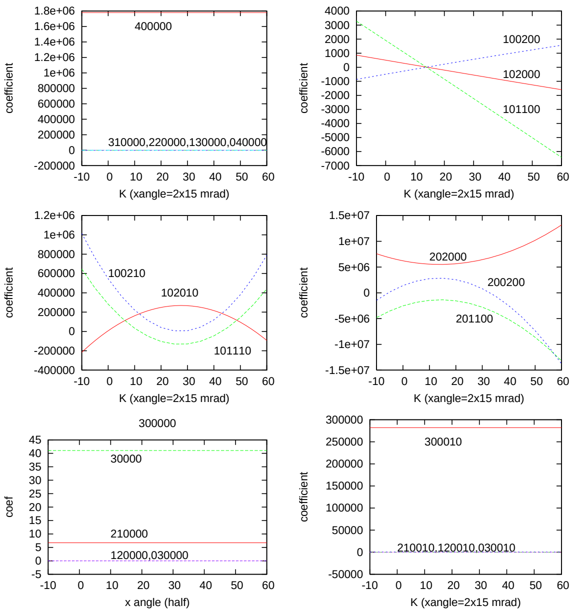

Figure 2: Coefficients of nonlinear terms as functions of the strength of the sextpole strengths.

nosity performance for the collision with a finite crossing angle.

Behaviors of the nonlinear terms are investigated for the strength of the crab waist sextupole. The crab waist sextupoles cancel the nonlinear terms related to xy^2 as is expected, while remain the terms related to the synchrobeta resonances.

REFERENCES

[1] K. Oide and K. Yokoya, Phys. Rev. A**40**, 315 (1989).

[2] P. Raimondi, D. Shatilov and M. Zobov, LNF-07-003-IR (2007).

[3] M. Bassetti and G. Erskine, CERN-ISR TH/80-06 (1980).

[4] K. Hirata, H. Moshammer and F. Ruggiero, Particle Accelerators, **40**, 205 (1993).

[5] A. Dragt and J. Finn, J. Math. Phys. **17**, 2215 (1976).

[6] K. Ohmi et. al., Phys. Rev. ST-AB, **7** 104401 (2004).

LOW EMITTANCE LATTICE AND FINAL FOCUS DESIGN FOR A SuperB PROJECT

Y. Ohnishi, KEK, Ibaraki, M. E. Biagini, P. Raimondi, INFN/LNF, Frascati(Roma),
A. Wolski, Liverpool University, Liverpool, Y. Cai, J. Seeman, M. K. Sullivan,
U. Wienands, SLAC, Menlo Park, California

Abstract

Very low emittances and small beta functions at the interaction point(IP) are needed to achieve the design luminosity of 10^{36} cm^{-2} s^{-1} for a SuperB project. Two rings of 4 and 7 GeV have been designed with the same emittances and damping times. A new Final Focus section has also been designed to strongly squeeze the colliding beams both in the horizontal and the vertical plane at IP, while providing local correction of the large chromaticity and exploiting the large crossing angle and *crab waist* concepts. Lattice features and chromaticity correction schemes will be discussed here. Dynamic apertures, with damping wigglers similar to those of ILC, will also be presented.

INTRODUCTION

Recently, an alternative scheme to achieve an extremely higher luminosity was proposed for the SuperB project [1]. The SuperB project is a next generation B-Factory for pursuing 10^{36} cm^{-2}s^{-1} luminosity, which is the subsequent collider of PEP-II and KEKB[2]. The strategy is to have an ultra-low emittance beams and ultra-low beta functions at the IP with a large Piwinski angle. The bene t of this scheme is that the overlap region of colliding beams becomes $\sigma_x/2\phi_x$, while keeping the bunch length relatively long. Consequently, the vertical beta function at IP can be squeezed up to a level of 100 μm in principle, and together with the *crab waist* scheme [3], the luminosity can be much improved with respect to a conventional colliding scheme.

LATTICE DESIGN

The High Energy Ring (HER) has 6 arcs and 6 straight sections. Each arc has 12 cells and 250 m long approximately, which connects each straight section. The Final Focus (FF), including the IP, is placed in a straight section, while a magnetic chicane to transport beams across the other ring is placed in the opposite straight section of IP. The wiggler magnets, which control emittances and damping times, and the RF cavities are placed in the other four straight sections. The geometry of the Low Energy Ring (LER) is same as HER. The beam energy of HER is 7 GeV and the circumference is 2.28 km. The horizontal emittance is 0.8 nm. The small emittance is achieved by using two wiggler sections in HER (four in LER) and the arc cells. Each wiggler section is 40 m long approximately with a 0.83 T eld and 40 cm period length. The LER lattice is similar to the HER lattice, while the beam energy of LER is 4 GeV. The lattice parameters are shown in Table 1. Figure 1 shows the beta functions and dispersion in the HER.

Table 1: Lattice parameters

	LER	HER
Energy (GeV)	4	7
Circumference (m)	2275	
Emittance (nm)	0.8	
Horizontal beta at IP (mm)	20	
Vertical beta at IP (mm)	0.2	
Bunch length (mm)	6	
Transverse damping time (ms)	25	
Energy spread	1×10^{-3}	
Momentum compaction	1.8×10^{-4}	3×10^{-4}
Synchrotron tune	-0.011	-0.02
Total RF voltage (MV)	6	18

The arc lattice utilizes a kind of theoretical minimum emittance(TME) lattice, which consists of two bending magnets and three quadrupole families(QF, QFB and QD). The arc cell is 23 m long and has a betatron phase advance of π in the horizontal plane and 0.4π in the vertical plane. The intrinsic emittance of the arc cells is 1.46 nm. Chromaticity in the arcs is corrected with three sextupole families (SD1, SD2 and SF). Each sextupole magnet is placed in the immediate vicinity of each quadrupole magnet, where is a large β function to ef ciently correct the chromaticity. The optical functions in the HER arc cell are shown in Fig. 2.

The FF is designed to realize very small β-functions at IP, small geometric aberrations with non-interleaved sextupole pairs, and corrections of the large chromaticity generated in the Interaction Region (IR). The nominal values for the β-functions at IP are 20 mm in the horizontal plane and 200 μm in the vertical plane, with a distance of 30 cm between IP and the rst quadrupole magnet in the FF doublet. Since SuperB is a double-ring collider, the beams in HER and LER collide at IP and are separated with the horizontal crossing angle of 34 mrad. In the FF the same bending magnets as in the arc section are used to make dispersions in the region for chromaticity corrections. All bending magnets have the same sign to reduce the arc length and make the geometry simple. These bending magnets and matching quadrupole magnets make the dispersion zero at IP and localized within IR. The layout of FF is geometrically symmetric. Half of the FF section

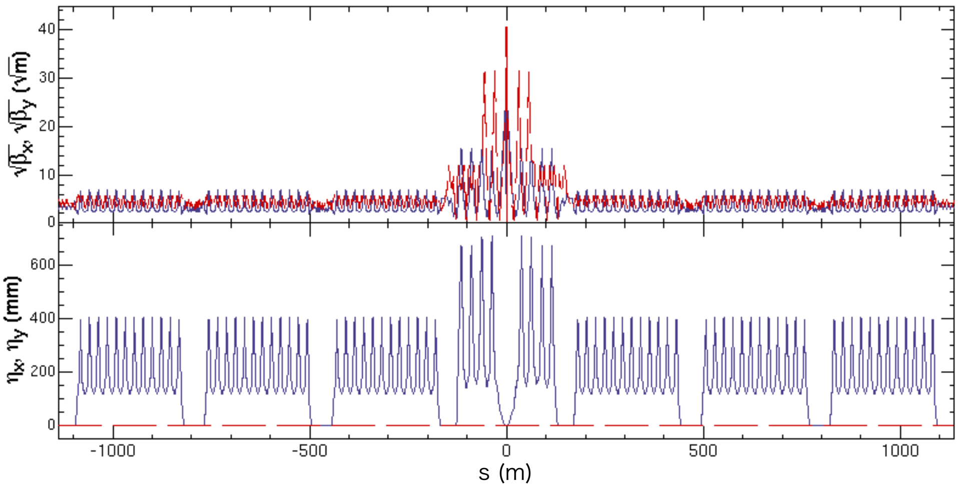

Figure 1: Optical functions, β-functions (upper) and dispersions (lower) in the HER. Solid and dashed lines show those in the horizontal and the vertical plane, respectively.

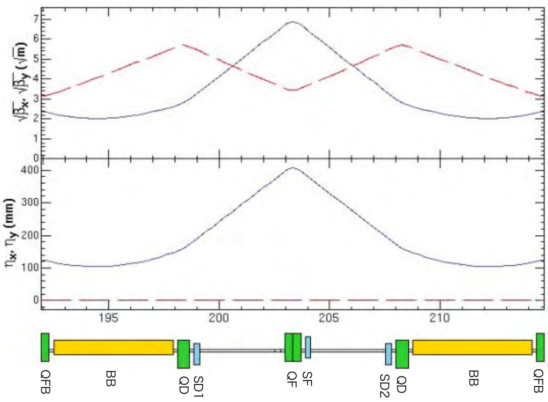

Figure 2: Optical functions, β functions(upper) and dispersions(lower) for the HER arc cell. Solid and dashed lines show those in the horizontal and the vertical plane, respectively.

is shown in Fig. 3. In order to make β-functions at IP very small, a large chromaticity is generated and should be corrected locally as much as possible. A local chromaticity correction is adopted in the FF design. The identical sextupole magnets are connected with a -I' transformation matrix:

$$\begin{pmatrix} -1 & 0 & 0 & 0 \\ m_{21} & -1 & 0 & 0 \\ 0 & 0 & -1 & 0 \\ 0 & 0 & m_{43} & -1 \end{pmatrix} \tag{1}$$

in the local chromaticity correction. The sextupole pairs reduce nonlinearities for each other, while correcting the chromaticity. Therefore, the dynamic aperture for the off-momentum particles can be increased. Two pairs of sextupole magnets for the local chromaticity correction are placed both in the horizontal plane (SFX0 and SFX4) and the vertical plane (SDY0 and SDY4). Additional sextupole magnets, which are IP phase sextupoles (SDM2 and SFM7), are introduced to improve the behavior of off-momentum particles. The location of the IP phase sextupoles is in a minimum β-function for on-momentum particles, while in a maximum β-function spot for off-momentum particles. In SuperB, the *crab waist* collision scheme is adopted to increase the luminosity. In this scheme, the waist position, which is the minimum position of the β-function, is adjusted by a kick from the sextupole magnets to suppress the hourglass effect in the vertical plane. Thus, the particles collide with the other beam at their waist point, and beam-beam interaction and betatron coupling resonances induced by the crossing angle are suppressed. The sextupole magnets (MCRAB, one of two in Fig. 3) for the *crab waist* are located in both sides of the matching section between the FF section and the arc sec-

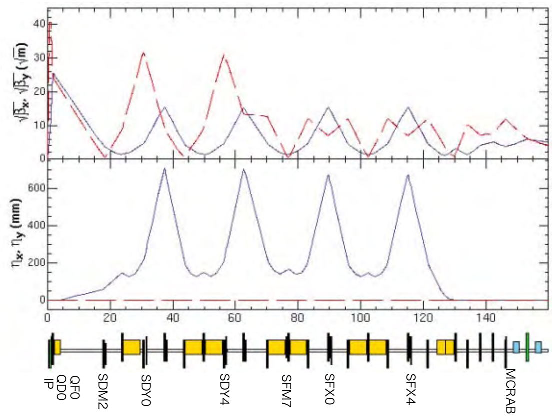

Figure 3: Optical functions, β-functions(upper) and dispersions(lower) for the FF section. Solid and dashed lines show those in the horizontal and the vertical plane, respectively.

tion. The β-functions at the *crab waist* sextupole are 14 m in the horizontal plane and 140 m in the vertical plane, respectively. The betatron phase advances between the sextupole magnet and IP are 6π in the horizontal plane and 5.5π in the vertical plane. The K_2 value of the sextupoles is taken to be 20(or -20) m^{-2}, which is 50 %(75 % for β_y^*=0.3 mm) of the nominal value determined by

$$K_2 = \frac{1}{\tan 2\phi_x \cdot \beta_{y,sext}\,\beta_y^*}\sqrt{\frac{\beta_x^*}{\beta_{x,sext}}}, \qquad (2)$$

where ϕ_x is the half crossing angle.

CHROMATICITY CORRECTION

The betatron tunes for HER have been chosen to be 48.57 in the horizontal plane and 23.60 in the vertical plane. The linear chromaticity is adjusted to be close to zero using three families of the sextupoles in the arc section and six families in FF. Figure 4 shows deviations of the betatron tunes and betatron functions at IP for the off-momentum particles. The betatron tunes and β-functions at IP are corrected within 5 % for the bandwidth of $\pm$1 % momentum deviation. There is a small discrepancy, especially the vertical β-function at IP between sextupoles when the *crab waist* are turned on and off, due to the dispersion for large off-momentum particles generated at the *crab waist* sextupoles. However, the difference between them is negligible concerned with the chromaticity correction.

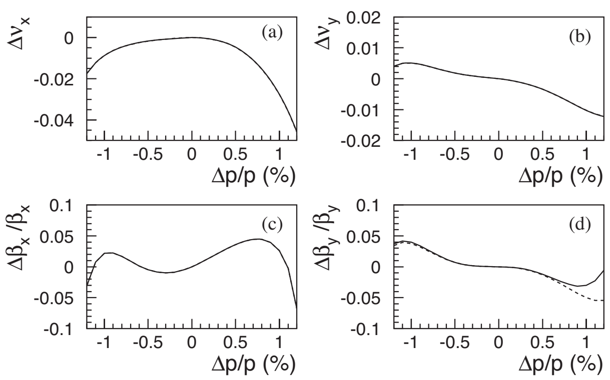

Figure 4: Chromatic effects for the HER ring. Betatron tunes(upper) and β functions(lower) as a function of momentum deviation in the horizontal and the vertical plane. The solid and dashed lines show the case in which the sextupole magnets for the *crab waist* on and off, respectively.

DYNAMIC APERTURE

A dynamic aperture is de ned by requiring stability in 1000 turns with a synchrotron oscillation and without radiation damping, which gives the exactly same result in one transverse damping time with radiation damping. The dynamic aperture is estimated by numerical tracking simulations using SAD [4], which is an integrated code for optics design, particle tracking, and so on. Figure 5 shows the dynamic aperture from the tracking simulations for HER, assuming the ideal lattice. The $2J_x$ and $2J_y$ are Courant-Snyder invariants in the horizontal plane and the vertical plane. The initial vertical amplitude, $2J_y$, is xed to be zero when the horizontal aperture is evaluated, and vice versa.

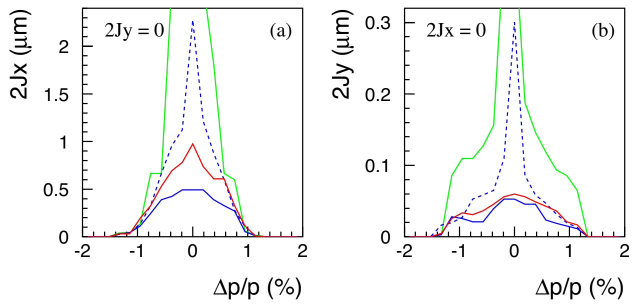

Figure 5: Horizontal aperture (a) and vertical aperture (b) as a function of momentum deviation. Green and blue solid lines show the sextupole magnets for the *crab waist* are turned off and on, respectively. Further octupole corrections are indicated by red solid lines. Blue dashed lines show the case without fringe effects for the *crab waist* on, while octupole corrections off.

CONCLUSION

The lattice design for the very low emittance and the FF of the SuperB have been presented. The large chromaticity generated at IR is corrected by the local chromaticity sextupole correction. The dynamic aperture is signi cantly reduced when the sextupoles for the *crab waist* turned on. If the nonlinear fringe eld (Maxwellian fringe) of the all magnets is turned off, the dynamic aperture is restored by 60 %. Strong quadrupoles in FF, especially, the fringe effect of the FF quadrupole magnets affects the dynamic aperture. The octupole magnets in the immediate vicinity of the FF quadrupoles (QD0 and QF0) improve the dynamic aperture in the horizontal plane by a factor 2 of the case without the octupole optimization. A new version, shorter version of this lattice is being studied at present, with modi cations of the phase advance/cell. From preliminary results it seems that increasing the horizontal phase advance/cell in the regular cells will allow to have a shorter, more e xible ring optics, without using wigglers.

REFERENCES

[1] “SuperB Conceptual Design Report”, INFN/AE-07/2,SLAC-R-856, LAL 07-15, March 2007.

[2] M.K. Sullivan, MOYKI01, this Conference.

[3] P. Raimondi, MOZAKI02, this Conference.

[4] K. Oide, Nucl. Inst. Meth. A 276, 427 (1989).

INTERACTION REGION DESIGN FOR A SUPER-B FACTORY*

M. Sullivan†, J. Seeman, U. Wienands, SLAC, P.O. Box 20450, Stanford, CA 94309, U.S.A
M.E. Biagini, P. Raimondi, INFN/LNF, Frascati (Roma), Italy

Abstract

We present a preliminary design of an interaction region for a Super-B Factory with luminosity of 1×10^{36} cm^{-2} sec^{-1}. The collision has a ±17 mrad crossing angle and the first magnetic element starts 0.3 m from the collision point. We show that synchrotron radiation backgrounds are controlled and are at least as good as the backgrounds calculated for the PEP-II accelerator. How the beams get into and out of a shared beam pipe is illustrated along with the control of relatively high synchrotron radiation power from the outgoing beams. The high luminosity makes radiative bhabha backgrounds significantly higher than that of the present B-Factories and this must be addressed as the design is further improved.

INTRODUCTION

Work toward an asymmetric-energy B factory design with a luminosity of at least 1×10^{36} cm^{-2}s^{-1} has been going on for a couple of years now. Initially, designs looked at ways of increasing the number of bunches, increasing the beam currents (up to 10-20 A) and lowering the β_y^* to achieve the large increase in luminosity [1]. Recently however, a new idea has come forward where one has a "crabbed waist" at the interaction point through the use of a fairly large horizontal crossing angle, very low emittance beams and extremely small β_y^* values in conjunction with modest beam currents (similar to present day B factories) and typical bunch lengths (~10 mm) [2]. The low emittance beams and the modest beam currents are a help in the design of an interaction region (IR) with a small radius detector beam pipe that has acceptable detector backgrounds.

FINAL FOCUS OPTICS

The final focus of the Super-B design calls for a small β_x^* (20 mm) and a very small β_y^* (0.2 mm). These small beta functions require the final focus magnets to be as close to the interaction point (IP) as possible in order to keep the maximum beta values as low as possible and minimize the chromaticity generated in the final focus. Table 1 lists the accelerator parameters that are important for the IR design.

We have adopted a beam-stay-clear (BSC) envelope that is similar to the one used in the PEP-II design [3]. The X value is defined as 15 uncoupled beam sigmas +1 mm for closed orbit distortion (COD). The Y value is defined as 15 fully coupled beam sigmas +1 mm COD.

* work supported by the Department of Energy under contract number DE-AC03-76SF00515.
†sullivan@slac.stanford.edu

Table 1: Accelerator parameters for a Super-B Factory design with L = 1×10^{36} cm^{-2} s^{-1} that influence the IR

	LER		HER
Energy (GeV)	4.0		7.0
Current (A)	3.95		2.7
No. bunches		3466	
Spacing (m)		0.63	
β_x^* (mm)	20		20
β_y^* (mm)	0.2		0.2
Emittance X (nm-rad)	1.6		1.6
Emittance Y (pm-rad)	4		4
Crossing angle (mrad)		34	

QD0

With the above parameters in mind we have positioned the first quadrupole magnet (QD0) to start 0.3 m away from the IP. A collision crossing angle of ±17 mrad separates the beam centers by only 5.1 mm and the two BSC envelopes by only 1.8 mm at 0.3 m away from the IP so the QD0 is a magnet shared by both beams. In order to produce similar final focus beta functions for the different energy beams, we have set the gradient of QD0 to be that required for the high-energy beam (HEB) for a magnet length of 0.75 m. This magnet is then too strong for the low-energy beam (LEB) so we shorten the length of this magnet to 0.46 m to get the correct integrated strength for the LEB. The beams therefore need to be separate enough at 0.76 m from the IP to be able to place a magnet that continues the vertical focusing for the HEB while making a field free region for the LEB. We label this 0.29 m long magnet QD0H. This also means the two beams enter separate beam pipes at this location (0.76 m).

QD0H and QF1

The beam separation at 0.76 m is 31.9 mm for the incoming LEB side and 36.4 mm for the incoming HEB side. The difference is due to the fact that the LEB is easier to bend than the HEB and that the QD0 magnetic axis is parallel to a line bisecting the beam trajectories but is offset so that the incoming beam (either LEB or HEB) is minimally bent by the QD0 field. The BSC envelopes at 0.76 m are about 3 mm for each beam, well inside a beam pipe of 10 mm radius, the same size as the detector beam pipe. We therefore select a beam pipe radius of 10 mm for each separate beam at 0.76 m. We then have 11.9 (31.9-20) and 16.4 (36.4-20) mm of space for two beam pipe walls and a magnet. Using permanent magnet (PM) material with a remnant field of 1.4 T, we can construct a cylinder with an inner radius of 12 mm and an outer radius of 20 mm (8 mm thick) that has enough strength to satisfy the HEB gradient requirements. The PM blocks have a very low residual field beyond the outer radius of the material and hence make a good field-free region for the LEB. This leaves enough room for a 2 mm thick beam pipe for each beam at this narrow location. Beyond 0.76 m from the IP the distance between the beams grows rapidly and it is relatively easy to accommodate separate beam pipes and magnets for the two beams.

The next quadrupole magnet (QF1) from the IP is an x focusing magnet that is 0.4 m long and is located between 1.45 m and 1.85 m from the IP. There are two separate magnets at this location, one for each beam and beyond QF1 the beam lines for both beams have the same layout with counterpart magnets at each z location. Figs. 1 and 2 show this IR layout.

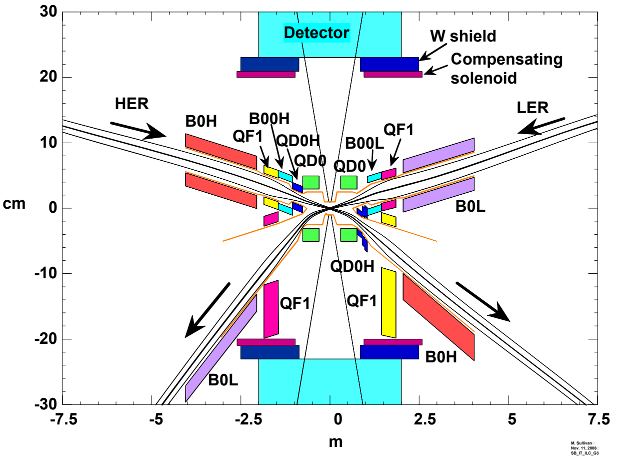

Figure 1: Layout of the Super B interaction region. Note the expanded vertical scale.

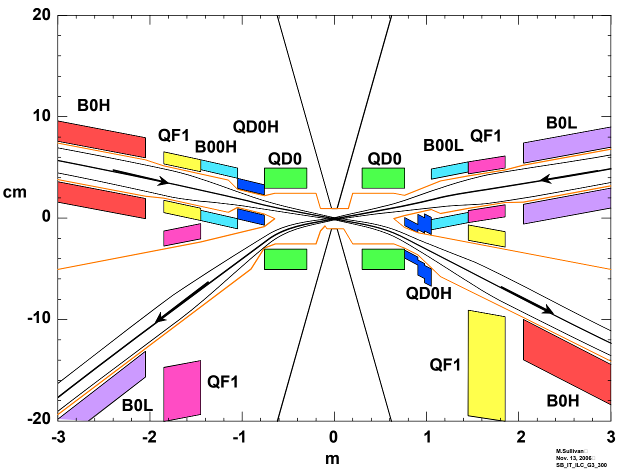

Figure 2: Closer view of the final focus magnets. The dark blue blocks are the QD0H permanent magnets. The design is different on each side of the IP. The incoming side has a narrow beam aperture and hence can be designed as a cylinder. The outgoing beam line for the HER has to accommodate the outgoing synchrotron radiation fan as well as the outgoing HER beam.

SYNCHROTRON RADIATION BACKGROUNDS

The detector beam pipe for the Super-B design has a 10 mm radius. This small radius means that the detector is more susceptible to synchrotron radiation (SR) photons from the incoming beams. This is especially true if the magnetic axis of the shared QD0 magnet is centered between the beam trajectories. In this case, the incoming beams are bent by the QD0 magnetic field and generate photons that cannot be shielded from the detector beam pipe unless the beam pipe radius is increased. Increasing the radius of the beam pipe effectively decreases the luminosity since the detector efficiency is decreased.

As mentioned above, we have moved the axes of the QD0 magnets so that they are much closer to the incoming beam trajectories thereby eliminating the QD0 magnet as a source of SR background for the detector.

The next most important background source after the QD0 is the focusing radiation coming from the incoming beams as they travel through the QF1 magnets. This radiation comes from the horizontal over-focusing of the beam and because of this over-focusing the angles of the photon trajectories are steeper making it more difficult to shield the detector beam pipe from this source. In order to control this background rate we introduce a small bending magnet between the QD0 and QF1 magnets on the incoming beam lines only. These bending magnets redirect the focusing radiation from the QF1 magnets away from the central Be beam pipe.

In summary, there are no photons coming from the incoming beams that are directly incident on the detector beam pipe. The remaining incoming photons that are incident on the surfaces near the detector beam pipe have been simulated with a program that uses EGS [4] to model the backscattering rate from these surfaces. An estimate of the solid angle acceptance for the detector beam pipe from these surfaces indicates that the rate of photons incident on the detector beam pipe from these secondary surfaces is comparable to the calculated background rate for the PEP-II interaction region. Figure 3 shows the photon-rate/beam-crossing on the nearby surfaces for photons over 10 keV.

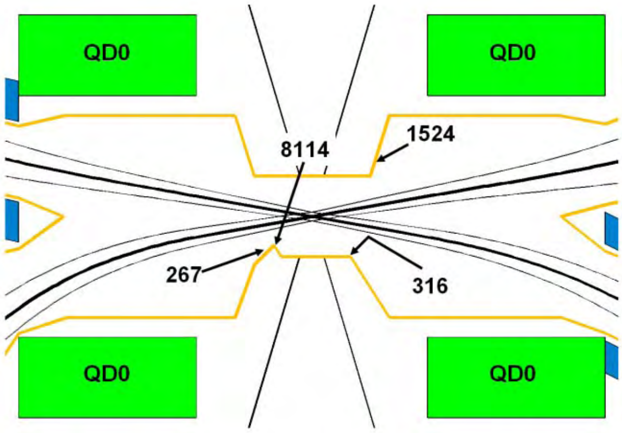

Figure 3: The mask tip is 3 mm in from the 10 mm radius pipe. This is the only surface that is inside the detector beam pipe so the overall masking design is quite open and has no obvious cavities for trapping higher-order-mode (HOM) power.

OUTGOING SR FANS

The exiting beams are strongly bent as they travel through the QD0 magnets. This is because the outgoing beams exit the shared QD0 magnet far off-axis. The outgoing LEB generates 88 kW of SR power in QD0 and the outgoing HEB generates 141 kW. The beam pipe for the outgoing beams is designed so that these high power fans do not strike any nearby surfaces and are absorbed on beam pipe surfaces that are meters away from the collision point. Figure 4 show the SR fans generated by the HEB and the LEB.

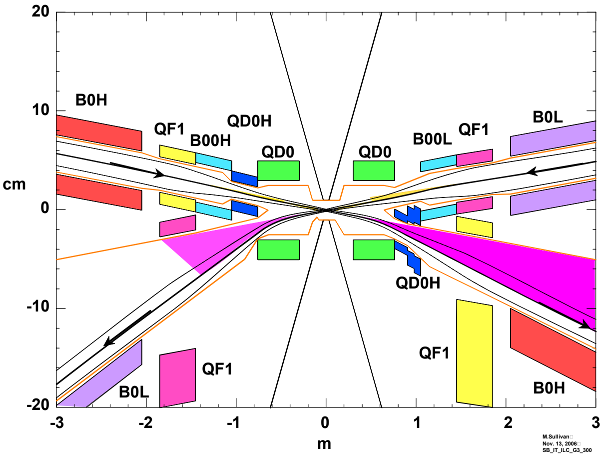

Figure 4: Interaction region layout with the outgoing high-power synchrotron radiation fans displayed. The outgoing beam pipes are shaped so that the radiation does not hit the pipe in the first few meters from the IP.

The larger beam pipes on the outgoing beam lines mean that the magnets on these lines must have large apertures. One possible design for the outgoing QF1 magnet is one similar to the horizontally split quadrupole magnets used in SPEAR 3 [5]. These magnets have no material in the horizontal plane and this allows the horizontal fan to pass through the magnet without striking the beam pipe. The outgoing B0 magnets can be C-shaped bend magnets. The two designs suggested above imply iron core magnets which would need to be shielded from the detector magnetic field. We would accomplish this by inserting a compensating super-conducting solenoid around both beam lines and into the detector far enough so that at least the QF1 and B0 magnets can be iron core magnets. Figure 1 shows a suggested layout of the compensating solenoid.

RADIATIVE BHABHAS

The strong bending of the outgoing beams also produces backgrounds for the detector by over-bending the beam particles that have undergone a radiative bhabha interaction at the IP. The gamma produced by this reaction and the reduced energy beam particle both can generate backgrounds in the detector if these particles strike beam pipes close enough to the detector. The gammas are generally produced in the direction of the beam and hence exit the IP along the crossing angle trajectories. In the case here the outgoing gammas are along the edge of the strong outgoing SR fans and hence do not intersect the beam pipe until the fans are several meters away from the collision point as mentioned above. However, the outgoing off-energy beam particles can be a source of background for the detector. Figure 5 shows a drawing of the trajectories of some of the radiative bhabha beam particles from the LEB and the HEB.

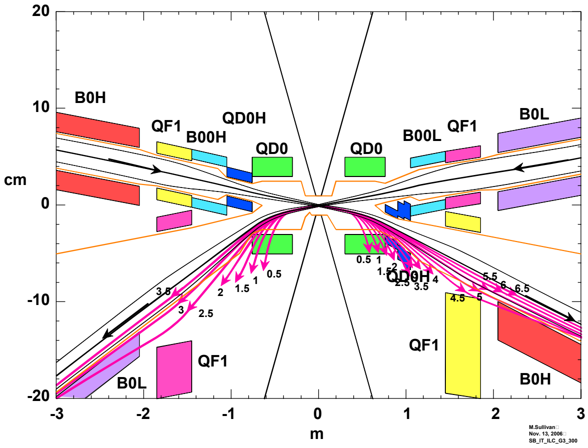

Figure 5: Trajectories of selected energies for beam particles from radiative bhabha interactions. The small number near the trajectory is the energy in GeV.

SUMMARY

We have constructed an interaction region for a Super-B factory design. The design incorporates the “crab waist” scheme for making high luminosity collisions and demonstrates that synchrotron radiation backgrounds can be controlled and are comparable to the present PEP-II accelerator. The design has strong bending of the outgoing beams through the shared QD0 magnet and this could benefit from further optimization. The strong bending makes powerful SR fans and locally bends out the beam particles from radiative bhabha interactions making backgrounds in the detector. Although the bending is comparable to that of the PEP-II IR design the Super-B design calls for much lower emittance beams and this bending might contribute to emittance growth.

REFERENCES

[1] M. Sullivan, *et. al.*, “A Preliminary Interaction Region Design for a Super B-Factory”, PAC’05, Knoxville, Tennessee, May 2005, p. 2077.

[2] P. Raimondi, “New Developments for Super B Factories”, MOZAKI02, These proceedings.

[3] “PEP-II an Asymmetric *B* Factory”, Conceptual Design Report, CALT-68-1869, LBL-PUB-5379, SLAC-418, UCRL-ID-114055, UC-IIRPA-93-01, June 1993.

[4] W. R. Nelson, H. Hirayama, D. W. O. Rogers, “The Egs4 Code System”, SLAC-R-0265, Dec 1985.

[5] “SPEAR 3 Design Report”, SLAC-R-609, Nov 2002.

OPTIMIZATION OF CHROMATIC OPTICS NEAR THE HALF INTEGER IN PEP-II*

G. Yocky#, Y. Cai, F-J. Decker, Y. Nosochkov, U. Wienands, SLAC, Menlo Park, CA 94025, USA; P. Raimondi, INFN/LNF, Frascati, Italy

Abstract

The PEP-II collider has benefited greatly from the correction of the chromatic functions. By optimizing sextupole family strengths, it is possible to correct the non-linear chromaticity, the chromatic beta, and the second order dispersion in both the LER and HER. Having implemented some of these corrections, luminosity was improved in PEP-II by almost 10%.

INTRODUCTION

Whilst investigating parameter space for potential luminosity gains and prospective difficulties in tune-space during PEP-II Run 5, the beta-function response to energy change was measured in both the HER and LER. Initially done as an investigation into large chromatic beta functions in the RF accelerating cavities in the straights as a source of strong synchro-betatron coupling, a method has been developed to address the global chromatic betatron functions as well as the interaction point bandwidth.

In order to measure the chromatic beta function, the SLAC Control Program (SCP) built-in phase-advance measurement package is used to measure the beta functions at several energies. The data then needs to be shipped to another computer for offline analysis in the Matlab programming environment.

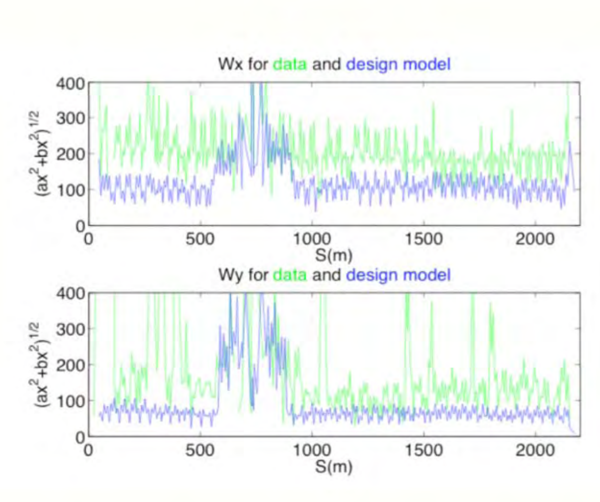

Figure 1: HER chromatic beta function in both the horizontal and the vertical planes for measured (green) and design (blue) lattices.

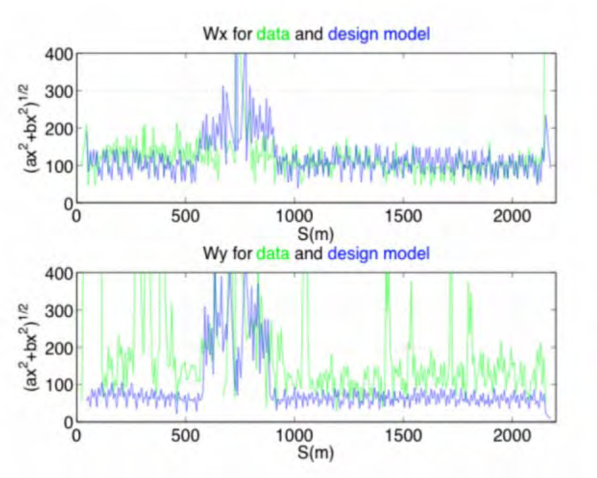

Figure 2: HER chromatic beta function in both the horizontal and the vertical planes for measured (green) and design (blue) lattices following correction.

CHROMATIC FUNCTIONS

Measurement of the W function

The chromatic beta function, or W function, can be calculated from the beta functions provided by the SCP phase advance package and the alphas which require some estimation. The W function is defined thusly:

$$W_x = \sqrt{a_x^2 + b_x^2}\ \text{, where}$$

$$a_x = \frac{\dfrac{\delta\beta_x}{\beta_x}}{\dfrac{\delta p}{p}}, b_x = \frac{\delta\alpha_x}{\dfrac{\delta p}{p}} - \alpha_x * \frac{\dfrac{\delta\beta_x}{\beta_x}}{\dfrac{\delta p}{p}}$$

and similarly for the vertical plane. Since the SCP online packages do not provide for a direct measurement of alpha, the "pseudo-alpha" is calculated:

$$\alpha = -\frac{1}{2} * \frac{\beta_{n+1} - \beta_{n-1}}{Z_{n+1} - Z_{n-1}}$$

where Z is the location in meters and β is the beta function at the BPM.

*Work supported by DOE contract DE-AC02-76SF00515
#yocky@slac.stanford.edu

Measurement of non-linear dispersion

In addition to measuring the beta functions as a function of the ring energy, we took several measurements of the non-linear dispersion. That is, at several off-energy points, a BPM orbit is saved and the dispersion calculated not just about the nominal running point. The MAD modelling program does give an expectation for how the non-linear dispersion should behave, and tests were run, however no fixes have been implemented as of this writing.

CHROMATIC FIXES

Chromatic Beta Optimization

During the latter part of PEP-II run 5, the first measurements of the W functions were taken. What we saw was that the HER horizontal W function was highly un-optimized (Fig. 1). A hybrid MAD/Matlab program was developed to fix the chromatic response of the beta functions. Since the design lattice is used as a starting point for the optimization due to limitation of properly representing the PEP-II lattices in MAD, there is some uncertainty when implementing these solutions. However, given that only sextupoles are varied for the fixes, hysteresis problems are minimized.

In practice, this amounted to wisely choosing local sextupole families to vary that would both flatten globally the W function and locally narrow the IP bandwidth so that off energy particles would minimally affect the spot size. Constraints on the system, however, make this a non-trivial problem. The beta function and dispersion in the ring must not be disturbed and the tune vs. energy response must either be made less sensitive or untouched.

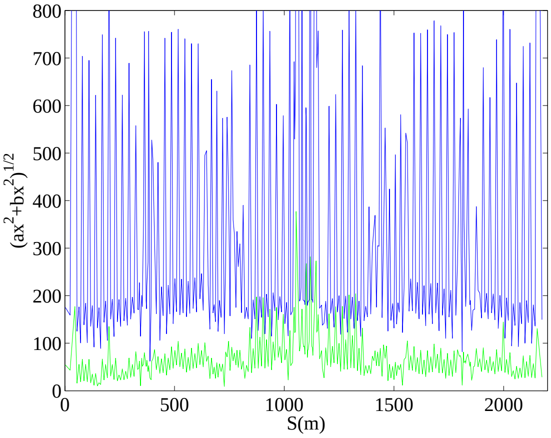

Figure 3: LER horizontal W function for the PSK lattice (blue) and optimized PSK lattice (green).

HER Fix

The first round of fix is seen in Figure 2. The HER horizontal W function has been corrected and the measurement of the lattice confirms this. After re-optimizing the machine via “typical” tuning (ie, operator tune adjustments, skew quadrupole tweaks, and closed orbit bumps in sextupoles), the luminosity was increased by a full 10%.

LER Fix

Following the success in the HER, the LER was tackled in a similar fashion. Given the nature of the LER lattice compared to the HER lattice, however, the solution was longer in coming.

LER PSK Lattice

In Run 6, a new LER lattice was implemented that introduced 12 new skew quadrupoles [1]. The initial measurement shows that the Wx was not addressed sufficiently in the initial design phase and required optimization (Fig 3). In fact, the initial chromatic response of the horizontal beta function was much worse than that of the original LER design lattice in use since commissioning.

By altering the four local horizontal sextupole families any where from 5% to a maximum of 10% (the sextupole power supplies allow for a 50% increase from the nominal design value), the horizontal W function becomes much better behaved (the green trace in Figure 3).

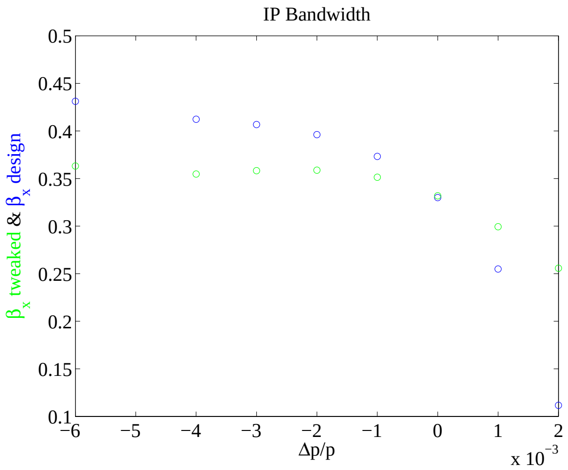

Figure 4: LER horizontal IP bandwidth.

As seen in Figure 4, the LER IP beta function variation with energy has been reduced significantly, as well. Before the fix, it can be seen that the IP beta becomes ill behaved with positive off-momentum particles. By reducing the IP bandwidth, less of the tune shift is “lost” to chromatic effects.

The horizontal chromaticity was increased by four units from the fix, thus allowing the global sextupoles to be lowered.

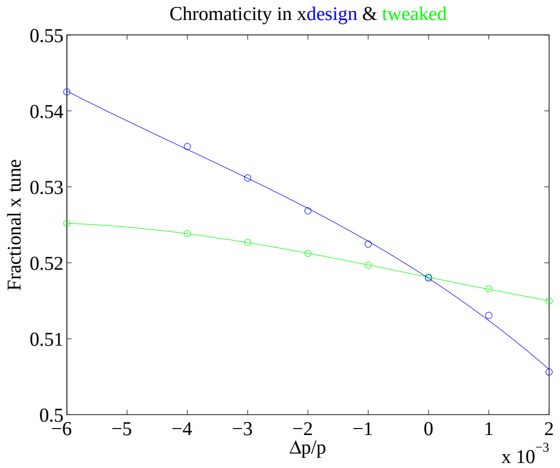

Figure 5: LER chromaticity for PSK lattice (blue) and chromatic-optimized PSK lattice (green).

While a vertical fix has not yet been calculated for the LER PSK lattice, the vertical response to the horizontal fix shows no ill results (Fig 6). In fact, the W functions around the ring have been reduced slightly and only a slight artefact at the interact point has been introduced—a Wy', as it were. Knobs built to specifically vary the W' at the IP have been tested in the machine and seem to show no effect on the luminosity.

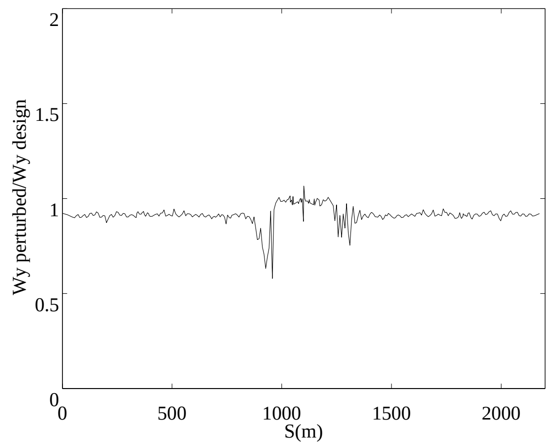

Figure 6: Ratio of perturbed vertical W function over design vertical W function for the LER horizontal W fix.

LIMITATIONS

In order for the W-function fixes to see any kind of significant effect in the machine, the first-order optics need to be squared away. A large beta beat will look like a large W function mismatch, for example. For this reason, the chromatic optics fixes come very late in the running of the collider, unfortunately. After the first-order optics are taken care of, however, significant luminosity improvements can be made with little machine time.

SUMMARY

PEP-II has benefited directly in the form of luminosity increases from the time taken both on the machine for acquisition and offline in the analysis of the data in improved luminosity. The measurement required to calculate the W functions in both the LER and HER takes less than 20 minutes of machine time and the solutions can be dialled in whilst the machine is in production luminosity delivery mode.

The MAD modelling program does have it's limitations in representing the PEP-II lattices as they're operated sufficiently, but the last three rounds of chromatic beta fixes derived from MAD have produced significant luminosity gains.

REFERENCES

[1] F-J Decker, et al., "Lowering the Vertical Emittance in the LER of PEP-II," PAC'07, Albuquerque, June 2007.

MEASUREMENT OF THE UCLA/URLS/INFN HYBRID GUN*

B. O'Shea†, A. Boni, A. Fukasawa, J.B. Rosenzweig, University of California, Los Angeles
D. Alesini, M. Ferrario, B. Spataro, INFN/LNF, Frascati (Roma), Italy
L. Ficcadenti, A. Mostacci, L. Palumbo, Sapienza Università di Roma

Abstract

The hybrid photoinjector is a high current, low emittance photoinjector/accelerator that is under design with collaboration from Roma University La Sapienza, INFN - Laboratori Nazionali di Frascati and the UCLA Particle Beam Physics Lab. The hybrid standing wave-traveling wave photoinjector uses a coupling cell to divide power between a high gradient 1.6 cell standing wave photoinjector, for electron emission and collection, and a lower gradient traveling wave accelerator, for acceleration to desired energies at low emittances. Simulation results show promising beam properties of less than 4 mm-mrad emittance, energy spreads of 1.5 percent, and currents as high as 1.2 kA at energies of 21 MeV. We report on the progress of RF design and results of cold test RF measurements at the UCLA Pegasus Laboratory, including methods for measurements and difficulties arising in the transition from simulation to physical measurements.

INTRODUCTION

The hybrid standing wave-traveling wave gun is a system designed for use in present laboratory research or for future implementation where a unit simpler than some of today's standard split gun and accelerators systems is desired. The simplicity of the system arises from the all-in-one philosophy, that is one only needs a radio frequency(RF) source and the system itself and one is ready for experiment. The power division system allows for the omission of RF components like circulators, which are expensive and difficult to produce for higher frequencies such as X-band. The power division system is an appropriately tuned coupling cell and iris which allows the combination of standing wave and traveling wave systems. The initial results are promising as we will show it is possible to maintain a larger field in the standing wave section than in the traveling wave section, while preserving the theoretical phase advance of the system. Beam dynamics simulations can be found elsewhere in these proceedings[1].

RF DESIGN

The design the of the hybrid system has been split into three sections: the gun, the traveling wave section and the coupling cell. Both the gun and accelerating sections are slight redesigns of current S-band 2.856 GHz models in use throughout the community. The gun is the standard 1.6 cell SLAC/BNL/UCLA design but is fed on axis via a coupling iris instead of the perennial side θ-coupling[2]. The traveling wave section is a $\frac{2\pi}{3}$ tube based on the design and procedure used by Agostino Marinelli [3]. The most critical piece, the coupling cell, isn't designed separately but *in situ* in the combined system. The coupling cell is present in all traveling wave structures as an impedance match but in the case of the Hybrid it is also designed to feed power into the standing wave gun[4].

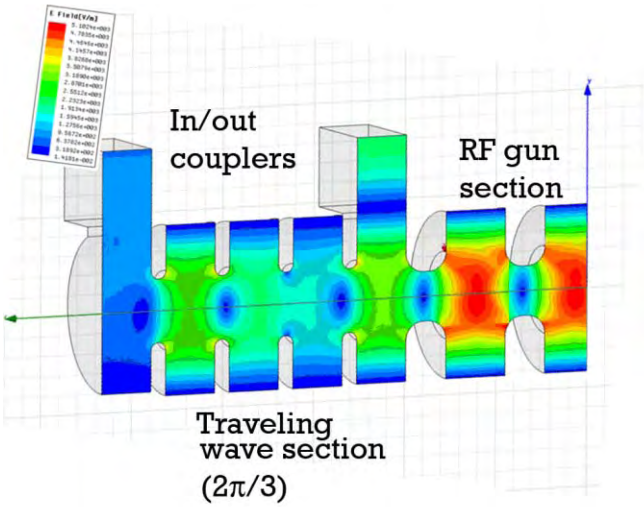

Figure 1: The hybrid gun as simulated in HFSS.

COLD TEST RESULTS

The Hybrid cold test model is a combined aluminum/copper device designed to include a single period in the traveling wave section using three cells. The device thus contains seven total cells: two copper standing wave cells, three aluminum traveling wave cells and aluminum input and output couplers. It was decided to machine the gun section out of copper due to poor performance of aluminum in previous models. The cells are held together by four steel threaded rods running axial along the device. In order to ensure an adequate mate the rods are placed through the cell-to-cell mating surfaces, this guarantees that the clamping does not cause unnecessary bowing or tension. A non-resonant perturbation method, developed by C.W. Steele, is used for measurement in both the standing wave and traveling wave sections.[5][6].

* Work performed under U.S. Department of Energy contract numbers DE-FG-98ER45693 and DE-FG03-92ER40693

† nadnerbity@gmail.com

Measurement Considerations

The Slater method for cavity measurement is inadequate for measurement of non-resonant devices and the use of both Slater and Steele methods can make measurements cumbersome and time consuming. In order to apply the Steele method to both SW and TW systems it is advisable to use an extremely small bead, in this case fashioned out of aluminum foil, when measuring resonant cavities. If too large a bead is used the system is thrown wildly out of resonance and the results are disappointing and inaccurate.

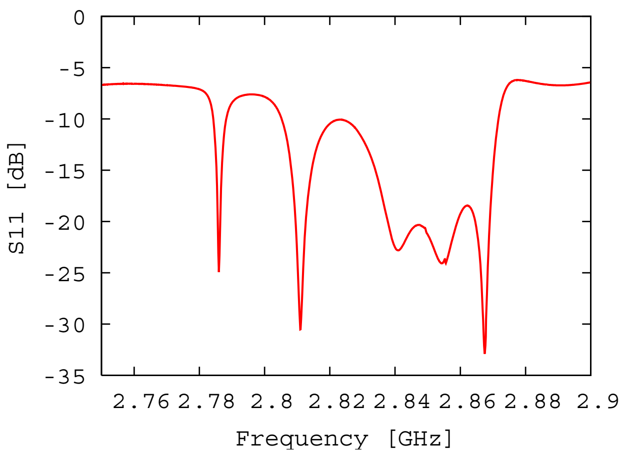

Figure 2: The S11 for the hybrid cold test model.

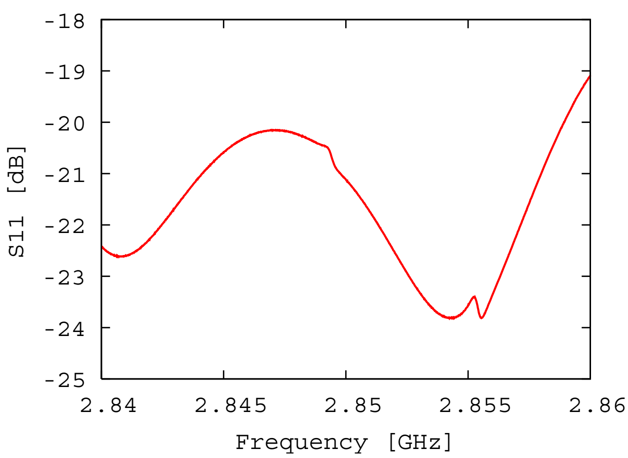

Figure 3: A closer look at the S11 between 2.84 and 2.86 GHz. Clearly seen here are the resonant markings of the standing wave section on the band pass of the traveling wave section. At 2.856 GHz is the π-mode and at 2.849 GHz is the 0-mode.

Tuning Procedure

The present bead pull system is a simple weight and stepper motor system where the motor rotates and pulls the bead through the cold test model, which requires a hole in the cathode plate. In order to properly measure the electric field on axis the measurement must be made at the correct frequency. The resonant frequencies of the gun are not always visible on the S11 curve and even when they can be seen, they can be ambiguous. In order to measure the pertinent standing wave information a semirigid coaxial line is straightened and a 1-2mm piece of the center conductor is exposed to form and antenna. When placed properly in the hole in the cathode plate the transmission from the input port to the antenna gives the frequencies of the 0 and π modes as well as mode separation.

Electric Field Measurements

Tuning screws were added to the standing wave section to counteract imprecise machining, uneven mating and poor clamping through slight variability in cavity frequency. The desired goal of higher fields in the standing wave section than in the traveling wave section can be seen in Figure 1, along with the results from the HFSS simulation.

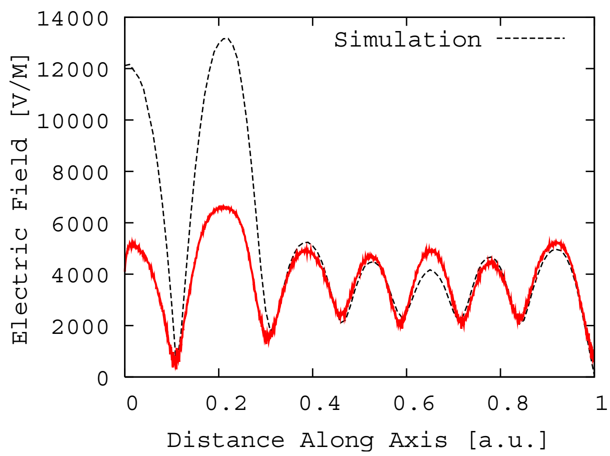

Figure 4: The electric field as measured in the hybrid cold test model. The solid line is the cold test measured value and the dashed line is the simulation result. The electric field has been normalized between the two measurements to clarify the results. The standing wave section is the section running from 0 to 0.3.

Phase Advance Measurements

As can be seen in Figure 3, the phase advance between cells is as to be expected as per the simulation results. The seeming zero degree phase change between the first and second cell is a result of the ambiguity between in 0 and π in measurement. The electric field can be used to determine the mode in that because the electric field goes to zero between the two cells the device must be operating in the π-mode. Most importantly the $\frac{\pi}{2}$ phase advance between the second cell and the third cell is evident[4].

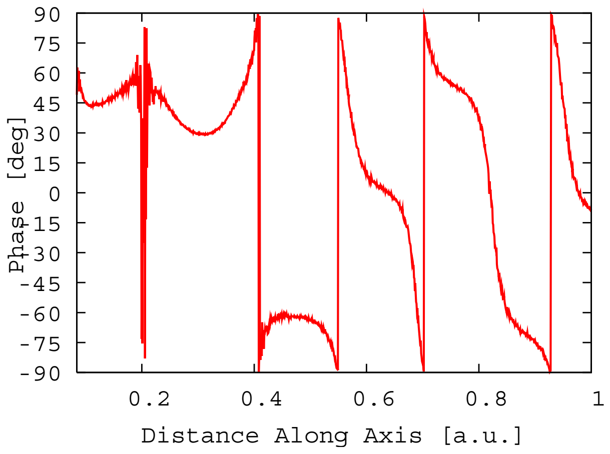

Figure 5: The phase advance as measured in the the hybrid cold test model. The key feature of a $\frac{\pi}{2}$ phase advance between the standing wave section and traveling wave section is evident. The standing wave section is the section running from 0 to 0.4.

Q Measurements

The method used for coupling energy into the gun does not lend itself well to the measurement of the unloaded Q of the cavity. While several methods have been used to determine the loaded Q of the cavity, lack of known coupling parameters makes it difficult to obtain the unloaded Q. A small bead to perturb the gun and the Steele method for determining on axis field levels were used to measure a loaded Q, but the results are only interesting in terms of previous values. In this case, perturbation methods are useful as far as determining relative cavity quality between prototype models but not absolute values. Between the two prototypes produced a rise from 4500 (aluminium) to 9000 (copper) was seen in the loaded Q value. While differences in material account in part for the change in Q value, mate method and machining tolerances also played a roll. An antenna made from a rigid copper wire can also be used to measure the loaded Q through traditional transmission methods but is also confounded by lack of known coupling parameters and poor repeatability.

CONCLUSION

Matching is clearly a delicate issue in the production of the hybrid as it determines the division of power between the two systems. As each cold test model becomes more advanced the machining precision and clamping system used in it's construction is taken to more intricate levels and the results improve.

The present design of the hybrid does not include laser ports in the 0.6 cell, thus in order for proper laser illumination of the cathode the original design of a large accelerating section immediately following the gun section must be changed to allow for a gap after n periods. This gap will allow the fitting of a mirror for reflection of light along the tube's axis. The present bead pull system will not be possible with the final design as there will not be a hole in the cathode. However, the shorter initial section of the hybrid gun will allow for bead drops and avoid the problem of controlling line deflection over the course of 3 meters.

Present considerations for fabrication of the hybrid are a standard braze for the gun and attached traveling wave section and a moving braze for the longer downstream acceleration section. For the gap between sections a simple waveguide, of correct phase length, can be used to transfer power from one section to the other.

Future plans include a high power model and a dual input coupling scheme. Most importantly the next step is to devise a method for reliable and repeatable Q measurement of the gun section. Also planned is an attempt to scale the device to X-Band, to take advantage of better beam properties especially at low charge, which is made possible by the lack of RF peripherals.

REFERENCES

[1] A. Fukasawa et al., "Charge and Wavelength Scaling of the UCLA/URLS/INFN Hybrid Photoinjector," these proceedings.

[2] D.T. Palmer et al., "Microwave Measurements of the BNL/SLAC/UCLA 1.6 Cell Photocathode RF Gun," SLAC-PUB-95-6799.

[3] A. Marinelli, "Progeto di un Accoppiatore in Guida d'Onda per una Struttura Accelerante ad Onda Viaggiante in Banda X," Thesis, June 2004.

[4] B. O'Shea et al., "RF Design of the UCLA/INFN/URLS Hybrid SW/TW Photoinjector," AAC'06, July 2006, Lake Geneva, WI.

[5] C.W. Steele, "Nonresonant Perturbation Theory," IEEE Trans. on Microwave Theory and Techniques, Vol. MTT-14, No. 2,1966,pp.70-74.

[6] D.V. Land, "Measurement of radio-frequency and microwave fields by nonresonant perturbation," IEE Proc, Vol 131, Part II, February 1984.

CTF3 COMBINER RING COMMISSIONING

F. Tecker*, R. Corsini, S. Döbert, P. Skowronski, P. Urschütz, CERN, Geneva, Switzerland
E. Bressi, CNAO, Milano, Italy
C. Biscari, A. Ghigo, INFN, Frascati, Italy
A. Ferrari, Uppsala University, Sweden

Abstract

The CLIC Test Facility 3 (CTF3) has the objective to demonstrate the remaining feasibility issues of the CLIC two-beam technology for a future multi-TeV linear collider.

One key issue is the efficient generation of a very high current 'drive beam' that serves as the power source for the acceleration of the main beam to high energy. This large current beam is produced by interleaving bunches in a combiner ring using transverse deflecting RF cavities.

The 84 m long CTF3 combiner ring and the connecting transfer line have been recently installed and put into operation. The latest commissioning results will be presented.

INTRODUCTION

The aim of the CLIC (Compact Linear Collider) study is to demonstrate the feasibility of a high luminosity, multi-TeV linear e+ e- collider [1]. The CLIC design is based upon normal-conducting accelerating structures operating at a very high gradient (100 MV/m) at an RF frequency of 12 GHz, using a two-beam-acceleration concept [2]. A high current electron beam (drive beam) runs parallel to the main beam and is decelerated to generate the RF power. The production of the high-intensity drive beam pulses with the right time structure is one of the main challenges in CLIC.

Initially, a long electron beam pulse is accelerated in a low frequency normal-conducting linac. Funnelling techniques in delay lines and rings are subsequently used to obtain the desired structure while increasing the beam intensity. Transverse RF deflectors interleave the bunches, hence the bunch spacing is reduced and the beam current is increased. The principle of this bunch train combination by transverse RF deflectors in a ring has been already demonstrated at low current [3] (this reference also describes the principle in detail).

Several critical issues still need to be addressed to demonstrate the CLIC technology. The experimental program of the CLIC Test Facility (CTF3) [4] addresses the main issues, i.e., the generation and use of the drive beam and the testing of high frequency structures and components, with the goal of demonstrating the CLIC feasibility before 2010, when the first LHC results should be available.

CTF3 is presently being built and commissioned at CERN by an international collaboration, including 22 institutes from 11 different countries.

The facility is situated in the buildings of the former LEP pre-injector complex, whose hardware is partly re-used, and is designed to work at a lower beam current and a lower energy than the CLIC drive beam (4 A at 150 MeV instead of 5.2 A at 2.4 GeV). It includes a 70 m long drive-beam linac followed by two rings, where the bunch train combinations will be carried out: a 42 m delay loop and an 84 m combiner ring. After such manipulations the drive beam will have a current of 30 A and will be transported to an experimental area to produce 12 GHz RF power for structure tests. In the same area, another linac will provide a main beam for a CLIC two-beam module and a test decelerator will be used for drive beam stability studies.

In 2003-2004 the injector, the linac, a mid-linac power station and an end-of-linac magnetic chicane with variable momentum compaction factor were installed and commissioned. The installation of the delay loop, under full responsibility of INFN-LNF (Italy), was completed during 2005. The commissioning of the delay loop has been essentially completed in May 2006. The first stage of the bunch combination was successfully demonstrated [5].

During autumn 2006, the transfer line TL1, linking the delay loop to the combiner ring was constructed and an essential part of the combiner ring installation took place. Fig. 1 shows the layout of TL1 and the combiner ring.

Since not all components were available for the instal-

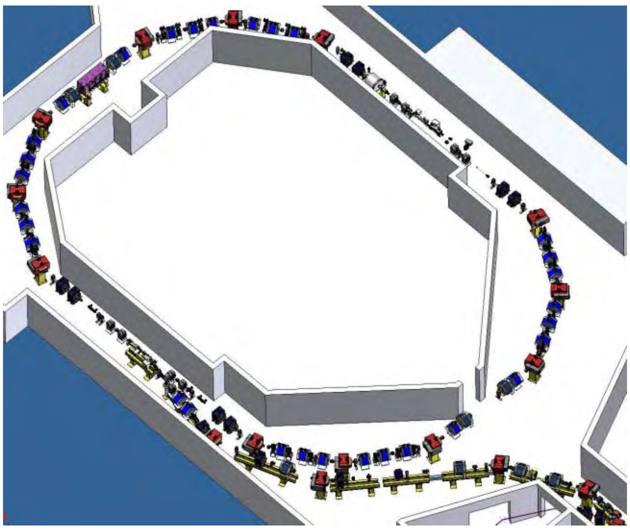

Figure 1: Layout of the TL1 transfer line and the combiner ring. The beam arrives after the delay loop (not visible) from the bottom right into TL1.

* tecker@cern.ch

lation, the whole ring could not be completed but the injection region and a measurement line after the first bend were installed. The injection region includes the transverse RF deflector needed for the bunch train combination, the measurement line contains a screen for optics studies and a beam dump.

The combiner ring installation was continued after a short commissioning run for TL1 (see below). The ring was finished including a short extraction line opposite the injection area by March 2007 except for a number of beam position monitors that were not yet available. These were finally installed during two weeks in April, together with modifications on the front-end electronics of the BPMs.

TRANSFER LINE TL1

2006 Run

The initial commissioning period of the transfer line TL1 in 2006 was only three weeks with an effective beam time of about 80 hours. During this time, the delay loop was bypassed, and short pulses of 3 GHz beam with up to 200 ns length and a current of 3.5 A were used for the commissioning. The beam energy was about 125 MeV. To keep radiation levels low, the whole commissioning was performed with a repetition rate of only 0.8 Hz.

The commissioning started on 21 November. Already on 23 November, the beam was transported to the end of the line with the nominal isochronous optics, only using trajectory steering. After some optimization, a current of 3 A could be injected into the combiner ring. The first injections were done by using dipole corrector magnets to bring the beam on the closed orbit, but the nominal injection with the transverse RF deflector could be established quickly afterwards with the same transmission.

Dispersion measurements were performed by scaling all magnet currents in the line by up to $\pm 1\%$ (see Fig. 2). The dispersion pattern measured agreed very well with the calculated dispersion for the first part of the line but there were some differences in the injection region at the end. Quadrupole scans for Twiss function determination were performed at the beginning of the line. The line was rematched for the measured initial conditions and a quadrupole scan was performed at the end of the line. The

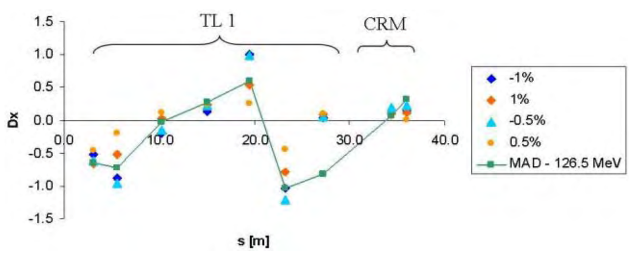

Figure 2: Dispersion measurement in TL1 and ring injection region. (The difference at the end of TL1 (s=27 m) is due to a defective pick-up.)

measured rms emittances were all in the range of 40 – 80 π mm mrad in both planes (100 π mm mrad nominal). The measured Twiss values differed somewhat from the MAD optics model expectations (as for the dispersion) indicating that there could be an error in the model description or problems with a quadrupole magnet in the line.

2007 Run

A short, 7 day run was scheduled initially at the beginning of April. The goal was to transport the beam to the combiner ring and make a turn in order to discover main obstacles and identify problems which have to be solved in the subsequent two week installation period. During this time, no particular emphasis was put on TL1.

During the last commissioning period starting at the end of April, the line was again rematched based on quadrupole scans at the beginning of the line. The beam could be transported through the line and injected into the combiner ring without problems. Still further measurements will be required to verify the proper functioning of the line in agreement with the optics model.

COMBINER RING

During the short initial 2007 run, it was envisaged to make a turn in the combiner ring. The beam could be transported half way through the ring to the extraction line with about 25% losses. It was difficult to obtain this transmission and the optics was not the design optics but empirically optimized. Due to the short time, no further studies could be performed.

After the two week installation break in April, another 10 weeks of commissioning are scheduled. The final objective for this period is the demonstration of the bunch recombination in the combiner ring by a factor 4. The first step was to establish full transmission in the ring over several turns with a 3 GHz beam, bypassing the delay loop. A first way of achieving circulating beam is by using a short RF pulse in only the transverse RF deflector that directs the injected beam on the closed orbit. When the RF pulse is stopped just after the passage of the injected beam, the RF field is not present any more when the beam returns after one full revolution and the injection is similar to an injection by a kicker.

Since the beam losses in the second arc persisted, the quadrupole currents were verified and it was found that the control cables for two of the quadrupole families in this region of the ring had been swapped.

Unfortunately, the commissioning was interrupted for almost two weeks due to a vacuum leak in the CTF3 linac that could only be repaired after a waiting time to allow for radiation level decay. When the commissioning restarted, it was still difficult to pass the beam through. The best result could be obtained with a beam optics that had one of the arc quadrupole families switched off, and the beam made up to three turns with losses. Following these results, it was decided to re-check the quadrupole polarities again. This had been previously done but no control was made after inverting the magnets that had had a wrong polarity. Indeed, it was found that one quadrupole (from the family that was off in the best-performing optics) in the region with losses had the wrong polarity.

After having corrected the polarity, it was possible to get the beam circulating with the nominal isochronous optics. Initially, the beam was lost over about 10 turns. Eventually the ring could be optimized such that after some losses over the first turns, the remaining beam was circulating up to 180 μs, corresponding to more than 600 turns.

While the setting up so far was done with a 3 GHz beam, a 1.5 GHz beam is required for the nominal recombination. When putting the 1.5 GHz subharmonic bunching (SHB) system in operation (only 2 of the 3 SHB cavities could be used due to a failure of a travelling wave tube), the same transmission could be immediately be obtained after optimization of the different cavity phases.

After achieving reasonable transmission, the pulse length of the transverse RF deflector was extended so that the RF field is still present after one turn. With the correct path length in the combiner ring, the beam should arrive at the zero-crossing of the RF field so that the beam is not deviated by the deflector. The geometry of the combiner ring was carefully chosen in the design, taking into account the path length in the arc dipole magnets, calculated based on the measured field distribution. A wiggler magnet in the ring allows a fine tuning of the path length within a total range of 9 mm.

The wiggler magnet current was changed and the beam was observed in the second turn after the deflector. A good transmission and trajectory could be obtained for a relatively low current of the wiggler. This shows that the length of the combiner ring has been designed correctly and that the correct path length for a combination by a factor four is experimentally accessible.

With the correct path length in the ring it is possible to obtain a combination by a factor two. A beam pulse of twice the combiner ring time of flight (2 x 280 ns) is injected with the RF deflector field on during this time. The bunches of the first 280 ns pass the RF deflector at the zero-crossing after one turn and are combined with the next 280 ns of incoming beam, increasing the beam intensity. Fig. 3 shows the result of this first combination by a factor two. The beam current could be increased from 3.5 A to about 6.5 A.

Beam losses are still present over the first turns and will have to be further minimized. The next steps will be to adjust the second RF deflector in amplitude and phase to produce a time-dependent local closed orbit bump in the injection region. This will make the nominal combination by a factor four possible. Furthermore, optics and dispersion studies of the ring will be performed. Finally, the first stage of combination by a factor two in the delay loop has to be set up again to demonstrate the nominal combination by a factor eight, when both the delay loop and combiner ring operate nominally.

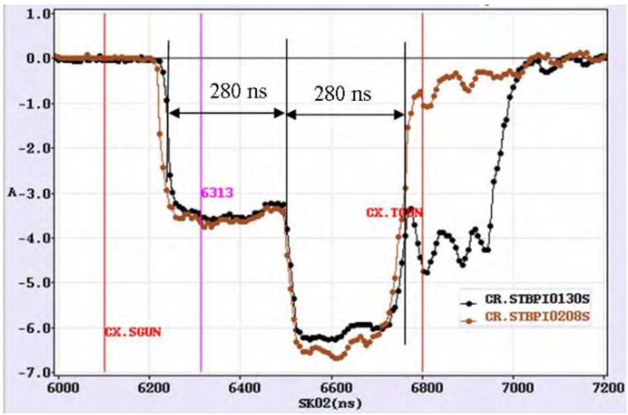

Figure 3: First recombination in the Combiner Ring. The traces show the beam current measured by 2 beam position monitors. The incoming beam pulse has twice the length of the CR (2 x 280 ns). During the second 280 ns, the bunches are interleaved with the bunches that made one revolution in the ring.

CONCLUSIONS

Beam through the newly installed transfer line TL1 could be quickly established with good transmission at the end of 2006. The CTF3 combiner ring commissioning has been ongoing since end of March 2007 with some interruptions for further installation work and due to equipment failures.

It took a certain time to set up properly circulating beam because of undetected errors in the quadrupole magnet cabling. After fixing these, a reasonable beam was finally obtained and a first preliminary bunch train combination by a factor two could be demonstrated.

Further optics and combination studies will continue in the following weeks of the running period, to confirm and extend the first observations with the goal to show the nominal bunch train combination with delay loop and combiner ring.

REFERENCES

[1] The CLIC Study Team (edited by G. Guignard), “A 3 TeV e+/e- Linear Collider Based on CLIC Technology”, CERN Report 2000-008

[2] H. Braun, R. Corsini (Ed.), “The CLIC RF Power Source: a Novel Scheme of Two-Beam Acceleration for Electron-Positron Linear Colliders”, CERN 99-06 (1999)

[3] R. Corsini et al., “Experimental Results on Electron Beam Combination and Bunch Frequency Multiplication”, Phys. Rev. ST Accel. Beams 7, 040101 (2004)

[4] G. Geschonke and A. Ghigo (Eds), “CTF3 Design Report”, CERN/PS 2002-008 (RF)

[5] R. Corsini et al., “Commissioning Status of the CTF3 Delay Loop”, EPAC ’06, 2006

OPTIMUM ELECTRON BUNCH CREATION IN A PHOTOINJECTOR USING SPACE-CHARGE EXPANSION

J.B. Rosenzweig, A.M. Cook, M. Dunning, R.J. England, P. Musumeci
Particle Beam Physics Laboratory, Department of Physics and Astronomy
University of California Los Angeles, Los Angeles, CA 90095, USA

M. Bellaveglia, M. Boscolo, L. Catani, A. Cianchi, G. Di Pirro,
M. Ferrario, D. Filippetto, G. Gatti, L. Palumbo, C. Vicario
Istituto Nazionale di Fisica Nucleare, Laboratori Nazionale di Frascati
00044 Frascati (Roma), Italy

S. Jones
Jet Propulsion Laboratory, California Institue of Technology
4800 Oak Grove Drive, Pasadena, CA 91101, USA

Abstract

Recent studies have shown that by illuminating a photocathode with an ultra-short laser pulse of appropriate transverse profile, a uniform density, ellipsoidally shaped electron bunch can be dynamically formed. Linear space-charge fields then exist in all dimensions inside of the bunch, which minimizes emittance growth. Here we study this process, and its marriage to the standard emittance compensation scenario that is implemented in most modern photoinjectors. We show that the two processes are compatible, with simulations indicating that a very high brightness beam can be obtained. An initial time-resolved experiment has been performed at the SPARC injector in Frascati, involving Cerenkov radiation produced at an aerogel. We discuss the results of this preliminary experiment, as well as plans for future experiments at the UCLA Pegasus laboratory to resolve the ellipsoidal bunch shape at low energy. Future measurements at high energy based on fs resolution RF sweepers are discussed.

INTRODUCTION

In order to obtain high brightness electron beams from photoinjectors, it is most common to rely on the process of *emittance compensation* [1]. Optimization of this process demands that the transverse fields be as uniform, and as linear (in radius r) as possible. The existing studies of emittance compensation have, to that end, assumed use of a uniform density electron bunch, having a cylindrical shape. However, this shape produces nonlinear fields near the bunch head and tail that result in emittance growth.

It is now known that a uniform ellipsoidal density distribution yields space-charge fields that are linear in all dimensions [2]. Under such conditions, it is conceivable that one may obtain essentially emittance growth-free dynamics. How to produce such a distribution has, until recently, remained an unanswered question.

In 1997, Serafini proposed the dynamic creation of an ellipsoidal bunch by launching an ultra-short, radially shaped bunch, which then evolves to achieve the desired longitudinal shape [3]. On the other had, it has recently been shown by Luiten, et al., that in obtaining the correct final ellipsoidal distribution, there is essentially no requirement on the shape of the initial laser pulse other than it be ultra-short [4]. Thus such laser pulses are a natural, and technically achievable way of producing an ellipsoidally shaped, nearly uniform density bunch.

As the beam dynamics just after photoemission are qualitatively different in the traditional emittance compensation scenario than in the Luiten-Serafini scheme, it is not immediately apparent that one may successfully combine the two. The UCLA-SPARC collaboration has recently shown [5] that this is indeed possible; further, the combination of emittance compensation and dynamic creation of the ellipsoidally shaped bunch produces results that in many ways are superior to those obtained in state-of-the-art designs. As the bunches that are produced are shorter than in standard cases, very high brightness beam creation is possible.

The basic idea behind the Luiten-Serafini scheme is simple: the bunch profile expands and deforms longitudinally to produce, in the final state, a uniformly filled ellipsoid of charge. In order to understand this process, the dynamics of space-charge-dominated bunch expansion have been studied [5] and may be summarized in a few points:

- The injected bunch surface charge density $\sigma_b = dQ_b/dA$ must not be too high, or image charge effects at the cathode distort the bunch profile. This is quantified by the condition $\alpha \equiv 4\pi\sigma_b/E_0 \ << 1$.
- The laser pulse length must be much shorter than the electron bunch length after expansion, in order to be able to ignore the details of the initial laser pulse profile. The bunch length after expansion is estimated as

$L_b \approx 2\pi\sigma_b m_e c^2/E_0^2$.

- To achieve the desired ellipsoidal bunch shape, one must choose the correct initial surface current density distribution: $\sigma_b(r) = (3Q_b/2\pi a^2)\sqrt{1-(r/a)^2}$.

While the analysis of the beam dynamics is useful, the central issue of joining this regime—now commonly known as the "blowout regime"—with emittance compensation must be explored with simulations and experiments.

BLOWOUT REGIME WITH EMITTANCE COMPENSATION: GENERAL STUDY

Initial UCLA `parmela` [6] simulations have been performed to explore joining the Serafini-Luiten scheme with the optimized emittance compensation working point of the SPARC injector at LNF. In order to have values of α which do not give excessive image charge effects, the beam charge is lowered and the beam radius is slightly enlarged. In the preliminary optimization, we launch a 0.33 nC beam with an initial longitudinal Gaussian distribution having $\sigma_t = 33$ fs, and a radial Gaussian with $\sigma_x = 0.77$ mm (cutoff at 1.8σ). The gun (1.6 cell, 2856 MHz) is run with a peak on-axis gradient of 120 MV/m; the beam is launched at 33 degrees forward of crest. This is a bit advanced in comparison to the nominal launch phase for a standard bunch, and serves to control the excessive beam energy spread after the gun. It is noted that the peak value of α in the present case is 0.11, as opposed to 0.42 in the LCLS design.

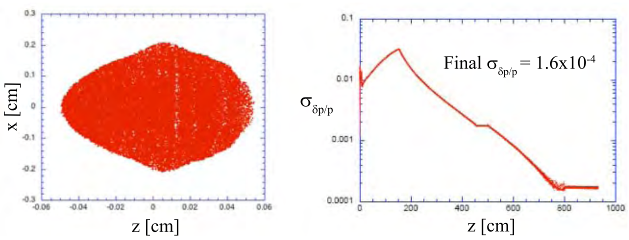

Figure 1: (left) `parmela` simulation results of electron bunch (x, z) distribution showing ellipsoidal bunch boundary, and (right) evolution of $\sigma_{\delta p/p}$ in z for emittance compensation case.

The formation of the quasi-ellipsoidal bunch is clearly shown in Fig. 1, which displays the bunch (x, z) distribution at a point 133 cm from the cathode, in the drift space after the gun and just preceding initial traveling wave linac section. Here the beam has 6.3 MeV mean energy, and its transverse dynamics are space charge-dominated. Thus one sees clearly the "inflated" ellipsoidal bunch shape. The final bunch length is 1.3 mm full width, corresponding to a peak current of 105 A. Thus even with one-third of the charge, this scheme should produce a higher current than obtained in simulations of the standard design.

As the longitudinal space-charge during much of the acceleration is also linear, and total pulse length T is short, the longitudinal phase space is very compact. The evolution of the relative momentum spread $\sigma_{\delta p/p}$ in z is shown in Fig. 1. The final achieved RMS value is $\sigma_{\delta p/p} = 1.6 \cdot 10^{-4}$, which is an order of magnitude smaller than that obtained in the standard LCLS type (or SPARC type) design.

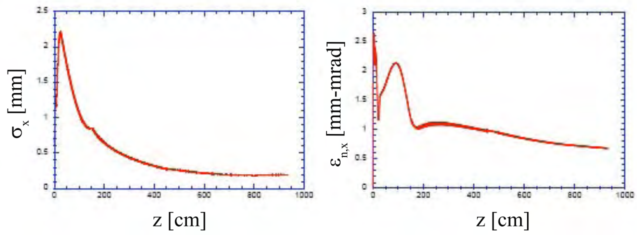

Figure 2: (left) Evolution of RMS transverse beam size σ_x and (right) evolution of RMS normalized emittance $\epsilon_{n,x}$ for emittance compensation case, from `parmela` simulation.

The evolution of the RMS transverse beam size σ_x , and the RMS normalized emittance $\epsilon_{n,x}$ are shown in Fig. 2. While the behavior of σ_x is similar in most respects to the standard design, the emittance behavior is not as familiar. Details can be found in Ref. [7]. This scheme works well, as the final value (still slightly decreasing) of $\epsilon_{n,x}$ at the end of the second linac (84.5 MeV energy) is 0.68 mm-mrad.

After acceleration to higher energy (84.5 MeV), the beam is not space-charge dominated, and the (x, z) profile no longer ellipsoidal. Nonetheless, the beam has excellent emittance. With a high initial current, and low intrinsic energy spread, this beam may be compressed further, with very high final peak current achievable [9].

INITIAL SPARC AND PEGASUS EXPERIMENTS

Experimental Signatures and Measurements

In the initial experiments, the electron bunch is imaged (time-integrated) at low energy (5-7 MeV) in the region after the gun, using a YAG detector. For time resolved measurements the beam spatial information will be converted to photons with a Cerenkov emitter. In order to have a manageably small angle of emission we use aerogel as the emitter, which has a small index of refraction (n = 1.005-1.02). The aerogels have been custom fabricated at the Jet Propulsion Laboratory. Simulations consist of providing electrons (typically 40,000) from `parmela` to `geant4` [10], which simulates the scattering of the electrons in the entrance foil and generates a collection of Cerenkov photons produced in the aerogel. The photon distributions that result are then passed to a *Mathematica* based, optical ray-tracing program, *Rayica*.

FIRST RESULTS

The first stage of experimentation on the blowout regime took place at INFN-LNF beginning at the end of March 2006 and has been reported on previously [7, 8]. The laser was reconfigured for short pulses (less than 0.5 psec FWHM) and up to 1.6 nC of charge. The conditions for observing the dynamic creation of nearly uniformly filled ellipsoidal charge distributions were not quite present; nevertheless, impressive first data was obtained.

Initial measurements of the longitudinal-transverse profile of the bunch were made with aerogel with index n = 1.008, with the Cerenkov emitter placed 2.4 m away from the cathode. Streak camera images were obtained using the transport system described in the previous section. Such a streak, after tilt correction, is shown in Fig. 3.

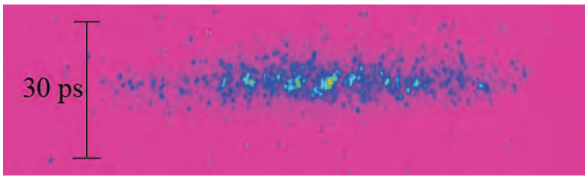

Figure 3: Streak image from initial SPARC experiment.

The image displays the profile obtained from a bunch with charge of 700 pC. In order to extract information from single shots concerning the streak image—which should represent the bunch density distribution in an (x, z) slice in the midplane of the bunch—a maximum likelihood analysis has been chosen to test for different assumed types of bunch distributions. The (x, z) slice distributions tested for consistency with the experimental data include: (1) a bi-Gaussian (thermal-type) distribution; (2) a uniformly filled ellipse (assumed arising from a parent uniformly filled ellipsoid); and (3) a nearly uniformly filled ellipse with a tail, which we choose to represent as a Fermi-Dirac distribution.

As all of the distributions assumed have contours of constant density that are elliptical, a systematic statistical approach is possible, in which one looks at the total integrated intensity inside of ellipses of size varying from zero area to an area covering the entire streak image. These ellipses are all required to have the same aspect ratio, which is given by the intensity profile itself, $R = \sigma_x/v_s\sigma_t$, where v_s is the streak velocity, and σ_t=3.45 psec for the streak in Fig. 3.

The data from the streak images was fit to these functions to determine which of the assumed three profiles gives the best fit. Such an exercise has been performed for the streak given in Fig. 3, with the results shown in Fig. 4. It is noted that the fit obtained from the Fermi-Dirac model gives an excellent match to the data.

CONCLUSIONS

While the first measurements have established the soundness of the basic experimental approach, much more remains to be done. Further experiments, including further

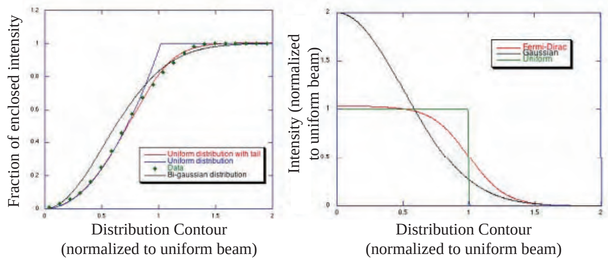

Figure 4: Analysis of streak data, with fraction of integrated intensity of data inside of elliptical contour shown. Best fit of data points to three models are shown: bi-gaussian distribution, uniform elliptical distribution, and Fermi-Dirac (uniform with tails) distribution.

exploration of low energy, time-resolved imaging of electron bunch profiles will be performed at the UCLA Pegasus laboratory in 2007-2008. The SPARC injector will soon be completed with the addition of post-acceleration linacs and beam diagnostics (e.g. RF sweeper). In this fully mature experimental scheme, a complete test of the consistency of the Luiten-Serafini scheme with emittance compensation should be possible.

ACKNOWLEDGEMENTS

The authors acknowledge useful interactions with Scott Anderson, Luca Giannessi, Marcello Quattromini; and Dirk Lipka for an introduction to `geant4`.

REFERENCES

[1] L. Serafini and J.B. Rosenzweig, Physical Review E **55**, 7565 (1997).

[2] I.M. Kapchinskii and V.V. Vladimirskii, in *Proc. Int. Conf. High En. Accs.*, CERN, Geneva, 274 (1959).

[3] L. Serafini, *AIP Conf. Proc.* **413**, 321 (1997).

[4] O. J. Luiten, et al., Phys. Rev. Lett. **93**, 094802-1 (2004).

[5] J. B. Rosenzweig, et al., Nucl. Inst. Meth. A **57**, 87 (2006).

[6] E. Colby, *UCLA PhD Thesis*, FERMILAB-THESIS-1997-03, FNAL (1997).

[7] J.B. Rosenzweig, et al., *Proc. 2006 FEL Conf.*, Berlin, 752 (2006).

[8] J.B. Rosenzweig, et al., *AIP Conf. Proc.* **877**, 649 (2006).

[9] J.B. Rosenzweig, et al., *Proc. 2005 Phys. App. High Br. Beams*, Erice (2006).

[10] S. Agostinelli, et al., Nuc. Inst. Meth. A **506**, 250 (2003).

THE UCLA HELICAL PERMANENT-MAGNET INVERSE FREE ELECTRON LASER*

R. Tikhoplav#, J. Frederico, G. Reed, J. Rosenzweig, S. Tochitsky, G. Travish UCLA, Los Angeles, CA 90095
G. Gatti INFN/LNF, 00044 Frascati (RM) Italy

Abstract

The Inverse Free Electron Laser (IFEL) is capable, in principle, of reaching accelerating gradients of up to 1 GV/m making it a prospective accelerator scheme for linear colliders. The Neptune IFEL at UCLA utilizes a 15 MeV Photoinjector-generated electron beam of 0.5 nC and a CO_2 laser with peak energy of up to 100 J, and will be able to accelerate electrons to 100 MeV over an 80 cm long, novel helical permanent-magnet undulator. Past IFELs have been limited in their average accelerating gradient due to the Gouy phase shift caused by tight focusing of the drive laser. Here, laser guiding is implemented via an innovative Open Iris-Loaded Waveguide Structure (OILS) scheme which ensures that the laser mode size and wave front are conserved through the undulator. The results of the first phase of the experiment are discussed in this paper, including the design and construction of a short micro-bunching undulator, testing of the OILS waveguide, as well as the results of corresponding simulations.

INTRODUCTION

New alternative acceleration schemes have been actively studied in recent years. One of them is the Inverse Free Electron Laser (IFEL) which allows energy transformation from a laser to the electron bunch propagating through a magnetic undulator with a matching period. A high-gain IFEL experiment has been successfully conducted at the UCLA Neptune facility [1]. That experiment used an undulator with a planer symmetry. In this paper we suggest using a helical undulator which employs a cylindrically symmetric geometry. Such geometry is interesting because it provides a better coupling to cylindrically symmetric electron beam and it also allows a bigger gap which makes aligning of a laser and an electron beams much easier.

EXPERIMANTAL SET-UP

The Neptune facility at UCLA consists of a 15 MeV Photoinjector linac which can provide a charge of up to 0.5 nC and a CO_2 laser with peak energy of up to 100 J. The IFEL utilizes a helical permanent-magnet undulator of Halbach geometry. To provide the guiding of 10.4 micron CO_2 laser beam through the udulator, we propose to use an open iris-loaded structure (OILS) waveguide.

*Work supported by US Department of Energy
#rodion@ucla.edu

We will first build a short (10 cm) undulator and a waveguide to test the coupling by observing a micro-bunching. Then, as a second step, we will build a long waveguide and a tapered undulator (80 cm).

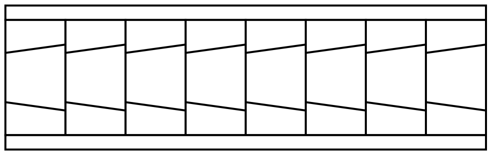

Figure 1: OILS Waveguide.

OILS Waveguide

A scheme for propagating a laser beam in an open iris structure has been analyzed in detail by M. Xie [2]. Such a scheme is analogous to propagation in a Fabry-Perot resonator with flat mirrors and it has not as yet been tested for the fundamental laser mode [3].

An important advantage of an OILS waveguide is its over-sized dimension compared to the laser wavelength. The structure consists of a number of stacked elements with a circular opening of radius *a* (see Fig. 1).

Each element has tapered edges with the angle of tapering greater than the diffraction divergence angle $\theta_d \approx \lambda/a$ so that the light sees it as an infinitely thin iris. The parameters of such a structure are given in Table 1.

Table 1: Laser and Waveguide Parameters

Parameter	**Value**
Total Length	80 cm (10 cm)
Diameter, $2a$	2.26 mm
Number of Elements	267 (33)
Thickness of an Element, L	3 mm
Wavelength, λ	10.6 um
Waist, w_0	0.7 mm
Laser Pulse Length	100 ps
Laser Pulse Energy	8 J
Laser Intensity, I	500 GW/cm^2
Peak Electric Field, E_0	1.94 GV/m

The structure can be visualized as an "unfolded" flat mirror Fabry-Perot resonator with Fresnel number:

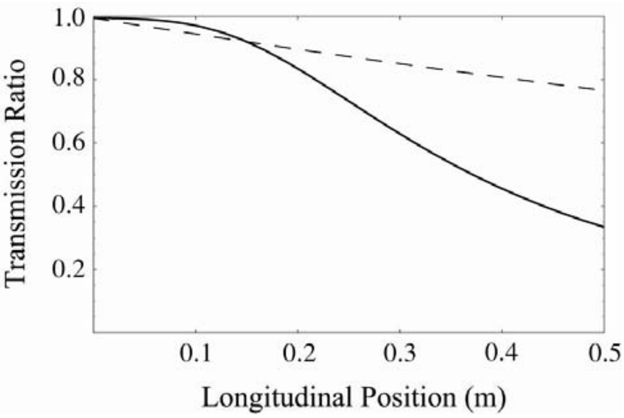

Figure 2: Genesis simulation of transmission of a Gaussian beam through OILS (dashed) and through an aperture in free space (solid).

$$N = a^2 / \lambda L = 40 \tag{1}$$

and quality factor:

$$Q = 2\pi L / \lambda \alpha_c = 1.7 \times 10^6 \tag{2}$$

where $\alpha_c = 8\nu_{01}^2 (M+\eta)\eta / [(M+\eta)^2 + \eta^2]^2$ is the loss per cell, and $\nu_{01} \approx 2.405$ is the first zero of Bessel function $J_0(\nu_{01}) = 0$, $\eta = -\varsigma(0.5)/\pi^{1/2} = 0.824$ and ς is Riemann's Zeta function; $M = [8\pi N]^{1/2}$. Theoretical losses over a length of 50 cm should be less than 25% [4], see Fig. 2. A 10 cm prototype has been successfully built and tested. 90% transmission has been achieved.

Undulator

To couple an electron and laser beams the electrons need to pass through a periodic magnetic field. To create such field we will use an array of magnets called an undulator. The laser wavelength, λ and undulator parameters are related as follows:

$$\lambda = \frac{\lambda_u}{2\gamma^2}\left(1 + K_u^2\right) \tag{3}$$

where λ_u is undulator period, γ is the Lorentz factor of electrons and $K_u = eB_u\lambda_u / 2\pi m_e c$ is the undulator constant, where B_u is the magnetic field in undulator, c is velocity of light, e and m_e are electron charge and mass respectively.

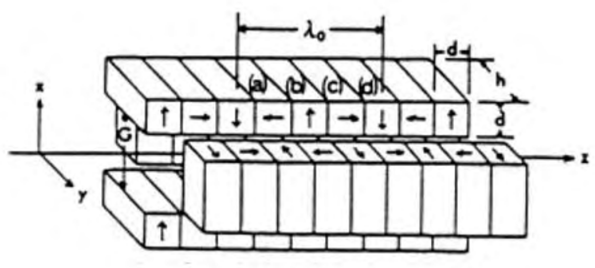

Figure 3: Undulator schematics. Arrows indicate the direction of magnetic field.

Table 2: Undulator and Electron Beam Parameters

Parameter	**Value**
Undulator Length	10 cm
Undulator Gap	13 mm
Undulator Constant, K_u	0.094
Field Amplitude , B	0.069 T
Undulator Period, λ_u	14.6 mm
Electron Energy	13.5 MeV
Electron Charge	0.1 nC
Normalized Emmitance	5 mm-mrad
Electron Beam rms Size	0.3 mm

We will use a Halbach type helical permanent magnet undulator. There are four magnets per period and there are four segments in transverse dimension as well, see Fig. 3. Each magnet piece is 11 mm by 11 mm by 4 mm magnetized to 1 T field. Each piece is imbedded into aluminum holder which can slide in radial direction to provide fine tuning. See Table 2 for the undulator and electron beam parameters.

The undulator and the OILS waveguide will be put into the vacuum box in the Neptune beamline, where it will be aligned with the CO_2 laser.

Coherent transition and Cherenkov radiation techniques will be used as a microbunching diagnostic tool.

SIMULATION RESULTS

A 3D magnetostatic code Radia [5] is used to simulate magnetic field map in the undulator, see Fig. 4. Radia constructs three dimensional objects with corresponding material properties and then solves the magnetization problem employing a Boundary Integral Method.

Genesis 1.3 [6] was used to model propagation of electron beam through undulator and its interaction with guided laser bean. Genesis is a time-independent electro-

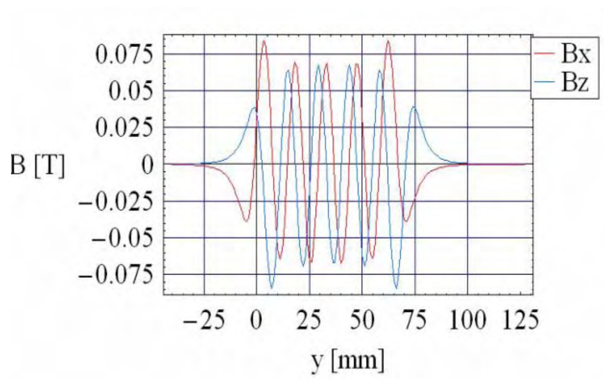

Figure 4: Simulation of the magnetic field in undulator.

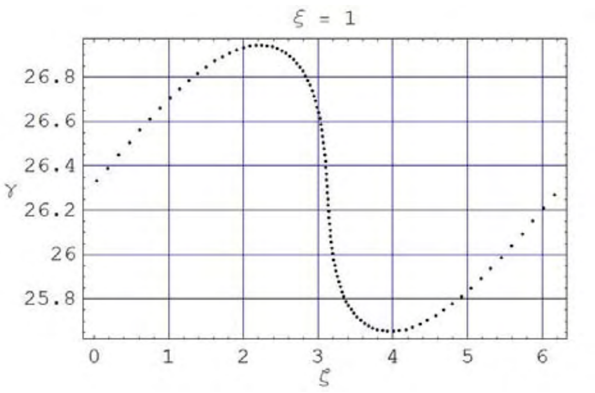

Figure 5: Genesis simulation of the energy-phase modulation after 30 cm drift.

magnetic propagator which tracks electron beam of a given shape including a space-charge effect. A 30 cm drift section was introduced into simulation to translate an energy modulation in the undulator into microbunching (see Fig. 5) which can be measured using the techniques described above.

SUMMARY

A novel helical undulator and OILS waveguide are being developed and will be implemented at Neptune facility at UCLA. The first stage consists of a bunching experiment using a short (10 cm) undulator. Then, as the second stage, a full scale 80 cm undulator will be built with 100 MeV/m acceleration gradient expected.

REFERENCES

[1] P. Musumeci, *et al*., *Phys Rev. Lett*. **94**, 154801 (2005).

[2] M. Xie, Proc. of 1997 Part. Accel. Conf. 660 (1997).

[3] R. Tikhoplav, *et al*., Proc. of 2002 Europ. Part. Accel. Conf. 984 (2002).

[4] J. Frederico, *et al*., these proceedings.

[5] www.esrf.eu/Accelerators/Groups/InsertionDevices/Software/Radia/

[6] pbpl.physics.ucla.edu/~rieche/

CHARGE AND WAVELENGTH SCALING OF THE UCLA/URLS/INFN HYBRID PHOTOINJECTOR*

A. Fukasawa#, J. B. Rosenzweig, A. Boni, B. D. O'Shea, UCLA, Los Angeles, CA 90095, USA
D. Alesini, M. Ferrario, B. Spataro, INFN/LNF, Frascati, Italy
L. Ficcadenti, A. Mostacci, L. Palumbo, Rome Univ., Rome, Italy

Abstract

The SW/TW hybrid photoinjector is being developed at UCLA, INFN/LNF, and University of Rome. The hybrid gun has SW cells and TW cells in one structure. It can produce the low emittance and high peak current beam. PARMELA simulation showed the emittance and the bunch length were 2.8 mm.mrad and 0.16 mm, respectively. With the charge and frequency scaling law of the photoinjector [1], low charge and higher frequency case were also calculated.

INTRODUCTION

The photoinjector with a BNL/SLAC/UCLA 1.6-cell RF gun has long been studied [2, 3], and now it became a standard of the low emittance beam production. The emittance is good, however, the bunch length is not short, and it is frequently required to be compressed. The hybrid gun can produce the low emittance and short beam in one structure.

The hybrid photoinjector consists of one accelerating structure which has both of standing and traveling wave cells (Figure 1). A standing wave structure is axially coupled to al traveling wave structure. It has a half cell and a full cell and acts as RF gun to produce low emittance beam. The beam is compressed in traveling wave structure by velocity bunching. Because the RF power is fed into the traveling structure, there is no reflection at the input port. Thus, it can omit a circulator which an RF gun generally requires. This feature enables to build a photoinjector at X-band frequency where no circulators at high power have been invented.

The study of the hybrid RF structure is detailed elsewhere [4, 5].

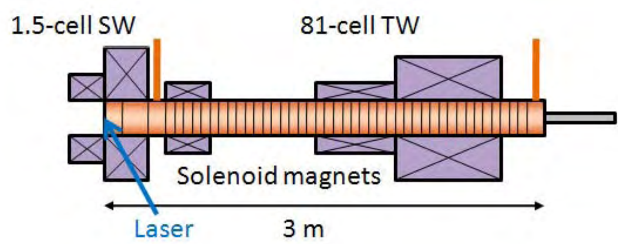

Figure 1: Schematic of the hybrid photoinjector.

S-BAND HYBRID PHOTOINJECTOR

The main parameters of the S-band hybrid structure are listed on Table 1.The standing wave (SW) section has a half cell and full cell, and it is operated at π mode. The length of the half cell is quarter of the RF wavelength, which is shorter than that of the 1.6-cell RF gun. This is because this guns accelerating field is as low as 60 MV/m and it takes more time to go through. The length of the input coupler is $(1/4+1/6)\lambda$ to put the beam at 0 degree for the velocity bunching as its phase is advanced by 90 degree to the full cell. The TW section has 81-cell $2\pi/3$-mode structure, and the average accelerating gradient is 13.5 MV/m.

As shown in Figure 1, there are five solenoids, including the backing coil, at the hybrid structure. The first two solenoids stay around the SW section. The waveguide prevents to put one big solenoid. Due to the laser port, the first solenoid became relatively large to get sufficient field. The third and fourth solenoids keep the beam size small after the beam is focused by the upstream solenoids. They also control the position of the emittance minimum. The field of the latter solenoid have larger field as the beam is accelerated. Figure 2 shows the solenoid field along z axis.

Table 1: Main properties of the hybrid photoinjector

Resonant frequency	2.856 GHz
SW cavity mode	π mode
TW cavity mode	2π/3 mode
Peak Field in SW	60 MV/m
Average field in TW	13.5 MV/m
Cell number of TW	81 cells
Total length	3.m

BEAM DYNAMICS

PARMELA was used to calculate the beam dynamics. 10 k particles were used in each simulation.

The distribution of the input beam was uniform and rectangular in both of the radial and longitudinal direction. The radius was 1 mm, the length 10 ps, and the charge 1 nC. 0.98 mm.mrad of the cathode emittance was included.

Figure 3 shows the typical evolution of the rms beam envelope, the normalized emittance, and the bunch length. The beam was focused by the first solenoid and maintained its size under the field of the downstream magnets. The emittance had two minimum, and we usually look at the second one. The bunch length was

*Work performed under US Department of Energy contract numbers DE-FG-98ER45693 and DE-FG03-92ER40693
#fuka@physics.ucla.edu

initially spread by space charge force as other. Soon after the beam entered into the TW section, it began to bunching. Earlier injection makes stronger bunching. If the beam suffers the over bunching, the minimum emerged around 1 m. The beam parameters are listed on Table 2.

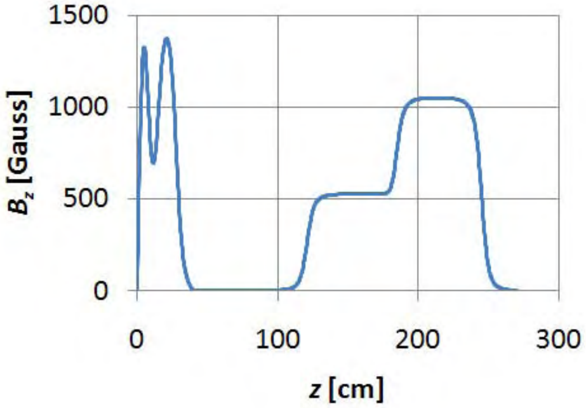

Figure 2: B_z along the axis calculated by using POISSON. The field was made by the solenoid around the hybrid structure.

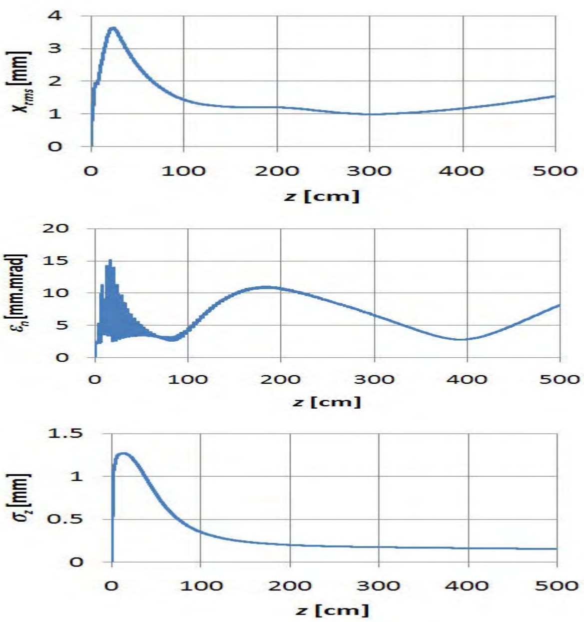

Figure 3: The evolution of the rms beam envelope (top), the normalized emittance (middle), and the rms bunch length.

Injection Phase Scan

The injection phase scan was made and the results are in the Figure 4. The emittance was picked at the second minimum while the bunch length was at 4 m of fixed position. The minimum bunch length was 0.10 mm at 46 degrees but the emittance was 6.5 mm.mrad. If you can guarantee the bunch length, 0.16 mm and 2.8 mm.mrad at 50 degrees may be better.

Table 2: Beam parameters of the hybrid photoinjector

Initial beam shape	Uniform, rectangular in r and z
Initial beam radius	1 mm
Initial beam length	10 ps
Injection phase	50 deg
Beam energy	21.1 MeV
Energy spread	2.3 %
Charge	1 nC
Bunch length	0.16 mm
Normalized emittance	2.8 mm.mrad

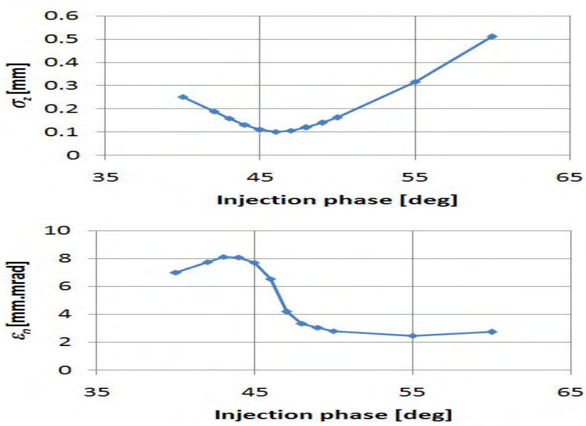

Figure 4: The rms bunch length (top) at 4 m and the normalized emittance at the second minimum (bottom) as a function of the injection phase of the beam at the cathode.

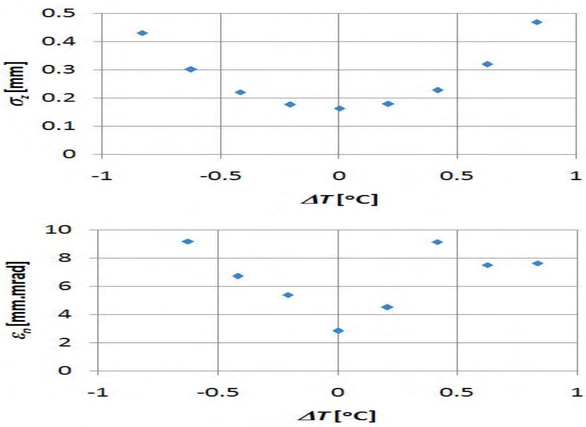

Figure 5: Temperature stabilities of the rms bunch length (top) and the normalized emittance (bottom). Both are the value at 4 m.

Temperature Stability

The amplitude and phase of the SW section are sensitive to the temperature as a high-Q cavity. Their variations were calculated by the HFSS as a function of the frequency, and they are converted at the rate of 48kHz/°C. Those values were put directly into the PARMELA simulation. Figure 5 depicts the effect to the beam dynamics. The emittance was more sensitive than the bunch length. The emittance became 4.5 from 2.8 mm.mrad by 0.2 °C rise while the bunch length was 0.16 to 0.18 mm.

Position Stability

The effect of the offset on the cathode was simulated. The bunch length did not show big change. The emittance degradation was 3.3 to 4.2 mm.mrad with 0.2 mm of the offset.

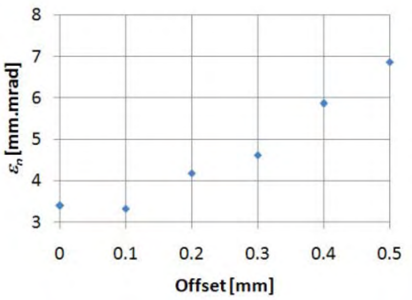

Figure 6: The effect of the beam position offset on the cathode. The normalized emittance was calculated at 4m.

Charge Scaling

The simulation of the various charges was performed according to the scaling law. The bunch size was scaled with $Q^{1/3}$. If the space charge is dominant in the emittance, the scaling factor is $Q^{2/3}$. The factor for the bunch length is $Q^{1/3}$. In Figure 7, PARMELA simulation and the simple estimation were shown. Although there is small deviation from the estimation, it shows good agreement with the scaling law. The emittance and the bunch length of 1-pC beam were 0.019 mm.mrad and 8.8 μm, respectively.

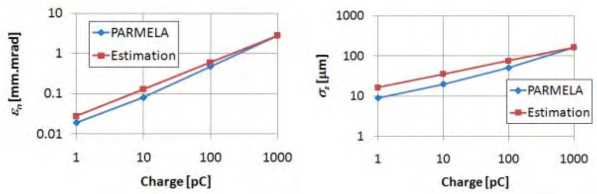

Figure 7: The charge scaling. Simple estimation was made by the factor of $Q^{2/3}$.

Frequency scaling

Frequency scaling was made with frequency scaling law. The field strength is proportional to the frequency, and the length and charge to the inverse of the frequency. They are well agreed with the law as shown in Figure 8. The emittance and the bunch length of 250 pC at 11.424 GHz were 0.79 mm.mrad and 43 μm, respectively. Coupled with charge scaling law, those of 0.25-pC beam were 0.005 mm.mrad and 2.2 μm.

SUMMARY

The beam dynamics of the SW/TW hybrid photoinjector was simulated by using PARMELA. The emittance and the bunch length of the beam with 1 nC were 2.8 mm.mrad and 0.16 mm, respectively. With 0.2 °C of temperature increase, they were 4.5 mm.mrad and 0.18 mm. Offset on the cathode did not affect the bunch length, but the emittance degrades by 0.9 mm.mrad for 0.2 mm of the offset. With 1-pC beam the emittance can be achieved as low as 0.0019 mm.mrad and the bunch length 8.8 μm. With frequency scaling law, X-band case are also calculated. The emittance became 0.79 mm.mrad and the bunch length 43 μm with 250 pC of the charge. When the charge was decreased down to 0.25 pC, the emittance and the bunch length were were 0.005 mm.mrad and 2.2 μm, respectively.

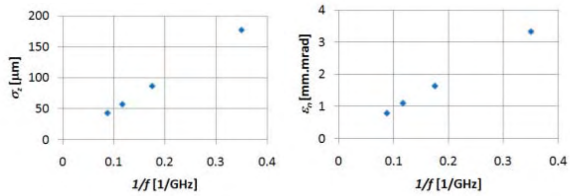

Figure 8: The frequency scaling. The frequencies are 11.424, 8.568, 5712, and 2.856 GHz from the left.

FUTURE WORK

Although the frequency scaling promised to produce good beams, it was still problems to realize it at X-band. The high field, which is four times higher than S-band, would be the problem. The heating and breakdown are the problem on the cavity design. As for the magnetic field, the conducting coils are no longer available because it requires too high current density. Permanent magnet is one of the solutions. It can produce higher field than conducting magnet.

In the S-band system, a shorter hybrid gun in combination with a TW structure is being considered for the normal injection of the driving laser. The laser ports on SW cells are obstacle to the solenoid as well as the emittance degradation problem.

REFERENCES

[1] J.B. Rosenzweig and E. Colby, "Charge and Wavelength Scaling of RF Photoinjectors: A Design Tool", Proceedings of the 1995 Particle Accelerator Conference (IEEE, 1995).

[2] D. Palmer, "The next generation photoinjector", PhD thesis, June 1998.

[3] A. Fukasawa et al., "The FINDER Photoinjector", these proceedings.

[4] B. D. O'Shea et al., "RF Design of the UCLA/URLS/LNFN Hybrid SW/TW photoinjector", AAC'06, Lake Geneva, WI, July, 2006

[5] B. D. O'Shea et al., "Measurement of the UCLA/URLS/LNF Hybrid Gun", these proceedings..

NEW BEAM DIAGNOSTIC DEVELOPMENTS AT THE PHOTO-INJECTOR TEST FACILITY PITZ*

S. Khodyachykh†, G. Asova, J. W. Bähr, C. Boulware, H.-J. Grabosch, M. Hänel, S. Korepanov, S. Lederer, M. Krasilnikov, A. Oppelt‡, B. Petrosyan, S. Rimjaem, T. Scholz, R. Spesyvtsev, L. Staykov, F. Stephan (DESY, Zeuthen, Germany), T. Garvey‡ (LAL, Orsay, France), J. Rönsch (Universität HH, Hamburg, Germany), D.J. Holder, B. Muratori (STFC/DL/ASTeC, Daresbury, Warrington, Cheshire, UK), L. Hakobyan (YerPhI, Yerevan, Armenyia), D. Alesini, L. Ficcadenti (INFN/LNF, Frascati, Italy), D. Richter (BESSY, Berlin, Germany)

Abstract

The Photo-Injector Test Facility at DESY in Zeuthen (PITZ) is an electron accelerator which was built to develop and optimize high brightness electron sources suitable for SASE FEL operation. Currently, in parallel to the operation of the existing setup, a large extension of the facility and its research program is ongoing. The beam line which has a present length of about 13 meters will be extended up to about 21 meters within the next year. Many additional diagnostics components will be added to the present layout. Two high-energy dispersive arms, an RF deflecting cavity and a phase space tomography module will extend the existing diagnostic system of the photo injector and will contribute to the full characterization of new electron sources. We report on the latest developments of the beam diagnostics at PITZ.

INTRODUCTION

The test facility PITZ [1] was built in Zeuthen in collaboration with international partners with the goal to develop and to optimize high brightness electron sources suitable for SASE FEL operation, to compare detailed experimental results with numerical simulations as well as to test new developments such as laser system, photo cathodes and new beam diagnostic elements.

PRESENT BEAM DIAGNOSTICS AT PITZ

The PITZ facility is an electron accelerator which consists of a 1.5 cell L-band RF gun with its photo-cathode laser system, followed by a low energy diagnostics section, a normal-conducting booster cavity and a high energy diagnostics section. Presently both, low and high energy diagnostics sections serve for the precise measurements of the following electron beam parameters:

Beam size, shape and position using YAG or OTR view screen stations combined with the CCD Cameras or using one of two installed wire scanners;

Beam charge using Faraday cups or integrating current transformators (ICT);

Bunch length using aerogel or OTR as radiators, and optical transmission line and a streak camera;

Transverse emittance using three emittance measuring systems (EMSYs) employing the slit scan method;

Beam momentum and momentum spread using a dipole magnet and a view screen at low energy (after the gun) or at high energy (after the booster);

Longitudinal phase space for this type of measurements low energy dispersive arm is equipped with an aerogel radiator and a readout for streak camera.

FUTURE BEAM DIAGNOSTICS AT PITZ

In parallel to beam operation we are permanently extending the diagnostic section in order to enable more detailed studies of the beam properties. The beam line which has a present length of about 13 meters will be extended up to about 21 meters towards the middle of 2008. A schematic layout of the future PITZ beam line is shown in Fig. 1. Several additional diagnostic components will be added to the present setup. Together with the new first high-energy dispersive arm (HEDA1), the deflecting cavity (RFD), and the phase space tomography module (PST), the second high-energy dispersive arm HEDA2 will extend the existing diagnostics system of the PITZ facility. At the beginning of 2008 a new normal conducting booster cavity will run into operation. This will reflect in an increase of the maximum beam momentum. Thus, all new diagnostics elements are designed to operate at beam momenta up to 40 MeV/c.

Upgrade of LEDA

The low energy dispersive arm (LEDA) is a 60° bending magnet located about 1 m downstream the cathode. This magnet is a copy of the dipole magnet used at FLASH facility. Contrary to FLASH, at PITZ only one booster cavity is used for the further acceleration of the beam. For solenoid current settings which correspond to the focusing of the beam downstream of the booster cavity, the beam

* This work has partly been supported by the European Community, contracts RII3-CT-2004-506008 and 011935, and by the 'Impuls- und Vernetzungsfonds' of the Helmholtz Association, contract VH-FZ-005.

† sergiy.khodyachykh@desy.de

‡ Presently at Paul Scherrer Institut, 5232 Villigen PSI, Switzerland.

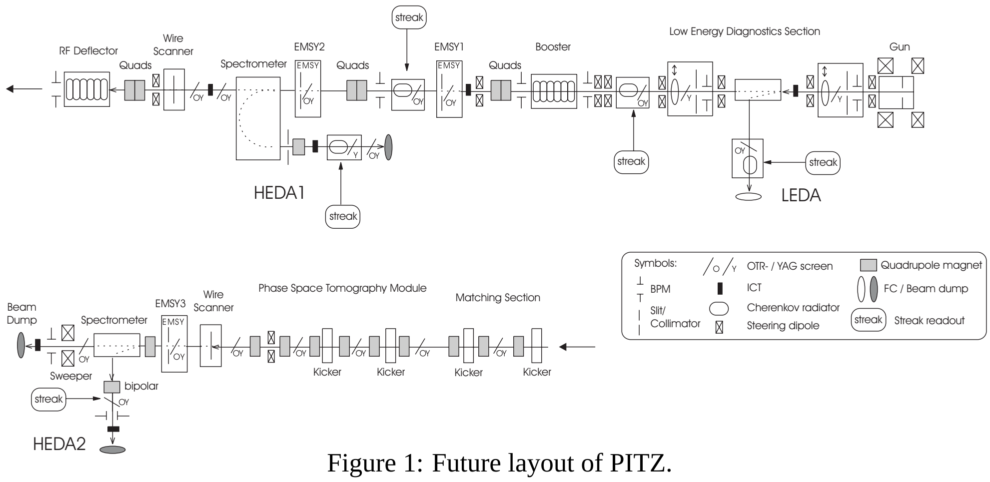

Figure 1: Future layout of PITZ.

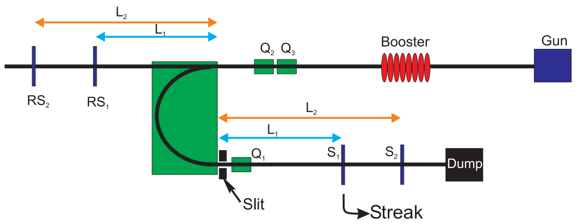

Figure 2: Simplified layout of PITZ with the first high energy dispersive section.

size at the position of the dipole magnet is larger than the vacuum chamber. Thus, the main drawback of the present magnet is the small inner size of the vacuum chamber of only 12 mm caused by a small distance between the pole shoes of only 20 mm. In the nearest future it is planned to re-machine the pole shoes of the dipole magnet of the LEDA and to re-design its vacuum chamber in order to increase the aperture of the vacuum chamber.

Moreover, in order to improve the resolution of the momentum measurements of the low energetic beam we are planning to use a slit upstream the mentioned dipole magnet. For this purpose the new actuator with the slit is under construction for the so-called double-diagnostic-cross (DDC). Moreover, the upgraded geometry of the DDC will improve the vacuum conditions and the situation with wake fields. The new DDC will be installed during the next shutdown.

HEDA1

The first high energy dispersive arm HEDA1 will be placed after the booster cavity, at about 7 m downstream the gun. This multipurpose device is designed [2] and will be put into operation in autumn 2007. It combines the functionality of (i) an electron spectrometer, (ii) a device for the characterization of the longitudinal phase space, and (iii) a transverse slice emittance measuring system. The layout of HEDA1 is schematically shown in Fig 2. It consists of a 180 degree dipole magnet having the bending radius of 300 mm followed by a slit, a quadrupole magnet, and two screen stations. One of the screen stations will be equipped with an optical read-out for a streak camera for investigations of the longitudinal phase space [3]. The functionality of HEDA1 will be enhanced with a setup that allows to measure the transverse emittance of the electron beam at different longitudinal positions along the bunch. The so-called slice emittance provides better understanding of the physics of a photoinjector, particulary the emittance compensation and conservation principles. Using proper phasing of the booster cavity, one can obtain linear correlation between the momentum and longitudinal distribution of the electrons in the bunch. A slit at the dipole exit selects the necessary slice from the energy chirped beam. This slice is scanned with the quadrupole magnet focusing in a plane orthogonal to the dispersion plane and the beam distribution is observed on screen.

The main advantage of the spectrometer based on a 180° dipole magnet is the simplicity to reconstruct the momentum distribution [4]. One uses the reference screen RS_i in the straight section and measures the contribution from the transverse beam size and divergence, which can be deconvoluted with the spectrum measured on the corresponding screen S_i to obtain the pure momentum distribution. This deconvolution is simple and straightforward if the distances L_1 (L_2) from the entrance of the dipole magnet to the measuring S_1 (S_2) and the reference RS_1 (RS_2) screens are equal. For this reason reference screen stations RS_1 and RS_2 are placed downstream of the dipole magnet in the main beam line. Additional components which contribute to the measurements at HEDA1 are two quadrupole magnets Q_2 and Q_3 located in front of the dipole magnet entrance. By focusing the beam on the screen RS_i with the help of these quadrupole magnets one controls the resolution of the momentum measurement on the corresponding screen S_i. The quadrupole magnets Q_2 and Q_3 will also be used as a part of the matching section for the phase space tomography diagnostics described below. HEDA1 will be installed at PITZ during the shutdown of summer 2007.

RF Deflecting Cavity

For a detailed phase space analysis it is planned to install an RF deflecting cavity. Travelling through this cavity, the electron beam will get a time dependent vertical deflection, so that a strong correlation between longitudinal z-coordinate and transverse position is introduced. Further analysis of transverse and longitudinal phase space of the deflected beam can be done in the tomography section and in the second High Energy Dispersive Arm HEDA2 (both described below), respectively. Figure 3 shows a schematic layout of the RF deflector (RFD) followed by a tomography module. For the RF deflector a travelling

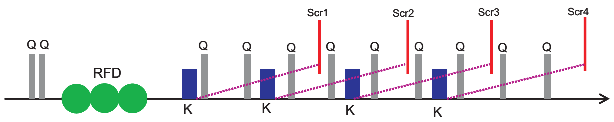

Figure 3: Simplified layout of the RF deflector followed by tomography section.

wave structure was chosen. It has small field filling time (∼0.1 μs). This allows to analyze single bunches without significant distortion of the others in a train of up to 3250 bunches, as foreseen for the European XFEL. To distinguish between deflected and non-distorted bunches several kickers K which kick the deflected bunch in horizontal direction are foreseen downstream the deflecting cavity. The physical design of the deflecting cavity has been done. The RF deflector has to provide a deflecting voltage of up to 1.8 MV and should cause minimal distortion of the beam phase space in the measurement directions. We have compared two travelling wave structures operating at 1.3 GHz and 3.0 GHz frequencies [5], showing a small advantage of the low frequency structure.

Phase Space Tomography Section

For detailed analysis of the transverse phase-space density distribution of the electron beam a phase space tomography section will be installed. The tomography section (Fig. 3) will consist of three FODO cells and four diagnostic stations for measuring the spatial beam density distributions. Several groups of quadrupole magnets distributed upstream along the PITZ beam line will be used to match the beam to the tomography section. Correct matching together with the proper geometry of the FODO cells and magnetic field strengths of its quadrupole magnets are chosen to deliver a phase advance of 45° between the screens. Using modern tomographic algorithms one reconstructs the phase space distribution of the electron beam. Details of the physical design of the tomography section are discussed in [6]. The technical design is almost finalized and hardware components are partly ordered, so that the module will be installed at PITZ in early 2008.

HEDA2

The second high-energy dispersive arm (HEDA2) is in the process of physical design. Similarly to HEDA1, it will be used to measure the momentum distribution, the longitudinal phase space using a Cherenkov radiator and a streak camera and slice emittance. In addition the longitudinal phase space will be studied using the RF-deflector. A major design request is to allow the measurement of the above mentioned beam parameters for bunch trains with up to 3250 pulses and a repetition rate of 10 Hz without significant temporal limitations of running hours. This requires a huge beam dump after the dispersive section, but due to the space restrictions the beam should be transported to the dump of the main beamline. The design considerations for this dispersive arm are discussed in details in [7].

Streak Measurements

A streak station for bunch length measurements after the booster was put into operation at the end of May 2007. The signal from the screen station (Cherenkov or OTR light) is transported to the streak camera by a 30 m long optical transmission line [3] and can be used for bunch length and longitudinal phase space measurements. In the future, using two quadrupole magnets placed directly after the booster, one will be able to conduct streak camera enhanced quadrupole scan for the slice emittance measurements. Future replacement of the refractive optics by reflective one will improve the temporal resolution of the system.

CONCLUSION

We described the new beam diagnostic developments at PITZ. Installation of the new components will open new possibilities in the characterization of the electron beam such as transverse slice emittance, phase space tomography and will provide an improved accuracy of the existing measurements, e.g. longitudinal phase space using an RF deflecting cavity.

REFERENCES

[1] F. Stephan et al., Photoinjector Test Facility under Construction at DESY Zeuthen, Proceedings of FEL 2000, Durham, NC, USA, 2000.

[2] S. Khodyachykh et al., Design and Construction of Multipurpose Dispersive Section at PITZ, Proceedings of DIPAC 2007, Venice, Italy, 2007.

[3] J.Bähr, J.Rönsch, Optical system for measurement of electron bunch length and longitudinal phase space at PITZ: extension and methodical investigations, Proceedings of DIPAC 07, Venice, Italy, 2007.

[4] S. Khodyachykh et al., Design of Multipurpose Dispersive Section at PITZ, Proceedings of FEL 2006, Berlin, Germany, 2006.

[5] S. Korepanov et al., An RF Deflector for the Longitudinal and Transverse Beam Phase Space Analysis at PITZ, Proceedings of DIPAC 2007, Venice, Italy, 2007.

[6] G. Asova et al., Design Considerations for Phase Space Tomography Diagnostics at the PITZ Facility, Proceedings of DIPAC 07, Venice, Italy, 2007, and references therein.

[7] J. Rönsch et al., Design Considerations of a Spectrometer Dipole Magnet for the Photo Injector Test Facility PITZ, Proceedings of DIPAC 07, Venice, Italy, 2007.

NON-INTERCEPTING ELECTRON BEAM TRANSVERSE DIAGNOSTICS WITH OPTICAL DIFFRACTION RADIATION AT THE DESY FLASH FACILITY*

E. Chiadroni†, M. Castellano, LNF-INFN, Frascati, Italy
A. Cianchi, INFN Roma “Tor Vergata”, Roma, Italy
K. Honkavaara, Universität Hamburg, Hamburg, Germany
G. Kube, DESY Hamburg, Germany
V. Merlo, F. Stella, University of Roma “Tor Vergata”, Roma, Italy

Abstract

Since knowledge of the characteristics of the accelerated beams is of a great importance for the successful development of the next generation light sources and linear colliders, characterization of the transverse phase space for high charge density and high energy electron beams is a fundamental requirement in many particle accelerator facilities.

The development of suitable beam diagnostics, non-invasive and non-intercepting, is necessary to measure the properties of such beams. Optical Diffraction Radiation (ODR) is considered as one of the most promising candidates, as shown by the interest of many laboratories all around the world[1],[2].

An experiment based on the detection of ODR has been set up at DESY FLASH Facility to measure the electron beam transverse parameters. The radiation is emitted by a 700 MeV electron beam passing through a 0.5 mm or 1 mm slit. The slit opening is produced by chemical etching on a screen made of aluminum deposited on a silicon substrate. Radiation is then detected by a high sensitivity CCD camera.

The status of the experiment and preliminary results are reported.

INTRODUCTION

Linear colliders and short wavelength Free Electron Lasers (FEL) require ultra-high brilliant electron beams of so much power density that no intercepting device can sustain it. Therefore, non-intercepting diagnostics is strongly desired.

Diffraction Radiation (DR) is emitted by a charged particle beam going through a slit in a metallic foil due to the interaction of the electromagnetic field (EM) of the charge with the boundary. The DR angular distribution is produced by the interference of radiation from both edges of the slit. The visibility of the interference fringes is correlated to the beam size[3]. The effect is also affected, in a slightly different way, by the angular divergence of the beam paving the way to an emittance measurement.

DR THEORY

DR is produced when a charged particle goes through a slit or passes by the edge of a metallic screen, due to the interaction between the EM field of the traveling charge and the target surface[4]. The intensity of the radiation increases linearly with the number of charges and is proportional to $e^{-\frac{2\pi a}{\gamma\lambda}}$, where a is the slit aperture, γ the Lorentz factor and λ the emitted wavelength. The factor $\frac{\gamma\lambda}{2\pi}$, called as DR impact parameter, is the natural size of the radial extension of the EM field, thus when $a \cong \frac{\gamma\lambda}{2\pi}$ DR is emitted.

Since the beam goes through the slit, DR is a non-intercepting diagnostics and therefore excellent to be used parasitically without spoiling the electron beam.

The angular distribution of the DR is mainly affected by beam parameters in the plane orthogonal to the slit aperture: when the transverse beam size is increased, both the peak intensity and the central minimum increase, resulting in the reduction of their ratio. The same effect is also shown when the slit is scanned vertically providing a method to determine the center of the slit by minimizing the minimum of the total intensity.

EXPERIMENTAL APPARATUS

Our experiment is carried out at FLASH, Free electron LASer in Hamburg, at DESY. FLASH is an excellent facility for this experiment, since it can drive long bunch trains, up to 800 bunches per macropulse allowing a high charge operation, and it has a good long term stability, a small transverse emittance ($\sim$ 2 mm mrad), and a high electron beam energy (up to 1 GeV in the near future).

Our experimental set-up is placed in the by-pass beam line (Fig. 1) very far (about 40 m) from the dipole magnets in order to minimize the contribution of synchrotron light.

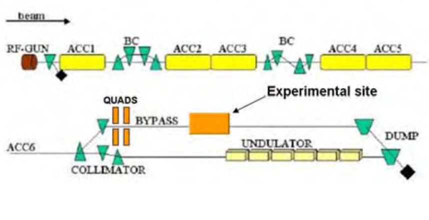

Figure 1: FLASH layout and experimental site.

The experimental apparatus has an aluminized silicon ni-

* Work supported by the European Community Infra-structure Activity under the FP6 “Structuring the European Research Area” program (CARE, contract number RII3-CT-2003-506395)

† enrica.chiadroni@lnf.infn.it

tride screen (DR screen) mounted at 45^o angle with respect to the beam direction. The DR screen is constructed by lithographic technique starting from a silicon nitride wafer and opening two slits, one of 0.5 mm and the other of 1 mm aperture, by means of chemical etching. The slits are spaced by 2 cm and the space between the slits is used as a standard OTR screen. The main advantage of the silicon nitride with respect to SiO_2[5] is a much less etching rate which preserves the silicon substrate from damages and makes the surface much more uniform. An aluminum layer is deposited by sputtering on the target to enhance the reflectivity.

Radiation from the target is reflected by a mirror and sent through an optical system to the camera. Two lenses, one to image the beam, the other one to produce the DR angular distribution, can be selected. They have different focal length in order to have the focus on the same plane. Two interferential filters, at 800 nm and 450 nm, and a polarizer may be inserted on the optical axis. Due to the very low radiation intensity, a high sensitivity CCD camera (Hamamatsu Model C4742-98-LGLAG2) is used. The optical system layout is shown in Fig. 2.

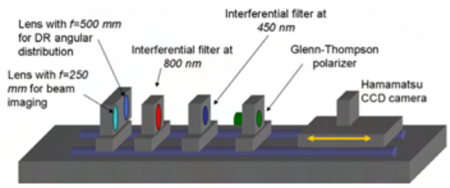

Figure 2: Sketch of the optical system.

PRELIMINARY RESULTS

In this section we report the preliminary results obtained with a 680 MeV electron beam energy going through a 0.5 mm slit. During measurements reported in this paper, FLASH was operated with up to 25 electron bunches (0.7 nC per bunch) per macropulse with 1 MHz bunch spacing. The macropulse repetition rate was 5 Hz.

The image of the beam and its intensity projection are shown in Fig. 3a and Fig. 3b, respectively. The retrieved rms size is about 80 μm. Since Optical Transition Radiation (OTR) is theoretically and experimentally well understood, we first verified our experimental setup by acquiring the OTR angular distribution (Fig. 4) and deriving from that the beam energy. The uncertainty on the beam energy, about 10%, is compatible with the uncertainty on both the focal length and the position of the focal plane. The disagreement on the minimum depth between the measured and the simulated curves might be attributed to a residual background and not to the angular divergence of the beam.

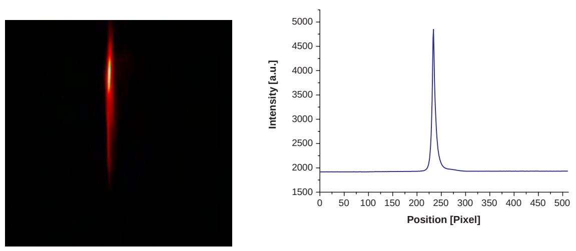

(a) Beam image (b) Beam projection

Figure 3: Image of the beam on the OTR screen (a) and its projection (b).

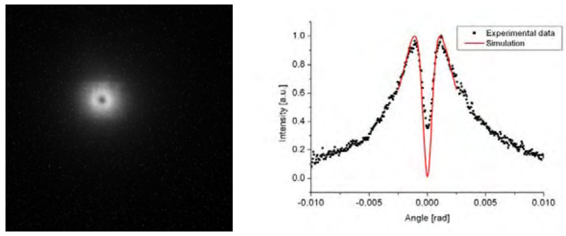

(a) OTR angular distribution and background (b) OTR projection

Figure 4: OTR angular distribution: a) image with background, b) measured and simulated projection.

Critical Issues

The main limitation during the measurements was given by the synchrotron radiation background coming not only from the dipole, but also from the quadrupole magnets upstream of our experiment and from multiple reflections in the vacuum pipe. As a consequence, the background is the image of a source apparently near (few meters) to the target itself, clarifying its peculiar shape and preventing from the knowledge of a theoretical behavior which would be easily subtracted.

The background image is every time acquired by moving the beam out of the screen by means of steering magnets upstream of the target. However, since the steered beam hits the vacuum pipe, this procedure gives rise to a large amount of X-rays. In order to increase the signal-to-noise ratio, a large number of images has been recorded. The images are then off-line processed in order to first eliminate X-rays and then subtract the background from the signal.

ODR Evidences

To take a snapshot of a clear signature of ODR angular distribution, several images of both signal and background have been acquired scanning vertically the slit aperture.

Figure 5 shows the vertically polarized angular distribution for three values of displacement of the beam with respect to the center of the slit. The corresponding measured angular distribution projection is shown in Fig. 6a). The black squares curve corresponds to the beam in the center (ODR). As we move far from the center, both the minimum and the maximum intensities increase and the visibility of

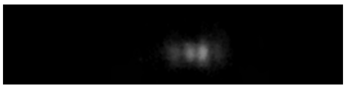

(a) 0 μm

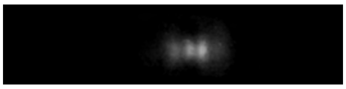

(b) 100 μm

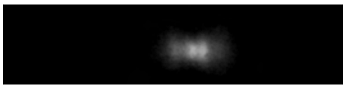

(c) 200 μm

Figure 5: Vertically polarized angular distribution for different position of the beam within the slit.

the interference fringes becomes less pronounced, as also shown by the simulation (Fig. 6b). The noisy and asymmetric curves are due to a residual background contribution.

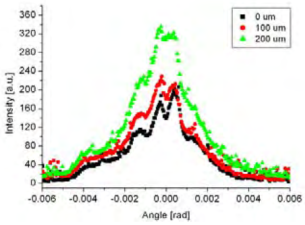

(a) Experimental data

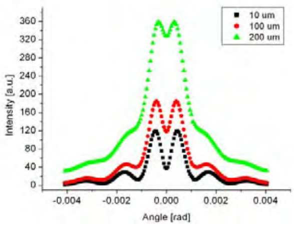

(b) Simulation

Figure 6: Angular distributions for different positions of the beam with respect to the center of the slit. Both the polarizer and the 800 nm filter are inserted.

As expected from theory, Fig. 7 shows the minimum intensity corresponding to the center of the slit. In optimum conditions and with a better background subtraction, this result might be used as independent measure to determine the beam size[6].

From the previous scan we determined the center of the slit and we performed a dedicated measurement of ODR signal and background to optimize the subtraction procedure. For this measurement, the projection of the ODR angular distribution image is shown in Fig. 8 (black squares). A simulation which takes into account a Gaussian distributed beam with $\sigma = 70$ μm and $\sigma^{'} = 30$ μrad, shows a good qualitative agreement with the measured ODR projection (Fig. 8, red line).

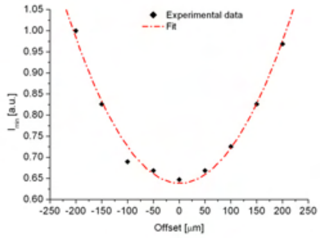

Figure 7: Measured dependencies of ODR minimum intensity as function of the displacement of the beam within the slit.

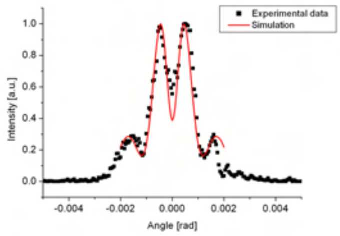

Figure 8: ODR angular distribution: 25 bunches, 0.7 nC per bunch, 0.5 mm slit. Polarizer and 800 nm filter are inserted.

CONCLUSIONS

The background is a severe limitation for a detailed and quantitative reconstruction of the beam parameters from the ODR angular distribution. To reduce its influence we have foreseen to mount a new thin shield in front of the target and replace the holder with one which is machined such that reflections are strongly suppressed.

In our data analysis we have put much effort on the image processing to clean images from X-rays and to subtract the synchrotron radiation background. This allowed us to prove a good qualitative agreement between the experimental data and the simulations.

REFERENCES

[1] P. Karataev et al., Phys. Rev. Lett. 93, 244802 (2004)

[2] A. H. Lumpkin et al., Phys. Rev. ST Accel. Beams 10, 022802 (2007)

[3] M. Castellano, Nucl. Instr. and Meth. in Phys. Res. A 394, 275 (1997)

[4] M.L. Ter-Mikaelian, “High-Energy Electromagnetic Processes in Condensed Media”, Wiley-Interscience

[5] E. Cianci et al., “Micromachined silicon slit for beam diagnostic in particle accelerator” Proc. SPIE, 4557, pp. 242-249 (2001)

[6] Dao Xiang and Wen-Hui Huang, Nucl. Instr. and Meth. in Phys. Res. B 254, 165 (2007)

DESIGN AND ELECTROMAGNETIC ANALYSIS OF THE NEW DAFNE INTERACTION REGION

F. Marcellini, LNF-INFN, Frascati, Italy

Abstract

A new interaction region (IR) vacuum chamber has been designed for the DAFNE upgrade aimed at testing of the crabbed waist collision scheme.

Compared to the existing IR vacuum chamber, the new one has a simplified design and consists essentially of the confluence of straight tubes, having a double Y shape.

Sharp discontinuities have been avoided to limit the beam impedance of the structure. However, the study of the electromagnetic interaction with the beam is necessary in order to avoid excessive power loss due to possible higher order modes (HOM) trapped in the Y-shape chamber. The first design of the chamber has been analyzed with HFSS and HOMs have been found and characterized. On the basis of these results some modifications in the geometry of the IR chamber have been introduced to eliminate or attenuate these trapped resonances. The results of these simulations are presented.

New electromagnetic shielding for the bellows inserted in the IR chambers, have been developed as well. The design criteria and the simulation results for these shielded bellows are also reported.

INTRODUCTION

The Φ-Factory DAFNE has been delivering luminosity to the KLOE, DEAR and FINUDA experiments since year 2000. FINUDA has concluded its run just this month. A significant upgrade of DAFNE, with the aim to increase the machine luminosity, is now in progress and will be completed before starting the run dedicated to the SIDDHARTA experiment. One of the most important operations foreseen for this upgrade is the installation of a new IR, suitably designed to exploit the “large crossing angle” and “crabbed waist” concepts according to the scheme presented at the 2nd Frascati Workshop on SuperB-Factory, March 2006 [1]. This scheme does not need very short bunches in the rings, that is the standard (but very expensive and difficult) way to increase the luminosity.

Operating with long bunches, the problems related to the beam coupling impedance of the vacuum chamber are relaxed, because the beam power spectrum is limited to a lower frequency region and possible high frequency impedance contributions are less dangerous. Nevertheless, great care has been taken to minimize the impedance of every new component and device designed for this upgrade.

Concerning the IR, at a first sight [2], owing to its simplified design, the new chamber layout should have smaller impedance with respect to that has been operating till now. A drawing of the vacuum chambers of one half of the IR is reported in Fig. 1. The beam pipe appears composed essentially by straight tubes without sharp discontinuities, except for the Y-shape section, where the common IR chamber is split in the two separate rings. HOMs could be trapped in the Y-section and, if the beam interacts with them, problems related to power losses may arise. This effect has been experienced at SLAC in the PEP-II collider, where power losses in the Y-shaped chamber of the order of several kW have been measured [3]. To evaluate parameters of the potentially dangerous HOMs, a frequency domain analysis of the structure has been carried out with the HFSS [4] code.

Figure 1: The new IR vacuum chamber layout (half).

Eight bellows will be installed on the IR (blue coloured in Fig.1) to compensate misalignments between pieces of chamber. Eight other bellows are on the chambers diametrically opposite to the IR. These bellows must be provided with a RF shield to avoid looking like cavities for the beam. Two different new shield designs have been developed starting from the experience gained in the shields of the existing DAFNE bellows [5] [6]. Also in this case, the design has been aided by checking the shielding properties of the proposed solutions by HFSS.

IR VACUUM CHAMBER

Even if all the possible discontinuities have been avoided in the design of the IR chambers, the points where the two rings join together in a single pipe are sources of beam produced e.m. fields. HFSS simulations have pointed out that these fields are able to give rise to trapped HOMs. The results of the eigenmode simulations are summarized in terms of mode frequencies, Q values and field configurations in Fig. 2. Only the modes having TE_{11} transverse configuration, which are the lower frequency modes, have been considered applying the proper boundary conditions on the symmetry planes. Despite the HOM electric field is directed horizontally it still contributes to the power losses since the beam trajectory is not symmetric with respect to the vacuum chamber axis. The pipes diameter is 55mm in all the three branches of the Y and the TE_{11} cut off is 3.2373GHz. In each of the two tables of Fig. 2, the 5th mode propagates out of the pipe as pointed out by a driven mode solution with matched ports at the structure ends. In a first design the diameter of the common pipe was larger (61mm) and afterwards it has been reduced to increase the frequency of the first trapped resonance and then to reduce the total number of HOMs.

TE11 modes Even IP symmetry	f [GHz]	Q
Mode 1	3.0517	14783
Mode 2	3.1484	15924
Mode 3	3.1873	11441
Mode 4	3.2019	12414
Mode 5	3.2314	

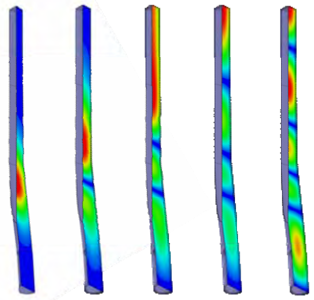

TE11 modes Odd IP symmetry	f [GHz]	Q
Mode 1	3.0499	15430
Mode 2	3.1461	13750
Mode 3	3.1863	10667
Mode 4	3.2113	10923
Mode 5	3.2404	

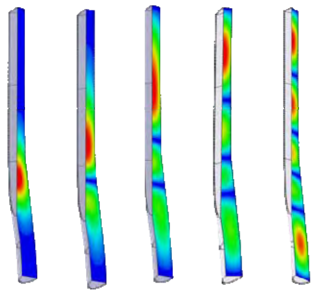

Figure 2: List of the first 10 TE_{11}-like modes found by HFSS eigenvalue solution with even and odd symmetry conditions with respect to the IP. The 5th mode frequency is above the cut off of the pipe.

The coupling impedance of each HOM depends on the component of the electric field which is parallel to the beam trajectory (reported in Fig. 3 for the 2nd odd, to give an example), on the power dissipated on the aluminium chamber walls and on the mode frequency.

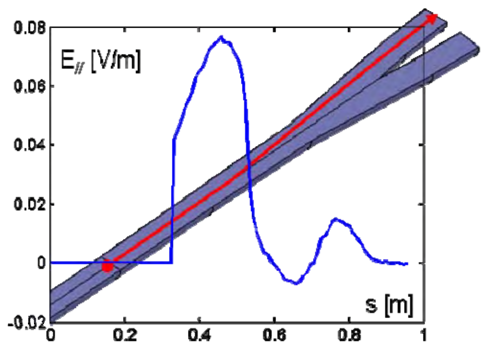

Figure 3: Electric field component tangential to the beam trajectory for the mode2 odd (from HFSS simulations).

Since the field is not concentrated in a relatively short gap, like in a cavity, but it interacts with the beam for a long distance, impedance is very sensitive to frequency variations through the transit time factor. The HFSS model used in simulations leaves out a number of small mechanical details and possible imperfections that could yield shifts of the actual HOM frequencies with respect to the calculated values. For this reason each mode impedance has been evaluated as a function of the mode resonant frequency around the nominal value obtained by simulations. The results are shown in Fig. 4.

The beam power spectrum (BPS) lines at the 8th and 9th RF frequency harmonics (FH) are the closest to the frequency of these HOMs.

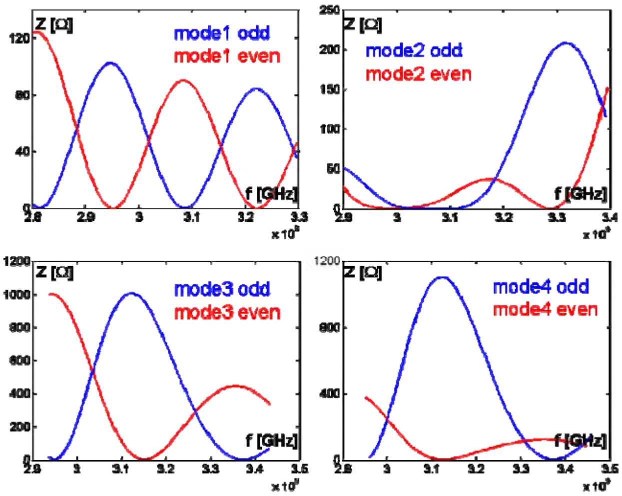

Figure 4: Coupling impedance of the 8 TE_{11}–like trapped modes as a function of their frequency.

But the 9th FH (3.314GHz) is above the frequency cut-off of the beam tube and the 8th FH (2.946GHz) is about 200MHz below the lowest frequency HOM. Therefore, if the HFSS evaluated frequencies are exact, no coupling between the BPS lines and the HOMs is possible and no beam power is dissipated on the chamber walls. The worst possible scenario should happen when the HOM with the highest impedance at the 8th FH (mode3 even) has a frequency shifted by more than 240MHz and it full couples to the 8th FH. In this case, considering a 2A beam stored current and a 2cm bunch length, the power losses would be about 1.7kW, dissipated on a 2m long pipe. The only mode having the field concentrated in a relatively short region is the mode 1 and, if full coupling occurs, the power losses would be less than 200W. Despite such a power seems to be manageable, two cooling channels have been placed at each Y-chamber junction.

BELLOWS SHIELDINGS

Four bellows are placed in each sector drawn in Fig. 1. They connect pipes having circular cross section with 88mm diameter. The inner radius of bellows convolutions is about 65mm, the outer one 80mm and the length about 50mm. Then a RF shield is necessary to hidden the chamber discontinuity to the beam.

The previously adopted shields [6] are made with a number of mini-bellows lined up very close to each other in order to reproduce the pipe section. This solution had the problem that the mini-bellows are tending to lose their elasticity and, when compressed, they could bend degrading the uniformity of the shield contour.

The new bellows shield has been designed as described in Fig. 5. Two cylindrical shells made of aluminium are fixed at the bellows ends and assure continuity to the beam pipes except for the gap between them. But even this gap is shielded by a number of adjacent Be-Cu strips placed all around the Al shells. The shape of the strips is preformed as two waves that give elasticity to the system and a central flat region that shields the shell gap.

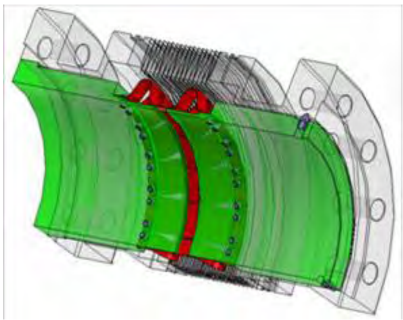

Figure 5: The new IR shielded bellows (a quarter section).

Fig. 6 shows the fields generated in the structure by the beam. The beam is represented by a current flowing along a coaxial conducting wire. The field coming out of the shield is completely negligible in the left plot where the strips are in contact with the two half shells. The unshielded field increases if this contact is lacking. The plot on the right of Fig. 6 shows the situation in presence of 0.3mm separation. Nevertheless, in both cases, to appreciate the presence of a field in the volume outside the shield without saturation inside, a logarithmic intensity scale has been used. The contact between strips and cylindrical shells will be ensured by a spring wrapped around the flat part of the strips [7].

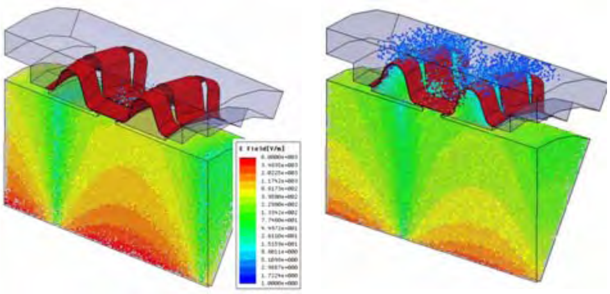

Figure 6: Beam generated fields in the shielded bellows at 3 GHz (HFSS simulations). Left: strips in contact with the cylindrical shells. Right: 0.3mm gap between them.

The coupling impedance of the structure has been evaluated in a frequency range from DC to 5 GHz and the result, reported in the plot of Fig. 7, is a confirmation of very low impedance values.

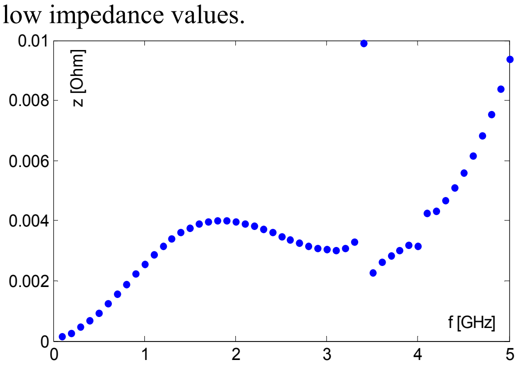

Figure 7: Shielded bellows coupling impedance.

The above described shielding has been preferred, because it is simpler to realize and cheaper with respect to a different solution previously designed and shown in the drawing of Fig. 8 (left). It consists of a grid of preformed Be-Cu strips. The number of the strips and their dimensions along the radial coordinate have been determined by several HFSS simulations. The plot on the right of Fig. 8 shows that, up to 5 GHz at least, the field remains sufficiently confined by the shield when the spacing is 10 degrees and the strip height is 20mm.

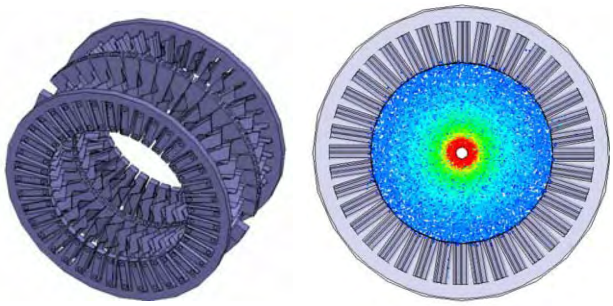

Figure 8: Study of an alternative bellows shielding.

CONCLUSIONS

The design of the new IR vacuum chamber for the DAFNE upgrade has been carried out with the goal to reduce the number of trapped HOMs and limit their effects in terms of interaction with the beam. The simulation results ensure a comfortable situation since the probability of HOM coupling with the power beam spectrum lines is very weak and, even if it occurs, the power losses can be easily managed.

The contribution to the impedance given by the new shieldings developed for the bellows of the IR is completely negligible.

REFERENCES

[1] M. Biagini et al., “DAPHNE Phi-Factory Upgrade for Siddharta Run”, this conference, MOOBKI02
[2] S. Tomassini et al., “DAPHNE Upgrade: A New Magnetic and Mechanical Layout”, this conference, TUPAN036.
[3] A. Novokhatskii, presentation at the 3rd SuperB Workshop, SLAC, June 2006, http://www-conf.slac.stanford.edu/superb/
[4] http://www.ansoft.com/products/hf/hfss/
[5] G.O. Delle Monache, A. Gallo, A. Ghigo, F. Marcellini, L. Palumbo, B. Spataro, G. Vignola, M. Zobov: "DAFNE Shielded Bellows", Nuclear Instruments & Methods in Physics Research A 402 (1998) 27-35.
[6] G.O. Delle Monache, A. Gallo, F. Marcellini, M. Zobov: "Power Losses in the DAFNE Shielded Bellows", G-43, 18/11/1996
[7] G. Sensolini, private communications.

RF MEASUREMENTS RESULTS OF THE FINAL BRAZED SPARC RF DEFLECTOR *

L. Ficcadenti, L. Palumbo, A. Mostacci, University ”La Sapienza”, Rome, Italy
D. Alesini, C. Vaccarezza, G. Di Pirro, LNF-INFN, Frascati, Italy
J. Rosenzweig, UCLA, Los Angeles, USA

Abstract

The longitudinal phase space and the horizontal beam slice emittance measurements of the SPARC $150MeV - 1nC$ electron beam, foresee the use of a RF deflector. The device is a five cells standing wave structure operating on the TM110-like dipole mode at $2.856Ghz$ and allows reaching a longitudinal resolution of $\sim 12um$ with $2MW$ of peak input power. In the paper we illustrate the RF measurements results on the final brazed copper device.

INTRODUCTION

The characterization of the longitudinal and transverse phase space of the SPARC [1] beam is a powerful tool in order to verify and tune the photoinjector performances. With the use of an RF deflector it is possible to measure the bunch length ([2] [3]) and, adding a dispersive system, the longitudinal beam phase space can be completely reconstructed. In the first section of this paper we briefly review the SPARC RF deflector design parameters. In the second paragraph we report the RF measurement results on the final copper device before the brazing. In the third paragraph we illustrate the adopted tuning procedure and the final RF measurement results on the brazed device. The conclusions are reported in the last section.

RF DEFLECTOR DESIGN PARAMETERS

A sketch of the complete longitudinal phase space measurement setup of the SPARC beam is shown in Fig. 1. The SPARC bunch is vertically deflected by the RF deflector and horizontally by a magnetic dipole: this allows to completely characterize the energy distribution of each bunch slice reconstructing the longitudinal phase space, as discussed in detail in [4]. The RF Defector is a 5-cell SW structure operating on the π mode 2. This structure allows

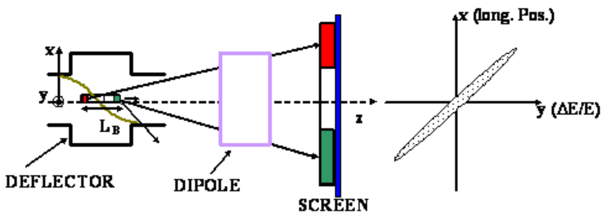

Figure 1: Layout of longitudinal phase space measurement setup.

* This work has been partially supported by the EU in the sixth framework program, Contract no. 011935 EUROFEL-DS1.

Table 1: SPARC RF deflector main dimensions and parameters.

Dimensions [mm]		Parameters	
b_2	60.72	$f_{res}[GHz]$	2.855961
b_1	59.93	Q_0	16540
b_0	60.04	$R_T[M\Omega]$	2.44
a	20	$\frac{R_T}{Q}[\Omega]$	147
t	9.5	β	1

reaching a maximum transverse deflecting voltage of more than $3MV$ with on input power of $\sim 2MW$ and a longitudinal resolution lenght of $\sim 12um$ [4]. The structure has been design using the electromagnetic codes MAFIA and HFSS. The dimensions and main parameters are reported in Table 1. The radius of the cells has been slightly adjusted in order to obtain a B-field flatness smaller than 5%. Concerning the coupler design it has been inserted in the central cell in order not to exite the nearest mode that have no field in the central cell. The dimension of the coupler window and of the coupler cell radius b_0 have been tuned in order to obtain a coupling coefficient $\beta = 1$ and a resonant frequency equal to $2.856GHz$ and to preserve a good B field flatness. The tuning system has been realized using metallic cylinders of $5mm$ radius that can compensate all possible machining errors.

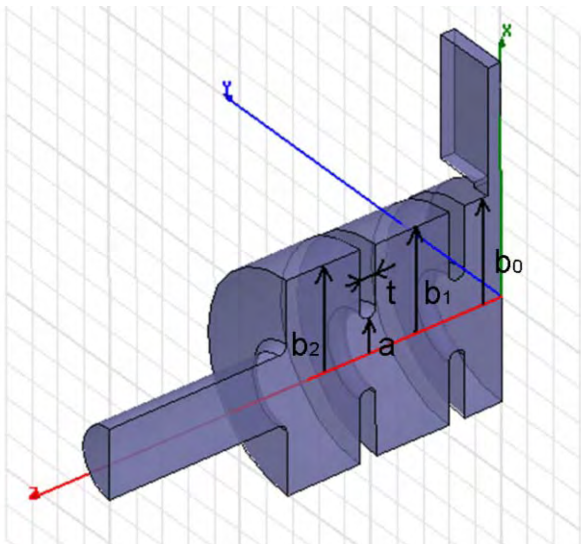

Figure 2: 3D sketch of a quarter of the SPARC RF deflector.

MEASUREMENT RESULTS BEFORE BRAZING

Resonant frequency and input port coupling measurements

The reflection coefficient at the coupler input port before the tuning procedure is reported in Fig. 3. As expected, it was possible to excite only three of five deflecting modes. The measured external quality factor of the working mode was $Q_{EXT} \cong 17050$, while the measured unloaded quality factor Q_0 was $\cong 15500$ and was lower than the expected one because of the fact that the structure was simply assembled and not brazed. The corresponding coupling coefficient β was $\cong 1.1$.

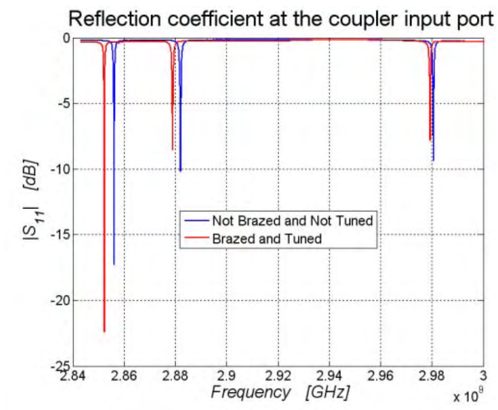

Figure 3: Measured reflection coefficient at the input port.

Field measurement results

The measurements of the field in the cavity have been done with the bead-pull resonant technique ([5] [6]). The measurement setup with the device before brazing is given in Fig. 4. The PC controls both the network analyzer (NA)

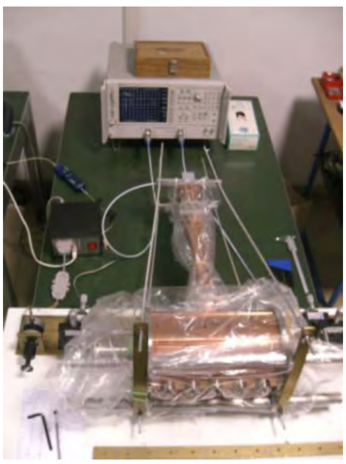

Figure 4: Measurement setup with the device before brazing.

HP8753E and the control circuit of the stepping motor. The nylon wire is kept straight by a $75g$ weight. Since the the deflection is given by both magnetic and electric fields, both components have to be measured for device characterization. With a small dielectric (teflon) cylinder we have measured the on axis E field component only while, with a small metallic cylinder both B and E field components. The detailed description of such type of measurements is reported in [4]. We have measured the field flatness of the on axis H field before brazing the cavity. The deflector were simply assembled by a dedicated metallic cage. The measurement results obtained in air at room temperature of about $22°C$ are reported in Fig. 5, in this case the tuners position were close to the internal surface. The field flatness

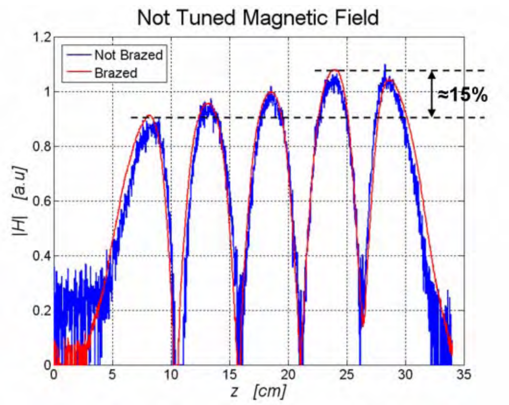

Figure 5: Measured on axis H field in the not tuned cavity.

was $\cong 15\%$ and the resonant frequency $\cong 2.8563GHz$ in good agreement with expectations even if a dedicated tuning was necessary to obtain a field flatness of the order of 5%.

MEASUREMENT RESULTS AFTER BRAZING AND FINAL TUNING

After the cavity brazing, the device has been installed in SPARC (Fig. 6) to tune the structure at the working temperature of $45°C$. The measurements of the H field profile is

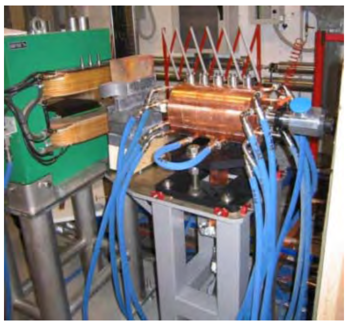

Figure 6: RF deflector installed in SPARC.

reported in Fig 5. As the plots shows, the brazing procedure has not modified the structure dimensions. The measurements before brazing is more noisy because we used a reduced NA input power. The H field measurements and the tuning has been done in air. For this reason, we tuned the structure at the frequency of $f_{res}^{air} \cong 2.8551 GHz$. To tune the deflector we have linearized the field profile sensitivity and the resonant frequency as a function of the tuner positions around the initial working point following the steps described below:

- we have measured H field peaks of each cell ($H_{0,i}$) at the initial resonant frequency (f_{res0});
- we have measured the sensitivity coefficients of the H field ($\frac{\partial H_i}{\partial t_j}$) and of the resonant frequency ($\frac{\partial f_{res}}{\partial t_j}$) as a function of tuner positions;
- to find the required relative tuner variations (Δt_j) we have resolved the following system:

$$\begin{cases} H_{0,i+1} - H_{0,i} = \displaystyle\sum_{j=1}^{5} \left(\frac{\partial H_i}{\partial t_j} - \frac{\partial H_{i+1}}{\partial t_j} \right) \cdot \Delta t_j \\ f_{res} - f_{res0} = \displaystyle\sum_{j=1}^{5} \left(\frac{\partial f_{res}}{\partial t_j} \right) \cdot \Delta t_j \end{cases} \quad (1)$$

where $i = 1, \cdots, 4$. and $f_{res} = 2.8551 GHz$ As example, the resonant frequency as a function of the first tuner position is reported in Fig. 7. In the same plot it is reported the linearized curve that gives the frequency sensitivity. Fig. 8

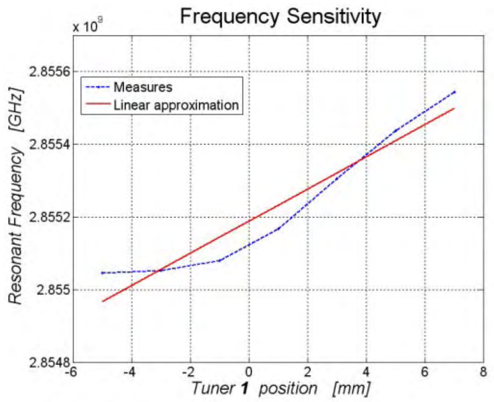

Figure 7: Frequency sensitivity at different tuner positions.

shows the H field amplitude in the first cell as a function of the tuner positions. The final tuned field profile at the frequency of $2.8551 GHz$ is reported in Fig. 9. The reached field flatness is $\cong 4\%$, according with the SPARC RF deflector requirements [4]. The final reflection coefficient at the coupler input port after brazing and tuning is reported in Fig. 3. The corresponding unloaded quality factor and coupling coefficient are $\cong 16000$ and $\cong 1.1$ respectively.

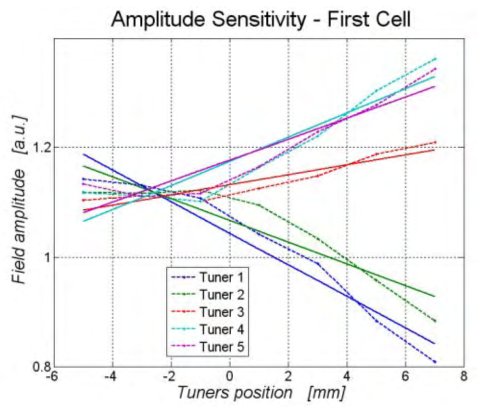

Figure 8: First cell field amplitude sensitivity at different tuner positions.

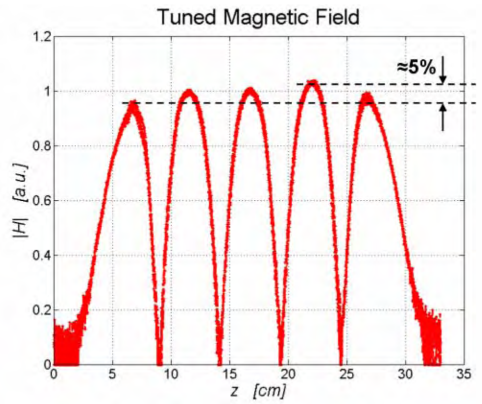

Figure 9: Measured on axis H field in the brazed tuned cavity.

CONCLUSIONS

The SPARC RF deflector as been successfully designed, realized and brazed at LNF-INFN. It is a five cell SW structure operating at $2.856 GHz$ made in copper. A complete RF characterization using bead-pull and scattering coefficient measurements, has been done before and after brazing. A dedicated tuning procedure has been implemented to reach a field flatness of few percent at the designed resonant frequency.

ACKNOLEDGEMENTS

The authors would like to thank A. Clozza, V. Lollo and R. Di Raddo for mechanical drawings, realization and technical support.

REFERENCES

[1] Preliminary TDR of SPARC, www.lnfn.infn.it, 2004.
[2] G.A. Loew, O.H. Altenmuller, SLAC, PUB-135, August 1965.
[3] P. Emma, et. al. LCLS-TN-00-12, 2000.
[4] D. Alesini, et. al.,NIM, A 568 (2006) 488-502.
[5] L.C. Maier,J.C. Slater, J. Appl. Phys.,23 (1) (1951).
[6] F. Caspers,G. Dome, CERN SPS/85-46 (ARF), 1985.

COMMISSIONING OF THE UCLA NEPTUNE X-BAND DEFLECTING CAVITY AND APPLICATIONS TO CURRENT PROFILE MEASUREMENT OF RAMPED ELECTRON BUNCHES*

R. J. England, B. O'Shea, J. B. Rosenzweig, G. Travish, UCLA, Los Angeles, CA 90095, USA
D. Alesini, INFN/LNF, Frascati, Italy

Abstract

A 9-cell standing-wave deflecting cavity has recently been constructed and installed at the UCLA Neptune Laboratory for use as a temporal diagnostic for the 13 MeV, 300 to 700 pC electron bunches generated by the Neptune photoinjector beamline. The cavity is a center-fed GlidCop structure operating in at $\mathrm{TM}_1 10$-like deflecting mode at 9.59616 GHz with a π phase advance per cell. At the maximum deflecting voltage of 530 kV, the theoretical resolution limit of the device is 50 fs, although with current beam parameters and a RMS spot size of 460 μm the effective resolution is approximately 400 fs. We discuss the operation and testing of the cavity as well as its intended application of measuring the temporal current profile of ramped electron bunches generated using the Neptune dogleg compressor, and we present the first measurements of the electron beam current profile obtained using the deflecting cavity.

INTRODUCTION

We recently proposed a scheme for generating relativistic electron bunches having a triangular or ramp-shaped current profile (i.e. rising linearly from head to tail and then dropping sharply to zero) and initiated an experiment to test this technique at the UCLA Neptune linear accelerator laboratory [4]. A triangularly ramped bunch approximates the so-called "doorstep" profile which has been predicted by both 1D and 2D plasma theory to be an ideal shape for the drive beam in a plasma wakefield accelerator (PWFA) [1, 2, 3], as it maximizes the *transformer ratio*, which is a figure of merit for the PWFA, defined by $R = E_+/E_-$ where E_+ is the peak accelerating field behind the bunch and E_- is the peak decelerating field within the bunch.

The proposed method for generating the ramped bunches is discussed in detail in Ref. [4]. In short, the technique requires injecting an electron bunch with a positive energy chirp (i.e. particles at the head of the bunch are at higher energy) into a dogleg, or dispersionless translating section, which serves as a bunch compressor. A cartoon of the experimental beamline is shown in Fig. 1. The bunch-shaping mechanism is dependent upon the z phase space transformation being *linear* (i.e. dominated by the linear longitudinal dispersion term or R_{56} in transport notation). However, since a chirped beam injected off-crest tends to have

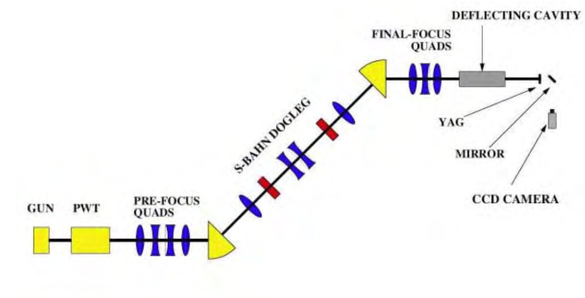

Figure 1: Cartoon drawing of experimental beamline.

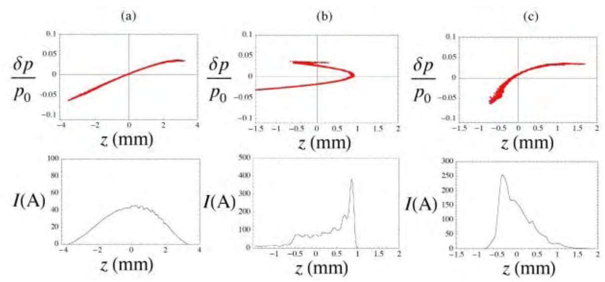

Figure 2: Plots showing (a) an initially chirped distribution in longitudinal phase space which has been artificially manipulated by imposing the simple transformation of Eq. 1 with (b) both the R_{56} and T_{566} terms included and (c) only the R_{56} term included.

a larger energy spread, the longitudinal dispersion contains a significant second-order contribution. The longitudinal transport to second order is therefore approximated by

$$z_f \approx z_0 + R_{56}\delta + T_{566}\delta^2, \qquad (1)$$

where z_0 and z_f are the initial and final longitudinal coordinates of a test particle and $\delta = \Delta p/p_0$ is the momentum error. The second-order contribution to the longitudinal dispersion is represented by the transport matrix element T_{566}. Elimination of the T_{566} contribution is accomplished by the use of sextupole corrector magnets, shown as red rectangles in Fig. 1.

The fundamental bunch-shaping mechanism is illustrated in Fig. 2, where an initially chirped distribution of particles in longitudinal phase space, shown in part (a), has been artificially manipulated by applying the transformation of Eq. 1 to each particle in the distribution. In part (b) both the linear and quadratic terms have been included

* Work supported by U.S. Department of Energy under Grant No. DE-FG03-92ER40693

(with values of R_{56} and T_{566} similar to those of the actual beamline) whereas in (c) only the linear R_{56} term is included. We see in part (c) that the linearized transformation in conjunction with the intrinsic RF curvature of the initial distribution produces a "hook-shaped" distribution with a ramp-shaped current profile.

Experimental measurements of the post-compression bunch length, obtained by coherent transition radiation (CTR) interferometry, as a function of sextupole strength have been reported previously and compared favorably with simulations using the particle tracking codes PARMELA and ELEGANT [4]. However, CTR interferometry does not provide detailed information about the longitudinal shape of the electron bunch. Consequently, a transverse deflecting mode cavity was designed and built as a temporal diagnostic capable of resolving the temporal structure of the sub-picosecond to several picosecond duration electron bunches generated by the Neptune linear accelerator beamline and dogleg compressor. When a beam is injected into such a cavity at the zero-crossing of the RF, it experiences a transverse momentum kick along the orthogonal transverse axis whose strength is approximately linear in the arrival time of the particles. As a result, the longitudinal distribution of the beam is deflected transversely and can be imaged on a simple profile monitor located downstream (see e.g. Ref. [5]).

DEFLECTING CAVITY DESIGN

The deflecting cavity which was recently built and commissioned for use in the Neptune laboratory is a 9-cell standing-wave structure, operating in a TM_{110}-like dipole mode. The cavity design is distinguished by a number of unique features. These include the high (X-Band) operating RF frequency of 9.59616 GHz, low input power requirement (50 kW), and the use of a knife-edge conflat-style vacuum seal machined directly into the mating faces of the cells, which allows the cavity to be easily disassembled and eliminates the need for brazing or welding, which can warp and detune the cells. The cavity material was chosen to be GlidCop Al-15. A drawing of the assembled prototype cavity is shown in Fig. 3 with a quarter section removed to reveal the interior of the structure. The 9-cell structure was designed in three phases (with two prototypes) using the commercial RF modeling code HFSS 9.2. A list of simulated and measured parameter values are shown in Table 1.

The temporal resolution limit due to the camera and optics used to image the final screen is approximately 50 fs. However the achievable temporal resolution of the deflecting cavity was found to be limited by the minimum spot size σ_0 that can be achieved on the downstream imaging screen when the cavity is turned off to a value of approximately 400 fs at the maximum cavity voltage of 530 kV.

A bead pull was performed using an uncalibrated aluminum bead. The resulting shift in frequency as a function of the bead position along the cavity axis (Fig. 4) was measured using a network analyzer. The frequency shift for a spherical bead is related to the field amplitudes E_0 and H_0 along the axis by the formula $\Delta f/f_0 = \pi a^2(|E_0|^2 - \frac{1}{2}|H_0|^2)/W_0$, where a is the bead diameter, and W_0 is the stored energy in the cavity [6]. Consequently, the positive peaks in Fig. 4 correspond with the irises where E_0 is maximum, and the negative peaks correspond with the centers of the cells where H_0 is maximum. The field imbalance appears magnified by the dependence of the plot on the square of the fields $|E_0|^2$ and $|H_0|^2$. However, taking the square roots of the magnitudes of the positive and negative peaks gives a maximum variation in cell-to-cell field strength of only 10%.

Table 1: Measured and Simulated Cavity Parameters

Parameter	Measured	HFSS	Units
Number of Cells	9	9	-
Pi-Mode Freq	9.59616	9.60084	GHz
Deflecting Voltage	0-530	528	kV
Quality Factor	13043	13672	-
Cell Radius	18.25	18.25	mm
Cell-to-Cell Distance	15.62	15.62	mm
Iris diameter	10	10	mm
Beam pipe diameter	10	10	mm
VSWR	1.04	1.028	-

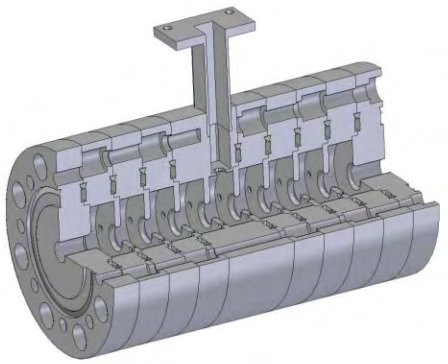

Figure 3: Cutaway drawing of the assembled 9-cell cavity design.

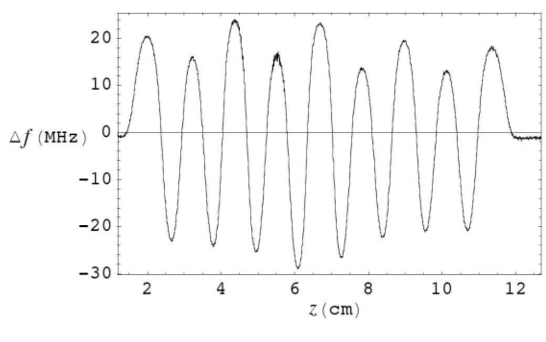

Figure 4: Bead pull field measurement of the deflecting cavity using a metallic bead.

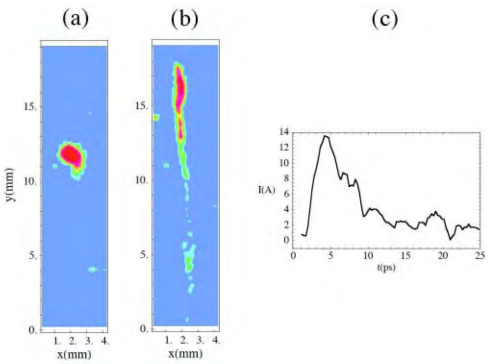

Figure 5: Deflecting cavity streaks of the uncompressed bunch with (a) deflecting cavity off, (b) deflecting cavity on, and (c) the reconstructed current profile.

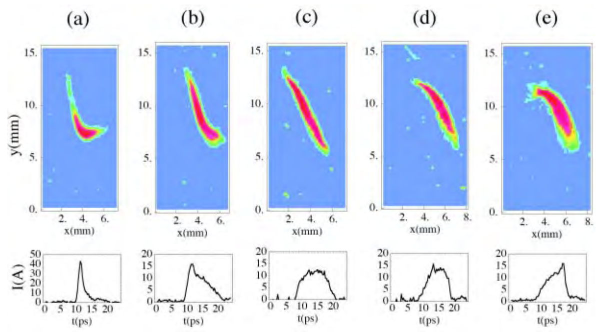

Figure 6: Deflecting cavity streaks and reconstructed current profiles of the (234 pC, 11.86 MeV) compressed bunch at sextupole field strength values of (a) κ = 0, (b) κ = 547 m^{-3},(c) κ = 1094 m^{-3}, (d) κ = 1641 m^{-3}, and (e) κ=2188 m^{-3}.

ELECTRON BUNCH PROFILE MEASUREMENTS

The bunch-shaping scheme for generating ramp-shaped electron bunches proposed in Ref. [4] relies upon injecting an electron beam that has been given a positive energy chirp in the linac (i.e. higher energy particles are at the head of the beam) into the sextupole-corrected dogleg compressor shown in Fig. 1. For an unchirped beam (i.e. on-crest in the linac), there is no significant compression in the dogleg section and the deflecting cavity streak measures the current profile of the uncompressed bunch. An example streak is shown in Fig. 5, indicating an asymmetrical longitudinal bunch shape, presumably inherited from the temporal shape of the UV photocathode drive laser pulse. The extracted RMS bunch length σ_t = 5.9 ps extracted from this plot is consistent with an estimate of the photocathode laser pulse length at the cathode derived from autocorrelation interferograms of the drive laser pulse.

Streaks taken with bunches chirped in the linac by choosing the injection phase to lie approximately 15 degrees back-of-crest, are shown in Fig. 6 for five different sextupole field strengths, along with corresponding current profile reconstructions. The slight horizontal tilt to the streaks is the result of a residual horizontal dispersion introduced by detuning of one of the dogleg quadrupole magnets. The result is a partial reconstruction of the longitudinal phase space, with the horizontal and vertical axes on the streak image representing energy and time respectively. This permits a visualization of the phase space transformation taking place as the sextupole field strength is varied. From the reconstructed current profiles, we see that the initial shape of the bunch in Fig. 6(a) resembles the prediction of our simple model in Fig. 2(b) and progresses toward a ramped distribution as the sextupole field is increased, and the nonlinear term T_{566} in Eq. 1 is reduced. It should be noted, however that the sextupole field value corresponding to $T_{566} = 0$ lies intermediate between the values corresponding to Fig. 6(c) and 6(d). Therefore, the ramped bunch shown in Fig. 6(e) is produced by overcompensating with the sextupoles, reversing the sign of the T_{566} and thereby reinforcing the hard-edged cutoff at the tail of the beam. This overcompensation is required due to the asymmetrical initial (pre-compression) bunch shape and slightly nonoptimal linac injection phase.

CONCLUSIONS

The UCLA Neptune deflecting cavity has been built, installed, tested, and found to operate well within specifications. The cavity has been used successfully to reconstruct the current profiles of electron bunches produced by the Neptune linear accelerator and dogleg compressor with approximately 400 fs resolution, and the results are consistent with the mechanism for generating ramp-shaped electron bunches which was proposed in Ref. [4].

REFERENCES

[1] K. L. F. Bane, Pisin Chen, and P. B. Wilson. On Collinear Wake Field Acceleration. Technical Report SLAC PUB-3662, Stanford Linear Accelerator Center, Stanford, CA 94305, April 1985.

[2] J. B. Rosenzweig. Acceleration and focusing of electrons in two-dimensional nonlinear plasma wake fields. *Phys. Rev. A*, 44:R6189–6192, November 1991.

[3] K. V. Lotov. Efficient operating mode of the plasma wakefield accelerator. *Physics of Plasmas*, 12:053105, 2005.

[4] R. J. England, J. B. Rosenzweig, G. Andonian, P. Musumeci, G. Travish, and R. Yoder. Sextupole Correction of the Longitudinal Transport of Relativistic Beams in Dispersionless Translating Sections. *Phys. Rev. ST-AB*, 8:12801, January 2005.

[5] G. A. Loew and O. H. Altenmueller. Design and Application of RF Separator Structures at SLAC. Technical Report PUB-135, Stanford Linear Accelerator Center, Stanford, CA, 1965.

[6] J. C. Slater. *Microwave Electronics*. Van Nostrand, Princeton, NJ, 1950.